Analysis of Three Body Decays in Quasi-Real Photoproduction

Robert Wishart

Submitted in fulfilment of the requirements for the
Degree of Doctor of Philosophy

School of Physics and Astronomy
College of Science and Engineering
University of Glasgow

April 2023

Abstract

This thesis presents preliminary measurements of the moments of angular distribution for the K^*K^+ mesonic final state using a quasi-real, linearly polarised photon.

Two of the main points of focus for this analysis were the development of the formalism for photoproduced vector-pseudoscalar decay and the tools by which the analysis was carried out. The formalism described how the moments of angular distribution could be extracted from the angular decay variables, and how they related to resonance decays in terms of partial waves. In extracting the moments, it was found that adapted Markov Chain Monte Carlo (MCMC) methods proved to be more effective in terms of extracting results from the data compared to the sole use of gradient descent based fitting algorithms.

These measurements are complementary to other decay channels and production mechanisms, with the global aim of probing the existence of exotic mesons. Data from this analysis was taken by the CLAS collaboration at the Thomas Jefferson National Accelerator Facility (JLab) by scattering from a liquid hydrogen target using a 10.6 GeV electron. This work was done within the MesonEx program at CLAS12 that aims to map the spectrum of mesons, and in doing so, gain a greater understanding of Quantum ChromoDynamics (QCD) and the strong force.

Contents

List of Tables

List of Figures

Declaration

The work in this thesis is based on research carried out at the Nuclear Physics Group, School of Physics and Astronomy, University of Glasgow, UK. No part of this thesis has been submitted elsewhere for any other degree or qualification and it is all my own work unless referenced to the contrary in the text.

Chapter 1

Summary

The existence of exotic mesons has been an open question in hadron physics for many years. The question derives from the nature of Quantum ChromoDynamics (QCD) and the quark model. Gell-Mann and Zweig's 'Quark Model' has successfully categorised many known hadrons based on their 'flavour' symmetry since its conception in the 1960s. Defined by their valence quarks, mesons and baryons are classified in the Quark Model using the 'Eightfold Way'. The theory of QCD is more complicated however than the picture that is presented by the Quark Model. QCD governs the strong force and does not prohibit the existence of so-called exotic states that would exist outwith the Quark Model. Hadronic states are quantum in nature, allowing the existence of virtual quark - anti-quark pairs and virtual gluon exchange. The extension of this fact is the notion of hadronic states beyond the Quark Model - for example, hybrid states that posit the existence of a valence gluon or glueball states that are feasible from the self-interacting nature of the gluon. Probing the existence of states beyond the Quark Model is key to gaining a further understanding of the strong force and QCD, and to take steps towards answering the fundamental questions in QCD, such as colour confinement.

The data that was used in this analysis was taken by the CLAS Collaboration at the Thomas Jefferson National Accelerator Facility (JLab). The CLAS12 detector is well positioned to hunt for exotic states as a result of an energy upgrade from 6 GeV to 11 GeV and detection at a luminosity of $10^{35}\text{cm}^{-2}\text{s}^{-1}$ [16]. Other experiments such as COMPASS have used pion beams to probe the existence of exotic states. The quasi-real photon beam used here provides measurements complementary to this, as well as providing access to additional polarised intensity components.

Previous experiments have developed reaction models that incorporated spinless beam and final state particles. In this analysis, a model was developed that encompassed the linearly polarised spin-1 photon impinging on a fixed proton target and producing a pseudo two-body decay to a vector-pseudoscalar final state - the $K^* + K^+$, with the $K^* \to K^- + \pi^+$. Exotic behaviour in this reaction would be exhibited by detecting partial waves in the decay quantum numbers not allowed by pure Quark Models. Partial waves can be extracted from the data either

by fitting the data directly with a set of wave amplitudes or by first fitting the moments of the decay angular distribution to the data. The focus here was to determine the moments as a function of meson mass, from which the full mass dependent partial waves may be extracted in a subsequent analysis.

The tools that were used in this analysis were developed specifically to tackle problems that generally occur in hadron spectroscopy analysis - big data and large parameter spaces. In this example, standard gradient descent based fitting algorithms were found to be unreliable. As a result, two adaptations of a Metropolis-Hastings Markov Chain Monte Carlo (MCMC) procedure were developed to allow a more efficient sampling of the posterior distribution, and therefore determine the globally optimised fit parameters.

The procedure by which moments of decay angular distributions were extracted from the data was validated using 'toy' studies - using the model to fit on generated data with known wave content. In this way effects such as systematic biasing of results, originating from effects like finite detector acceptance, for example could be studied. Part of this analysis was dedicated to understanding and eliminating such unwanted features in the parameter extraction.

Preliminary results for the moments of angular distribution are presented, with the caveat that the collaboration is in the process of cooking the data and so only an initially calibrated subset of the data was available. The results presented here are dominated by statistical uncertainties so analysing the full better calibrated data set will provide significant improvements in this regard and allow extraction of partial waves.

Chapter 2

Background

2.1 The Strong Force and QCD

Along with gravity, electromagnetism and the weak force, the strong force is one of the four fundamental forces of nature. It is described by Quantum Chromodynamics (QCD) and is responsible for a large proportion of the mass in the observable universe. The strong force acts on quarks that in the quark model form bound states in the form of either baryons (three bound quarks) or mesons (a bound quark - anti-quark pair). A particle that is formed of quarks is called a hadron. Hadrons are held together through the interaction of integer spin bosons, called gluons, which mediate the strong force. There are six types of quark that are included in the standard model. The lightest of these are the up, u, and down, d, quarks. These carry the electric charge $+\frac{2}{3}$ and $-\frac{1}{3}$ respectively. The other quark that is included in what is known as the 'light quark sector' is the strange quark, s, that also has the electric charge $-\frac{1}{3}$. There are three further quarks that complete the standard model, these are (along with their electric charge): charm (c, $+\frac{2}{3}$), top (t, $+\frac{2}{3}$), bottom (b, $-\frac{1}{3}$).

As noted, the quarks carry electric charge and therefore interact electromagnetically as well as via the strong force. There is the comparison to be made between our theories of the strong force and electromagnetism. Electromagnetism is mediated by the photon with the symmetry group $U(1)$ as described by Quantum ElectroDynamics (QED). On the other hand, the strong force is mediated by the gluon, the gauge boson of the strong interaction, with the symmetry group $SU(3)$. The gluon and the photon are both spin-1, massless gauge bosons. Importantly, and analogously to the electric charge of electromagnetism, there is a charge associated with the strong force known as the 'colour charge'. The name holds no association to colours as we know them, rather it is simply a convention, with each quark carrying the 'red', 'blue' or 'green' charge. For a given anti-particle, the same convention applies, anti-particles can be 'anti-red', 'anti-blue' or 'anti-green'. Fundamentally, every particle acting under the strong force must be colour neutral, or rather, a colour-singlet state, and this is known as colour confinement [27]. In other words, in the example of baryons containing three quarks, one quark must be red, one

blue and one green. In the case of a meson, the colour of the quark must be equivalent to the anti-colour of the anti-quark. There is no known case of coloured quarks existing individually in unbound states.

More formally, some important properties of the gluon become clear by understanding the nature of the symmetry group $SU(3)$. In this context, quarks are identifiable as spinors in the fundamental representation of the Lie group of $n \times n$ unitary matrices. The gluons, on the other hand, exist as vectors in the adjoint representation which can be thought of as the set of endomorphisms on the set of $n \times n$ unitary matrices. For the Lie group $SU(n)$, the dimension of the adjoint representation is $n^2 - 1$ which gives 8 gluons. If QCD did have the symmetry group $U(3)$, then there would exist a ninth gluon that would exist in a colour singlet state, often written as $(r\bar{r} + b\bar{b} + g\bar{g})/\sqrt{2}$ [28]. There is no explanation from first principles that explains why QCD has the group $SU(3)$ rather than $U(3)$, however all experimental evidence supports this hypothesis [28].

Following this discussion, the significant difference between the strong force and electromagnetism is the fact that the photon does not carry the electric charge whereas the gluon does have a colour charge. This has the implication that the gluon is self-interacting, which has several implications on the theory of QCD. One particular effect that derives from this is known as 'asymptotic freedom'. In describing the origin and role that asymptotic freedom plays in QCD, it is again useful to consider the comparison with QED in electromagnetism. Consider an isolated charge in a vacuum. In this situation, the effect of the charge is to partially polarise the vacuum by creating instances of virtual pairs of particle - anti-particle pairs (such as electrons and positrons). This isolated dipole charge acts to align in the field of the charge with opposing charges attracted. The net effect is a partial cancellation of the field at some finite distance from the charge. This effect is known as 'screening'. In QCD, interacting particles are also electrically charged and so the principle of screening exists here too. As the gluon also carries the colour charge the same principle applies again, with the difference that the anti-magnetic moment of the gluon acts to increase the polarity of the vacuum rather than to counteract it in the way of QED. This is called 'anti-screening' and acts in competition to the screening factor in QCD. Quantifying which of these factors dominates the other, the formula to calculate the scale factor, also known as the strong coupling constant, is given by:

$$\alpha_{QCD}(Q) = \frac{6\pi}{(33 - 2n_f)\log(\frac{Q}{\Lambda})}, \tag{2.1}$$

where $\frac{Q}{\Lambda}$ is an energy scale factor and n_f is the number of quark flavours. The value Λ is experimentally derived and has a value $\Lambda \sim 0.2$ GeV [29] while Q is the energy parameter on a relative scale on which the function is based. The dependence of the strong coupling constant on the energy Q is shown in Figure 2.1, noting the logarithmic scale on the x-axis. As a result, at a beam energy of 1 TeV, α has a value of ~ 0.1. In natural units, the quantities of energy

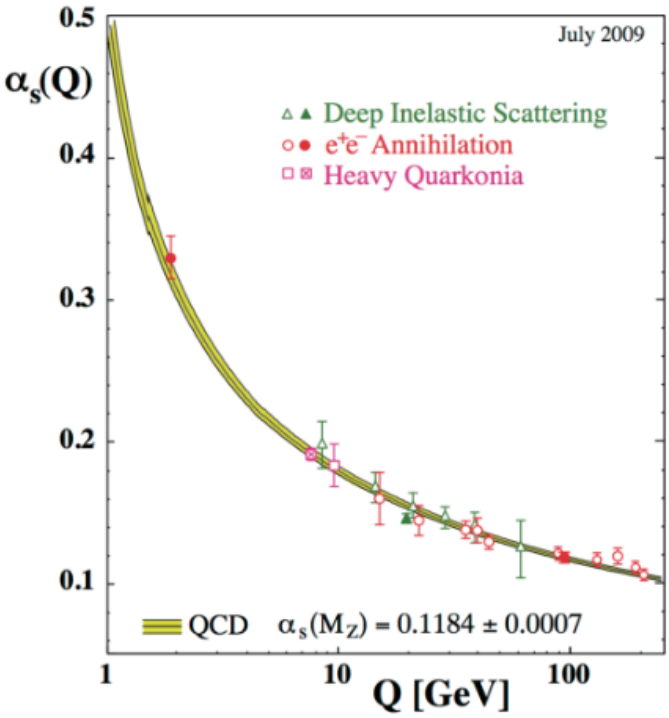

Figure 2.1: The dependency of the strong coupling constant on energy scale [1]. The strength of the constant increases with decreasing energy and increasing length.

and length have an inverse relationship such that $[E] = [l]^{-1}$, where energy is denoted E and length is denoted l. Based on this, as the energy increases, the length scale decreases and α decreases with increasing distance. Relating the value of the strong coupling constant to length, the value of α is of order one at distances comparable to the proton radius. In terms of the sign of the scale factor, there are six flavours of quark and as such anti-screening dominates due to the relative coupling strengths. The system is asymptotically free as the energy scale increases. The discovery of asymptotic freedom won the Nobel prize in 2004 for David Gross and Frank Wilczek and separately for David Politzer for their independent formulation of the theory in 1973 [30] [31] [32] [33].

Examining the properties of the strong coupling constant more closely allows us to learn more about QCD. Asymptotic freedom states that as the energy of two strongly interacting particles increases, the influence that each particle exhibits on the other decreases exponentially and in the limit of high energy two strongly interacting particles will exert no influence on the other. In terms of scattering experiments, high energy is equivalent to probing small scattering lengths and problems can be solved perturbatively. On the other hand, as we move towards experiments at lower energy scales, the assumption that these interactions can be described perturbatively no longer holds. Strong interactions with particles at lower energy (or equivalently larger scattering lengths) must be solved using non-perturbative methods that, in general, lead to a more complex formalisms that must include more modelling or experimentally driven work.

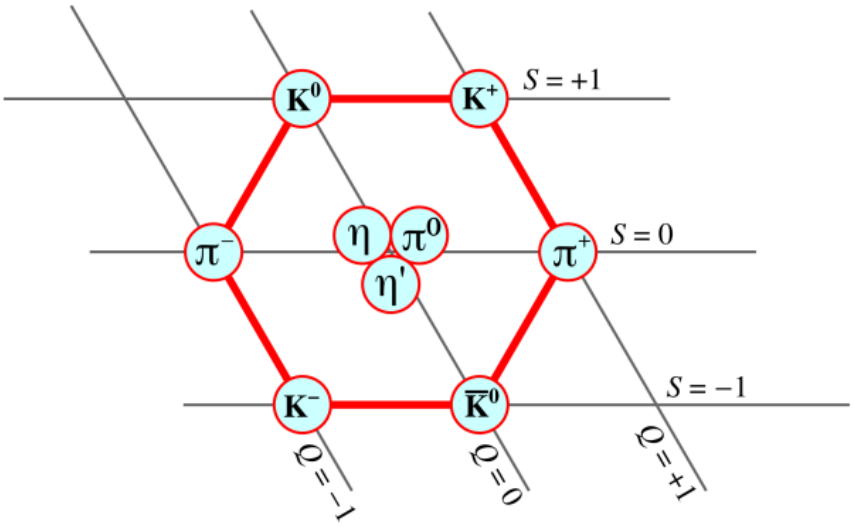

Figure 2.2: The pseudoscalar meson nonet, characterised by quantum numbers $J^P = 0^-$. Taken from [2].

2.2 The Quark Model

The quark model of Gell-Mann and Zweig postulates that all basic hadrons can be categorised based on their quark content into mesons and baryons, with their constituent quark content being a quark - anti-quark pair or a three quark bound state respectively. The nature of the eightfold way follows from the group symmetry $SU(3)$, the group being of order 3 as a consequence of there being three colour charges.

In the case of mesons, it is necessary to combine a colour state (from the quark) with its anti-colour state (from the anti-quark). In group representation, these states are labelled as **3** and $\overline{\mathbf{3}}$ respectively. In forming a bound state from a quark and an anti-quark, one may use Young Tableaux as a means of deriving the group structure that comes from this combination [34]. The calculation shows that the bound state of a quark and an anti-quark is composed of a singlet state, denoted in group representation theory by 1, and an octet state, denoted 8. In full this is written: $3 \bigotimes \overline{3} = 1 \bigoplus 8$, giving 1 + 8 = 9 bound meson states. Together the octet and singlet state compose a nonet of nine states, with an individual nonet characterised by spin and parity. The well known pseudoscalar nonet defined with spin = 0 and negative parity is shown in Figure 2.2. In a similar way, the baryons are categorised into decuplet, octet and singlet states.

2.3 Beyond the Quark Model

An active area of study in hadron physics is whether there are states that exist beyond this quark model picture. In other words, do states exist that belong outside the qqq and $q\overline{q}$ systems - so-called 'exotic' states. Potential candidates for exotic states are tetraquarks ($q\overline{q}q\overline{q}$), pentaquarks ($qqqqq$), hybrids ($q\overline{q}g$) and glueballs ($ggg$), notably hybrids and glueballs are particularly exotic

due to the presence of valence gluons. The evidence for the existence of an exotic state will differ depending on the type of state under question, such as finding more states than are predicted by the quark model or from unexpected properties of a decay (such as an anomalous decay width).

2.4 Hybrid Mesons

Evidence for hybrid states can lie in the quantum numbers such as spin, parity and charge conjugation (J, P and C) that adhere to conservation laws. For a standard meson in the quark model, the parity and charge conjugation quantum numbers are given:

$$P = (-1)^{L+1}, \tag{2.2}$$

$$C = (-1)^{L+S}, \tag{2.3}$$

where L is the angular momentum between the quark and anti-quark and S is the total spin of the quark and anti-quark (which can be 1 if aligned or 0 if anti-aligned). Given this, some combinations of quantum numbers are allowed and some will be forbidden. For example, in J^{PC} notation, vector meson states with $J^{PC} = 1^{--}$ are allowed however states with $J^{PC} = 1^{-+}$ are not. In an experiment, if a particle were seen with exotic quantum numbers then this would be evidence for the existence of exotic states. The exotic quantum numbers would derive from a constituent gluon in a hybrid state and there is some current evidence that a 1^{-+} hybrid state exists which is discussed in Chapter 3.

There is still much speculation on the mechanism by which hybrids can be formed - among some candidate models are the 'bag model' and the 'flux tube model'. The bag model bases the theory of hadron structure on the principle that a strongly interacting particle is the confinement of a field to some region of space [35]. In the context of hadrons, and in particular mesons, the bag model allows colour neutral states of quarks, anti-quarks and gluons, thus bringing into question the relation between conventional $q\bar{q}$ and hybrid $q\bar{q}g$ states. A proposed explanation for this is that the standard spectrum of quarks can be produced from expansions of the sort $|q\bar{q}\rangle + O(\sqrt{\alpha_s})|q\bar{q}g\rangle$ [36]. The gluon with quantum numbers $J^P = 1^-$ when combined with the quark/anti-quark pair can give rise to quantum numbers that exist outside the scope of that of the quark and anti-quark. The flux tube model is phenomenologically different from the bag model. In the flux tube model, a quark and anti-quark pair are bound by a potential that can be modelled in terms of excitation modes as a string bound between two fixed points [37]. Excitation modes of the 'gluonic string' give rise to orbital angular momentum of the system that can permit the quantum numbers of the system as a whole to be exotic. Further modelling of hybrid states will be aided by more conclusive experimental results on the presence of exotics, which so far has not been forthcoming.

2.5 Hadron Spectroscopy from Lattice QCD

The search for exotic states is fuelled by advances in both the experimental and theoretical sides of hadron spectroscopy. From an experimental standpoint, there have been numerous results published while a summary of the current experimental status of the relevant parts of hadron spectroscopy will be detailed in Chapter 3.

On the theoretical side, calculations performed from Lattice QCD have given the hadron physics community insight into details of exotic states that have been notoriously hard to come by due to the nature of the strong force as discussed previously. The first ideas relating to Lattice QCD were formulated by Kenneth Wilson in 1974 and with advancements in computing and developments in theory LQCD has come to the forefront of theoretical hadron physics at the turn of the century [38] [39]. In the absence of a non-perturbative method of solving QCD calculations, Lattice QCD incorporates the notion of the discretisation of space constructed using a grid in space - or a lattice, from which the theory takes its name. In the simplest regard, when the lattice spacing becomes infinitesimally small the principles of QCD are re-emergent. The resurgence of Lattice QCD at the end of the 20th century arose from what came to be known as the 'quenched approximation' - that the perturbative part of the expansion of hadronic structure was based on the gluonic field, and that the simplicity of the problem (and hence the computational expense) could be improved by considering the properties of hadrons based on a simple gauge field [40]. Lattice QCD passed early tests, such as predicting the masses of quarks and hadrons like the proton and the most recent developments in the field are aiming to improve errors arising from systematic effects in order to benefit from improved computing and algorithmic advances [40] [41].

Lattice QCD predictions and the experimental search for exotic states go hand in hand in the sense that evidence for the existence of exotic states in one will drive efforts to consolidate or disprove such a claim in the other. By 2010, there had been a collection of evidence gathered in the experimental field that pointed towards a small set of possible candidates for hybrid mesons, these states were labelled $\pi_1(1400)$, $\pi_1(1600)$ and $\pi_1(2015)$ [42] [43]. In this nomenclature $\pi_n(m)$, n refers to the total angular momentum quantum number of the meson J, and m to its approximate associated mass. Due to the large overlap in operator space between these states and gluonic construction operators, the best current hypothesis is that the lowest mass hybrids would have the quantum numbers $J^{PC} = 1^{-+}$ [44]. The full spectrum of mesons that are produced from Dudek et al. is shown in Figure 2.3.

An analysis by Meyer and Van Haarlem in 2010 nicely summarised the knowledge of exotic states at the time [43]. They arrive at their conclusion that the $\pi_1(1400)$ can be explained as a non-resonant multiquark state and due to its relatively low mass, not a likely candidate for a hybrid state, although still requiring further confirmation from experimental work. There is even less evidence available for the possible existence of the $\pi_1(2015)$ and more data is needed before a conclusive statement can be made on the existence of this hybrid candidate.

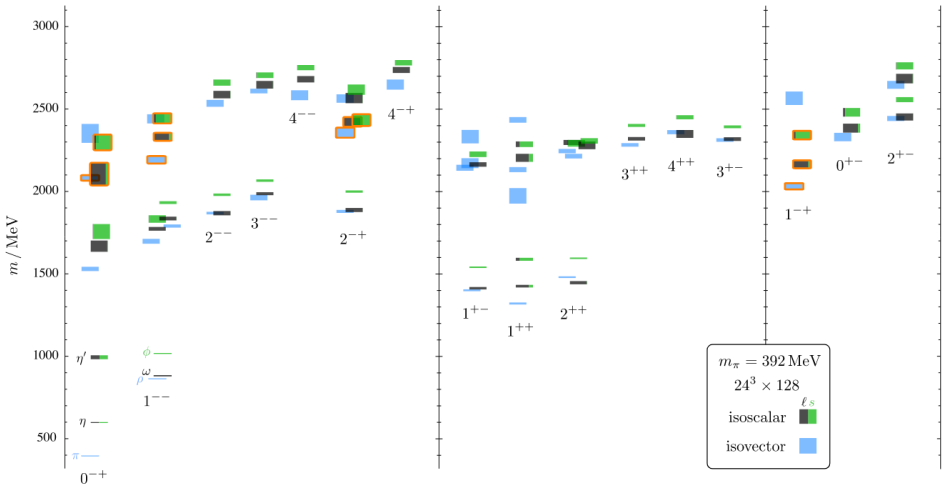

Figure 2.3: The spectrum of mesons from Lattice QCD in terms of their J^{PC} quantum numbers. The right-hand column contains exotic states that exist outwith the structure of the quark model. The mass scale is explained as the mass of a state is scaled by the mass of the Ω-baryon produced on the same lattice scale, as such any dependence on the lattice scaling is removed. Taken from [3].

On the other hand, the $\pi_1(1600)$ is a good candidate for a hybrid meson. From the Lattice QCD standpoint, this is supported by model predictions and despite the mass of the state still being on the low side, Meyer and Van Haarlem give their view that the chance of this state being a non-resonant multiquark state is less likely. Additionally, there is a wealth of data that has been analysed on channels coupled to the decay of the $\pi_1(1600)$, with signals being attributed to the $\pi_1(1600)$ seen in the $\eta'\pi$, $f_1\pi$ and $\rho\pi$ decay modes [43]. The potential hybrid nature of the $\pi_1(1600)$ led to deeper theoretical investigation of properties of the meson - in particular relating to the decay of the meson, since hybrid candidates are possible in a number of decay channels. Further, there could be no coupling to decay channels as in formulation of Lattice QCD at the time the hybrid candidates were generated as stable particles, contrary to the very nature of QCD.

To this end, the Hadron Spectrum collaboration published a paper in 2021 in which there is a first demonstration of the generation of the 1^{-+} hybrid meson candidate as a resonance [4]. Their analysis is described by an eight channel scattering of the state with quark masses of each of the quarks in the light sector fixed at 700 MeV. The published results of the study are that the lattice spectra that are produced can be described by a hybrid octet with SU(3) symmetry and the appearance of a narrow resonance. This narrow resonance is located above the pseudoscalar-pseudoscalar, pseudoscalar-vector and vector-vector kinematic decay thresholds but below the pseudovector-pseudoscalar threshold. The relevance of this is that the coupling of the open channels (the ones in which the threshold is kinematically below the position of the pole) is relatively weak compared to that of the coupling to the pseudovector-pseudoscalar. The relative coupling strength is shown in Figure 2.4 from which can be seen the dominance of the $b_1\pi$ decay

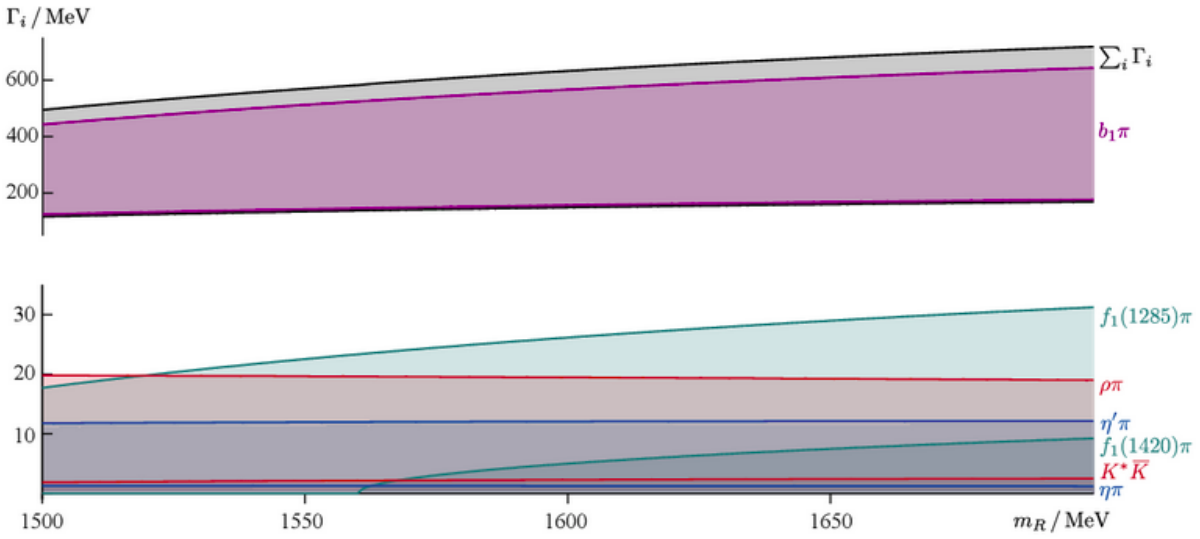

Figure 2.4: The relative coupling strengths of decay modes of the $\pi_1(1600)$ meson varying with the resonant mass of the pole. Taken from [4].

mode relative to the other decay modes ($\rho\pi$ or $\eta\pi$ for example).

This is a fact that is challenging for experimentalists as the main decay of the b_1 is to $b_1 \to \omega\pi$, with the ω meson decaying to a three pion final state. In full, analysis of this decay chain would therefore require the detection of five pions and the analytic complexity that unavoidably comes with it. In any case, the decay modes that have been studied so far are of the highly suppressed decay modes of the $\pi_1(1600)$ and are yet to give conclusive results of the possible hybrid motivating further study such as the current work on the three body final state. States with other proposed exotic quantum numbers shown in Figure 2.3, have so far no experimental evidence [43].

2.6 Photoproduction

As described in Chapter 3, many of the early experiments in search of evidence for exotic states used a hadronic beam. However, there are suggestions that events produced from photons are a more suitable ground on which to search for exotics due to implications of the flux tube model [37]. In their model, they describe the flux tube as being excited, with preferred quantum numbers being 1^{--} and 1^{++} for a pion beam based on spin and parity considerations. A state with exotic 1^{-+} quantum numbers can be produced using pions but this requires a spin flip in quark exchange rather than purely gluonic exchanges. A photon beam on the other hand does not require a spin flip. This can be explained by looking at the quantum numbers in the production of a 1^{-+} state. In accordance with the vector meson dominance model, a photon interacts with a hadronic target through the scattering of a vector meson such as ρ, ω with the same quantum numbers as the photon, $J^{PC}_{\gamma} = 1^{--}$. Additionally, the lowest lying gluon ex-

citation mode, the Transverse Electric (TE) mode, has been shown to have quantum numbers $J_g^{PC} = 1^{+-}$ [45]. As a result,

$$J_\gamma^{PC} \times J_g^{PC} = 1^{--} \times 1^{+-} = 1^{-+}. \tag{2.4}$$

Therefore, it is expected that experiments with a spin-1 beam such as photoproduction should offer enhanced opportunity to study hybrid states compared to a spin-0 hadronic pion or kaon beam. The quoted value given in [45] states that production of exotics in photoproduction compared to hadron production should be improved by a factor between 5 and 10.

Chapter 3

Hybrid Meson Experimental Status

There is already data that has been analysed with reference to the search for exotic hybrid meson states, taken from a variety of experimental facilities. The data for the current experiment uses a quasi-real photon beam, and results from experiments such as these are complementary to experiments that use a pion beam, for example. This chapter will provide an overview of the experiments that have been performed to date in response to the search for hybrid mesons and comment on their results. Ambiguity apparent in some of the results can be attributed to general features of the search for exotics. Due to the extremely small relative branching fraction in the decay, it is not possible to claim the existence of an exotic particle based on the inspection of a mass spectrum, rather it is generally required to first extract the partial waves of the decay.

Evidence for resonance behaviour in an exotic wave results from a peak in the intensity of the wave and the behaviour of the wave relative to other waves. Intensities of partial waves are often modelled using Breit-Wigner amplitudes and so enhancement of a signal of this form is evidence of the partial wave in the decay. In addition to the peak in intensity, evidence for a particular partial wave in the decay of a resonance derives from the interference of that wave with another, giving a resultant phase motion. The phase difference is constant between a resonant and non-resonant component, however between two different resonant components there will be an associated 'turning over' in the relative phase. Factors such as the phase motion and the question of whether a signal is even resonant are often a source of uncertainty in the results.

3.1 Early Results

The earliest instance of a positive recorded result for a hybrid exotic state came in 1988 from Alde *et al.* who reported a broad state with quantum numbers 1^{-+} being present in the $\eta\pi^0$ decay channel with mass, $m = 1.406 \pm 0.02$ GeV and width, $\Gamma = 0.18 \pm 0.02$ GeV [46]. This result, in line with all the early results in this search are based on pion-production experiments. Although a subsequent analysis of the same channel contradicted this result [36], quoting from the Alde paper '*The discovery of other exotic states should now be firmly expected*' pre-empts

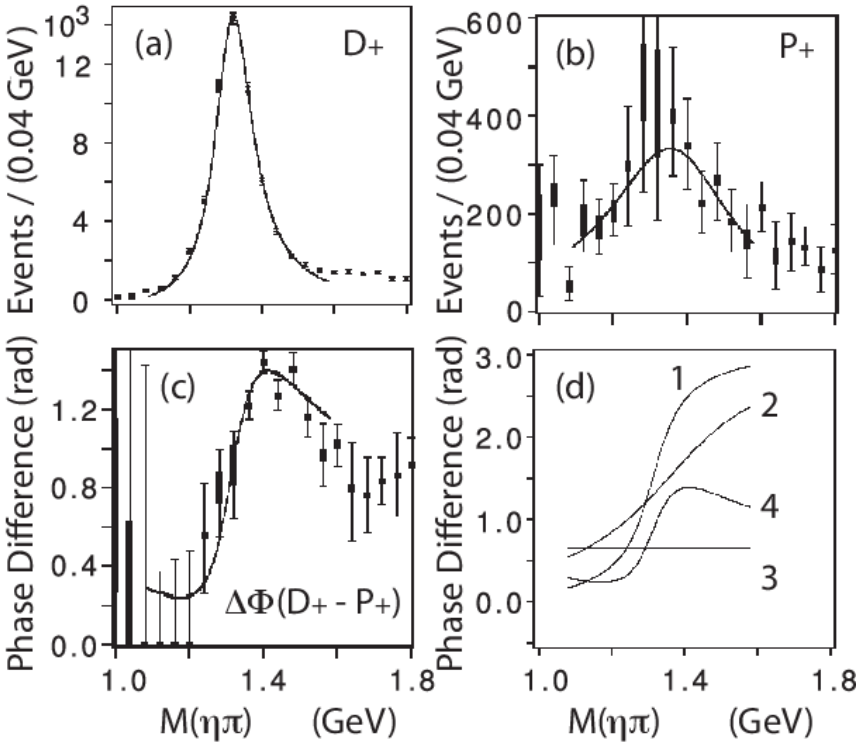

Figure 3.1: The results from the E852 analysis in the search for the $\pi_1(1400)$. Frame (a) shows the resonance peak of the 2^{++} associated with the $a_2(1320)$. Frame (b) shows that of the exotic 1^{-+} wave. Frame (c) shows the phase difference between the two waves of the $a_2(1320)$ and the $\pi_1(1400)$. Frame (d) shows the components that make up the exotic wave phase difference. Figure taken from [5].

the interest of the hadron physics community with exotic states for years to come. In a similar experiment by Aoyagi et al. (1993) it was noted that there was an enhancement in the P-wave decay around the same 1.4 GeV mass in the $\eta\pi^-$ decay channel, however it was noted there was no confirmed phase difference relative to the D-wave in this analysis [47].

3.2 Further Searches for the $\pi_1(1400)$

Further searches for the $1^{-+}\pi_1(1400)$ yielded positive results - at Brookhaven National Lab the E852 Collaboration reported a result with mass of $(1.37 \pm 0.016^{+0.05}_{-0.03})$ GeV and a width of $(0.385 \pm 0.04^{+0.065}_{-0.105})$ GeV and with phase motion representative of a resonance relative to the measured $a_2(1320)$ [5]. The results from this experiment are shown in Figure 3.1. In addition to this, the VES Collaboration noted results with an associated phase motion as shown in Figure 3.2 [6]. The mass and width of this state was 1.316 ± 0.012 GeV and 0.287 ± 0.025 GeV respectively. Some later commentators on this analysis had expressed doubts on the resonant nature of this state due to its unexpected light and broad nature and suggested its appearance could be due to inelastic scattering mechanisms [36].

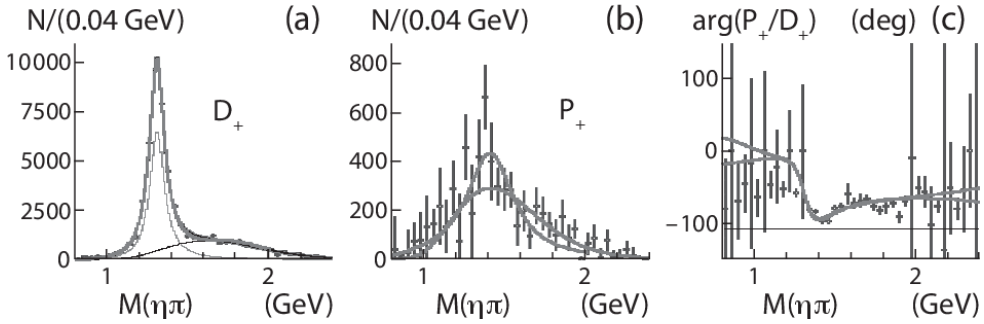

Figure 3.2: From left to right: the presence of the D_+, P_+ waves and their relative phase motion in the VES $\eta\pi$ experiment. Taken from [6].

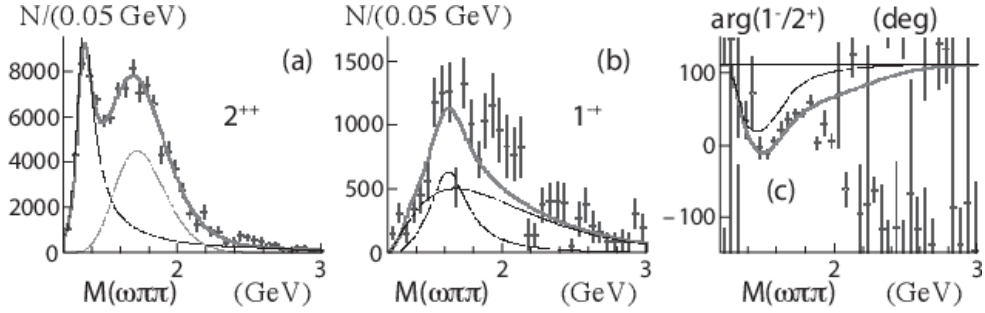

Figure 3.3: In the decay of $b_1\pi$, from left to right: the D_+ wave, the exotic P_+ wave and the relative phase between the two waves. Taken from [7].

3.3 First Investigation in Other Mass Ranges

The hunt for exotics was not limited to the $\pi_1(1400)$ (and not necessarily limited to the 1^{-+} quantum numbers either). In the $\eta\pi$ channel, the VES Collaboration noted the emergence of a resonance but with a mass nearer 1.8 GeV and quantum numbers 0^{-+} and thus being labelled the $\pi(1800)$ [48]. Another early candidate for an exotic state that emerged in multiple decay chains and at various experimental facilities was the $\pi_1(1600)$. The VES Collaboration reported seeing a state with exotic quantum numbers with a mass of $\sim$1.6 GeV in the pion production of the $b_1\pi$, $\eta\pi$ and $f_1\pi$ final states [7]. Some of the results of this study are shown in Figures 3.3, 3.4. This state was also broad, with a mass of (1.61 ± 0.02) GeV and a width of (0.29 ± 0.02) GeV. Additionally, the E852 Collaboration detected the state in the $\rho\pi$ decay channel with a mass that was consistent with that of the VES result as shown in Figure 3.5 [8]. There was no mention of the other reaction channels in the BNL paper.

Despite the apparent abundance of evidence for the existence of hybrid states, some of it was contradictory. For example, the 1999 report by the VES Collaboration reported a branching fraction for the $b_1\pi$ decay mode approximately equal to that of the $\eta\pi$ and $\rho\pi$ decay modes that are expected to be highly suppressed in comparison to that of the b_1 [7] [36]. Further, there was inconsistencies in the proposed mass values of the states with reference to any theoretical predictions for the states using models at the time. Lattice QCD predicted that the lightest hybrid state would lie around 2 GeV and the flux tube model predicted the spectrum of hybrids

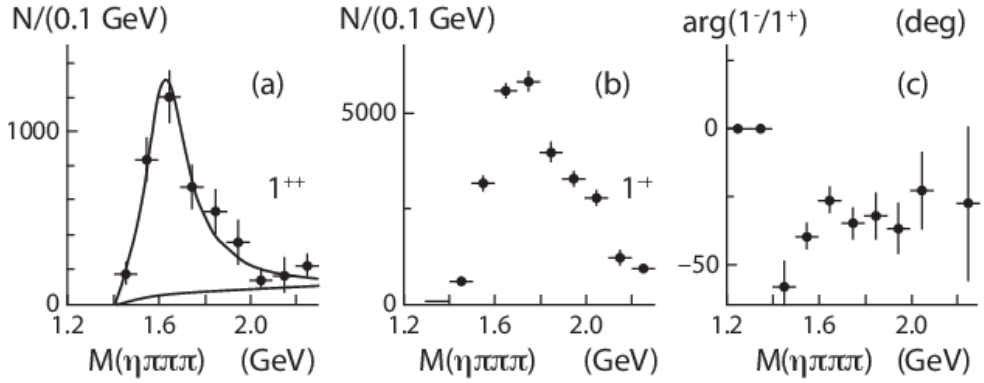

Figure 3.4: In the decay of $f_1\pi$, from left to right: the D_+ wave, the exotic P_+ wave and the relative phase between the two waves. Taken from [7].

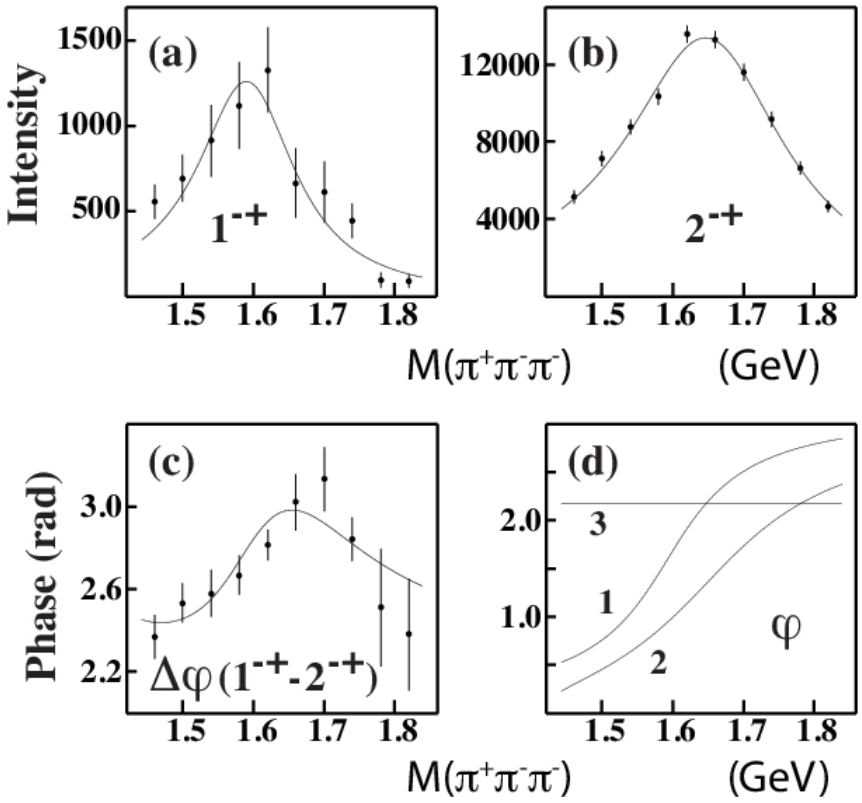

Figure 3.5: Results of the E852 experiment in the search for the $\pi_1(1600)$ in the three charged pion final state. Subfigures (a) and (b) show the intensity of the 1^{-+} and 2^{-+} waves respectively. Subfigure (c) shows their relative phase motion and (d) shows the phases. Taken from [8].

to begin in the 1.9 - 2 GeV region, in contrast to the experimental results described above [49]. In addition, on the experimental side, it was noted that it could not be ruled out that there were more factors at play, such as the reliability of the background subtraction, and the production mechanism that was being modeled to fit data - for example, if non-resonant effects could in fact be used to describe what was being seen in the data [36].

3.4 First Problems in Wave Set Selection

Subsequent analyses were performed with the intention of attaining data sets with much greater statistics in order to investigate the features of the original experiments that were not understood. A result from Dzierba *et al.* (2006) used a dataset that was over an order of magnitude greater in size than the largest data published to date (that of the E852 Collaboration in [8]) [50]. This analysis was the first to explicitly confront the problem of wave set selection in an analysis such as this, and to explore the instability that it entails in terms of quantifying results. Beginning with a large parent wave set, they explored a method in which waves were removed if their removal did not entail a worsening of the likelihood compared to the same set with that wave included. This resulted in two fits to the data with wave sets named the 'low wave' and 'high wave'. When the low wave set was used, there was behaviour in the mass range around 1.6 GeV that is consistent with earlier results from VES and BNL, however, using the high wave set showed no enhancement in the exotic wave in this mass region. Both wavesets showed phase motion of the exotic wave relative to the dominant $a_2(1320)$. Their final conclusion was that this did not show evidence of an exotic meson.

The fact that the phase motion of the exotic 1^{-+} is consistent across wavesets is explored briefly in [51]. One argument is that the $\pi_1(1600)$ that is present in the data may become overwhelmed by stronger resonances as more are added to a waveset. On the other hand, the competing point can be made that background effects can easily become entwined with less prominent waves and the problem of differentiating between low intensity waves becomes increasingly difficult as the parameter space of the waves gets larger. Also noted is the effect that other dominant resonances can have. A possible explanation given for the appearance of an exotic signal in the 1.6 GeV region is leakage from the prominent $\pi_2(1670)$ in some final states, which would discount the need for a $\pi_1(1600)$ signal at all to provide a good account of the data.

3.5 The COMPASS Experiment

3.5.1 COMPASS $\pi^-\pi^-\pi^+$ data

The largest sample of π production data that has been taken to date was by the COMPASS Collaboration based at CERN [9]. The published data from COMPASS was taken using a π beam

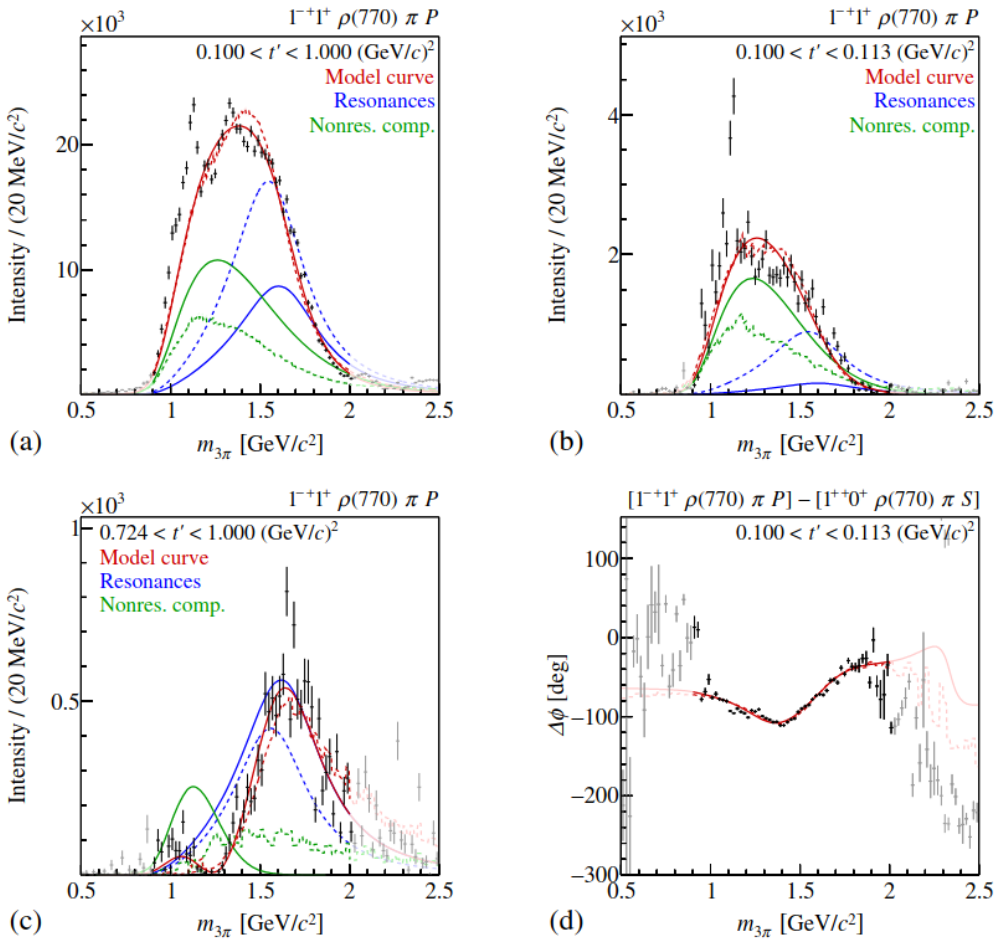

Figure 3.6: Results from the COMPASS Collaboration in the search for the $\pi_1(1600)$ in the three π final state. (a) the intensity of the $J^{PC}I^G = 1^{-+}1^+\rho(770)\pi - P$ wave summed over t. (b) and (c) the intensity of the wave in the lowest and highest $t-$bins respectively. (d) the phase of the wave relative to the $1^{++}0^+\rho(770)\pi S$ wave in the lowest $t-$bin. Taken from [9].

at 190 GeV/c on a proton target and was based on a dataset of 4.6×10^7 events in the $\pi^-\pi^-\pi^+$ final state. A set of 88 partial waves were used in this fit, reduced from a starting set of 126 iteratively if the intensity for any given wave was below the relative intensity threshold of 10^{-3}. One result of this analysis was the emergence of a resonant $\pi_1(1600)$ - strongly dependent on the square four-momentum transfer variable t'. The behaviour of the exotic wave was modelled using a resonant component and a non-resonant part described using an amplitude for two body decays as a function of the breakup momentum q and the momentum transfer t'. It was found that at low values of t' close to 0.1 GeV^2 the non-resonant process was dominating through constructive interference with the resonance but at higher values of t', the non-resonant component decreases rapidly leaving a peak in the mass region expected of the $\pi_1(1600)$. The final quoted results state that for the resonance, the mass is $1.6^{+0.11}_{-0.06}$ GeV and the width $0.58^{+0.1}_{-0.23}$ GeV, with the large systematic uncertainties arising from the significant model dependence in the analysis. These results are shown in Figure 3.6.

3.5.2 COMPASS $\eta\pi$ and $\eta'\pi$ data

In addition to the $\pi^-\pi^-\pi^+$ reaction channel, the $\eta\pi$ and $\eta'\pi$ reaction was also analysed by COMPASS [52]. The advantage of this channel compared to that described above is the fact that in the pseudoscalar-pseudoscalar final state, if the state has odd angular momentum then it is an exotic state (since the angular momentum coincides with the total angular momentum). A total of 4.5×10^9 events were collected in this sample. They noted that there was an intensity peak in the $\eta\pi$ system at 1.4 GeV and in the $\eta'\pi$ system at 1.7 GeV. The phase motion of the two peaks is different however when compared with the respective $L = 2$ wave as shown in Figure 3.7. Their conclusion from this analysis was that in the $\eta\pi^-$ decay channel, the intensity of even partial waves are relative to those in the $\eta'\pi^-$ decay channel. However, odd partial waves are suppressed in the $\eta\pi^-$ channel relative to the $\eta'\pi^-$ channel, underlining the importance of flavour symmetry.

3.5.3 COMPASS $\eta\pi$ and $\eta'\pi$ data - JPAC analysis

Data from COMPASS in the $\eta\pi$ and $\eta'\pi$ final state was also analysed by A. Rodas et al. (Joint Physics Analysis Center (JPAC)) [10]. This was the first analysis to be performed using a coupled channel approach in order to study the results for the $\pi_1(1400)$ and the $\pi_1(1600)$. Using an approach based on the principles of the S-Matrix, they were able to determine poles for the $a_2(1320)$ and $a_2'(1700)$ that are consistent with single channel analyses relating to these resonances. In relation to the exotic waves, they found that one pole is sufficient to model the observed structures at 1.4 and 1.6 GeV that were seen in the COMPASS data [9] [52]. Their pole is defined with a mass of $1.564 \pm 0.024 \pm 0.086$ GeV and a width of $0.492 \pm 0.054 \pm 0.102$ GeV and varies in terms of the systematic effects as shown in Figure 3.8. This is consistent with the result in the three pion final state providing solid evidence for the existence of a 1^{-+} exotic hybrid state.

3.6 Previous Photoproduction Measurements - First Data taken at CLAS

Complimentary to pion production experiments, photoproduction has also been used to produce the three pion final state. The largest set of such events that have been reported on to date is the CLAS experiment that ran at Jefferson Lab from 1998 to 2012. The CLAS experiment was thought to be fertile ground for the study of photoproduced exotics, with studies showing the cross sections of hybrid production would be high enough that the proposed JLab experiment could observe these states [53]. The CLAS experiment was designed to run with a 5.744 GeV electron beam creating a tagged photon beam with high luminosity [11] on a hydrogen target - the first experiment to use a photoproduced final state in the search for exotics. This analysis

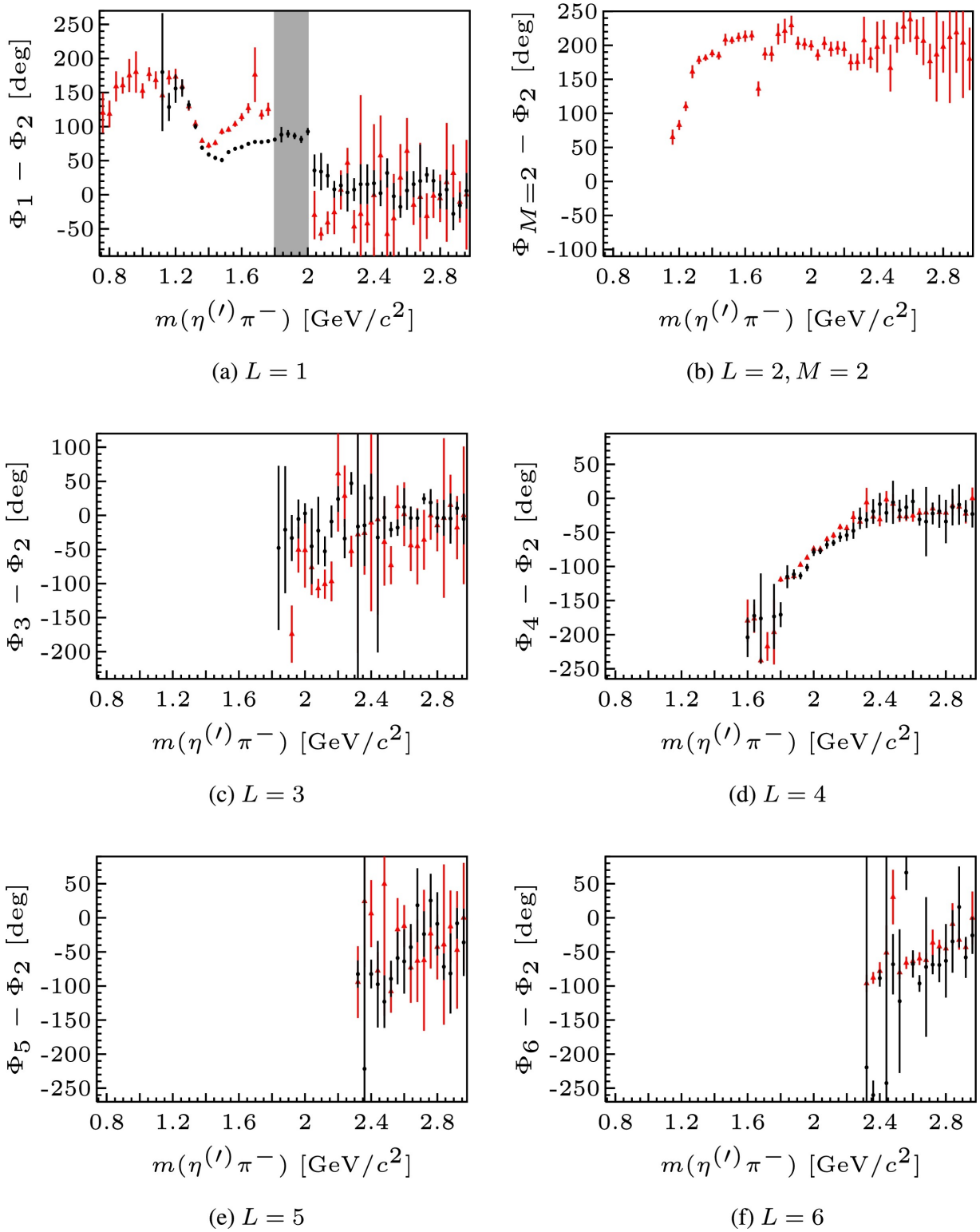

(a) $L = 1$ (b) $L = 2, M = 2$

(c) $L = 3$ (d) $L = 4$

(e) $L = 5$ (f) $L = 6$

Figure 3.7: The phases of the $M = 1$ partial waves of $\eta\pi$ (red) and $\eta'\pi$ (black) relative to the $L = 2, M = 1$ wave in the respective $\eta\pi$ and $\eta'\pi$ system.

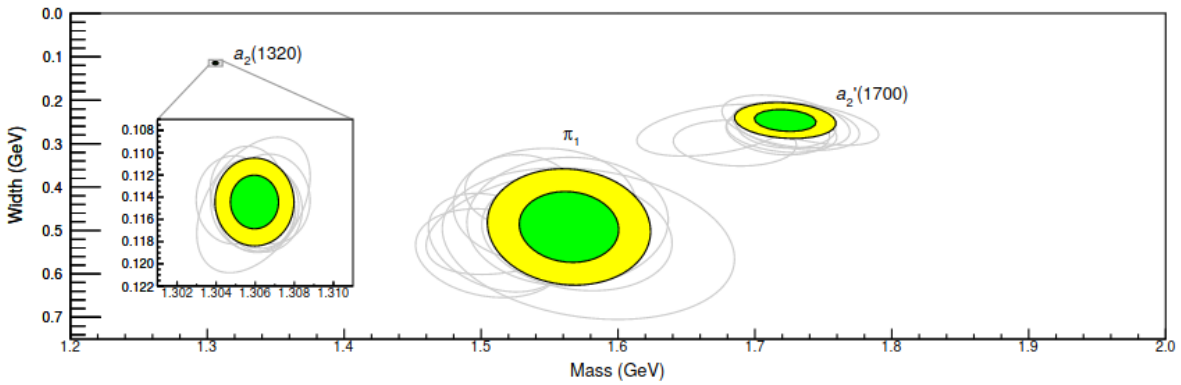

Figure 3.8: Plot showing the positions and widths of the three resonance poles found from the JPAC analysis of COMPASS data. Taken from [10].

was investigating the three pion final state production reaction: $\gamma p \to \pi^+\pi^+\pi^- n$, notably with a charge exchange in contrast to the previous pion beam experiments. The results of the analysis noted the presence of resonances $a_2(1320)$ and $\pi_2(1670)$ in the data sample but no evidence of an exotic signal to the level that was expected by other studies as shown in Figure 3.9 - Close and Page (1995) had suggested the 1^{-+} could be produced at an intensity level of 10% of that of the $a_2(1320)$. The CLAS result placed an upper limit of 2% on this relative intensity. A suggested resolution to this is that C-parity inhibits the production of the charged π_1, but not other mesons decaying to $\rho\pi$. It may be that the exotic is produced largely from Pomeron exchange and therefore would be more readily produced in a neutral exchange production process with a neutral final state meson [54].

3.7 Other Relevant Analyses outwith Three Body Decay

One analysis that is particularly relevant to this thesis was by Atkinson *et al.* (1984) [12]. In the $\gamma p \to \pi^+\pi^-\pi^0\pi^0 p$ reaction channel Atkinson reported an enhancement in the $\omega\pi^0$ system that was consistent with the 1^+ wave decay of the $b_1(1235)$ resonance. The decay of the $b_1(1235)$ is of particular interest here; as noted in Chapter 2 there is expected to be an enhanced decay mode of the $\pi_1(1600)$ in the $b_1\pi$ reaction channel. The event sample that was isolated from this experiment is shown in Figure 3.10. Another important point of this study was that in the analysis of the decay, moments were used to fit the data. There are simplifications in this system from factors such as a greatly reduced waveset but in principle, this is the same method with which the moments were extracted in this analysis. Other current analyses are ongoing in the study of the $b_1(1235)$ at GlueX [55].

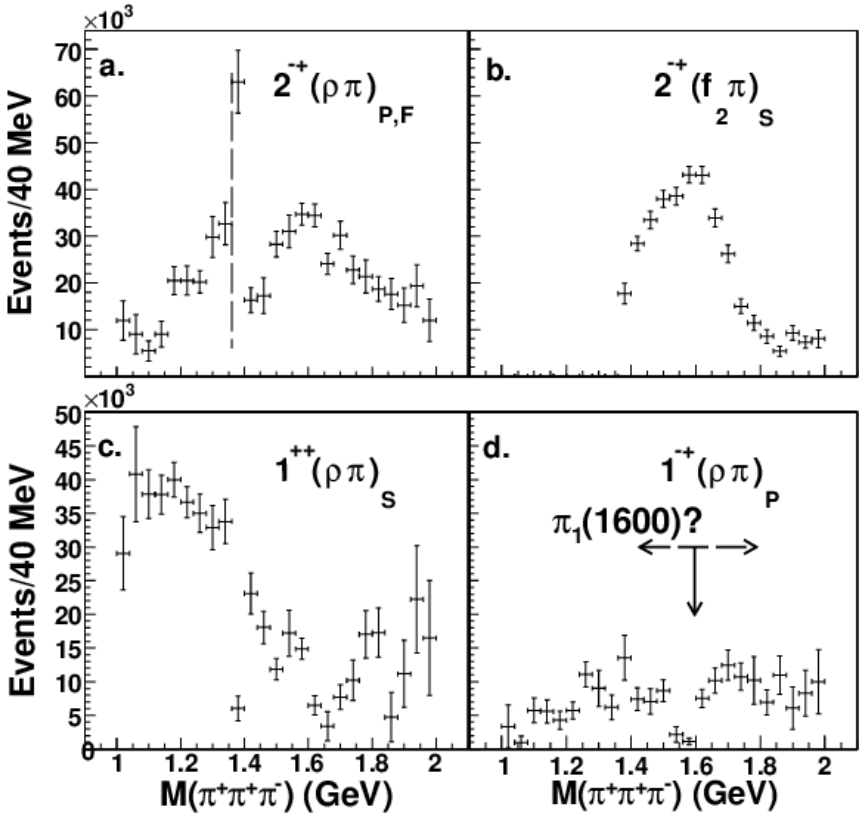

Figure 3.9: An array of results from the CLAS experiment in the search for the photoproduced $\pi_1(1600)$. Plot (d) shows the 1^{-+} wave and the position and width of the expected signal. Taken from [11].

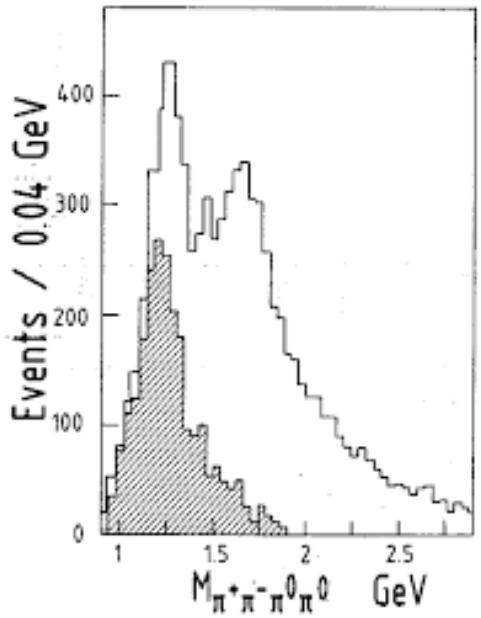

Figure 3.10: The invariant mass of $\pi^+\pi^-\pi^0\pi^0$ from the Atkinson analysis. The invariant mass of $\omega\pi^0$ is shown as the shaded histogram. Taken from [12].

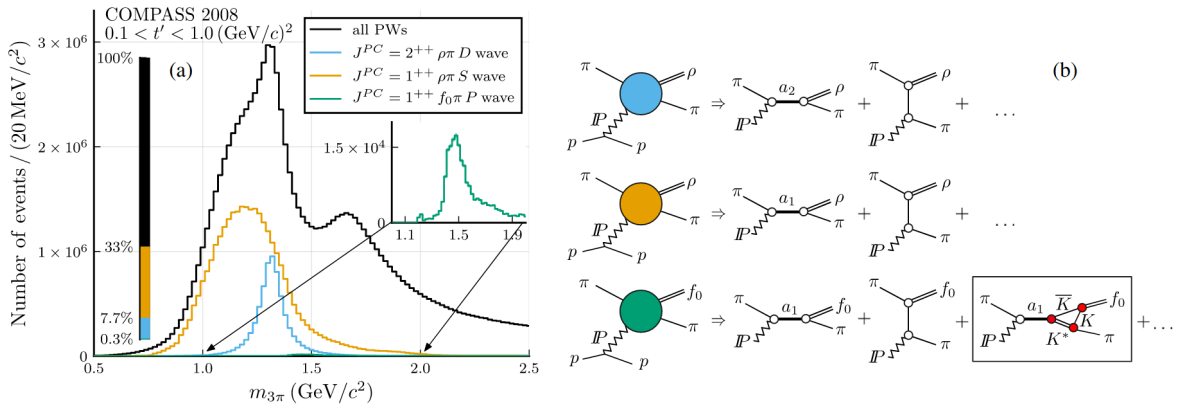

Figure 3.11: Results from the PWA of the 2008 COMPASS data. Specifically the $1^{++}\,f_0\pi - P$ wave shown in green. Taken from [13].

3.8 Some other exotic meson candidate states

3.8.1 $a_1(1420)$

The search for new resonances is not limited to states with $J^{PC} = 1^{-+}$. Figure 3.11 shows some of the wave contributions to the COMPASS dataset that were described in Section 3.5. One of the smaller contributions that is of particular interest is the $1^{++}\,f_0\pi - P$ wave. The resonance behaviour of this state was confirmed and therefore not an effect of the analysis parameterisation. Since it was measured as having quantum numbers $I^G J^{PC} = 1^- 1^{++}$ this could not be a standard $q\bar{q}$ meson states. An analysis by Alexeev *et al.* provided as explanation for this behaviour as a model based on a triangle singularity in the amplitude [13]. In place of the standard quasi-two body scattering, the $a_1(1260)$ decays primarily into a $K^*\overline{K}$ system. There is then a rescattering resulting in the $f_0\pi$ final state. Their conclusion stated that there was no need to postulate the existence of a new $a_1(1420)$ meson as the resonance behaviour could be explained using known resonances and a rescattering procedure.

3.8.2 Heavy Exotic Mesons

The search for exotic states is not limited to the light quark sector. In particular, at higher masses there have been a number of discoveries that have been suggested for candidate exotics. Some of the earliest proposed heavy exotic states were found at the Belle experiment in Japan and at Fermilab in the US. Belle noted the discovery of a particle they termed the $X(3872)$ in 2003 and the $Z(4430)$ in 2007, while Fermilab originally called an unknown particle the $Y(4140)$ - all three of which were proposed tetraquark states [56] [57] [58]. The nature of the tetraquark states was still unknown - with the four quark states having the possibility of being either 'pure' tetraquark states of four bound quarks or being composed of a more loosely bound meson molecule type structure. The search for heavy exotic states continues mainly at the LHCb

experiment at the LHC with the recent announcement of a number of new states, for example, the $c\bar{c}u\bar{s}$ four quark state in 2021 and the $c\bar{s}u\bar{d}$ and $c\bar{s}\bar{u}d$ in 2022 [59] [60].

Chapter 4

Experimental Setup

The CLAS12 experiment was sited at the Thomas Jefferson National Accelerator Centre, more commonly referred to as Jefferson Lab or JLab, located in Newport News, Virginia. The experimental facility at JLab was composed of the electron beam, provided by the Continuous Electron Beam Accelerator Facility (CEBAF), and four experimental halls, each with their own specific physics program. An aerial view of JLab showing each labelled experimental hall can be seen in Figure 4.1. The data for this analysis was collected in experimental Hall B.

Hall B housed the CEBAF Large Acceptance Spectrometer (CLAS) detector that was operational from 1998 to 2012. From 2012, work began on a series of upgrades to the detector setup to compensate for an upgrade to the maximum beam energy from 6 GeV to 12 GeV. Physics operations and data taking recommenced in 2017 with the CLAS12 detector in Hall B. This chapter will describe in more detail the detector setup as well as the beam provided by the CEBAF.

4.1 CEBAF Design and Hall B Beamline

The design of the accelerator facility at JLab was comprised of two linear accelerators, the North and South linear accelerator (LINAC), connected by two arced sections in which the beam was magnetically steered. It was for this reason that the facility was described as a 'racetrack'as shown in Figure 4.2.

Electrons were generated by firing a 250 MHz pulsed laser at a Gallium-Arsenic target and injected into the accelerator using a LINAC in beam bunches of 4ns - the electron beam was said to be continuous as the frequency of beam bunches was considerably higher than other pulsed beam facilities. The linear accelerators utilise superconducting magnets to provide the most effective acceleration of electrons. The principle was known as superconducting radio frequency (SRF) and requires cooling niobium using liquid helium to approximately 2 K which was important for removing electrical resistance. The CEBAF configuration from the 6 GeV era was comprised of 42 cryomodules, each containing 8 SRF niobium cavities. With the upgrade to CLAS12, the same footprint was retained allowing use of the same beam tunnel (with the

Figure 4.1: An aerial view of Jefferson Lab labelling each experimental hall [14].

addition of the beam pipe required for Hall D). In order to achieve the increase in beam energy, additional C100 cryomodules were placed at each end of the existing LINAC design [61]. With the addition of the new cryomodules to the original setup, the energy gain increased from 600 MeV/linac to 1100 MeV/linac [62] [63].

Electrons that were injected into the racetrack do five laps of the facility (using different magnets at the arc region with each lap) before being steered into Hall B (as well as the other halls). The wide physics program in Hall B necessitates an electron beam at various energies and currents, with targets ranging from hydrogen to lead. As such, the main challenges facing the beamline design in this hall were the large acceptance of CLAS12 and the close proximity of sensitive detector equipment to the beam and the target [16]. The beam was profiled using various detectors and scanners to ensure the beam impinging on the target was of good quality and well positioned [64]. The beam position was measured by three beam position monitors (BPMs) that themselves consist of three resonant cavities that can measure the beam position and intensity across the cavity. The information from the BPMs was continually monitored in a feedback loop. In addition to the beam position, the beam profile was also measured by three HARP scans placed upstream of the target - a full diagram of the Hall B beamline is shown in Figure 4.3. These consist of thin tungsten and iron wires that were moved through the beam to scatter electrons that were then detected via Cherenkov light in photomultiplier tubes. As this

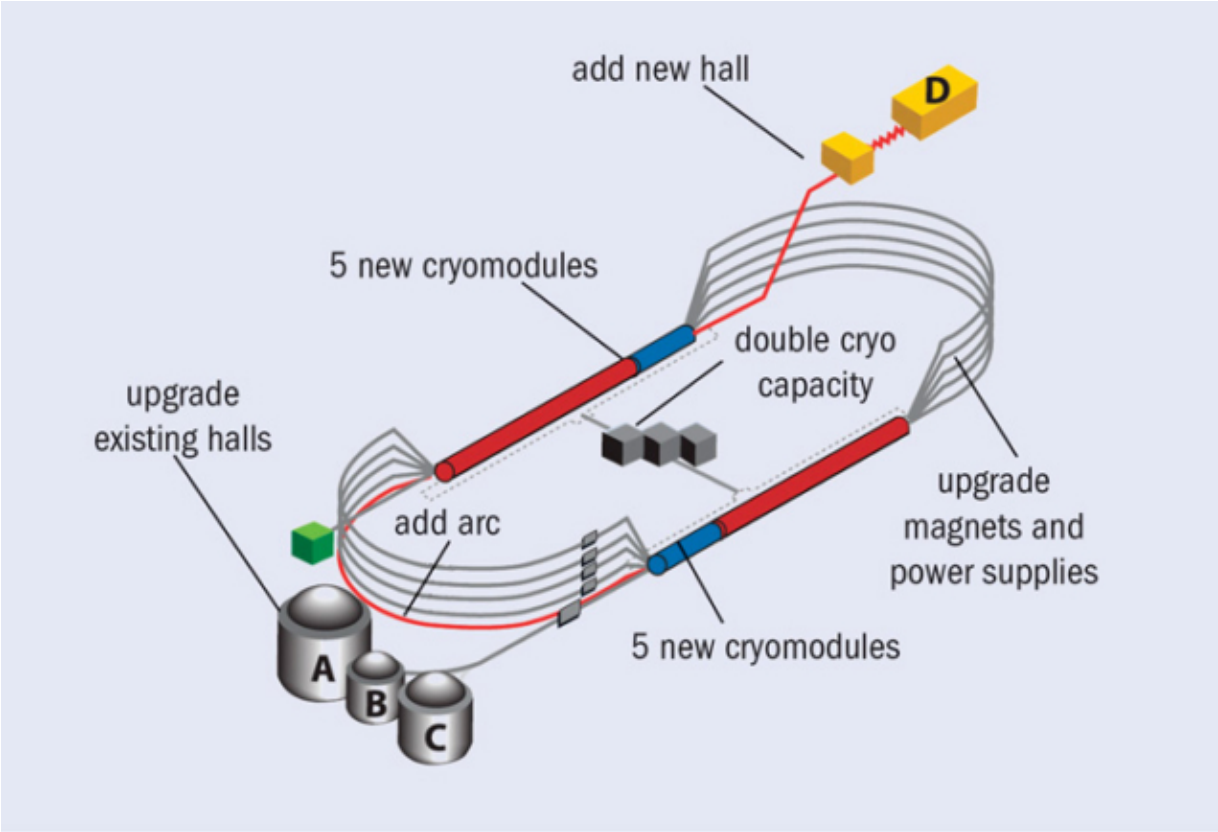

Figure 4.2: Racetrack layout of the CEBAF design with detailed upgrades. Taken from [15].

interferes with the beam, this was done only after changes in configuration to the setup when no data was being taken.

Another important matter was protecting the beam in regions downstream of the target, specifically how to ensure the safety of the detectors positioned in this region. The main sources of background were Møller radiation, small-angle electron scattering and electromagnetic effects like pair-production and Bremsstrahlung radiation [64]. The drift chambers of CLAS12 required optimised shielding where background processes have a negative effect on track reconstruction [65]. The shielding itself was managed in a few ways. Low energy particles were focused along the beamline by the strong solenoidal magnet around the target away from the detectors and into heavy shielding materials far downstream of the target. In addition, a tungsten cone was mounted on the central support of the forward electron detector (Forward Tagger) with a 5cm diameter hole at the centre of the cone for the beam.

Finally, far downstream of the target there was the Faraday cup in which the beam was deposited. It was constructed from a conductive cup and measures the accumulated charge required for normalising cross sections.

In the fall 2018 run period, the beam will operate in Hall B at a maximum energy of 11 GeV after 5 full linac passes and at a typical current of 70 nA [66].

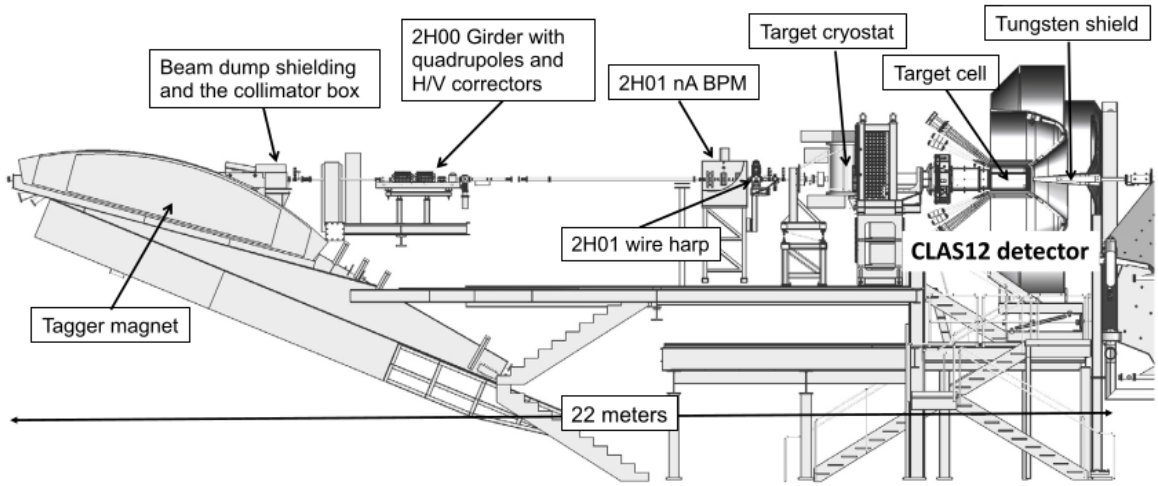

Figure 4.3: Illustration of the beamline in Hall B. Taken from [16].

4.2 Target

The experimental setup in Hall B was based on a fixed target configuration. There can be a variety of targets used for various experiments, ranging from cryogenic hydrogen to solid lead targets. Experimental running was sorted into 'Run Groups' as a means of differentiating between the type of target and beam condition. The data on which the current analysis was performed was taken using a liquid Hydrogen (LH_2) target and a 10.6 GeV electron beam at 70 nA. This was called Run Group - A (RG-A) data.

In RG-A, the target cell was composed of a small Kapton cell, 20 mm in diameter and 5 cm in length and was housed within a vacuum. Along either side of this cell was $\sim$ 40 cm of air that separates the upstream and downstream beamlines from the vacuum, contained by 50 μm thick Al windows. The target itself was located inside the central detector and in the field free region of the 5 T solenoidal magnetic field [66].

4.3 CLAS12 Superconducting Magnets

The CLAS12 spectrometer has as a part of its configuration both toroidal and solenoidal superconducting magnets as illustrated in Figure 4.4. The Solenoid was a superconducting magnet located around the target and was used to deflect low energy particles of energies 0.3 - 1.5 GeV. In addition, the magnet was used to focus Møller radiation away from the Forward Detector as described in Section 4.1. The magnet was composed of five series coils in total, wound with 17mm thick copper stabilised NbTi Rutherford cable. The first two coils were wound on the inside of a steel bobbin, with coils three and four fixed on the outer side of this same bobbin. The final coil was used as an 'active shield', meaning that the stray magnetic field of the inner coils was limited, and this was wound in its own bobbin and connected to the other four coils in

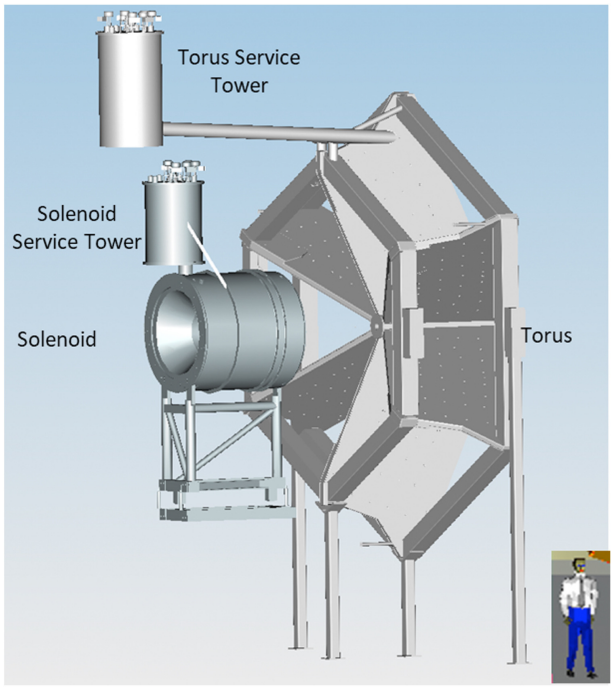

Figure 4.4: Illustration of the position of the solenoidal and toroidal magnets with the detectors absent. Taken from [17].

reverse. The sensitivity of the detectors placed very close to the solenoid field necessitate this outer coil [17].

The toroidal magnet was located downstream of the solenoid in the Forward Detector region. The function of this magnet was to deflect higher energy particles (0.5 - 10 GeV) which were tracked in drift chambers. The toroidal magnet was composed of six coils that were connected in series and, similar to the solenoid, made of NbTi Rutherford cable; with the difference that the thickness in the torus was 20 mm. The coils were shaped to be incorporated into the Forward Detector as shown in Figure 4.4, the shape of these coils was referred to as a double-pancake trapezoid [17]. The service towers for both the torus and the solenoid provide cooling via liquid Helium. The magnets were cooled using conduction methods due to space restrictions which limits the size that the magnets can be.

4.4 The Central Detector

The CLAS12 detector was composed of the Forward Detector (FD) and the Central Detector (CD). The central detector was located around the target in the field of the solenoid magnet. It was composed of a set of individual detectors used for particle identification with a polar angular coverage of 35° to 125° and 360° azimuthal angle coverage [18]. The innermost part of the central detector was the Silicon Vertex Tracker (SVT), followed by the Barrel MicroMegas Tracker (BMT), and together the SVT and the BMT form the Central Vertex Tracker (CVT). Surrounding the CVT was the Central Time of Flight Detector and the Central Neutron Detector

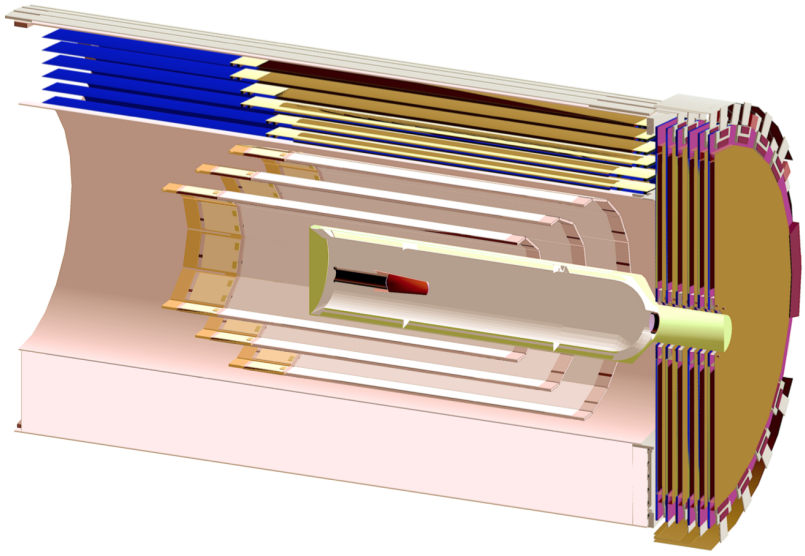

Figure 4.5: Diagram showing the layers of the SVT and BMT surrounding the target cell. Upstream of the beam was from the left of this plot. Taken from [18].

(CND) as the outermost layer.

4.4.1 The Central Vertex Tracker

The Central Vertex Tracker was made up of the Silicon Vertex Tracker and the Barrel MicroMegas Tracker which together can reconstruct the momentum and the vertex position of charged particles emanating from the target. The momenta of charged pions, charged kaons and protons was measured with an efficiency greater than 90% and resolution less than 5%. The angular resolution was $\delta\theta \leq 10-20$ mrad and $\delta\phi \leq 5$ mrad within polar angles of 35°-125° [67].

In terms of construction, the CVT consists of three double-sided layers of silicon sensors that form the SVT and a further six strips of micromegas that make up the BMT. Three of the BMT strips were aligned with the beamline and three segments run perpendicular. Using the BMT improves the angle and momentum resolutions to meet the required specifications for the CVT [18]. The layout of the layers of the SVT and BMT are shown in Figure 4.5. The specifications and spatial limitations of the solenoid magnet necessitate the use of silicon detector technology. The energy band gap of silicon is 1.12 eV at room temperature and it is this intrinsic property of silicon that makes it most suitable to be used in the CVT [67]. The band gap was small enough that the ionising particles will generate a large number of charge carriers even after taking into account the energy loss per unit length travelled for an ionising particle. On the other hand, the band gap was large enough that the pair production process of electrons and holes was sufficiently low that background current was negligible.

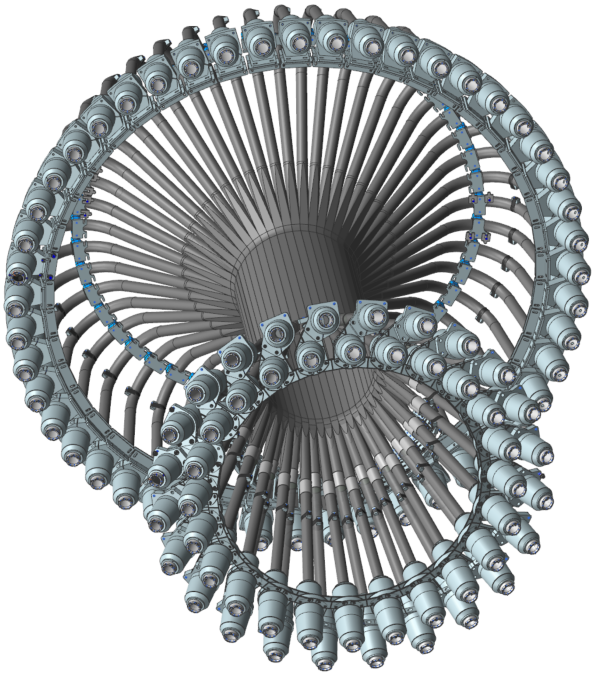

Figure 4.6: Illustration of the Central Time of Flight system in CLAS12. The scintillator bars form the barrel shape with the PMTs mounted on lightguides at both ends of the bar. In this figure, the beam direction is into the page. Taken from [19].

4.4.2 The Central Time of Flight Detector

Immediately surrounding the CVT was the Central Time of Flight detector (CTOF), that was used to measure the time of flight for charged particles in the central detector. The plastic scintillator bars of the CTOF form the shape of a barrel as shown in Figure 4.6, at a radial distance of 25cm from the target [19]. At each end of a bar light guides were attached, which were 1 m long in the upstream region and 1.6 m long in the downstream region. The light guides were required so that the field sensitive photomultiplier tubes (PMTs) on the end of the light guides were situated in the low strength fringe regions of the solenoidal field. In this configuration, the PMTs experience an inhomogeneous magnetic field of 1kG in the upstream and 400G in the downstream - a field strength that was at the limit of what their magnetic shields can withstand [19]. The time resolution for each individual counter was around $\sigma_{TOF} = 80$ ps.

4.4.3 The Central Neutron Detector

The outermost part of the central detector was the Central Neutron Detector (CND). The CND has the primary aim of detecting neutron candidates to be used in measurements of beam spin asymmetries in deeply virtual Compton scattering experiments (n-DVCS) [20]. In addition to this, the detector may be useful whenever a recoil neutron was produced. In terms of design, the

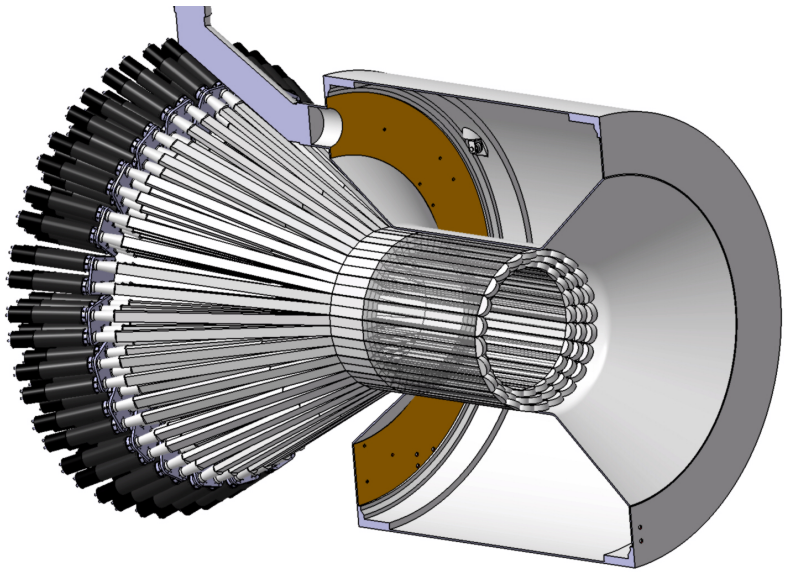

Figure 4.7: The central neutron detector in CLAS12 showing the scintillator barrel and PMTs. Taken from [20].

CND shares many similar features with the CTOF. The CND also was constructed as a barrel scintillator, in this case formed of three layers, and the PMTs were joined to the scintillator using u-bend light guides that allow the PMTs to be located in fringe field region at the downstream end. A diagram of the setup is shown in Figure 4.7.

4.5 The Forward Detector

The Forward Detector was located downstream of the Central Detector, with particles in the region of the forward detector influenced by the toroidal field. It was the coils of the torus that support the six sectors of the drift chamber in the forward detector as well as the other parts of the detector used for particle identification such as the calorimeter and the forward time of flight detector. The forward detector has a full azimuthal angle coverage and that in the polar angle of around 5° to 35° [18]. The full construction of the Forward Detector is described in the following sections. Details on the detectors that were relevant to this analysis are specified in Chapter 7 on particle identification.

4.5.1 The Forward Tracker

The toroid magnet supports the drift chamber system in the Forward Detector and together they were known as the Forward Tracker. The magnet structure requires that the drift chambers be split into six sectors in the azimuthal plane, with coils between each sector. In order to maximise the azimuthal coverage, and since there was no particle detection on the magnetic coils, these and the complimentary electronics were designed to be as thin as possible [21]. Due to the success

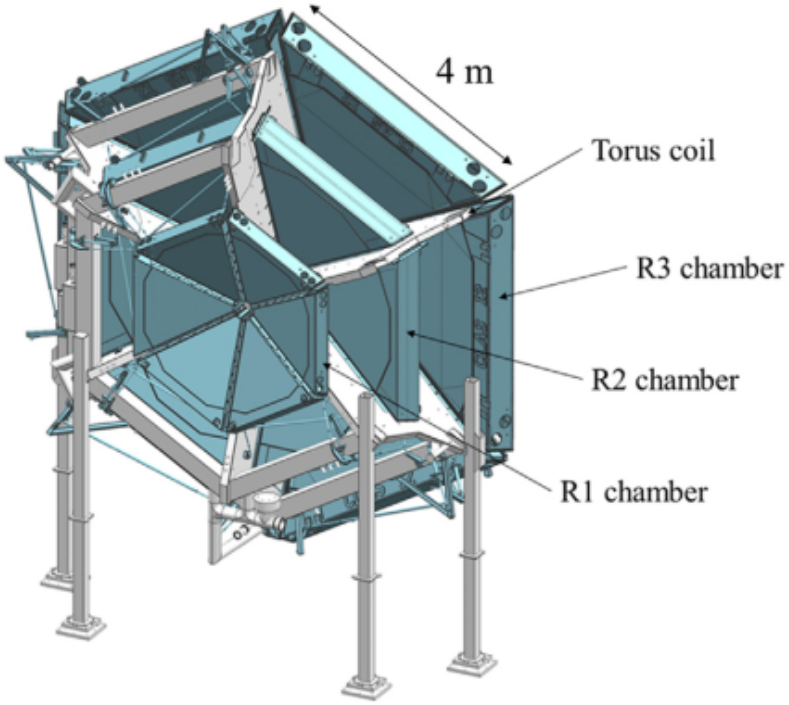

Figure 4.8: Diagram of the CLAS12 drift chamber in blue showing the three layers and the six sectors in the azimuthal plane. The magnetic coils are shown in grey. Taken from [21].

of the drift chamber from the prior CLAS experiment, the design remained largely unchanged for CLAS12, with the exception that the full system was moved further downstream. With this shift, the total polar angular coverage decreased, but the tracking efficiency was improved at higher luminosity [21]. The drift chamber was composed of three layers, referred to as R1, R2 and R3, with R1 located furthest upstream. In relation to the magnetic field, R1 was located just before the field, R2 was inside the field and R3 was located just after the field and at a distance from the target of 2.3 m, 3.5 m and 4.9 m respectively. Depending on the charge of the particle and the toroidal field direction, the particles will be bent inwards or outwards with respect to the beamline. The three regions of the drift chamber and the six sectors are shown in Figure 4.8. Each region of the drift chamber system was composed of two superlayers, that were themselves constructed of six layers. The layers were formed using field wires ($30\mu m$ gold-plated tungsten) and sense wires (80 μm gold-plated Cu-Be) as shown in Figure 4.9, with the hexagonal shape of the field wires forming the six layers per superlayer. In order to achieve resolutions of the same scale relative to each other, the two superlayers were oriented at a stereo angle of -6° and 6° respectively.

The function of the Forward Tracker was to detect particles of momenta greater than 0.2 GeV in the polar angle range of 5° to 40°. Particles below the 0.2 GeV limit were bent out of the drift chamber acceptance [21]. It was physics requirements that drove the design specifications for the drift chambers. In addition to the requirement for a luminosity of $10^{35}\text{cm}^{-2}\text{m}^{-1}$, scattered

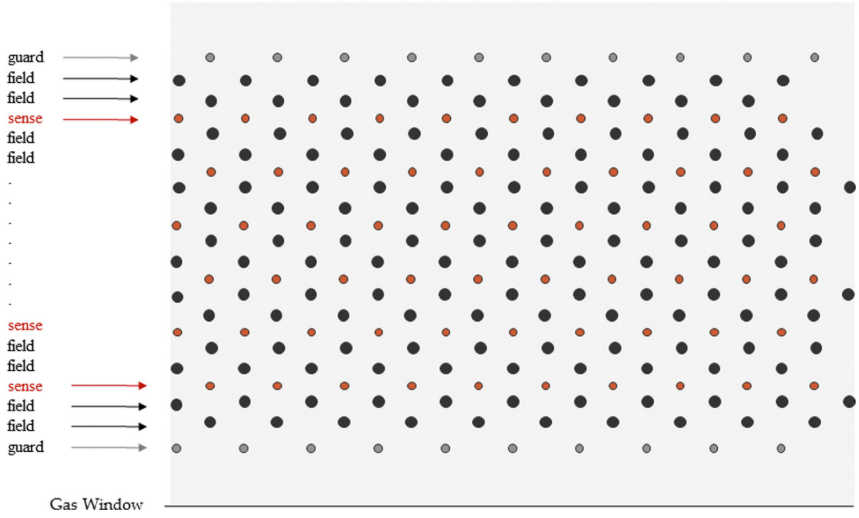

Figure 4.9: Illustration of the layers of the drift chamber formed from the hexagonal shape of the field wires in black, with a sense wire shown in red at the geometric centre of each hexagon. Taken from [21].

electrons had to be sufficiently well reconstructed. Studies on simulated data were used to arrive at a limit of $\frac{\delta p}{p} = 0.3\%$ for 10 GeV electrons scattered at small angles ($\sim 7^\circ$) [21]. The design and function of the Forward Tracker allows these and other requirements within the physics program in CLAS12 to be met.

4.5.2 The High Threshold Cherenkov Counter

Immediately upstream of the Forward Tracker was the High Threshold Cherenkov Counter (HTCC), one of three Cherenkov detectors that were present in the CLAS12 detector. The main purpose of the HTCC was to separate electrons from pions at momentum less than 4.9 GeV. This was done in the polar angle region between 5° and 35° with $\sim 99\%$ efficiency for electrons and a pion rejection rate of 500 to 1 [68]. Additionally, as the HTCC was placed in front of the drift chambers, the HTCC was made to provide as little as possible interference to tracking in the Forward Tracker.

The HTCC works in principle by detecting Cherenkov radiation. Cherenkov radiation is produced when a particle travels faster than the speed of light in a given dielectric material with refractive index n. In the case of the HTCC, the gas that was used was carbon dioxide (CO_2). In such a material, it is possible that particles can travel at velocities β such that $\frac{c}{n} < \beta < c$. For a charged particle travelling through a dielectric material, there is a local excitation in the material around the moving charge. At the relaxation of this polarisation, electromagnetic waves are released in wavefronts moving at phase velocity $v = \frac{c}{n}$. If the phase velocity is greater than the velocity of the moving charge then there may be a build up of waves in the direction of motion but there is no overlapping wavefronts. On the other hand if the phase velocity is less than the velocity of the charge then there are overlapping wavefronts, there is constructive interference

Figure 4.10: The HTCC mirror.

and one observes a 'light cone' of Cherenkov light being produced. It is by detecting this light that high momenta particles can be detected.

In the HTCC, Cherenkov light that was produced was reflected once and detected by a PMT. The mirror was chosen to be an ellipsoidal multifocal design as shown in Figure 4.10 in order to maximise the strength of the signal that could be detected. The mirror was included as part of the HTCC and brought to the lab fully assembled before being included in the CLAS12 detector. The final restriction listed here was a consequence of the need for the detector to be light and self-supporting. The fully assembled HTCC is shown in Figure 4.11.

4.5.3 The Forward Time of Flight Detector

The main method by which charged particles in the Forward Detector were identified was comparing time-of-flight measurements to momenta [69]. A time-of-flight resolution of 80 ps allowed discrimination between pions and kaons up to ~ 3 GeV [69].

Relative to the other detectors of the Forward Detector, the FTOF was placed immediately downstream of the LTCC in the 'shadow' of the torus coils. The FTOF was split into six identical 60° sectors, with each sector being composed of three panels, named 1a, 1b and 2. The panels were triangular in shape to fit the dimensions of the sectors of the Forward Detector and were composed of scintillator detectors with PMT readout. Each sector has a polar angle coverage of 5° to 45°, with the 1a and 1b panels providing coverage from 5° to 35° and the panel 2 from 35° to 45°. The geometry of the detector is shown in Figure 4.12, with panel 1a not shown as it was located immediately behind panel 1b in this plot. These two panels were required to achieve the 80 ps resolution requirement for the detector.

Figure 4.11: The fully assembled HTCC.

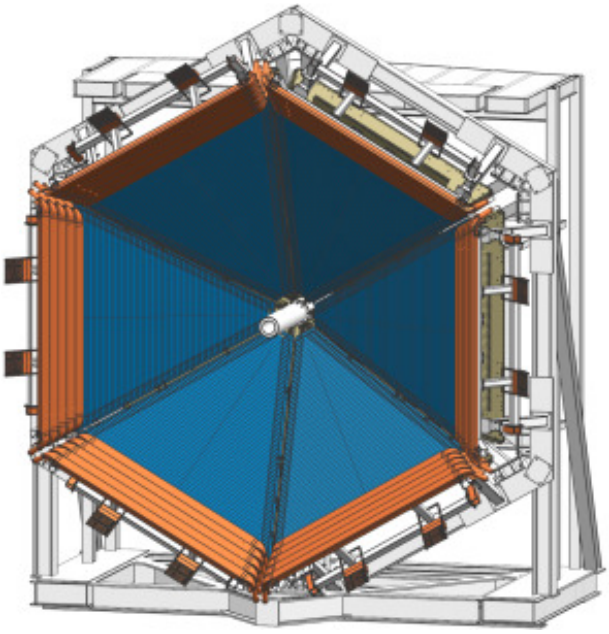

Figure 4.12: The Forward Time-of-Flight detector. The 1b panel is shown in dark blue and panel 2 in orange. The 1a panel was positioned directly behind (downstream) of panel 1b.

4.5.4 The Electromagnetic Calorimeter

The furthest downstream detector in the Forward Detector was the Electromagnetic Calorimeter (ECAL). The purpose of the ECAL was to identify electrons, as well as measure neutral photons and neutrons. The ECAL consists of two main parts. The first of these was the existing electromagnetic calorimeter (EC) from CLAS6 [70]. With the CLAS12 upgrade in beam energy, the EC itself was no longer able to be used in isolation as it became inefficient when particle energies exceeded 5 GeV. To complement the EC in the 12 GeV upgrade, the pre-shower calorimeter (PCAL) was added in front to create the full ECAL in CLAS12. With this improvement, the radiation length of the calorimeter was increased from 16 to 20.5 g cm^{-2} [22]. Both the EC and the PCAL were made from layers of plastic scintillator strips. In the EC, there were thirteen layers per 'view', with the view referring to the rotation angle of the layer as each successive layer was rotated by $\frac{2\pi}{3}$. In each of the three views (called U,V and W) there were thirteen layers (subdivided into an inner 5 and outer 8 layers to form the EC inner and EC outer). Each layer in the scintillator was 10 mm thick, with a 2.2 mm thick lead sheet placed between each layer [70]. In the PCAL the configuration was similar, with the three views being constructed from five layers of 10 mm scintillator material between 2.2 mm thin lead sheets [22]. The construction of the PCAL is shown in Figure 4.13.

In the ECAL, an electromagnetic shower was created in the lead sheets and recorded in the scintillators. A particle hit was found if there was an energy deposit above a given threshold in the scintillator coincidentally in each U, V and W view of the ECAL and this forms a cluster. The peak position was found from the geometric midpoint of the scintillator strips recording

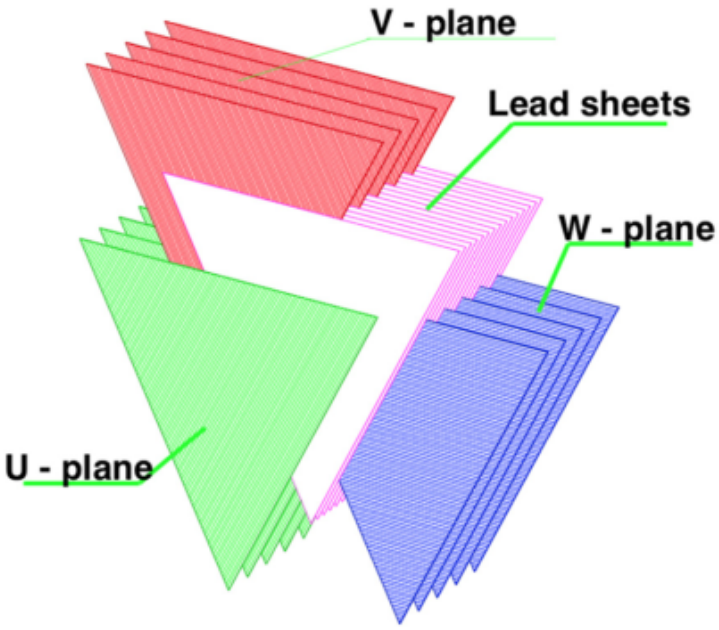

Figure 4.13: Illustration of the PCAL showing five layers in each of the views, with lead sheets placed between each scintillator layer. Taken from [22].

the highest local energy deposition. The design provides sufficient spatial resolution for close proximity clusters in the ECAL to be separated and contains the electromagnetic shower to maximise the efficiency and energy resolution for individual clusters.

4.6 The Forward Tagger

Placed between the HTCC and the Drift Chambers in the Forward Detector, the FT was specifically designed to detect electrons in the 2.5 - 4.5° polar angle range and an energy range of 0.5 - 4.5 GeV. In keeping with much of the CLAS12 detector setup, spatial constraints were an important factor that influenced its design and operation. The full Forward Tagger was required to fit in about 40 cm of space between the HTCC and the support for the torus magnet. At 2.5° this position corresponds to a position of 8 cm from the beamline [23]. The Forward Tagger calorimeter (FT-cal) was used to measure the scattered electron's energy, the Forward Tagger Micromegas (FT-trk) was used to measure the polar and azimuthal angles while the Forward Tagger Hodoscope (FT-Hodo) differentiates between electrons and photons. The FT-Hodoscope was placed upstream of the FT-trk that was itself upstream of the FT-cal. The FT-tracker was not however used in this analysis.

Due to the magnetic field and reduced spatial capacity, the FT-Cal uses avalanche photodiodes (APDs). The readout in these APDs was influenced by the large electromagnetic background that was present at the given luminosity of $10^{-35}\text{cm}^{-2}\text{s}^{-1}$. In order to reduce the pile-up in the FT-Cal, the scintillator was chosen to be approximately of the same dimension as the

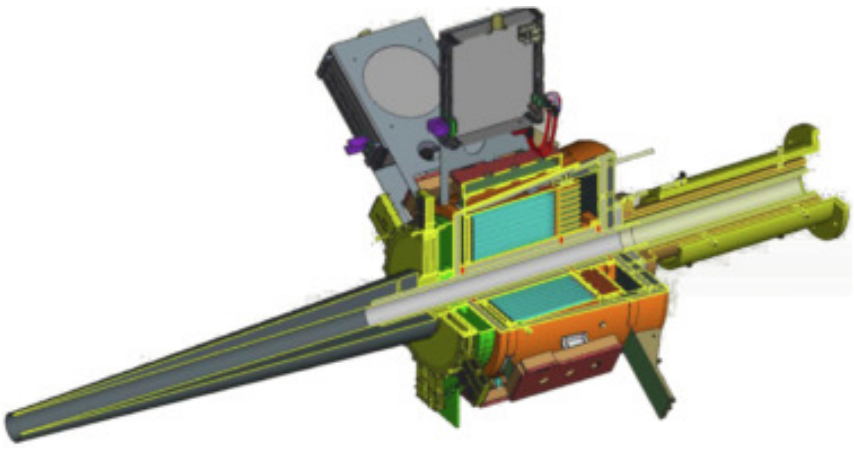

Figure 4.14: A computer generated model of the Forward Tagger. The calorimeter is shown in cyan, the hodoscope in green and the micromegas tracker in yellow. The Lead cone that acts as a Møller shield is shown just upstream of the FT (to the left in this figure). Taken from [23].

transverse shower diameter of a given hit. The scintillator material that was chosen was Lead Tungstate ($PbWO_4$) with each crystal having dimensions 1.5 x 1.5 x 20 cm^3 - the long dimension was placed parallel to the beamline. This satisfies the detector requirements of containing the cluster shower ($PbWO_4$ has a Molière radius of 2.1 cm) and a fast scintillator decay time (2.1 ns).

The FT-Hodo was used in the photon/electron determination. It was made of 232 plastic scintillator tiles, if a hit was detected in the hodoscope that geometrically matches to a hit in the calorimeter then an electron event was recorded, otherwise the event was recorded as a photon. The FT-trk that was used to detect the scattering angle of the electron uses the same technology as that used in the Micromegas detector in the Central and Forward Detectors [71]. A CAD drawing of the Forward Tagger is shown in Figure 4.14.

4.7 The Data Acquisition System

The CLAS12 Data Acquisition System (DAQ) was in place to collect the data that comes from the detector in Hall B. The DAQ begins with the Read Out Controllers (ROCs) at the front end. These were linked to the Event Builder (EB) component using TCP connectors. From the EB, the constructed events were passed to the Event Transfer (ET) and finally the Event Recorder (ER). At the front end, the ROCs were made up of VME/VXS crates, linux servers and VTP (VXS trigger processing boards). The VTPs were installed in each VME/VXS crate but read out as independent ROCs. The EB, ET, and ER were all multi-threaded programs written in C. Events were built on the EB and passed to the ET, the function of which was to allow filtering, monitoring and processing of the data. Finally, the ER records the events to disk, with the multi-threading allowing writing to one or more disks to increase performance as required with event order being preserved through the process [72].

A notable advantage of the multi-threaded nature of the DAQ was that increases in performance were easily implemented. At the beginning of the CLAS12 implementation, the requirement was for a data rate of 100 MB/s and an event rate of 10 kHz, however during the construction of the detector this was increased to 200 MB/s. It has been shown that there was scope for further increase should this be required in the future up to a data rate of 1 GB/s and an event rate of 30 kHz if the livetime was slightly reduced - in the 2018 running of CLAS12, data and event rates of 500 MB/s and 15 kHz were achieved with a livetime of 95 %. The higher figures could be achieved with a reduced livetime of around 90 % [72] [18].

In order to attain an event rate of around 500 MB/s, the CLAS12 DAQ uses a hardware trigger system to eliminate events that were not relevant for physics processes. For example, in every physics process, the scattered electron should be measured in order to determine photon energy and other general reaction kinematics such as the momentum transfer. Whether the scattered electron was measured in the FD or FT, along with other hadronic detection conditions forms a set of trigger conditions that reduces the trigger rate significantly. The final trigger rate was about 2×10^4 events/s, which corresponds to the given 500 MB/s in the DAQ. This was reduced from around 5×10^6 before any trigger conditions were given. Over half of the triggers were defined by detecting the scattered electron in the Forward Detector and just over a quarter of triggers with the electron being detected in the Forward Tagger. Some triggers were used purely for data monitoring and were strongly pre-scaled [18]. The trigger that was used specifically for this analysis was known as the MesonEx trigger. The MesonEx trigger was defined by one electron hit in the FT, at least two charged tracks in two different sectors of the FD and a detected electron energy less than 5 GeV.

Chapter 5

Three Body Photoproduction Formalism

This section will describe the process of constructing a model from which the moments of angular distribution can be extracted from data. The model begins on a general three body decay but will include simplifications relevant to this analysis, such as all three final state particles being spin-0 and events decaying through an intermediate vector particle. This final factor means the model can be reduced to a pseudo-two body reaction.

5.1 Reaction Basics

The reaction formalism for the decay of a three body final state is equivalent to that given by the COMPASS Collaboration [73]. Consider the reaction:

$$a + b \to (1 + 2 + ... + n) + c, \tag{5.1}$$

where a is the beam, b is the target, c is the recoil and $X = 1 + 2 + ... + n$ is the breakdown of a resonance X into final state particles. This reaction is illustrated in Figure 5.1 for the case of $n = 3$. The invariant mass of X is defined by $m_X^2 = E_X^2 - \underline{p}_X^2$, where E_X^2 and $\underline{p}_X^2$ are the energy and 3-momentum of the particle X, respectively. The squared total invariant mass of the reaction and the momentum transferred between the top and bottom vertex of Figure 5.1 are denoted by the Mandelstam variables $s = (p_a + p_b)^2$ and $t = (p_a - p_X)^2$, respectively.

Here a model was developed assuming the n-body final meson decay products were produced via t-channel exchange processes and by inserting a complete set of states with well defined quantum numbers for the intermediate state X. For the purpose of the formalism the production and decay of the resonance was considered distinct. At fixed $\sqrt{s}$, the kinematic distribution of the final state depends on the mass of the resonance, m_X, the Mandelstam variable t and $(3n - 4)$ phase space variables denoted τ_n. Since the reaction is produced with a linearly polarised photon beam, it is also dependent on the angle between the photon polarisation vector and the production plane, denoted Φ. The polarisation of the beam is useful as this gives access to

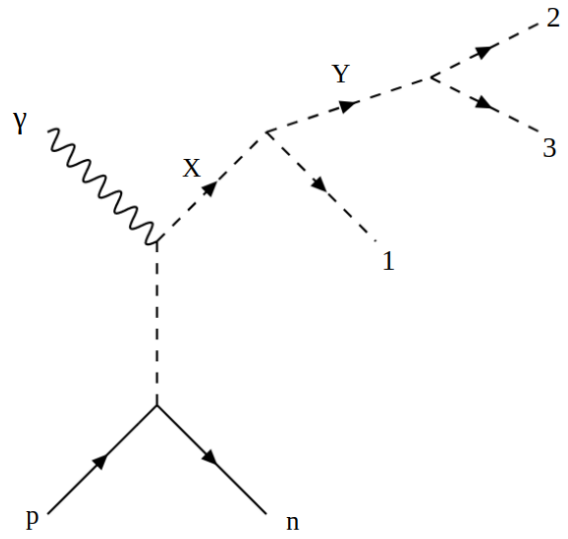

Figure 5.1: The reaction channel for the 3-pseudoscalar final state.

polarised intensities.

The total amplitude for the production and decay of the resonance X was taken as a product of three parts: the production of X, $T_{a+b\to X+c}(m_X,t)$, the propagation of X, $Z_X(m_X)$ and the decay amplitude, $\psi_{X\to FS}(m_X,\tau_n)$, that contains the decay of the resonance into a given n-body final state via some decay chain. Putting this together, the total amplitude was given by:

$$M_{\gamma N\to X\to FS} = T_{\gamma N\to X}(m_X,t)Z_X(m_X)\psi_{X\to FS}(m_X,\tau_n) \tag{5.2}$$

In accordance with most other analyses that have been performed on multiparticle final states, the isobar model was used. This means that the final state was assumed to be a sequence of two body decays. Therefore, by modelling a two body decay and applying it recursively it was possible to model the full decay.

5.2 The Decay Amplitude for Two body decays

Consider first a general two-body decay of a resonance X into (possibly unstable) final state particles written $X \to Y + 1$.

An appropriate choice of frame simplified this amplitude significantly. Boosting to the rest frame of the resonance the daughter particles of the decay are produced back-to-back and therefore it can be described solely by two decay angles, θ_{GJ},ϕ_{GJ}, in the Gottfried-Jackson frame, as detailed in appendix A. The helicity basis was used to represent the two particle states. As such, we write the two body decay amplitude for a state X of total spin and projection J_X and M_X respectively as:

$$A_X^{J_X,M_X}(m_X) = Z_X(m_X) \sum_{\lambda_Y,\lambda_1} \langle \theta_{GJ},\phi_{GJ};\lambda_Y,\lambda_1|\hat{T}(m_X)|J_X,M_X\rangle, \tag{5.3}$$

where $\hat{T}(m_X)$ is the transition operator from the initial state into the two particle final state $\langle \theta_{GJ},\phi_{GJ};\lambda_Y,\lambda_1|$ which is defined by the decay angles and helicities of the respective particles. In front of the sum are dynamical factors that are dependent on the mass of the decaying particle. By inserting a complete set of states the amplitude becomes now also dependent on the orbital (L) and intrinsic (S) angular momentum of the decay:

$$\begin{aligned} A_X^{J_X,M_X,L_X,S_X}(m_X,\theta_X,\phi_X) &= Z_X(m_X) \\ &\times \sum_{\lambda_Y,\lambda_1} \langle \theta_{GJ},\phi_{GJ};\lambda_Y,\lambda_1 \mid J_X,M_X;\lambda_Y,\lambda_1\rangle\langle J_X,M_X;\lambda_Y,\lambda_1 \mid J_X,M_X;L_X,S_X\rangle \\ &\times \langle J_X,M_X;L_X,S_X \mid \hat{T}(m_X) \mid J_X,M_X\rangle. \end{aligned} \tag{5.4}$$

Using eqn (53) given in Salgado and Weygand (2018) [74], we have

$$\langle \theta_{GJ},\phi_{GJ};\lambda_Y,\lambda_1 \mid J_X,M_X;\lambda_Y,\lambda_1\rangle = \sqrt{\frac{2J_X+1}{4\pi}} D^{J_X}_{M_X\lambda_X}(\phi_{GJ},\theta_{GJ},0), \tag{5.5}$$

where $D^{J_X}_{M_X\lambda_X}(\phi_{GJ},\theta_{GJ},0)$ is the Wigner D-function that is defined by

$$D^{J_X}_{M_X\lambda_X}(\phi_{GJ},\theta_{GJ},0) = \langle J_X,M_X|\hat{R}(\phi_{GJ},\theta_{GJ},0)|J_X,\lambda_X\rangle, \tag{5.6}$$

where $\hat{R}(\phi_{GJ},\theta_{GJ},0)$ denotes a rotation by polar angle θ_{GJ} and azimuthal angle ϕ_{GJ}. Therefore, the Wigner D-function is essentially an object that rotates the state $\langle J_X,M_X|$ to a state $\langle J_X,\lambda_X|$ through the angular rotation defined by the matrix $\hat{R}(\phi_{GJ},\theta_{GJ},0)$.

From eqn (54) given in Salgado and Weygand (2018) [74],

$$\begin{aligned} \langle J_X,M_X;\lambda_Y,\lambda_1 \mid J_X,M_X;L_X,S_X\rangle &= \sqrt{\frac{2L_X+1}{2J_X+1}} (J_Y,\lambda_Y;J_1,-\lambda_1 \mid S_X,\lambda) \\ &\times (L_X,0;S_X,\lambda_X \mid J_X,\lambda_X), \end{aligned} \tag{5.7}$$

and $\langle J_X,M_X;L_X,S_X \mid \hat{T}(m_X) \mid J_X,M_X\rangle = R_X(m_X)T_{\gamma N\to X}$ consists only of dynamical factors. The

full two body amplitude is given by substituting (5.5) and (5.7) into (5.4):

$$A_X^{J_X,M_X,L_X,S_X}(m_X,\theta_X,\phi_X) = R_X(m_X)T_{\gamma N\to X}\sum_{\lambda_Y,\lambda_1}\sqrt{\frac{2L_X+1}{4\pi}}(J_Y,\lambda_Y;J_1,-\lambda_1\mid S_X,\lambda)(L_X,0;S_X,\lambda_X\mid J_X,\lambda_X) \times D^{J_X*}_{M_X,\lambda_X}(\phi_X,\theta_X,0), \quad (5.8)$$

where $R_X(m_X) = Z_X(m_X)\,F_{L_X}(m_X)$ encompassed the mass dependent terms, and $F_{L_X}(m_X)$ is the Blatt Weisskopf centrifugal barrier factor, described in Section 8 of Salgado and Weygand (2018) [74]. Taking the conjugate of the Wigner D-function was simply convention here.

5.3 The Decay Amplitude for Three body decays

In the case of a three (or more) body decays, the isobar model assumes that one of the decay products from the decay of the resonance itself decays. In Section 5.2, this unstable product was written as the isobar Y. For this three body decay, the two body amplitude was applied twice recursively with the total amplitude for the three body decay written:

$$A_X^{J_X,M_X,L_X,S_X}(m_X,\theta_X,\phi_X) = \sqrt{\frac{2L_X+1}{4\pi}}R_X(m_X)T_{\gamma N\to X}\sum_{\lambda_Y,\lambda_1}(J_Y,\lambda_Y;J_1,-\lambda_1\mid S_X,\lambda_X)(L_X,0;S_X,\lambda_X\mid J_X,\lambda_X) \times D^{J_X*}_{M_X,\lambda_X}(\phi_{GJ},\theta_{GJ},0)A_Y^{J_Y,M_Y,L_Y,S_Y}(m_Y,\theta_{HF},\phi_{HF}), \quad (5.9)$$

for some reaction $X\to Y+1$ where particle Y decays such that $Y\to 2+3$. The dynamical factors in the term have been taken outside the sum, the two Clebsch-Gordan coefficients remain inside the summation.

5.4 The Decay into Three Pseudoscalar particles

The decay amplitude $\psi_{X\to FS}$ is written as

$$\psi_{X\to FS}(m_X,\tau_3) = \sqrt{\frac{2L_X+1}{4\pi}}R_X(m_X)T_{\gamma N\to X} \sum_{\lambda_Y}(J_Y,\lambda_Y;0,0\mid S_X,\lambda_X)(L_X,0;S_X,\lambda_X\mid J_X,\lambda_X)\,D^{J*}_{M_X,\lambda_X}(\phi_{GJ},\theta_{GJ},0) A_Y^{J_Y,M_Y,L_Y,S_Y}(m_Y,\theta_{HF},\phi_{HF}). \quad (5.10)$$

The simplifications in eqn (5.10) arise from eqn (5.9) as the final state was composed of three spinless particles. In the decay of the resonance since particle 1 has spin = 0 ($J_1 = 0$) and consequently helicity = 0 ($\lambda_1 = 0$), the first Clebsch-Gordan coefficient became $(J_Y, \lambda_Y; 0, 0 \mid S_X, \lambda_X) = \delta_{J_Y S_X} \delta_{\lambda_X \lambda_Y}$. Since particles 2 and 3 were also spin-0, the full amplitude can be written as:

$$\psi_{X\to FS}(m_X, \tau_3) = \sqrt{\frac{2L_X+1}{4\pi}} R_X(m_X) \times \sum_{\lambda_X} (L_X, 0; S_X, \lambda_X \mid J_X, \lambda_X)\, D^{J*}_{M_X,\lambda_X}(\phi_{GJ}, \theta_{GJ}, 0) \times \sqrt{\frac{2L_Y+1}{4\pi}} R_Y(m_Y) D^{S_X*}_{\lambda_X,0}(\phi_{HF}, \theta_{HF}, 0) \quad (5.11)$$

Eqn 5.11 introduces the decay angles of the intermediate particle Y in the helicity frame, denoted θ_{HF} and ϕ_{HF}. In the same way that the Gottfried-Jackson frame was in the rest frame of the resonance X, the helicity frame is in the rest frame of the isobar Y, as shown in Appendix A.

Up to this point, the amplitude was written in terms of some given X and its associated quantum numbers, as well as the parameterisation of the isobar decay. For a full model for a decay however, the amplitude must allow for all possible quantum numbers and decay chains for X that were allowed by the strong interaction. Introducing an index i that takes into account all the information that is required to describe a decay, each amplitude depends on:

$$\begin{aligned} i :&= \{I^G, J^P, M_X; \text{isobars, total intrinsic spins, orbital angular momentum}\} \\ &= \{I^G, J^P, M_X, Y, S_X, L_X\} \end{aligned} \quad (5.12)$$

Each i represents a distinct partial wave. The total amplitude for the scattering was written by summing over all waves:

$$M_{fi}(m_X, t, \tau_n) = \sum_{i}^{N_{waves}} \Big[\sum_{k\in i} C_{ki}(t)\Big] \psi_i(m_X, \tau_n), \quad (5.13)$$

where the sum over k is over those resonances that contribute to a given i and $C_{ki}(t)$ are the coupling amplitudes at the beam/X/exchange vertex. The same resonance may appear in several waves, with different l and several resonances may be included in the same wave, with different mass dependence.

5.5 The Reflectivity Basis

In any formalism that models a reaction of the strong interaction, parity must be conserved. Although parity violation is not explicitly forbidden in this process, it is accepted from experiments

that parity is conserved. The incorporation of parity conservation into the model was done using the reflectivity basis [74]. The reflectivity basis was defined by first choosing a quantisation axis in the production plane. A possible choice for such an axis is the beam direction as in the definition of the Gottfried-Jackson frame.

The reflectivity operator is then defined as follows: a parity transformation involves a momenta flip for all particles and a rotation of π around the normal to the production plane (the y-axis). This combined transformation is known as the reflectivity transformation and is written $\hat{\Pi}_y$. Building states that are invariant under this transformation will ensure parity conservation is built into the model.

Consider a single particle spin state, $|J,M\rangle$, that exists in the production plane. The reflectivity operator acting on this state gives

$$\hat{\Pi}_y|J,M\rangle = P(-1)^{J-M}|J,-M\rangle. \tag{5.14}$$

Therefore, to construct reflectivity states it is necessary to construct eigenstates that are linear combinations of canonical states[1] with opposite spin projections. In other words:

$$|J,M\rangle^{\varepsilon} = N_M[|J,M\rangle - \varepsilon P(-1)^{J-M}|J,-M\rangle], \tag{5.15}$$

where N_M is the normalisation factor:

$$N_M = \begin{cases} \frac{1}{\sqrt{2}}, & M \neq 0 \\ \frac{1}{2}, & M = 0. \end{cases} \tag{5.16}$$

The normalisation term ensures the total multiplicity of the state is $(2J+1)$, as in the canonical basis.

The state in the reflectivity basis is characterised by the spin projection of the resonance M and the reflectivity quantum number ε. That is, the production amplitudes in the reflectivity basis can be written as

$${}^{\varepsilon}T_{J,M} = T_{J,M} - \varepsilon P(-1)^{J-M}T_{J,-M}, \tag{5.17}$$

where the superscript ε denotes the state is in the reflectivity basis and the lack of denotes the canonical basis.

There is a distinction to be made in terms of the application of the reflectivity basis in a two body reaction vs a three body reaction. In both cases, there is no interference between waves of different reflectivity. However, uniquely for a two pseudoscalar final state, the reflectivity quantum number gives information on the naturality of the exchange particle - the naturality of a particle is defined by $\eta = P(-1)^J$ for parity P and total angular momentum J. For bosons,

[1] Canonical states are those defined by a total angular momentum J and a spin projection M

$\varepsilon = \pm 1$ and since reflectivity is conserved there is the restriction that

$$\varepsilon_{beam} + \varepsilon_{exchange} = \varepsilon_{resonance}. \tag{5.18}$$

When the final state is not simply two pseudoscalars the same conclusion cannot be made. In this case, there will be no interference of waves of different reflectivity only. The implication of this fact on the pseudo two-body decay will be discussed in Section 5.12.

5.6 Photoproduction

Using a linearly polarised photon beam allows more information to be extracted in the experiment through the measurement of unpolarised and polarised intensities. This section will provide more detail on the formalism incorporating linear polarisation and how it allowed extra information to be measured.

5.6.1 Photon Polarisation

An introduction to the photon polarisation is given here as a summary of Section 4.1 from [74]. First, consider a real photon beam in a linearly polarised state. It will be shown in section 5.6.2 how the low Q^2 electron scattering is equivalent to using linearly polarised photons. By the Lorentz condition for transverse waves, the linear polarisation vector of the photon will be in a plane perpendicular to the direction of momentum. As such, there will be two possible spin polarisation states of the photon. Classically, one spin state is aligned with the electric field vector. Call these two spin states $|P_1\rangle$ and $|P_2\rangle$. We define $|P_1\rangle$ is aligned with the direction of the electric field and $|P_2\rangle$ forms the orthogonal basis.

Experimentally, the polarised beam in the reaction is a mixture of pure spin states $|P_1\rangle$ and $|P_2\rangle$. All the information on these spin states for the reaction is contained in the photon spin density matrix, ρ_γ. If the incoming spin state is denoted $|in\rangle$, then:

$$|in\rangle\langle in| = \sum_{i,j} \rho_{\gamma,ij} \tag{5.19}$$

$$= \rho_\gamma. \tag{5.20}$$

External spins are accounted for in an incoherent sum taking into account factors like the spin flip/non-flip of the nucleon for example.

The sum over i, j in equation (5.19) referred to the sum over the two spin states. In the $|P_1\rangle, |P_2\rangle$ basis, the expansion of this sum is

$$\rho_\gamma = W_1 |P_1\rangle\langle P_1| + W_2 |P_2\rangle\langle P_2|, \tag{5.21}$$

where $W_{1,2}$ are the relative weights of each spin state respectively. Labelling the number of photons in spin state 1(2) as $N_{1(2)}$, where $N_{1(2)} = \langle P_{1(2)}|\rho_\gamma|P_{1(2)}\rangle$. The normalisation is then given by

$$N = N_1 + N_2, \tag{5.22}$$

where N is the total number of photons. The partial polarisation, $\mathscr{P} \in [0,1]$ is defined as:

$$\mathscr{P} = \frac{|\,N_1 - N_2\,|}{N} \tag{5.23}$$

In this definition, the weights W_1 and W_2 are given by the ratios

$$W_{1(2)} = \frac{N_{1(2)}}{N}. \tag{5.24}$$

Using relations (5.22)(5.23), the weights can be rewritten as

$$W_1 = \frac{1+\mathscr{P}}{2}, \quad W_2 = \frac{1-\mathscr{P}}{2}. \tag{5.25}$$

Using relation (5.24) in equation (5.21) gives

$$\rho_\gamma = \frac{1+\mathscr{P}}{2}|P_1\rangle\langle P_1| + \frac{1-\mathscr{P}}{2}|P_2\rangle\langle P_2|. \tag{5.26}$$

From here the matrix representation follows:

$$\rho_\gamma = \frac{1}{2}\begin{pmatrix} 1+\mathscr{P} & 0 \\ 0 & 1-\mathscr{P} \end{pmatrix}. \tag{5.27}$$

As stated, this is the photon spin density matrix in the $|P_1\rangle, |P_2\rangle$ basis. The SDM changes from the $|P_1\rangle, |P_2\rangle$ basis to a different basis [74]. In the Gottfried-Jackson basis the photon spin density matrix is

$$\rho_{\gamma,GJ} = \frac{1}{2}\begin{pmatrix} 1+\mathscr{P}\cos 2\Phi & -\mathscr{P}\sin 2\Phi \\ -\mathscr{P}\sin 2\Phi & 1-\mathscr{P}\cos 2\Phi \end{pmatrix}, \tag{5.28}$$

where Φ is the angle defined by the axis of transverse spin polarisation relative to the X production plane. In the helicity basis the SDM becomes:

$$\rho_{\gamma,Hel} = \frac{1}{2}\begin{pmatrix} 1 & -\mathscr{P}e^{-2i\Phi} \\ -\mathscr{P}e^{2i\Phi} & 1 \end{pmatrix}. \tag{5.29}$$

5.6.2 Virtual Photoproduction

The scattering of the electron from a proton can be modelled through the exchange of a virtual photon of energy $\nu = E - E'$, where E, E' are the energies of the incoming and scattered

electrons respectively. The 3-momentum of the virtual photon is $\underline{q} = \underline{k} - \underline{k}'$, where $\underline{k}, \underline{k}'$ are the 3-momenta of the incoming and scattered electron. Using this, it was possible to define two important quantities. The invariant mass of the beam and target system is s, defined as:

$$s = (\nu + M)^2 - \underline{q}.\underline{q}, \tag{5.30}$$

where M is the mass of the target proton. In addition to this, the squared 4-momentum of the virtual photon is

$$Q^2 = \underline{q}.\underline{q} - \nu^2. \tag{5.31}$$

The emission of the photon by the electron here can be described as off mass shell as Q^2 is not zero as it would be for a real photon. There can also be a component of the polarisation in the longitudinal direction, the direction of momentum of the photon. Writing the longitudinal polarisation component as $\mathscr{P}_L$, and now with the photon SDM in three dimensions to account for the possible polarisation in the z-direction, the SDM can be written [75] [76]:

$$\rho_\gamma = \begin{pmatrix} \frac{1}{2}(1+\mathscr{P}) & 0 & -\frac{1}{2}\mathscr{P}_L(1+\mathscr{P})]^{\frac{1}{2}} \\ 0 & \frac{1}{2}(1-\mathscr{P}) & 0 \\ -\frac{1}{2}\mathscr{P}_L(1-\mathscr{P})]^{\frac{1}{2}} & 0 & \mathscr{P}_L \end{pmatrix}, \tag{5.32}$$

where it can be observed eqn (5.27) is retained as the first two rows and columns. The longitudinal polarisation is given by [77]:

$$\mathscr{P}_L = \frac{Q^2}{\nu^2}\mathscr{P}, \tag{5.33}$$

with the scattering kinematics giving the virtual photon polarisation:

$$\mathscr{P} = \left[1 + 2\frac{(Q^2+\nu^2)}{Q^2}\tan^2\left(\frac{\theta}{2}\right)\right]^{-1}, \tag{5.34}$$

where θ was the angle between the incoming and scattered electron in the rest frame of the proton.

The 4-momentum of the virtual photon was used to characterise the regime in which the reaction takes place. This analysis is based on the assumption that $\mathscr{P}_L \ll \mathscr{P}$ since $Q^2 \ll 1$ and $\nu \sim 10$. In experiments using unpolarised electron beams, in the low-Q^2 limit, the physics is equivalent to using a linearly polarised photon beam [76], with the degree of polarisation calculated from the electron scattering angle.

5.6.3 Polarised Intensities

Using a linearly polarised photon beam allows us to obtain more experimental observables from the reaction. The photon spin density matrix (SDM) contains all the information about the spin

of the photon. The photon SDM can be decomposed as a basis of 2×2 Hermitian matrices as [78]:

$$\rho_\gamma(\Phi) = I + \underline{\mathscr{P}}_\gamma(\Phi).\underline{\sigma}, \tag{5.35}$$

where I is the identity matrix, $\underline{\sigma} = (\sigma_1, \sigma_2, \sigma_3)$ are the Pauli matrices and the dependence on the angle between the electron scattering plane and the production plane, Φ, has been made explicit in $\underline{\mathscr{P}}_\gamma$. In terms of intensities, the photon SDM manifests itself as

$$\mathscr{I}(\Omega, \Phi) = \mathscr{I}^0(\Omega) + \underline{\mathscr{I}}(\Omega).\underline{\mathscr{P}}_\gamma(\Phi), \tag{5.36}$$

where $\underline{\mathscr{I}} = (\mathscr{I}^1, \mathscr{I}^2, \mathscr{I}^3)$ is the vector of polarised intensities and Ω is the relevant set of X decay angles.

Taking the photon spin density matrix in the helicity basis [79], in which the polarisation vector, in accordance with eqn (5.35), was written:

$$\underline{\mathscr{P}}_\gamma(\Phi) = \mathscr{P}(-\cos 2\Phi, -\sin 2\Phi, \frac{Q^2}{\nu^2}). \tag{5.37}$$

It follows that the intensity can be expanded as:

$$\mathscr{I}(\Omega, \Phi) = \mathscr{I}^0(\Omega) - \mathscr{P}.\mathscr{I}^1(\Omega)\cos 2\Phi - \mathscr{P}.\mathscr{I}^2(\Omega)\sin 2\Phi - \mathscr{P}.\mathscr{I}^3(\Omega)\frac{Q^2}{\nu^2}. \tag{5.38}$$

5.7 The Meson Resonance Spin Denity Matrix

The spin density matrix of the resonance was introduced in Section 5.9 and will now be fully defined in terms of the intensity and the photon spin density matrix. As given in eqn (5.13), the total amplitude for the scattering is $M_{fi}(m_X, t, \tau_n)$ which was derived from the understanding that M_{fi} takes an initial state to a final state, in other words written as:

$$M_{fi} = \langle out|\hat{T}|in\rangle, \tag{5.39}$$

where $\hat{T}$ is the transition operator from the initial state to the final state. The intensity is then given by:

$$\mathscr{I} = \sum_k |M_{fi}|^2 = \sum_k M_{fi} M^*_{fi}, \tag{5.40}$$

where k is the sum over external spins - the spin parameters outside of those used to characterise the decay, such as the spin of the proton in this case. Substituting eqn (5.39) for M_{fi} gives

$$\mathscr{I} = \sum_k \langle out|\hat{T}|in\rangle (\langle out|\hat{T}|in\rangle)^* \tag{5.41}$$

$$= \sum_k \langle out|\hat{T}|in\rangle \langle in|\hat{T}^\dagger|out\rangle. \tag{5.42}$$

Noting the definition of eqn (5.19), $|in\rangle\langle in| = \rho_\gamma$ and by assuming that the transition amplitude $\hat{T}$ can be split into an amplitude for production $\hat{T}_p$ and decay $\hat{T}_d$, then:

$$\mathscr{I} = \sum_k \langle out|\hat{T}_d\,\hat{T}_p\,\rho_\gamma\,\hat{T}_p^\dagger\,\hat{T}_d^\dagger|out\rangle. \tag{5.43}$$

A complete set of states is given by:

$$\sum_i |X_i\rangle\langle X_i| = 1, \tag{5.44}$$

where the set i is given by eqn 5.12. Inserting eqn (5.44) into eqn (5.43) gives:

$$\mathscr{I} = \sum_k \langle out|\hat{T}_d \sum_{X_i} |X_i\rangle\langle X_i|\hat{T}_p\,\rho_\gamma\,\hat{T}_p^\dagger \sum_{X_{i'}} |X_{i'}\rangle\langle X_{i'}|\hat{T}_d^\dagger|out\rangle. \tag{5.45}$$

The term $\langle out|\hat{T}_d \sum_X |X\rangle$ that takes some given intermediate state X to the final state is given by the decay amplitude, $\sum_i \psi_i$, where the sum over i is the sum over all the decays X to the final state. We can write:

$$\mathscr{I} = \sum_k \sum_i \psi_i \langle X_i|\hat{T}_p\,\rho_\gamma\,\hat{T}_p^\dagger\,|X_{i'}\rangle \sum_{i'} \psi_{i'}. \tag{5.46}$$

From this, we define the spin density matrix of the resonance to be

$$\rho_{bb'} = \sum_k \langle X_i|\hat{T}_p\,\rho_\gamma\,\hat{T}_p^\dagger\,|X_{i'}\rangle = \sum_k T_b^k \rho_\gamma T_{b'}^k, \tag{5.47}$$

where T_b^k are the production amplitudes and b is the set $b = \{j = J_X, l = L_X, m = M_X, s = S_X\}$, the quantum numbers that define the decay. In the same way that the spin density matrix of the photon contained all the spin information about the initial state photon, the SDM $\rho_{bb'}$ contains all the spin information of the resonance.

The characteristic features of the photon spin density matrix influence the way the reaction is described. From eqn (5.35), given a polarised beam and unpolarised target the intensity is made up of four terms, $\mathscr{I}^0, \mathscr{I}^1, \mathscr{I}^2, \mathscr{I}^3$, that can be denoted $\mathscr{I}^\alpha$ where $\alpha = 0,1,2,3$. Subsequently the resonance spin density matrix is indexed by α, separating unpolarised and different polarised parts $\rho_{bb'}^\alpha$. Following from eqns (5.35), (5.36) and (5.47), it is clear that the terms in the photon spin density matrix (and consequently the terms in the intensity $\mathscr{I}^\alpha(\Omega,\Phi)$) are dependent on

the Pauli matrices; therefore the resonance spin density matrix is written in full as:

$$\rho^{\alpha}_{bb'} = \sum_{k}^{ext.spins} T^{k}_{b} \sigma^{\alpha} T^{k}_{b'}. \tag{5.48}$$

The intensity written in terms of the resonance spin density matrix is:

$$\mathscr{I}^{\alpha}(\Omega,\Phi) = \sum_{i,i'} \psi_i \rho^{\alpha}_{bb'} \psi_{i'} \tag{5.49}$$

5.8 Polarised Intensity in terms of Partial Waves

It is possible to write explicit relations for the components of the spin density matrix in terms of the partial wave amplitudes, T_b. The polarised intensities that are a part of the full intensity were accessible when the experiment uses a polarised photon beam, so it was natural to think that the polarised intensities were directly related to information extracted from the photon - namely the photon spin (or helicity in the helicity framework).

Writing the explicit form of the spin density matrix in the helicity basis for each of the components of the intensity gives:

$$\rho^{\alpha}_{rr',mm'} = \sum_{k} \sum_{\eta\eta'} T^{k,\eta}_{r,m} \sigma^{\alpha}_{\eta\eta'} T^{k,\eta'}_{r',m'}, \tag{5.50}$$

where $T^{k,\eta}_{r,m}$ are the production amplitudes now indexed by $r = \{j,l,s\}$ and m, to make the dependence on m explicit. This expression made the sum over photon helicities (η) clear also, where $\eta(\eta')$ refers to $\lambda_\gamma = +1(-1)$.

Expanding the sum over photon helicities uses the Pauli matrices:

$$\sigma^0 = \begin{pmatrix} 1 & 0 \\ 0 & 1 \end{pmatrix}, \sigma^1 = \begin{pmatrix} 0 & 1 \\ 1 & 0 \end{pmatrix}, \sigma^2 = \begin{pmatrix} 0 & -i \\ i & 0 \end{pmatrix}. \tag{5.51}$$

Now substituting eqns (5.51) into eqn (5.50) gives

$$\rho^{0}_{rr',mm'} = \sum_{k} T^{k,\eta}_{r,m} T^{k,\eta}_{r',m'} + T^{k,\eta'}_{r,m} T^{k,\eta'}_{r',m'}, \tag{5.52}$$

$$\rho^{1}_{rr',mm'} = \sum_{k} T^{k,\eta'}_{r,m} T^{k,\eta}_{r',m'} + T^{k,\eta}_{r,m} T^{k,\eta'}_{r',m'}, \tag{5.53}$$

$$\rho^{2}_{rr',mm'} = i \sum_{k} -T^{k,\eta'}_{r,m} T^{k,\eta}_{r',m'} + T^{k,\eta}_{r,m} T^{k,\eta'}_{r',m'}, \tag{5.54}$$

for each component of the meson spin density matrix.

The intensity can be written in terms of the resonance spin density matrix by substituting

eqn (5.11) for the decay amplitude into eqn (5.49) as:

$$\mathscr{I}^{\alpha}(\Omega,\Phi) = \sum_{k}\sum_{i,i'}^{N_{waves}} \sqrt{\frac{2L_X+1}{4\pi}}\sqrt{\frac{2S_X+1}{4\pi}}\sqrt{\frac{2L'_X+1}{4\pi}}\sqrt{\frac{2S'_X+1}{4\pi}} \times (L_X,0;S_X,\lambda_X|J_X,\lambda_X)(L'_X,0;S'_X,\lambda'_X|J'_X,\lambda'_X) \times D^{J_X}_{M_X,\lambda_X}(\phi_{GJ},\theta_{GJ},0)D^{J_Y}_{\lambda_X,0}(\phi_{HF},\theta_{HF},0)R_{Yi}(m_Y) \times D^{J'_X*}_{M'_X,\lambda'_X}(\phi_{GJ},\theta_{GJ},0)D^{J'_Y*}_{\lambda'_X,0}(\phi_{HF},\theta_{HF},0)R^{*}_{Yi'}(m_Y) \times \rho^{\alpha}_{rr',mm'}. \quad (5.55)$$

Rewriting eqn (5.55) in terms of the set $\{j = J_X, l = L_X, m = M_X, s = S_X\lambda = \lambda_X\}$ gives:

$$\mathscr{I}^{\alpha}(\Omega,\Phi) = \sum_{r,r'}\sum_{m,m'}\sum_{\lambda,\lambda'} \sqrt{\frac{2l+1}{4\pi}}\sqrt{\frac{2s+1}{4\pi}}\sqrt{\frac{2l'+1}{4\pi}}\sqrt{\frac{2s'+1}{4\pi}} \times (l,0;s,\lambda|j,\lambda)(l',0;s',\lambda'|j',\lambda') \times D^{j}_{m,\lambda}(\phi_{GJ},\theta_{GJ},0)D^{s}_{\lambda,0}(\phi_{HF},\theta_{HF},0)R_{Yi}(m_Y) \times D^{j'*}_{m',\lambda'}(\phi_{GJ},\theta_{GJ},0)D^{s'*}_{\lambda',0}(\phi_{HF},\theta_{HF},0)R^{*}_{Yi'}(m_Y) \times \rho^{\alpha}_{rr',mm'}. \quad (5.56)$$

5.9 The Intensity Using Moments of Angular Distribution

To rewrite eqn (5.56) in terms of the moments of angular distribution required the Kronecker product of Wigner D-functions. Noting that in eqn (5.56), there were two sets of such D-functions of the same variable that formed a reducible representation, the irreducible representation was found using the outer product relation between D-functions:

$$D^{j}_{mk}(\alpha,\beta,\gamma)D^{j'}_{m'k'}(\alpha,\beta,\gamma) = \sum_{J=|j-j'|}^{j+j'}\sum_{M=-|m+m'|}^{|m+m'|}\sum_{K=-|k+k'|}^{|k+k'|}(j,m;j',m'|JM)(j,k;j',k'|JK)D^{J}_{MK}(\alpha,\beta,\gamma). \quad (5.57)$$

The sum over J,S in the moment variables runs from $J = 0,1,...,j+j'$ and $S = 0,1,..,s+s'$, with the sum over $M = -|m+m'|,...,|m+m'|$ and $\Lambda = -|\lambda+\lambda'|,...,|\lambda+\lambda'|$ as described in eqn (5.57).

This relation was true for two 'non-conjugate' D-functions. In the intensity however, when we consider the D-functions for each set of variables there was a D-function and a conjugate

D-function. Relation (5.57) adapts in this case to [80]:

$$D^{j}_{mk}(\alpha,\beta,\gamma)D^{j'*}_{m'k'}(\alpha,\beta,\gamma) = \sum_{J=|j-j'|}^{j+j'} \sum_{M=-|m+m'|}^{|m+m'|} \sum_{K=-|k+k'|}^{|k+k'|} \left(\frac{2J+1}{2j'+1}\right)(j,m;J(m+m')|j',m')(j,k;J(k+k')|j',k') D^{J}_{(m+m')(k+k')}(\alpha,\beta,\gamma). \quad (5.58)$$

Now using equations (5.56) and (5.58), the polarised intensities are given by:

$$\mathscr{I}^{\alpha}(\Omega,\Phi) = \sum_{S\Lambda JM}\left(\frac{2J+1}{4\pi}\right)\left(\frac{2S+1}{4\pi}\right)H^{\alpha}(S,\Lambda,J,M) \times D^{J*}_{M,\Lambda}(\phi_{GJ},\theta_{GJ},0)D^{S*}_{\Lambda,0}(\phi_{HF},\theta_{HF},0), \quad (5.59)$$

with the moments, which are essentially Fourier coefficients of the angular distributions, being combinations of partial wave intensities described by:

$$H^{\alpha}(S,\Lambda,J,M) = \sum_{r,r'}\sum_{m,m'}\sum_{\lambda,\lambda'}\left(\frac{\sqrt{(2l'+1)(2l+1)}}{2j'+1}\right)\left(\sqrt{\frac{2s+1}{2s'+1}}\right)(l,0;s,\lambda|j,\lambda)(l',0;s',\lambda'|j',\lambda') \times (s,\lambda;S,\Lambda|s',\lambda')(s,0;S,0|s',0)(j,m;J,M|j',m')(j,\lambda;J,\Lambda|j',\lambda') \times \rho^{\alpha}_{rr',mm'} \times R_{Yi}(m_Y)R^{*}_{Yi'}(m_Y). \quad (5.60)$$

The intensity is by definition a real number, however each term is a sum over complex D-functions. Appendix B shows that the intensity is always real when considering the sum over the quantum numbers of the moments, S,Λ,J and M.

5.10 The Sum over Moments

As explored in Section 5.9, the moment parameters $S\Lambda JM$ were defined by the quantum numbers of the waves. The sum over J and S ranges from $|j-j'|$ to $|j+j'|$ and $|s-s'|$ to $|s+s'|$ respectively and the helicity and spin projection quantum numbers of the resonance define M and Λ from eqn (5.57). There are some simplifications and symmetries however that reduced the set of moments that are required to fit the intensity.

5.10.1 Negative Spin projection moments

The case of negative spin projection moments could be split into two cases. Firstly, if M and Λ were both negative. In this case, the relation:

$$H(S,\Lambda,J,M) = (-1)^M H(S,-\Lambda,J,-M) \tag{5.61}$$

defined by S.U. Chung (2014) [80] and explored further in Appendix B is used to replace $H(S,-\Lambda,J,-M)$.

Secondly, if only the component Λ was negative, the expansion of the moment in terms of quantum numbers of the wave, given by eqn (5.60) was used. Consider only the parts that are dependent on the helicity quantum number. The sum over λ,λ' gave six terms, four that are detailed below and the terms $(l,0;s,\lambda\,|\,j,\lambda),(l',0;s',\lambda'|\,j',\lambda')$ that are not affected by the value of Λ. Considering only the Clebsch-Gordan coefficients which are dependent on Λ:

$$\begin{aligned}
&(s,\lambda;S,-\Lambda|s',\lambda')(j,\lambda;J,-\Lambda|j',\lambda')\\
&+(s,\lambda;S,-\Lambda|s',-\lambda')(j,\lambda;J,-\Lambda|j',-\lambda')\\
&+(s,-\lambda;S,-\Lambda|s',\lambda')(j,-\lambda;J,-\Lambda|j',\lambda')\\
&+(s,-\lambda;S,-\Lambda|s',-\lambda')(j,-\lambda;J,-\Lambda|j',-\lambda').
\end{aligned} \tag{5.62}$$

Using the following symmetry relation for Clebsch-Gordan coefficients:

$$(s,\lambda;S,\Lambda|s',\lambda') = (-1)^{s+s'+S}(s,-\lambda;S,-\Lambda|s',-\lambda'), \tag{5.63}$$

then the sum (5.62) can be recast as:

$$\begin{aligned}
&(s,-\lambda;S,\Lambda|s',-\lambda')(j,-\lambda;J,\Lambda|j',-\lambda')\times(-1)^q\\
&+(s,-\lambda;S,\Lambda|s',\lambda')(j,-\lambda;J,\Lambda|j',\lambda')\times(-1)^q\\
&+(s,\lambda;S,\Lambda|s',-\lambda')(j,\lambda;J,\Lambda|j',-\lambda')\times(-1)^q\\
&+(s,\lambda;S,\Lambda|s',\lambda')(j,\lambda;J,\Lambda|j',\lambda')\times(-1)^q,
\end{aligned} \tag{5.64}$$

where $q = s+s'+S+j+j'+J$. Now the terms listed in (5.64), and therefore the moment $H(S,-\Lambda,J,M)$ differ only by a factor $(-1)^q$ from the moment $H(S,\Lambda,J,M)$. If q is even (odd), then $H(S,\Lambda,J,M) = (-)H(S,-\Lambda,J,M)$ and the negatively indexed moment was not required in the fit as it is fully defined by the positive index moments. The same argument can be applied for moments indexed by negative M terms by the relation (B.4). In full, moments indexed by negative values were not required in the fit.

5.10.2 Restriction on polarised moments

From eqn (5.60), the sum over the quantum numbers will force $H^2(S,0,J,0) = 0$ for any S,J. This is due to the fact that since $M = \Lambda = 0$ then the Clebsch-Gordan coefficients constrain the quantum numbers of the waves such that $m = m'$ and $\lambda = \lambda'$. For every set of quantum numbers $r = r_1, r' = r_2$ in eqn (5.54), there will be an exact copy such that $r = r_2, r' = r_1$. In other words, for every $T^{k,\eta'}_{r,m} T^{k,\eta}_{r',m'}$ term in the summation in eqn (5.60), there will be a term $-T^{k,\eta}_{r',m'} T^{k,\eta'}_{r,m}$. The net result is the cancellation of all terms in these spin density matrix elements and the moment is identically zero.

5.10.3 Truncation of the Moments based on Wave Contribution

In some cases, there was a restriction placed on the moments originating from the assumed waveset. For example, if it was assumed that the highest order waves in a fit were of $j_{max} = 3$, with $m_{max} = 3$ then the highest order moments allowed would have $J,M = 6$. Further restrictions may be placed on the waves under the assumption that higher order spin projections will be restricted in photoproduction. For example, if the $m = \pm 3$ spin projections are not allowed.

5.10.4 Restrictions deriving from a Pseudo Two-Body Decay

Some restrictions on the indices of the moments derived directly from the assumed pseudo two-body nature of the decay process. In fixing the isobar in the decay model to be a vector state, its spin is $s = s' = 1$ and $S = 0,2$ since eqn (5.60) contains the Clebsch-Gordan coefficient $(s,0;S,0|s',0)$, only non-zero in this case for $S = 0,2$ and identically zero for $S = 1$. The difference in the value of the moments $H(0,0,J,M)$ and $H(2,0,J,M)$ for fixed J,M was contained only in the Clebsch-Gordan coefficients containing S. In other words, the wave contribution in these moments was the same, differing only by a scale factor that originated from the Clebsch-Gordan coefficients.

We can compare the vector-pseudoscalar final state to the pseudoscalar-pseudoscalar final state that has been discussed in [78]. In the two pseudoscalar example, moments are defined by quantum numbers J,M. Compare this with the vector-pseudoscalar example discussed here. The restrictions placed on the set of S,Λ,J,M limit the number of independent moments to four times that of the two pseudoscalar example - for each J,M the moments $H(0,0,J,M), H(2,0,J,M)$, $H(2,1,J,M)$ and $H(2,2,J,M)$ are the only moments that are allowed and mutually independent.

5.11 Parity of Resonances

Knowing the spin quantum numbers of the wave gives enough information to be able to work out the parity of a resonance in the decay to three pseudoscalars. Since both of the products

of the decay of the isobar were pseudoscalars, $J_Y = L_Y$ and the parity of the isobar was related directly to its spin such that

$$P_Y = P_2 P_3 (-1)^{L_Y} \tag{5.65}$$
$$= (-1)(-1)(-1)^{J_Y} \tag{5.66}$$
$$= (-1)^{J_Y}, \tag{5.67}$$

where P_Y, P_2 and P_3 are the intrinsic parity of the isobar and two daughter particles respectively. Now the parity of the resonance can be calculated in the same way with:

$$P_X = P_1 P_Y (-1)^{L_Y} \tag{5.68}$$
$$= (-1)(-1)^{J_Y}(-1)^{L_X} \tag{5.69}$$
$$= (-1)^{J_Y+1}(-1)^{L_X}. \tag{5.70}$$

So for a given wave defined by quantum numbers $b = \{J_X, L_X, M_X, S_X\}$, the parity of the isobar could be fully defined from the spin of the isobar and angular momentum of the decay.

5.12 Partial Waves and Moments

Moments provide a well defined summary of a data set from which partial waves may be extracted. It is from the partial waves that a clearer picture of the wave content of a decay is given. Two methods were considered from which waves could be related to the moments.

The first of these is defined by eqn (5.60). The waves will relate to the moments in the expansion using relations (5.52), (5.53) and (5.54). Each wave in this context is defined by the set of quantum numbers $b = \{j, l, m, s\}$ so an inversion from moments to waves is required to be well defined in terms of each quantum number. If the number of wave parameters (i.e. magnitude and phase) defined by the set b is less than the set of linearly independent moments then an inversion from moments to waves may be possible.

Another formalism with which the partial wave content of moments could be defined was written in collaboration with V. Mathieu (University of Barcelona). In this case, the moments are defined in terms of couplings such that

$$H^{\alpha}(S,\Lambda,J,M) = \sum_{i,i'} \sum_{m,m'} \sum_{\lambda,\lambda'} \left(\frac{2s+1}{2s'+1}\right)^{\frac{1}{2}} (s,\lambda;S,\Lambda|s',\lambda')(s,0;S,0|s',0) \times (j,m;J,M|j',m')(j,\lambda;J,\Lambda|j',\lambda')\, F^{i}_{\lambda}\, F^{i*}_{\lambda'}\, \rho^{\alpha}_{ii',mm'}, \tag{5.71}$$

where F^i_λ are the couplings defined as

$$F^i_\lambda = \sum_l \left(\frac{2l+1}{2j+1}\right)^{\frac{1}{2}} a^i_{l,s}(l,0;s,\lambda|j,\lambda), \tag{5.72}$$

with $a^i_{l,s}$ the LS couplings with parity $(-1)^{l+1}$. The motivation for this alternative approach is to separate the resonance from its decay. In this context, there is a distinction made between the resonances that are defined by their spin and parity, and their decay, defined by l. The resonance X is defined by spin j and parity P and the isobar solely by s since the decay of the isobar to two pseudoscalars specifies natural parity. The set $i = \{j,P,s\}$ defines the resonance content of the decay and is contained by the spin density matrix. The symmetry of the LS couplings then define the parity of the decay wave.

In reality, no information is gained or lost using either formalism. The latter simply makes the symmetry of the decay explicit. To see that they are equivalent, substitute eqn (5.72) into (5.71) to get

$$\begin{aligned} H^\alpha(S,\Lambda,J,M) = \\ \sum_{i,i'}\sum_{m,m'}\sum_{\lambda,\lambda'}\left(\frac{\sqrt{(2l'+1)(2l+1)}}{2j'+1}\right)\left(\sqrt{\frac{2s+1}{2s'+1}}\right)(l,0;s,\lambda|j,\lambda)(l',0;s',\lambda'|j',\lambda') \\ \times(s,\lambda;S,\Lambda|s',\lambda')(s,0;S,0|s',0)(j,m;J,M|j',m')(j,\lambda;J,\Lambda|j',\lambda') \\ \times \rho^\alpha_{ii',mm'}\, a^i_{l,s}\, a^{i'*}_{l',s'}, \end{aligned} \tag{5.73}$$

where there is an equivalence between $\rho^\alpha_{rr',mm'}$ from eqn 5.60 and $\rho^\alpha_{ii',mm'}a^i_{l,s}a^{i'*}_{l',s'}$ from eqn 5.73

The unknowns of eqn (5.73) are $\rho^\alpha_{ii',mm'}$, $a^i_{l,s}$ and $a^{i'*}_{l',s'}$. The quantum numbers j,m,s are contained in the spin density matrix as well as the parity of the resonance X. It is enough to use the LS coupling and the parity to find the spin of the decay wave, l. In other words, the set of unknowns in this framework is the set $b = \{j,l,m,s\}$, as defined in the original formalism.

5.12.1 SDMEs in the Reflectivity Basis

It is useful to write the spin density matrix in the reflectivity basis as, in this basis, the photon helicity is traded for the reflectivity quantum number that makes the symmetry of the relations involving the waves explicit. Writing the production amplitude in the reflectivity basis in terms of the helicity amplitudes gives

$${}^{(\varepsilon)}T^i_{m;\lambda_p\lambda_n} = \frac{1}{2}[T^i_{\lambda_\gamma m;\lambda_p\lambda_n} - \varepsilon\eta_X(-1)^m T^i_{-\lambda_\gamma -m;\lambda_p\lambda_n}], \tag{5.74}$$

where $\eta_X = P_X(-1)^{J_X}$ is the naturality of particle X. The naturality of the exchange particle is related to the reflectivity of the production amplitudes as at high energy (V. Mathieu, University of Barcelona):

$$T^i_{-\lambda_\gamma - m;\lambda_p\lambda_n} \simeq -\eta\,\eta_e(-1)^m T_{\lambda_\gamma m;\lambda_p\lambda_n}, \tag{5.75}$$

where η_e is the naturality of the exchange particle. Components with different reflectivity have no interference as a direct result of parity conservation [74]. The parity relations for the reflectivty amplitudes are:

$${}^{(\varepsilon)}T^i_{m;-\lambda_p-\lambda_n} = \varepsilon(-1)^{\lambda_p-\lambda_n}{}^{(\varepsilon)}T^i_{m;\lambda_p\lambda_n}. \tag{5.76}$$

As a result of the non-interference between reflectivity components, we have:

$$\sum_{\lambda_p\lambda_n} {}^{(\varepsilon)}T^i_{m;\lambda_p\lambda_n}\,{}^{(\varepsilon')}T^{i'*}_{m';\lambda'_p\lambda'_n} = 2\delta_{\varepsilon\varepsilon'}\sum_{k=0,1}[J_X^{P_X}]^{(\varepsilon)}_{m,k}[J_X^{\prime P'_X}]^{(\varepsilon')*}_{m',k}, \tag{5.77}$$

where k denotes the sum over incoherent contributions, such as the spin flip of the nucleon. In this particular choice of basis there are only two possible values for k - 0 denoting no spin flip and 1 for spin flip. In this basis, the spin density matrix elements written in terms of partial waves are:

$${}^{(\varepsilon)}\rho^0_{ii',mm'} = \sum_k [J_X^{P_X}]^{(\varepsilon)}_{m,k}[J_X^{\prime P'_X}]^{(\varepsilon')*}_{m',k} + \eta_X\eta'_X(-1)^{m+m'}[J_X^{P_X}]^{(\varepsilon)}_{-m,k}[J_X^{\prime P'_X}]^{(\varepsilon')*}_{-m',k}, \tag{5.78}$$

$${}^{(\varepsilon)}\rho^1_{ii',mm'} = \varepsilon\sum_k \eta_X(-1)^m[J_X^{P_X}]^{(\varepsilon)}_{-m,k}[J_X^{\prime P'_X}]^{(\varepsilon')*}_{m',k} + \eta'_X(-1)^{m'}[J_X^{P_X}]^{(\varepsilon)}_{m,k}[J_X^{\prime P'_X}]^{(\varepsilon')*}_{-m',k}, \tag{5.79}$$

$${}^{(\varepsilon)}\rho^2_{ii',mm'} = i\varepsilon\sum_k \eta_X(-1)^m[J_X^{P_X}]^{(\varepsilon)}_{-m,k}[J_X^{\prime P'_X}]^{(\varepsilon')*}_{m',k} - \eta'_X(-1)^{m'}[J_X^{P_X}]^{(\varepsilon)}_{m,k}[J_X^{\prime P'_X}]^{(\varepsilon')*}_{-m',k}. \tag{5.80}$$

5.13 Quantum Numbers in the Decay

This section provides an example of how the quantum numbers and conservation rules can be used to define a decay process and how this relates to the resonance X decay in the vector-pseudoscalar case. In terms of describing the spin formalism, the arguments in this section will build largely on those from Section 5.4, in which there was the discussion on how the decay $X \to Y + 1$ involves the spinless particle labelled '1' (as well as the final state particles labelled '2 ' and '3' from the decay of the isobar).

Consider the known spin relation

$$|L-S| \le J \le |L+S|, \tag{5.81}$$

where J is the total spin, L is the orbital angular momentum and S is the intrinsic angular momentum and first look at the isobar decay $Y \to 2+3$. Since both daughter pions are spinless, the

total intrinsic spin of the final state $S_2 + S_3 = 0$ and so $J_{2+3} = J_Y = L_Y$, with the first equality coming from the conservation of angular momentum. In order to fully characterise the isobar Y, take $s = J_Y$ and λ for the helicity of the isobar (in the helicity basis).

For the decay of the resonance into the isobar and a spin-0 particle: $X \to Y + 1$, write that $S_X = J_Y$, and as the spin of the isobar is not identically zero, the relation (5.81) no longer collapses simply to an equality, we retain

$$|L_X - S_X| \leq J_X \leq |L_X + S_X|. \tag{5.82}$$

The potential complications that arise from this expression can be partly constrained using parity considerations. The strong interaction conserves parity which places some restrictions on the allowed decay modes, for example, consider the decay $a_2(1320) \to \rho\pi$, a potential decay for the resonance X. We know the J^P for the a_2, ρ and π are given by $2^+, 1^-$ and 0^- [81]. The $a_2(1320)$ meson has positive parity and for the decayed system, the parity is given by

$$P_X = P_\rho P_\pi (-1)^L \tag{5.83}$$

$$= (-1)(-1)(-1)^L. \tag{5.84}$$

In other words, by the conservation of parity, only decays of even L are allowed. Further, in order for the inequality (5.82) to hold, one cannot have the decay in an S-wave ($L_X = 0$). Therefore the result follows that the a_2 meson decays in a D-wave.

However, in terms of a reaction formalism that takes into account a given number of states X, the calculation is not as simple. To provide an example, consider the spin state $J = 2$. Two very well known mesons with $J = 2$ are the $a_2(1320)$ and $\pi_2(1670)$. As has just been discussed, the a_2 decays in a $L = 2$ D-wave to $\rho\pi$, the π_2 on the other hand decays in a $L = 1$ P-wave to $f_2\pi$ [82]. This shows that in order to form a complete picture of the decay, all quantum numbers are needed independently.

5.14 Counting Waves and Moments

Given that the moments can be extracted from the data, there remains the question of extracting the partial waves. For this to be possible there should be more moments (constraints) than wave parameters (unknowns). Having more moments than partial wave unknowns is a requirement but is not a sufficient condition for the extraction of partial waves from moments. We can calculate the number of unknowns and constraints that we have here.

J_{max}	$N_{moments}$
2	53
3	99
4	157
5	227
6	309

Table 5.1: The number of moments as a function of J_{max}.

5.14.1 Number of Moments

The number of linearly independent moments is given by

$$N_{moments} = 3\left(1 + \sum_{J=1}^{J_{max}} \Gamma(J+1)\right) - 2J_{max}, \tag{5.85}$$

where

$$\Gamma = \begin{cases} 3, & J = 1 \\ 4, & J \geq 2. \end{cases} \tag{5.86}$$

This is derived as follows: $1 + \sum_{J=1}^{J_{max}} \Gamma(J+1)$ is the number of unpolarised moments. This sum is multiplied by 3 since there is the set of $\alpha = 0, 1, 2$ moments. There are $2J_{max}$ moments with $M = \Lambda = 0$ from the $\alpha = 2$ case to be removed. The total number of moments are shown in Table 5.1 for all moments up to and including $J = M = 6$.

5.14.2 Number of Waves

The number of waves is determined by the maximum allowed values of each quantum number. The formula for the number of waves is given as:

$$N_{waves} = \sum_{j=1}^{j_{max}} 3(2j+1) + 1. \tag{5.87}$$

For each j, there are $(2j+1)$ contributions from the $-m, ..., m$ spin projection of each wave. Additionally, there are 3 contributions from each decay wave from $l = j-1, j, j+1$. The final contribution is from the $j = 0$, $l = 1$, $m = 0$ wave which is the only allowed wave with $j = 0$. From eqns (5.78)(5.79)(5.80), for each wave there is a positive and negative reflectivity component. Therefore the number of waves is doubled to include this quantum number in the decay. The total number of waves in the decay is shown as a function of j_{max} in Table 5.2. In this analysis it was assumed that $j_{max} = 3$, giving a total of 90 waves.

j_{max}	Number of waves
1	20
2	50
3	90

Table 5.2: Number of allowed waves as a function of j_{max}.

j_{max}	N_{waves}	$N_{unknowns}$	$N_{moments}$
1	20	38	53
2	50	98	157
3	90	178	309

Table 5.3: Relating the unknowns in waves to moments.

5.14.3 Relating the Number of Waves and Moments

The number of unknowns is directly related to the number of waves. Each wave has a real and imaginary part (or magnitude and phase) and therefore, there are $2 \times N_{waves}$ unknowns. There are two restrictions placed on the waves and by fixing the phase of one of the waves in each reflectivity (since the phase in each case is a relative phase), reducing the number of unknowns by 2. The results are summarised in Table 5.3. Since in every case, the number of unknowns was less than the number of moments, in theory the waves could be unambiguously determined from the moments.

5.15 Isobar Mass dependence

As noted in a previous section, the mass (and t) dependent part of the amplitude can be dealt with in subsequent mass or t dependent fits to the extracted partial waves. This is done by binning the data in mass so any dependence on these variables is assumed small. In a simple two-body reaction this method worked without complications, however for the decay into three final state particles the mass of the intermediate isobar may need to be accounted for if it is a broad state i.e. $R_{Yi}(m_Y)$ in eqn (5.56).

Note in the current analysis, it was assumed the narrow K^* isobar could be isolated via a background subtraction. Knowing that the decay was $X \to K^* + K^+$ reduced this analysis to a single vector + pseudoscalar final state. In this approximation the mass dependence of the isobar can be neglected.

In a full analysis however, the mass of the isobar would need to be included. This section provides a short note on how this might be done. The dynamical propagation term can be parameterised by a Breit-Wigner amplitude of constant width such that:

$$Z_r(m_r; m_0, \Gamma_0) = \frac{m_0 \Gamma_0}{m_0^2 - m_r^2 - i m_0 \Gamma_0}, \tag{5.88}$$

which is suitable for narrow resonances. For wider resonances, one can still use a Breit-Wigner parameterisation but now with a dynamical width given as:

$$Z_r(m_r;m_0,\Gamma_0) = \frac{m_0\Gamma_0}{m_0^2 - m_r^2 - im_0\Gamma_{m_r}}, \tag{5.89}$$

where

$$\Gamma(m_r) = \sum_{j}^{\text{decay modes}} \Gamma_j \frac{q_j}{m_j}\frac{m_0}{q_{j,0}}\frac{F_{L_j}^2(q_j)}{F_{L_j}^2(q_0)}, \tag{5.90}$$

and m_r is the mass of the resonance. As well as accommodating wider resonances, this parameterisation takes into account the opening of the decay phase space for the decay modes of the isobar r across the resonance width. The term $F_{L_j}(q)$ is the barrier factor. The ratio $\frac{q}{q_0}$ serves as a measure of the breakup momenta at $\frac{s}{M_0^2}$.

The reason for why dynamical amplitudes are used rather than constant width can be found using the complex plane and considering threshold effects. Schwarz reflection principle states that if there is a pole on the second Riemann sheet (sheet 2) at say $s = s_0$, then there must be a corresponding pole at $s = s_0^*$. A constant Breit-Wigner amplitude of constant width however only contains a pole at $s = M_0^2 - iM_0\Gamma_0$ which violates analyticity. The distinction is made however at points far above threshold where the pole at s_0 is much closer to the physical axis (and therefore in this case, far more important) than the pole at s_0^*. From the properties of Riemann sheets, the pole at s_0 can be reached under the right-hand branch cut but to reach the pole at s_0^*, one needs to go around the other side of the branch cut - the overall effect is that the physical amplitude will be strongly affected by s_0 and far less so for s_0^*.

On the other hand, nearer threshold the effect of the branch cut is not as prevalent, the pole at s_0^* becomes closer to the physical axis nearer threshold and the effect from this pole can no longer be ignored - both poles will now contribute. In these such situations, using a Flatté distribution which is parameterised as

$$D_r^{Fl}(m_r;m_0,\Gamma_0) = \frac{m_0\sqrt{\Gamma(m_r)\Gamma_0}}{m_0^2 - m_r^2 - im_0\Gamma(m_r)}, \tag{5.91}$$

is more appropriate. An example of a resonance where this is important in the analysis is the $f_0(980)$ [83].

In summary, parameterisation of a mass state for the isobar is not required when the data sample is assumed to decay through a fixed state. The inclusion of a mass dependent isobar state in a complete decay model is work for a future analysis.

Chapter 6

Likelihood Calculation and Markov Chain Monte Carlo

As described later in this section, there are various ways in which parameter estimation can be performed. The common feature of these algorithms is the calculation of a likelihood, here the extended maximal likelihood (EML). A discussion of EML is given in the following section.

6.1 Extended Maximum Likelihood Fitting

The likelihood $\mathscr{L}$ in an analysis is the probability of finding the data, x given the set of parameters θ of a model. The discussion of maximum likelihood estimation follows that common to several other analyses [73] [74]. Maximum likelihood estimation involves the maximisation of this function for the set of parameters θ. For a probability density function f depending on m measurable quantities of observables, x, and r model parameters, θ, the likelihood function is given by the product of the probability of each of p of the data points in x for the parameter set θ:

$$\mathscr{L}(x;\theta) = \prod_{n=1}^{p} f(x_n;\theta). \tag{6.1}$$

In a maximum likelihood fit, equation (6.1) is restricted with the normalisation condition:

$$\int_{\Omega} \mathscr{L}(x;\theta) d^n x = 1, \tag{6.2}$$

where Ω denotes all θ space. It is the relaxation of relation (6.2) that defines the principle of extended maximum likelihood estimation. Condition (6.2) is replaced by

$$\int_{\Omega} \mathscr{L}(x;\theta) d^n x = \mathscr{N}, \tag{6.3}$$

for $\mathscr{N}$ the number of expected events. The probability of observing N events when we expect $\mathscr{N}$ events in a counting experiment is given using a Poisson distribution:

$$P(N) = \frac{\mathscr{N}^N}{N!} e^{-\mathscr{N}}. \tag{6.4}$$

The full likelihood is then given by:

$$\mathscr{L}(x;\theta) = \frac{\mathscr{N}^N}{N!} e^{-\mathscr{N}} \prod_{n=1}^{N} f(x_n;\theta) \tag{6.5}$$

Due to computer precision, the natural logarithm of the likelihood is often used. Taking the logarithm will not affect position of the maxima of the function. The log-likelihood is then:

$$ln(\mathscr{L}(x;\theta)) = ln\left[\frac{\mathscr{N}^N}{N!} e^{-\mathscr{N}} \prod_{n=1}^{N} f(x_n;\theta)\right]. \tag{6.6}$$

The expression for the log likelihood can be simplified. In accordance with [74], the function $f(x_n;\theta)$ can be normalised as

$$f(x_n;\theta) = \frac{F(x_n;\theta)}{\mathscr{N}}. \tag{6.7}$$

Using this:

$$ln(\mathscr{L}(x;\theta)) = ln\left[\frac{1}{N!} e^{-\mathscr{N}} \prod_{n=1}^{N} F(x_n;\theta)\right]. \tag{6.8}$$

Expanding the terms on the RHS gives:

$$ln(\mathscr{L}(x;\theta)) = -ln[N!] - \mathscr{N} + \sum_{n=1}^{N} ln[F(x_n;\theta)]. \tag{6.9}$$

When maximising the likelihood, the constant term $-ln[N!]$ can be dropped leaving the function to be maximised in terms of θ:

$$ln(\mathscr{L}(x;\theta)) \propto \sum_{n=1}^{p} ln[F(x_n;\theta)] - \mathscr{N}. \tag{6.10}$$

6.2 Monte Carlo Normalisation

The term labelled $\mathscr{N}$ in Section 6.1 was described as the expected number of events, which can be approximated using simulated data. The process by which simulated data was created is described in Chapter 7. The number of expected events is given by:

$$\mathscr{N} = \int f(x_n;\theta)\eta(x_n)dx_n, \tag{6.11}$$

where $\eta(x_n)$ is the acceptance function. In other words, the Monte Carlo normalisation is the product of the intensity of the events x_n and the acceptance function. The acceptance function can be found from using the simulated data that will accept or reject generated phase space events based on the detector geometry. The number of expected events can be approximated as:

$$\mathcal{N} \simeq \sum_{k}^{M} f(x_n;\theta), \tag{6.12}$$

for M accepted Monte Carlo events.

6.3 Maximising the Likelihood with Minuit

Parameter estimation is a fundamental part of this analysis. The question then of how one extracts the parameters is central to the reliability of the final result. For many years, the fitting package Minuit has been reliably used in optimisation problems [84]. Minuit was developed by CERN physicist Fred James in the 1970s, originally written in Fortran [85] and latterly in ROOT [86] in C++. The package has been used successfully in many particle physics analyses and comprises five optimisation algorithms - the default of these Migrad, uses a gradient descent based minimisation approach in parameter estimation.

The principle of a gradient descent based algorithm is based on a continuous and differentiable function, f, in the neighbourhood of a point, x, in possibly multidimensional space. Since f is continuous and differentiable at x, the gradient of f exists (denoted Grad($f(x)$) or $\nabla f(x)$). $\nabla f(x)$ denotes the direction in which the gradient is most positive at x, so in order to find a minima, one can construct a recursion type relation

$$x_{n+1} = x_n - \eta \nabla f(x_n), \tag{6.13}$$

in which the 'jump' is made from x_n to x_{n+1} by a length η in the direction of $-\nabla f(x_n)$. In a well defined function, after a finite number of iterations, the fit will converge to a local minimum. An illustration of the gradient descent algorithm in a simple two dimensional example is shown in Figure 6.1. The step-size factor η is the variable geometric length between the points x_n and x_{n+1} and is synonymous with the 'learning rate' parameter of many machine learning problems - the name deriving from the intuitive notion that a higher learning rate will lead the algorithm to achieve a desired outcome in a faster time frame [87].

There are instances in more complicated problems however where the limitations of gradient descent algorithms become more evident. For example, consider a parameter space that may contain many local minima. In the first instance, the gradient descent approach will be fundamentally unstable as small changes in starting parameters can result in radically different final results as the algorithm finds itself in different local minima. From a heuristic point of view, the

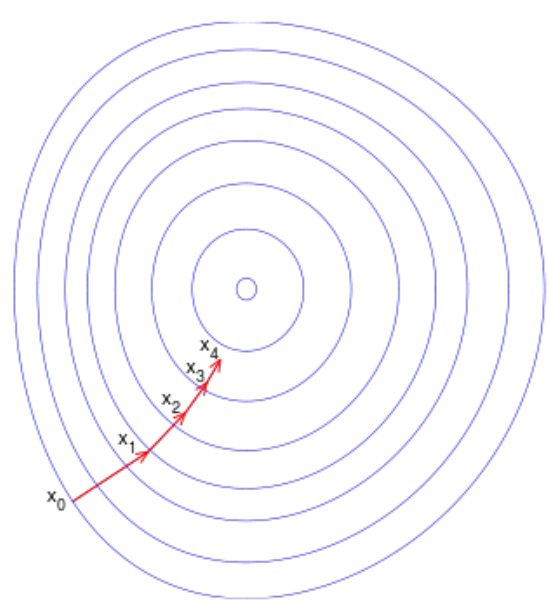

Figure 6.1: The gradient descent algorithm from an initial point, x_0, towards a local minimum. Taken from [24].

algorithm cannot map the global structure of the space in which it acts - information on the parameter space will be lost. With a view to resolving some of these issues, Markov chain Monte Carlo (MCMC) methods can be considered.

6.4 Introduction to MCMC

Markov Chain Monte Carlo methods form a broad set of algorithms that are widely applicable in many areas of physics. In order to best perform the analysis, there should be some investigation into the nature of the problem to form an understanding of the most efficient and robust method by which the problem can be solved. Due to the vast number of ways that MCMC methods can be implemented, the choice of a particular algorithm is not always a straightforward task. The basis of the MCMC approach is based on Bayes' Theorem. Named after Reverend Thomas Bayes and published posthumously by Richard Price, it offers an alternative view of statistics that differs from the frequentist picture that is common in everyday science [88] [89]. The guiding principle of Bayes' theorem is that the previous knowledge about the system is incorporated in such a way that it is made explicit. This is a deviation from frequentist statistics in which the uncertainty in any final result derives purely from the measurement technique. Leading on from this, conceptually in Bayesian statistics there is some inherent uncertainty associated with parameter values regardless of the precision of the experiment in contrast with frequentist methods, in which there is the assumption that the experiment is underpinned by some true and exact value, with the uncertainty arising from measurement procedures.

6.5 Bayes theorem and MCMC

In order to understand the underlying principles of MCMC it is instructive to first become familiar with Bayes theorem and the role this can play in the process. Bayes theorem is expressed as:

$$p(\theta|x) = \frac{p(x|\theta)p(\theta)}{p(x)}, \tag{6.14}$$

where θ is the set of parameters of a model, x is the data, $p(\theta|x)$ is known as the posterior, $p(x|\theta)$ the likelihood, $p(\theta)$ the prior and $p(x)$ the evidence. In this notation, $p(\theta|x)$ is the probability of attaining the parameters θ, given the data x. In the context of an analysis, the posterior is what we would like to find out - attaining the probability for the set of parameters given the data set. The likelihood is familiar in terms of a standard Minuit analysis - the probability of the data given the set of parameters. The prior is used to make the assumptions and previous knowledge on the model parameters explicit. The evidence can be thought of as a normalisation and is often neglected, leaving:

$$p(\theta|x) \propto p(x|\theta)p(\theta). \tag{6.15}$$

The underlining feature of MCMC methods is that a chain of samples is constructed from the exploration of the parameter space in such a way that the chain will converge on maxima in the likelihood and explore the space around it. To create the chain there is a sequence of calculations of the likelihood with the selected samples forming the chain. To illustrate this process, consider a basic Metropolis-Hastings algorithm, the steps involved in this algorithm are listed below:

1. Given a one-dimensional space for some parameter θ and its prior distribution $p(\theta)$.

2. From some initial point θ_0 sampled randomly from the prior, propose a new point (the proposal point) labelled θ_p using some proposal function called $Y(\theta_{n+1}|\theta_n)$. Often, Y is chosen to be a Gaussian function but it should always be symmetric such that $Y(\theta_{n+1}|\theta_n) = Y(\theta_n|\theta_{n+1})$.

3. The value of the likelihood is calculated at the initial and proposed value θ_p. If the value of the likelihood increased then the proposed step is accepted and added to the chain such that $\theta_1 = \theta_p$. If the value of the likelihood decreased then the point is accepted with some probability

$$r = \frac{\mathscr{L}(\theta_0)}{\mathscr{L}(\theta_p)}, \tag{6.16}$$

   such that $0 < r < 1$. In this way, a point that generates a greater decrease in likelihood will result in a smaller value of r and will be accepted with less frequency that points that have a value of r closer to one.

4. Return to and repeat from step 2 until a chain of predetermined length N is completed.

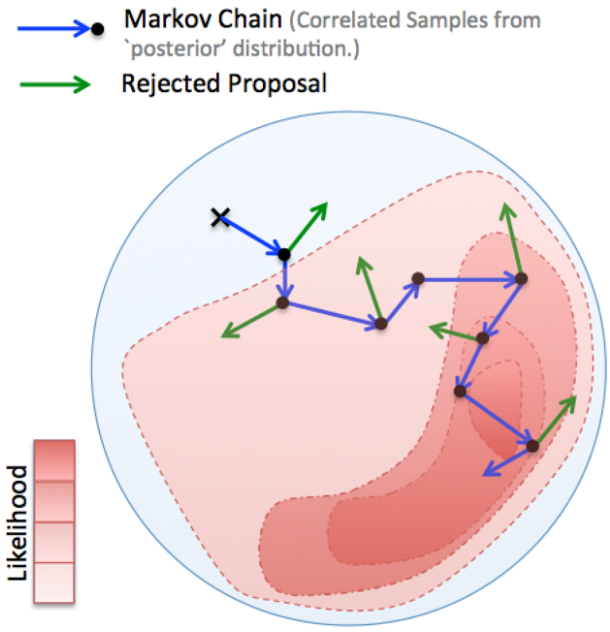

Figure 6.2: Illustration of the stepping process from an initial point, labelled by **X**, towards the region of higher likelihood probability. Accepted steps are shown blue, rejected steps in green and regions of increasing likelihood probability are shown as increasingly darker pink. Taken from [25].

The algorithm began with a prior on the space of the variable, proposed a step and calculated the likelihood based on the proposed point. The result of the combination of the prior and the likelihood gives, from Bayes' theorem, a posterior probability that will estimate the parameter given the data. Repeating the process of proposing steps to create a chain of accepted samples will form a final probability distribution when you project the chain onto the parameter θ.

A diagram demonstrating the process of sampling from the parameter space in two dimension is shown in Figure 6.2. This example illustrates the working of an MCMC algorithm in the most basic sense. The challenges faced by a MCMC are dependent on many factors, generally increasing in complexity with the dimensionality of the parameter space. By the very nature of the algorithm, samples of the chain are correlated, with the degree by which they are not independent potentially affecting the quality of the analysis. In addition to this, there is the question of at what point the chain has suitably converged to the posterior distribution - in other words, what should be the value of N_c, the total number of steps in the chain. Further, the starting point for the chain will generally not be located in close proximity to the likelihood maximum. There will be what is known as a 'burn in' period for the chain as the sampler traverses the space from the starting value to the region of high posterior probability. Inclusion of this burn in period in a chain from which results are calculated will ultimately bring about deviations on results. Therefore it is required to discard a number of steps from the beginning of a chain. The length of the burn in period is also difficult to know *a priori*. These factors will be discussed in detail in the following sections.

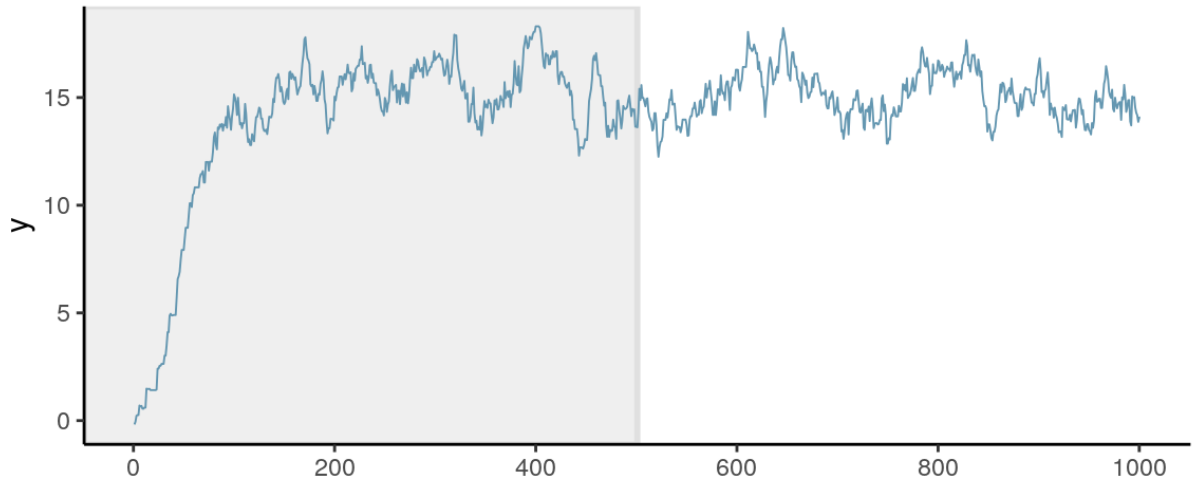

Figure 6.3: Illustration of an example parameter y plotted against the step number. The sample values of the parameter increase from zero through the burn-in phase until a value of around 15. By eye, the chain begins fluctuating around 100 steps. The shaded area shows a possible burn-in stage that should be thrown away, 500 steps in this case. Taken from [26].

6.5.1 Burn in period for an MCMC chain

In general, the initial value for a chain will not be located close to the region of high posterior probability. As a result, the behaviour of the chain will resemble that shown in the trace plot in Figure 6.3. In this example, there is a steady increase in the parameter y from the initial value to a value around 15, after which the chain fluctuates around this value. By inspection, the change in behaviour of the chain occurs around 100 steps into the chain and so this is a fair estimation for the burn-in period. It is sufficient to throw away any number of initial samples that at least include the length of the burn-in period. In this case, the burn-in is set as 500 steps, as shown by the shaded part of the plot.

6.5.2 Chain correlation

Once a given number of events are discarded as a burn-in period, the accepted steps create the chain from which results are taken. From the properties of the Markov Chain algorithm successive points in the chain are correlated to some extent. This is known as autocorrelation. In general, the degree of autocorrelation of the chain is again problem dependent. In addition to this, the autocorrelation of a chain can be related to the step size of the chain. If the step size is decreased then the chain will move slowly in a localised region of the space and consequently, the autocorrelation of the chain will increase. A larger step size will return a chain with a lower value for the autocorrelation. On the other hand, a larger step size tends to decrease the overall acceptance of the chain. In a general case, the optimised chain acceptance is 23.45%, and the proposal function should be configured to reflect this [90].

A quantitative description of autocorrelation is given as a function of the lag, τ, by:

$$\hat{c}_f(\tau) = \frac{1}{N-\tau}\sum_{n=1}^{N-\tau}(f_n - \mu_f)(f_{n+\tau} - \mu_f), \tag{6.17}$$

where

$$\mu_f = \frac{1}{N}\sum_{n=1}^{N} f_n \tag{6.18}$$

is the mean value of the chain f with total number of samples N [91]. The lag is given by the difference in the position in the chain of the samples under consideration. Qualitatively, the autocorrelation function enumerates the product of the difference of the chain entry and the mean with the difference of the lagged chain entry with the mean, summed across each subsequent entry of the chain. In other words, how quickly does the chain vary in position relative to the mean. More useful is the normalised autocorrelation function given by:

$$\hat{\rho}(\tau) = \frac{\hat{c}(\tau)}{\hat{c}(0)}. \tag{6.19}$$

Using the autocorrelation function, the integrated autocorrelation time is defined as:

$$A_f = \sum_{\tau=-\infty}^{\infty}\hat{\rho}_f(\tau), \tag{6.20}$$

which for a chain of finite length N, is written:

$$A_f = \sum_{\tau=-N}^{N}\hat{\rho}_f(\tau) = 1 + 2\sum_{\tau=1}^{N}\hat{\rho}_f(\tau). \tag{6.21}$$

In practice, it is not necessary to use a full length chain when calculating the autocorrelation time and the autocorrelation is calculated for some value $M < N$, with the criteria for M detailed by Sokal (1996) [91] where it is recommended that the value of M satisfies

$$M \geq C \times A_f, \tag{6.22}$$

where $C \sim 5$. This process is said to work well for chains that are of length over $1000A_f$.

Autocorrelation for a chain is dependent on a number of factors. For example, autocorrelation will naturally rise in MCMCs with a greater number of parameters or in cases where the parameters of the fit are highly correlated with each other. In addition to this, the autocorrelation function refers individually to the parameters of the fit (as denoted by the subscript in $\rho_f(t)$). In the majority of cases, different parameters in the same analysis will have similar autocorrelation lengths but this is not guaranteed. For these reasons, software was written to plot the autocorrelation function against lag to see the behaviour of the chain as a whole rather than

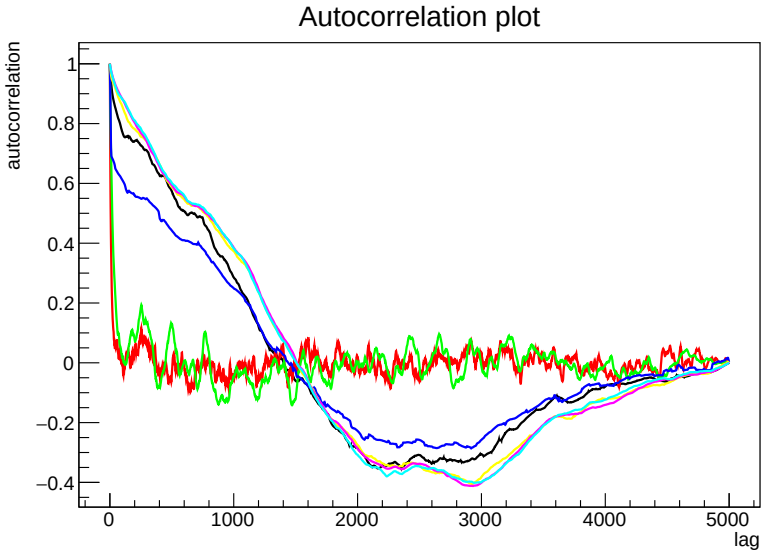

Figure 6.4: An example autocorrelation plot, showing the autocorrelation function plotted against the lag. Each colour represents a parameter of the fit.

outputting a singular value for the integrated autocorrelation time. An example autocorrelation plot is shown in Figure 6.4. From the normalisation, the autocorrelation function has a value of 1 at zero lag, falling as the lag increases. The integrated autocorrelation time is approximately the point at which the autocorrelation function first crosses the line $y = 0$, after which the plot of the function should remain close to zero, fluctuating around this value. Each coloured line shows a different parameter of the fit, specifically for this example it is clear to see the similarity between the parameters coloured by the black and yellow lines and separately for the other parameters - lines of the autocorrelation plot that follow each other closely are a good indication of correlation between parameters.

In a chain where large autocorrelations are prevalent, one possibility is to use chain thinning to reduce autocorrelations. For a chain with integrated autocorrelation length A, say, taking only every Ath entry of the original chain will give a set of samples that are effectively independent and free from autocorrelations. The trade-off from a method such as this is the added computational time that arise from throwing away what can be a large majority of samples, and in practice this is not always feasible. Other methods by which the autocorrelation can be dealt with will be discussed in Section 6.6.

6.5.3 Chain Termination

An acceptable value for the samples in the chain, N_c, depends on a number of factors, some of which were mentioned above (such as autocorrelation considerations). By making plots of some of the chain characteristics it is easier to gain an understanding of the chain's behaviour and to be able to estimate whether a sufficient number of samples have been gathered. There is

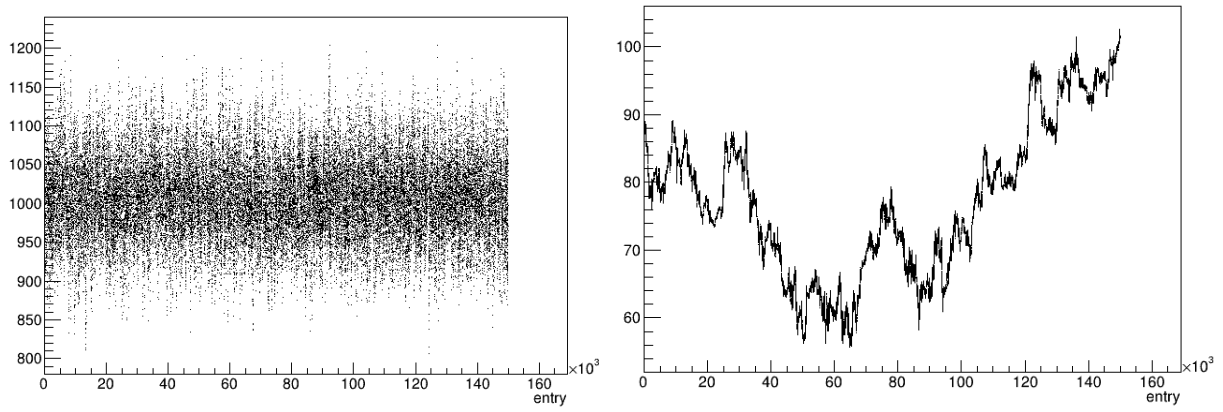

(a) Desired behaviour of an MCMC algorithm

(b) A poorly posed MCMC algorithm

Figure 6.5: An example comparison of two MCMC chains. The value of some parameter is plotted against the chain entry number.

no theoretical reason not to accept 'too many' steps - after reaching some threshold, accepting more steps to the chain will have minimal effect on the value and error associated with each parameter. The goal of MCMC is to determine parameter posterior distributions accurately and efficiently and a greater number of steps provides greater accuracy. However at some point just adding more points will not significantly affect the derived parameter values and uncertainties

Some features of MCMC algorithms can be identified from particular distributions. For example, in Section 6.5.1, it was noted that after passing burn in, a chain will explore the area in the local neighbourhood of a maximum. A trace plot - a plot of the position of the chain in one dimension of parameter space against the chain entry - should contain samples drawn randomly from the posterior distribution. Figure 6.5 is an example of the trace plots that show the difference between a chain that is efficiently sampling the parameter space and a poorly conditioned chain. Figure 6.5b is representative of a chain with very high autocorrelation and is evidence that the chain will not provide reliable results. The plot in figure 6.5a is more indicative of a chain that consists of a set of samples randomly drawn from the posterior distribution, and as such, more robust results would be extracted.

In addition to the trace plots, corner plots can provide evidence for the performance of a chain. A corner plot consists of one-dimensional histograms of the samples of the chain for each parameter in addition to two-dimensional histograms for each combination of parameters. A ROOT class was developed to give a corner plot as an output at the conclusion of an MCMC chain, as shown in Figure 6.6. In this example of seven parameters, each one-dimensional histogram is of a general Gaussian shape. The shape of the one dimensional histograms may not be Gaussian but this will be dependent on the actual posterior distribution, for example, if the true parameter value is in a region at the limit of the allowed parameter space then the histogram will become non-symmetric. From the two-dimensional histograms, correlations between parameters become easier to see. A distribution that is largely isotropic around the mean is indicative of

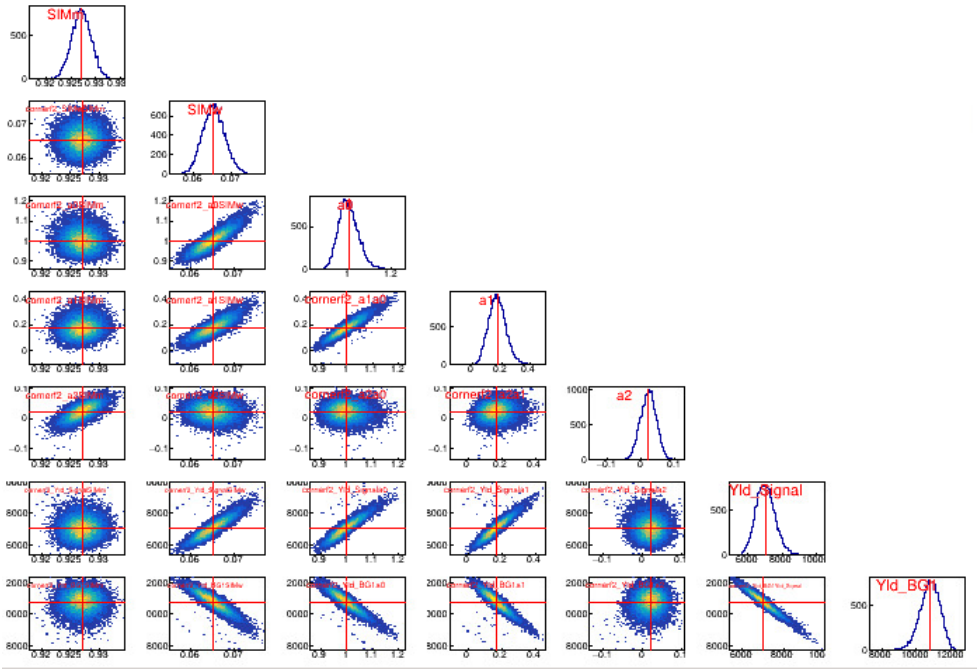

Figure 6.6: An example of a corner plot from a completed MCMC for a fit of seven parameters consisting of one and two-dimensional histograms. Red lines indicate the mean of all samples.

the absence of correlations, however if the shape of the histogram becomes more elliptical then this shows correlations being present, with the more elliptical the distribution corresponding to more correlated variables. A plot that slopes up from left to right is a positive correlation and sloping down from left to right a negative correlation. In higher dimensional parameter spaces however the efficiency of MCMC algorithms can be negatively affected by strong correlations between parameters. There are modifications that can be made to the Metropolis-Hastings algorithm to better suit individual issues in problems such as these, this will be discussed in Section 6.6.

6.6 The Covariance Matrix Step Proposal Approach

The Covariance matrix step proposal method (and the RMS step proposal method discussed in the following section) were developed specifically for a physics analysis such as this one. It was necessary to adapt the standard Metropolis-Hastings algorithm due to the very high dimensional parameter spaces and large data volumes that are characteristic of these kinds of physics analyses. Specifically, this was a problem encountered at the stage of fitting the moments of angular distribution to the data, as described in Chapter 8. The package Minuit was not able to converge in fitting a set of moments to data. The sequential proposal (SP) adaptation of the Metropolis-Hastings algorithm on the other hand was able to somewhat successfully sample the space. The SP algorithm sampled the space such that each MCMC step was in only one randomly chosen dimension in parameter space, each of the other parameters were unchanged in that step. The

step in one dimension was accepted or rejected based on eqn 6.16, after which a new step in one of the other dimensions was proposed.

The limitations of the standard SP algorithm can be understood in terms of the autocorrelation, trace plots and the corner plots. In an idealised MCMC analysis, every step in the chain after burn in would be fully mutually independent. In reality this was not practically possible, however the chain should be tuned to reduce the correlation between samples within the confines of the problem. Since the SP algorithm held all but one parameter constant in each step, for an analysis of n parameters, the autocorrelation of the chain for each parameter was increased by a factor n.

An algorithm was developed that could reduce this issue. If the steps of a chain were proposed simply by taking a step in each parameter, as shown with the red arrows in Figure 6.7, correlations between parameters in the data are ignored. It is more difficult for the chain to step into regions of high probability (along the diagonal in this case), especially as the dimensionality increased, making it largely inefficient in exploring the parameter space. The way this was accounted for was using the covariance matrix for the distribution. After a sufficiently long initial phase of SP the samples in the chain were used to determine a covariance matrix which was used to propose steps more in line with a principal component system as shown by the green in Figure 6.7. The covariance incorporates information on the correlation between variables as well as the magnitude of the distribution in space. The point of the covariance matrix MCMC was that the chain still performed a random walk through the space, but the steps that were proposed were more efficient.

This covariance matrix method was implemented in *brufit* in three steps as follows.

1. Initialise a SP chain for a given number of steps.
2. Calculate the covariance matrix of the SP chain using the RobustEstimator algorithm [92].
3. Use the resulting covariance matrix as a step proposal function for a second adapted Metropolis-Hastings chain.

In the covariance matrix chain, every parameter was varied in every step, as opposed to the first chain that varied only one parameter each step. A comparison of the autocorrelation plots for the same analysis using the SP algorithm and the covariance matrix approach are shown in Figure 6.8. For a moments fit, explained in detail in Chapter 8, the chain samples for the same variables are shown using both methods in Figure 6.9.

As a further optimisation, part of the algorithm was adapted so that the acceptance was always within an optimal window. Every 1000 steps the acceptance of the chain was calculated using the formula above. If this was within an acceptance window that was specified by the user then the chain continued. If this was outside the acceptance window then an overall step-size scale factor was adjusted to bring the acceptance within the window.

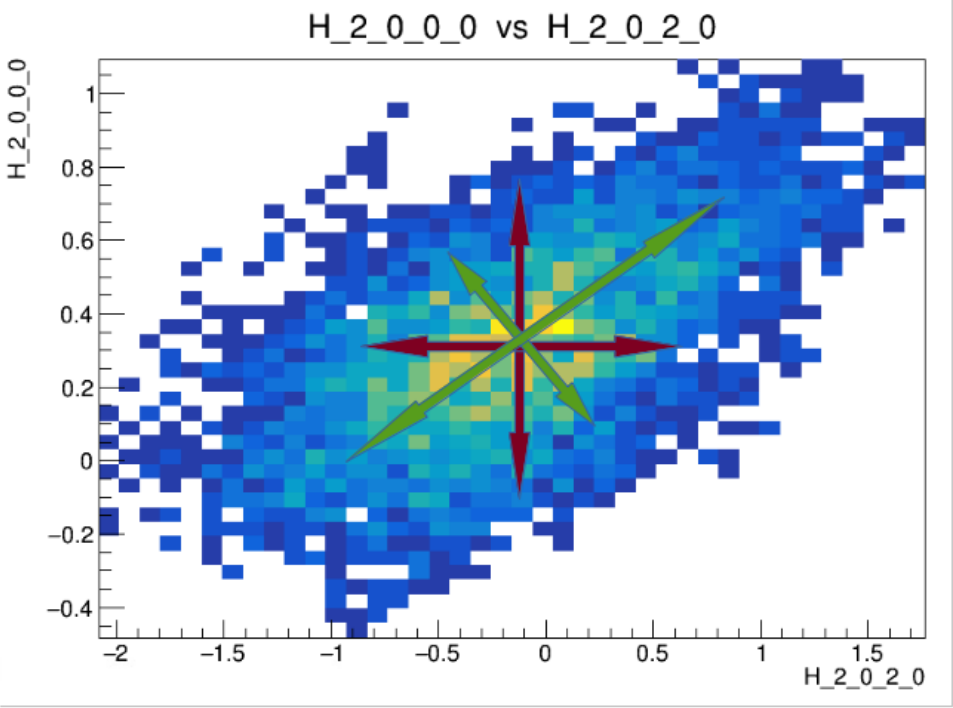

Figure 6.7: An example of the sample distribution for two parameters in a moments fit. The maroon arrows are representative of the direction of a step taken using a sequential proposal algorithm. The green arrows are more likely steps proposed using the covariance matrix step proposal function.

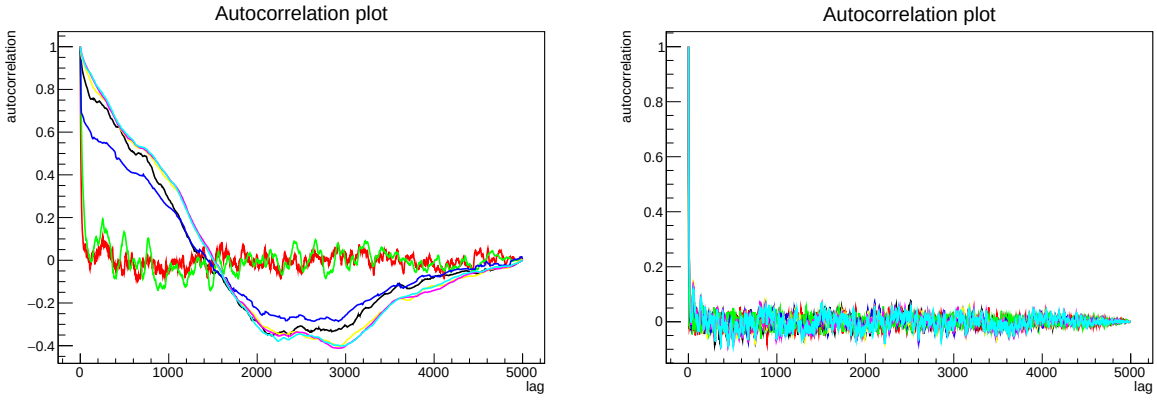

(a) Using the sequential proposal function.

(b) Using the covariance matrix approach.

Figure 6.8: Comparison of the autocorrelation plots for the sequential proposal and covariance matrix approaches. Note 5000 points were used in the MCMC chain.

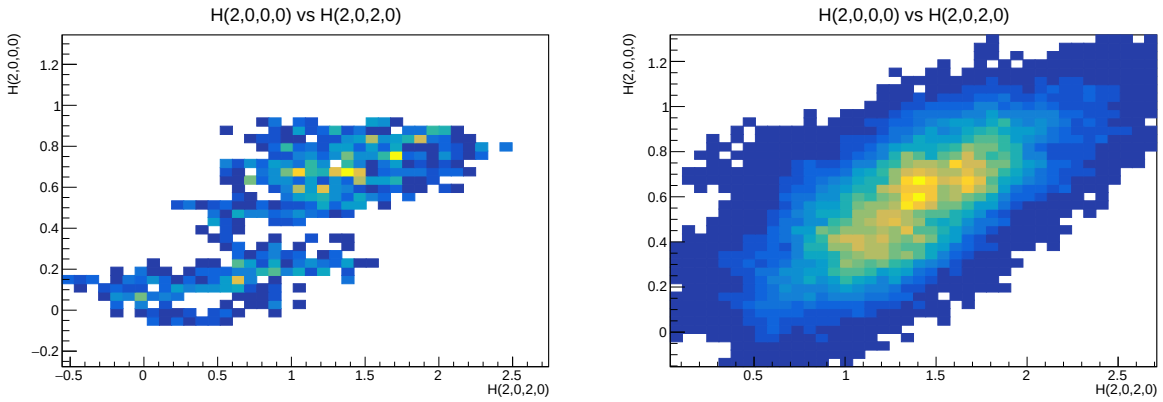

(a) Using the sequential proposal function.

(b) Using the covariance matrix approach.

Figure 6.9: Comparison of the distribution of chain samples for the sequential proposal and covariance matrix approaches, as outlined in Chapter 8. Note each chain contains 40,000 events.

As a side note, it was found that this acceptance tuning led to better determined covariance matrices for the proposal function, particularly when there was a large number of parameters. Having this 'safeguard' in place meant that the chain did not become trapped in regions of low probability. If the acceptance was too low for example then not enough points were being accepted. In this case, the scale parameter would be increased to slightly reduce the step size, resetting the chain in a more optimal acceptance window. This process was repeated until the chain successfully terminated.

6.7 The RMS Matrix Step Proposal Approach

As noted above, different MCMC algorithms will be best suited to different types of parameter spaces. The covariance matrix step proposal algorithm was best used in cases of very correlated sets of parameters and in problems with a moderate number of parameters (approximately in the range 5-20). The limitation on this algorithm was the calculation of the covariance matrix itself from the SP chain. As the parameter space became larger however, beyond around ~ 20 parameters, the error in the calculation of the covariance matrix made the result unreliable. This became clear as the acceptance of the covariance matrix chain was too low or the matrix itself was singular. An alternative approach to the covariance matrix that was created was to use the sequential proposal chain to define the RMS matrix.

The RMS matrix approach was similar in many ways to that of the covariance matrix. The sequential proposal chain was used to define the RMS matrix that was then used as a step proposal function for a second chain. The difference in the algorithms was in the calculation of the covariance and RMS matrix. The covariance matrix is composed of auto-covariance terms as diagonal entries with off diagonal terms incorporating the covariance between different parameters. Larger magnitudes of off-diagonal terms are representative of stronger correlations

between parameters. On the other hand, in the RMS matrix all off-diagonal terms were defined to be zero and diagonal entries were defined as the RMS value from each parameter. The RMS matrix approach did not incorporate the correlations between parameters although it does step in each parameter at the same time. It was able to handle a greater number of parameters than the covariance matrix approach as the simpler approach of the RMS matrix made its calculation more robust in higher dimensions compared to the covariance matrix. The RMS matrix was successfully used in problems with over 50 parameters.

6.7.1 Additional features of the RMS matrix approach

There were some other features of the RMS matrix approach that were designed specifically for use in the case of a high number of parameters. As described in Section 6.6, the RMS matrix algorithm also used the automated updating feature of the covariance matrix approach. After the burn-in had been passed, every 1000 steps the acceptance of the chain was calculated. If the calculated acceptance was outside the desired window (as specified by the user) then the step size normalisation would update so that

$$\text{new norm} = \frac{\text{old norm}}{\text{desired acceptance}}, \tag{6.23}$$

where the norm is the parameter step size divisor and the desired acceptance is a factor set by the user - usually set to the optimal value of 0.234.

Another problem associated with analyses such as this was that occasionally the chain would 'get stuck' in regions of space from which it could not escape. This was not a problem in lower dimensional spaces but became apparent with a higher number of parameters. In these situations, the acceptance of the chain would fall to zero regardless of the step size that was being used at the time. When the acceptance of the chain fell below a pre-set threshold the chain would revert back to the mean value of the sequential proposal chain. From this point the sampling would continue.

Chapter 7

Data Analysis and Event Selection

This section will detail the process of taking the data from JLab and through the event selection process. The data that was taken at JLab was stored in Data Summary Tape files (DSTs) in the Hall B High Performance Output (HiPO) file format [93]. The sections below detail the method that was used to reconstruct events for the $e^-K^+K^-\pi^+$ final state from the full set of events.

7.1 Data used in this analysis

The data that was used in this analysis was taken in the 'Fall 2018' run period in Hall B. Here, a 10.6 GeV beam was incident on a proton target as part of the Run Group A (RG-A) dataset. The Fall 2018 run contained data using both electron inbending and outbending toroid magnetic field configurations for the Forward Detector systems. The data was first calibrated and tracks reconstructed before this analysis stage. Not all the data from the DSTs was relevant for every analysis and therefore during cooking, the data was filtered into skims using conditions relevant for that skim. In particular, this analysis used skim 3 data that is defined as having at least one electron candidate in the Forward Tagger and at least two charged tracks in the Forward Detector. All of the skim 3 data files were transferred from JLab to Glasgow to be analysed.

7.2 Event Reconstruction

The journey of processing the data in the form of HiPO files to ROOT TTrees was performed using '*chanser*' [86] [94]. *Chanser* stands for CLAS12 HiPO Analyser and is a software package that is built upon *clas12root* which gives access to HiPO data in a ROOT object orientated environment [95]. It has been designed in such a way that users can easily create their own final state classes for their own specific analyses. In addition to this, *chanser* was developed to handle particle combinatorials that were essential in multi-body final states such as the one in this analysis. Finally, using *chanser* gives the user the option to apply default cuts to the data or to 'flag' events that pass or fail selection criteria. Flags can be applied to data at a later stage

and meant that it was not necessary to process full data sets every time a new configuration was desired. The event selection criteria that are detailed below were incorporated into the *chanser* final state class for the relevant topology.

7.3 Event Selection

A number of cuts were applied to this dataset with the intention of removing background events while retaining as much of the well-reconstructed signal events as possible. The following sections will detail the method by which the $e^-K^+K^-\pi^+$ events were created, as well as the cuts that have been made to the data with the intention of background reduction.

7.3.1 Particle Combinatorials

In a single DST event, which corresponds to an event with an experimental trigger, there was often a number of candidate tracks for a single particle. One of the key features of *chanser* is that it has built in the capability to loop over all candidate tracks for each particle. A separate physics event is then created for each possible combinatorial, as a result there was often more than one combinatorial event produced from each DST event. From now on, reference to an 'event' will mean reference to each combinatorial event rather than the DST event.

The purpose of combinatorials comes from the ambiguous identification of final state particles in the detector. In this analysis, it was assumed that the charge of the particle was correctly determined. Then, if there were more than one particle of a given charge in a DST event that was asked for in the final state topology, a combinatorial event was made for each candidate combination in the DST event. In order to reduce background events, cuts were then applied using time-of-flight and momentum information (as detailed in the following section) so that only correct combinatorial events that were consistent with the final state species were retained. For example, if in a single DST event there were three positive tracks for a K^+ and two negative tracks for a K^- then in total there would be six combinatorial events. The process of taking combinatorials avoids the systematically unreliable approach of simply taking the 'best candidate' for each event. In this analysis, the maximum number of tracks considered per species was set to be five. Once this has been given the output ROOT TTree will contain one entry for each combinatorial event.

7.3.2 Timing based selection cuts

As detailed in Chapter 4, CLAS12 contains an array of detectors that can be used to reconstruct events. In this analysis, the primary method of particle identification was achieved using the time-of-flight method. As noted in Section 4.5.1, detection of particles with momentum greater than 0.2 GeV was possible in the drift chambers in the Forward Tracker. Currently the poorer

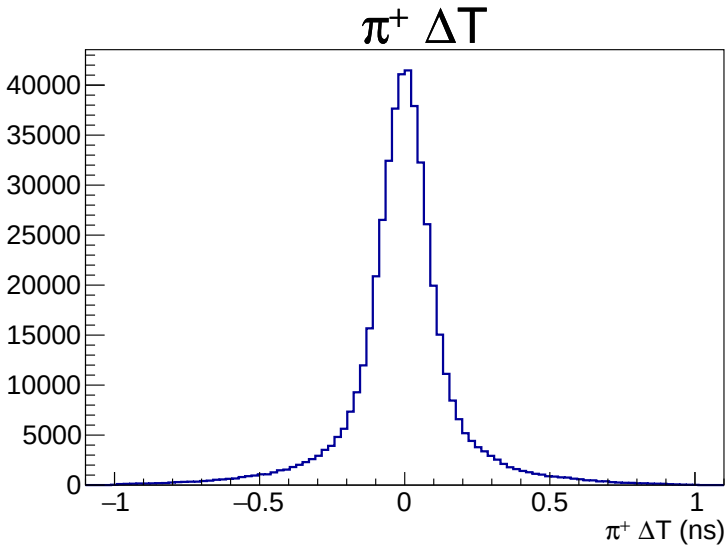

Figure 7.1: An example of the ΔT plot of the π^+ from the $KK\pi$ final state topology.

resolution of the Central Detector prohibited its inclusion in this analysis. Using the momentum and time-of-flight for a track particle identification proceeded as follows. For a hit detected with momentum P, the β value of the hit was defined by:

$$\beta = \frac{P}{\sqrt{P^2 + m^2}}, \tag{7.1}$$

where m is the mass hypothesis of the particle under consideration. The time of flight was then calculated from:

$$T_P = \frac{D}{(\frac{\beta}{c})}, \tag{7.2}$$

where D was the measured path length of the track and c is the speed of light in a vacuum. This calculated time-of-flight was subtracted from the time-of-flight measured from the FTOF detector, T_{TOF}, to give a value for $\Delta T = T_{TOF} - T_P$. A one-dimensional representation of a ΔT distribution is shown in Figure 7.1. Tracks with a correct mass hypothesis formed an approximate normal distribution centred on zero.

Evidence of the presence of misidentified background in the event sample could be clearly seen in two-dimensional plots of P vs ΔT, as shown in Figure 7.2. Well reconstructed events in this data sample appear in the band centred on the ΔT axis at zero, while background events are shown in the additional band above 2 GeV/c^2 that appears on the left hand side of this plot.

Rather than place a window cut on the ΔT value, it was optimal to use a momentum dependent cut to remove background events. A cut of the form:

$$(\Delta T + c_1) \times (P + c_2) = 1, \tag{7.3}$$

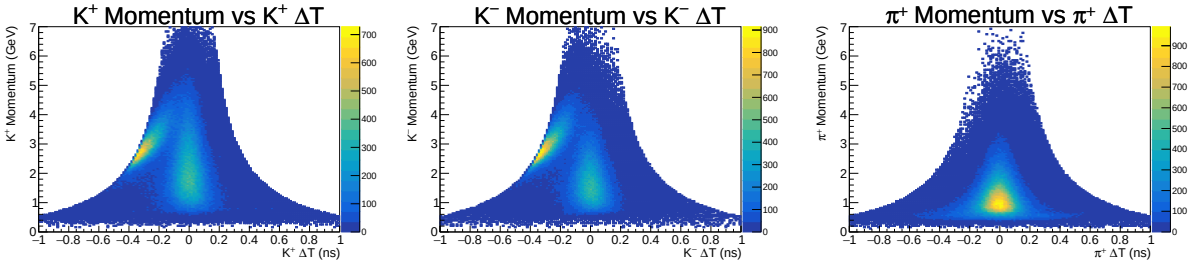

(a) π^+ (b) K^+ (c) K^-

Figure 7.2: Two-dimensional plots of the particle momentum vs its ΔTime value for the π^+, K^+ and K^- before the removal of any background events.

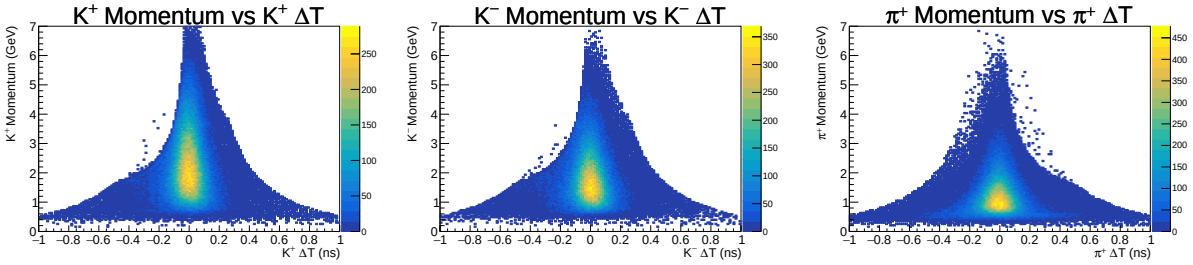

(a) π^+ (b) K^+ (c) K^-

Figure 7.3: Two-dimensional plots of the particle momentum vs its ΔTime value for the π^+, K^+ and K^- with the Event Builder Pid applied.

where c_1 and c_2 are parameters that can be fixed to optimise background rejection. This cut was used largely as a replacement for the event builder pid cut. From Figure 7.3 there was a visible removal of kaons at higher momentum when the event builder PDT was applied. For this reason, momentum dependent ΔTime cuts were in place of the event builder cuts. The values $c_1 = 0.03, c_2 = 0.2$ were used in the momentum dependent ΔTime cuts to create the distribution in Figure 7.2, removing a large sample of background events while retaining the vast majority of good events. The same cut was used for the other final state hadrons. The momentum vs ΔTime plots after the application of the cuts are shown in Figure 7.4. The residual background was subtracted as discussed in Section 7.4.

7.3.3 Fiducial Cuts

The ΔT cuts detailed above are specific to this analysis. There was however an effort made by the collaborators working with RG-A data to develop a set of common analysis procedures. The details of these cuts can be found in [96]. Among these common analysis procedures are the Fiducial cuts on the drift chambers. As described in Section 4.5.1, the drift chambers consist of three layers, each containing six sectors arranged around the beamline. This configuration is designed to maximise the detector coverage. The space in the detector plane between the sectors houses the toroidal magnets and no events are detected in this region. Some events

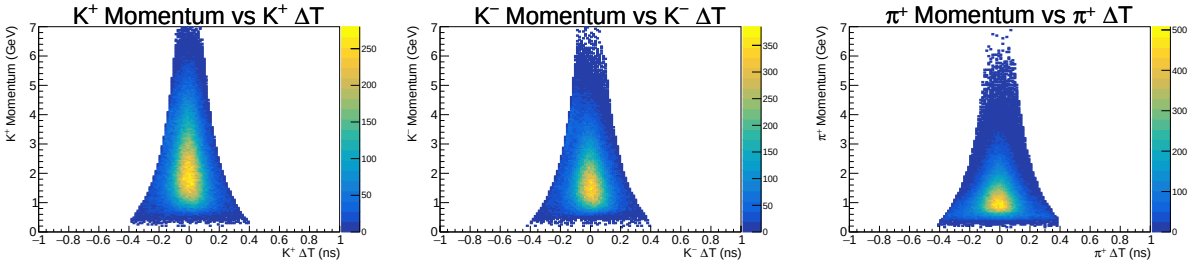

(a) π^+ (b) K^+ (c) K^-

Figure 7.4: Two-dimensional plots of the particle momentum vs its ΔTime value for the π^+, K^+ and K^- after the momentum dependent ΔTime cuts have been applied.

that are detected at the edges of the sectors might not be properly reconstructed and should be removed. The fiducial volume (inside which events are kept) was defined and excluded some events that are detected close to the edge of the detector. Details of the shape of the fiducial cuts and the parameters used to reconstruct the fiducial volme were found in the common analysis note. The fiducial volume cuts on hadrons in the drift chamber were relevant for this analysis and implemented in *chanser*.

7.3.4 MesonEx Trigger

It is required that all the events that were used in this analysis passed the conditions required of the MesonEx trigger which required that hadrons that were detected in the Forward Detector were found in more than one sector and that the detected electron energy in the Forward Tagger was less than 5.5 GeV.

7.4 Background Subtraction using sPlot

7.4.1 Missing Mass sPlot

The cuts described in Section 7.3 are based upon the particles that are detected in this topology - the electron in the FT and pions and kaons in the FD. However, due to the difficulty with measuring neutral particles, the neutron that would be measured in the CD was reconstructed from the other particles. Using conservation of energy and momentum we have,

$$p_N = p_e + p_p - p_{K^+} - p_{K^-} - p_{\pi^+}, \tag{7.4}$$

$$E_N = E_e + E_p - E_{K^+} - E_{K^-} - E_{\pi^+}. \tag{7.5}$$

The reconstructed mass of the neutron (m_N), also called the missing mass here, is then given by:

$$m_N = \sqrt{E_N^2 - p_N^2}. \tag{7.6}$$

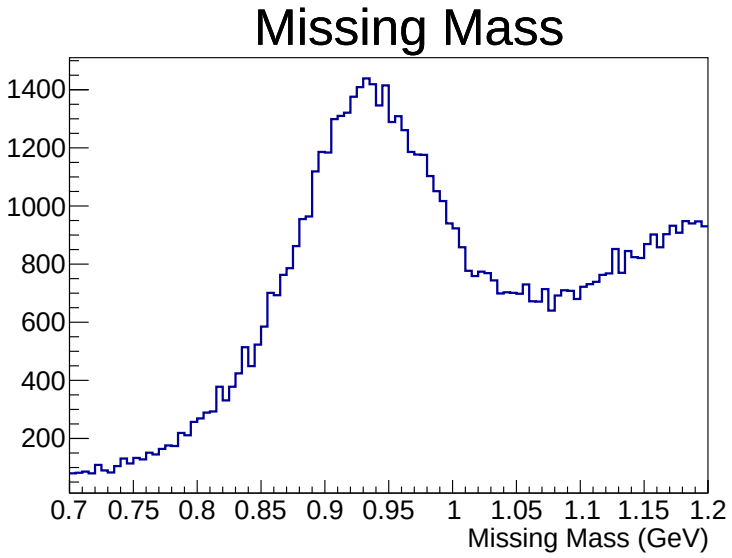

Figure 7.5: A histogram of the missing (neutron) invariant mass after the kinematic cuts from Section 7.3 have been applied.

True signal events in the sample formed a missing mass peak, centred on the neutron mass - 0.939 GeV. The missing mass plot of all events that remained after the cuts detailed in Section 7.3 is shown in Figure 7.5. This plot shows the appearance of a peak - the well reconstructed neutron events - as well as the set of background events that remain in this sample. The technique known as sPlot was used in order to remove background events.

The function of the sPlot is to resolve components of a mixture based on a known property of a distribution [97]. In this case, it was assumed that the missing mass of the good events can be described by a peak centred on the neutron mass, the missing mass is known as the discriminatory variable here. It is noted that sPlot should only be used on two variables (discriminatory and reconstructed) that are uncorrelated and independent. Figure 7.6 shows a small negative correlation and some variation between the missing mass and the invariant mass of $K^+K^-\pi^+$. To minimise such effects, the sPlot was done by binning in 0.1 GeV bins from 1.6 - 2.7 GeV in the $K^+K^-\pi^+$ invariant mass which mirrored the binning scheme that was used in later fits. Across the $K^+K^-\pi^+$ invariant mass range it was assumed that the distribution shown in Figure 7.5 could be modelled with a signal distribution based on a template from simulated data and a Chebyshev polynomial for the background. Using the signal and the background as described and the covariance matrix MCMC approach described in Section 6.6 yielded the fitted distribution, for the 1.9 - 2.0 GeV invariant mass bin this is shown in Figure 7.7.

The sPlot was used to provide event weights for signal and background sWeights, based on the discriminatory variable. To calculate the weights, the PDF shapes were fixed and the yields were fitted via the log likelihood [97]. For a two-species fit of signal and background, this is given by:

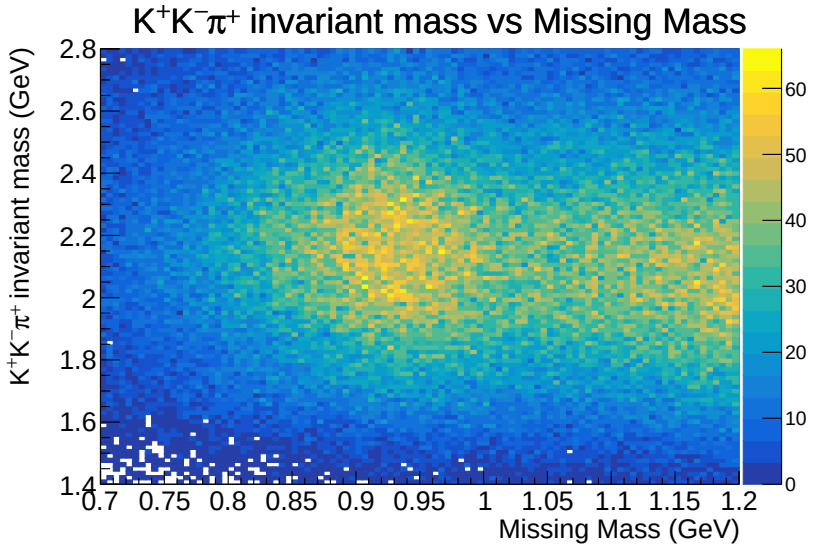

Figure 7.6: The $K^+K^-\pi^+$ invariant mass vs the missing mass.

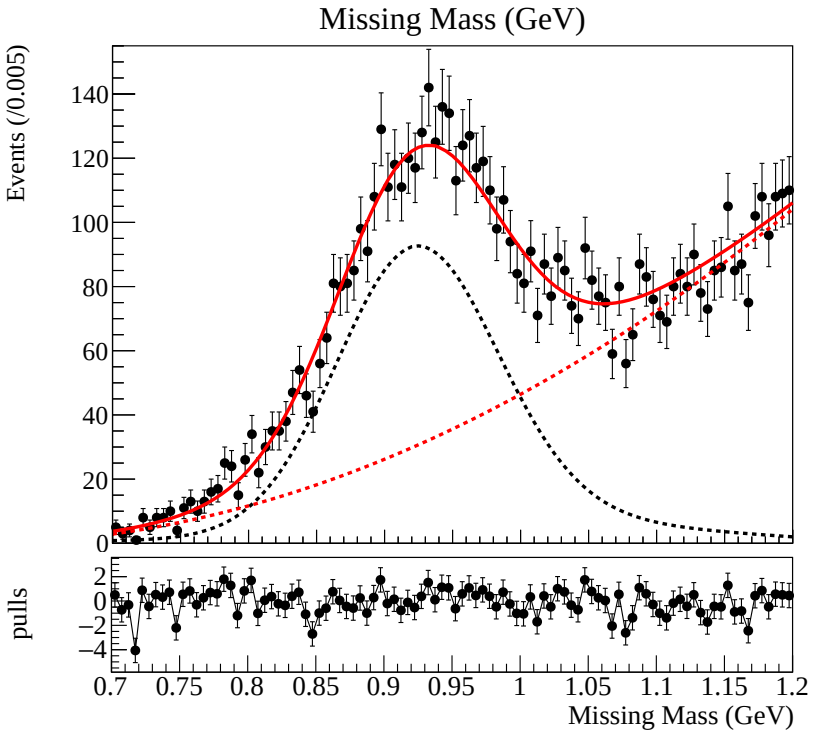

Figure 7.7: Illustration of the fit in the 1.9 - 2.0 GeV invariant mass bin of a signal taken from simulation and a Chebyshev polynomial background. The dashed black line is the signal, the dashed red is the background and the solid red curve is the full fit.

$$\mathscr{L} = \sum_{e=1}^{N} ln\left[N_{sig} f_{sig}(y_e) + N_{bg} f_{bg}(y_e)\right] - \sum_{i=1}^{N_s} N_i, \tag{7.7}$$

where

- N is the total number of events in the sample
- N_s is the number of species of events in the data sample
- $N_{sig}(N_{bg})$ is the number of expected events for the signal (background) species
- y is the set of discriminatory variables
- $f_{sig}(f_{bg})$ is the probability density function of the discriminatory variables for the signal (background) species
- $f_i(y_e)$ is the value taken by the pdf for each value e

The *sWeights* derive from the covariance matrix (V) resulting from the fit of the discriminatory variable [98]:

$$V^{-1}_{i,j} = \frac{\partial^2(-\mathscr{L})}{\partial N_i \partial N_j} = \sum_{e=1}^{N} \frac{f_i(y_e) f_j(y_e)}{\left(N_{sig} f_{sig}(y_e) + N_{bg} f_{bg}(y_e)\right)^2}, \tag{7.8}$$

where $i, j = \{sig, bg\}$. The *sWeights* ($\mathscr{W}$) were calculated from the covariance matrix as follows:

$$\mathscr{W}_{sig}(y_e) = \frac{V_{sig,sig} f_{sig}(y_e) + V_{sig,bg} f_{bg}(y_e)}{N_{sig} f_{sig}(y_e) + N_{bg} f_{bg}(y_e)}, \tag{7.9}$$

$$\mathscr{W}_{bg}(y_e) = \frac{V_{bg,sig} f_{sig}(y_e) + V_{bg,bg} f_{bg}(y_e)}{N_{sig} f_{sig}(y_e) + N_{bg} f_{bg}(y_e)} \tag{7.10}$$

The sWeights can be applied to distributions of other variables in the event and this is what is meant by 'signal-weighted' distributions, where background is effectively subtracted. The calculation of the sWeights is done by the RooStats [99] library as part of the *brufit* package [100]. The sPlot technique has been extensively used in a range of publications, from Pentaquark analyses at LHCb to lower energy hadron physics studies [101] [102].

There were several features of known resonances that became apparent in invariant mass plots after the application of the signal weights from the missing mass sPlot. The two-dimensional invariant mass plots are shown for the each of the isobar combinations in Figure 7.8.

7.4.2 K^* sPlot

From the invariant mass plots it was possible to see prominent structures in the data, for example, the $K^*(892)$ and $\phi(1020)$ as labeled in Figures 7.8, 7.9. In the case of a three body decay in

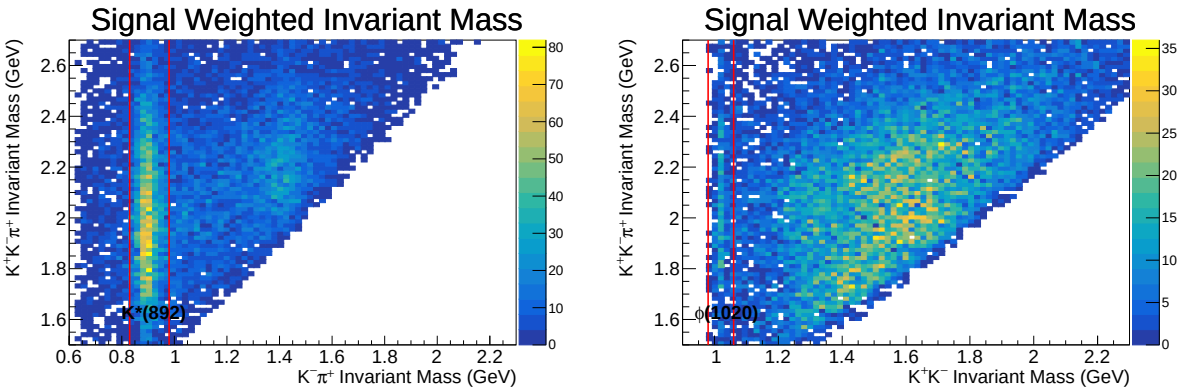

(a) The invariant mass of the three body $K^+K^-\pi^+$ system vs the invariant mass of the two body $K^-\pi^+$.

(b) The invariant mass of the three body $K^+K^-\pi^+$ vs the invariant mass of the two body K^+K^-.

Figure 7.8: Two-dimensional plots of the invariant mass of $K^+K^-\pi^+$ vs $K^-\pi^+$ and K^+K^- respectively with signal weights applied from the missing mass sPlot.

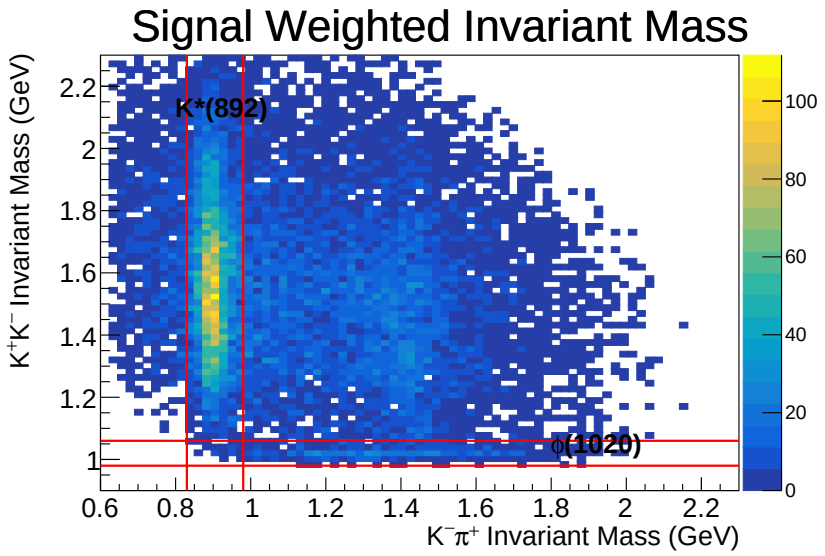

Figure 7.9: Two-dimensional plot of the invariant mass of K^+K^- vs the invariant mass of $K^-\pi^+$.

the isobar model there will be 2×2 sets of decay angles - a (θ, ϕ) pair for the decay of the resonance (denoted GJ) and a pair for the decay of the isobar (denoted HF). The Kinematics class in *chanser* was used to define the decay angles in their relevant frames - the Gottfried-Jackson frame for the resonance and the Helicity frame for the isobar, details of the frames of reference are given in appendix A. This analysis was focused on isolating the K^* isobar signal, therefore defining the pseudo-two body nature of the decay into the K^* vector and K^+ pseudoscalar. Decay angles were therefore taken with respect to the decay frame of the three body $K^+K^-\pi^+$ and two body $K^-\pi^+$ for the resonance and isobar respectively. Plots of the decay angles with missing mass sWeights applied are shown in Figures 7.10, 7.11. Since there were two decay channels, there were a further two sets of decay angles, defined with respect to the decays of the $X \to Y + \pi^+$ and $Y \to K^+ + K^-$. This decay channel was not considered in

this analysis, however plots of these decay angles are shown in appendix C.

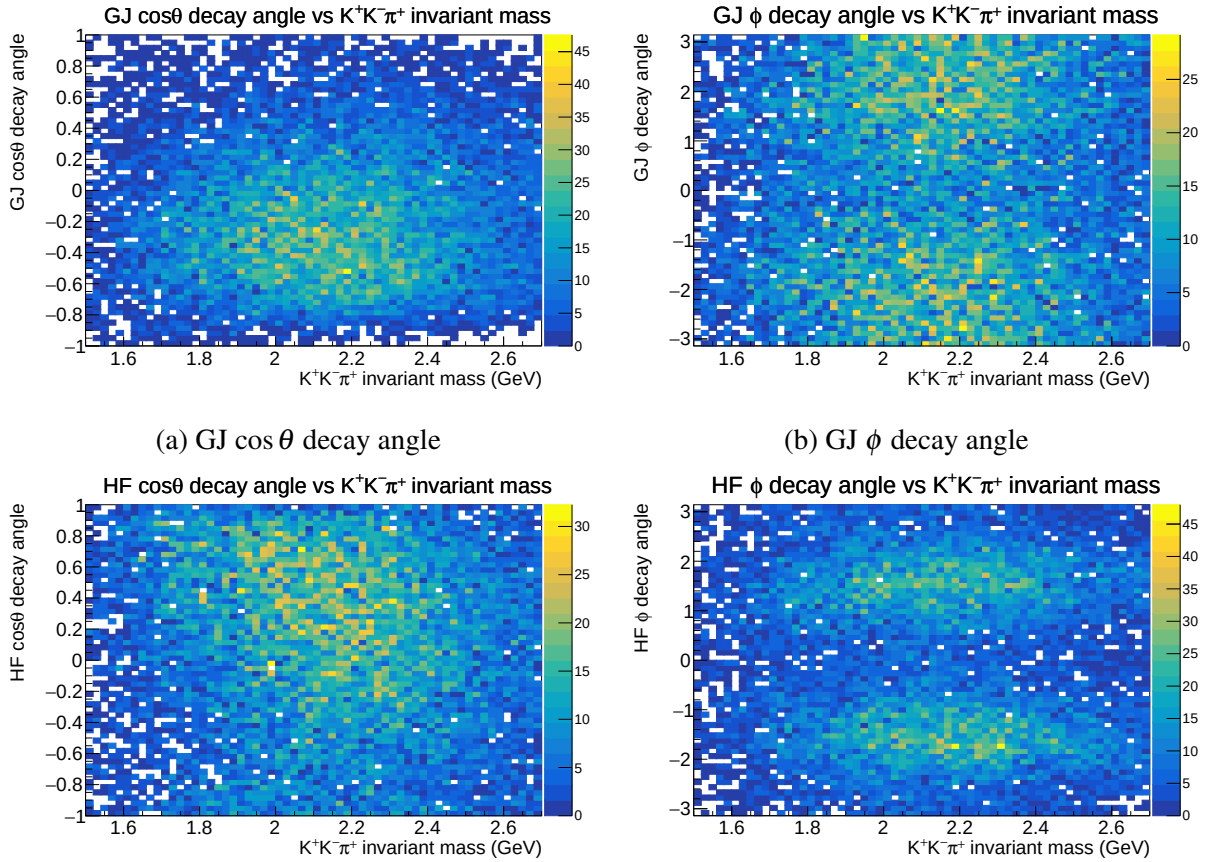

(a) GJ $\cos\theta$ decay angle

(b) GJ ϕ decay angle

(c) HF $\cos\theta$ decay angle

(d) HF ϕ decay angle

Figure 7.10: Two-dimensional plots of the invariant mass of $K^+K^-\pi^+$ vs the four decay angles of $X \to Y + K^+$, $Y \to K^- + \pi^+$ - after the application of missing mass sWeights.

In this framework, a file containing the weights is saved and can be implmented in any subsequent fits - it is possible to perform a secondary sPlot fit on data with sWeights from a previous fit applied. The signal weights that were extracted from the missing mass sPlot shown in Figure 7.5 do not differentiate between isobars chains. In order to extract weights for a $X \to K^* + K^+$ decay, the invariant mass of the $K^-\pi^+$ was used. The invariant mass of the $K^-\pi^+$ weighted with the signal from the missing mass sPlot is shown in Figure 7.12b. A clear peak is shown in this distribution at ~ 0.9 GeV. This was consistent with the PDG mass for the K^*, given as 0.892 GeV [81].

As shown in Figure 7.12a, there was no evidence of correlation or significant dependence between the missing mass and the $K^- + \pi^+$ invariant mass, so from the discussion on sPlot above, a secondary sPlot was performed with the $K^-\pi^+$ invariant mass as the discriminatory variable. The second sPlot was modelled using the simulated K^* distribution for the K^* resonance along with a Chebyshev polynomial background, also done using the covariance matrix MCMC approach. This second sPlot is shown in Figure 7.13. The plots of the decay angles with

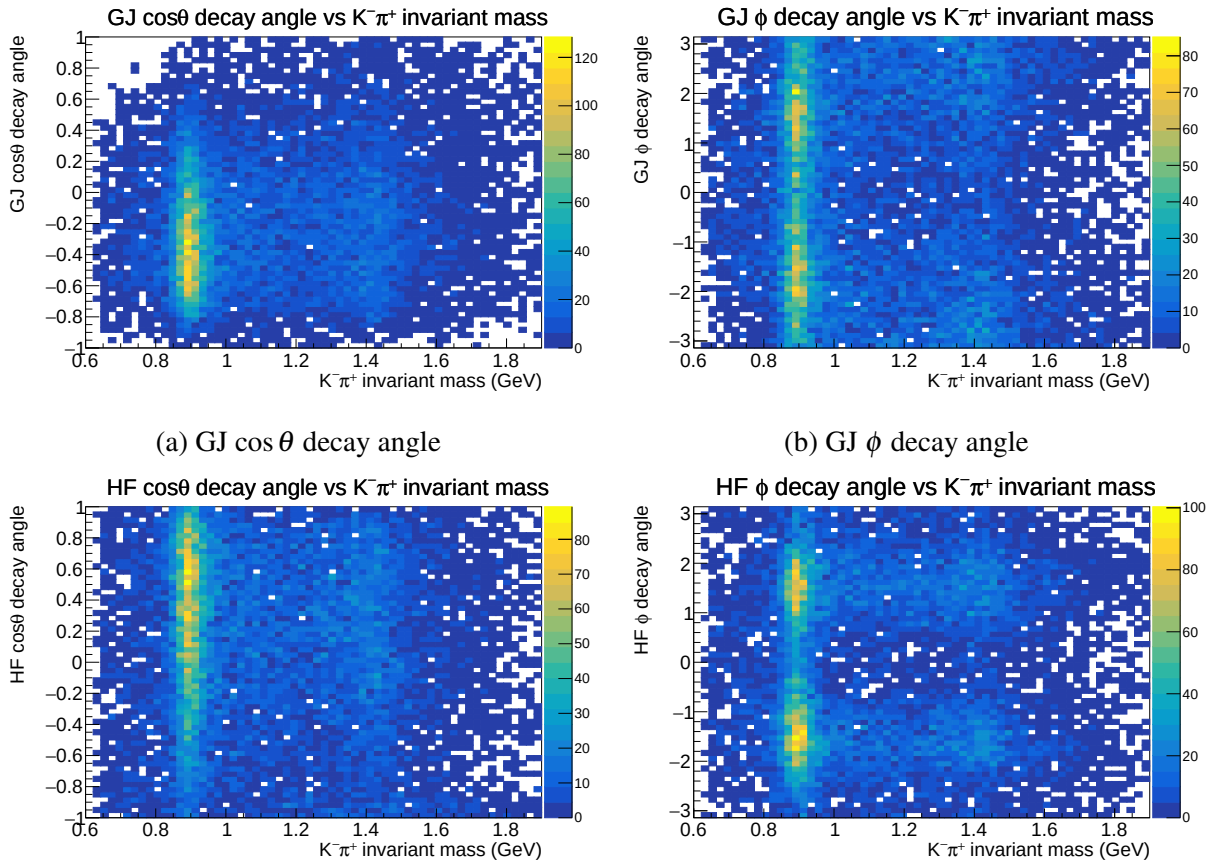

(a) GJ $\cos\theta$ decay angle

(b) GJ ϕ decay angle

(c) HF $\cos\theta$ decay angle

(d) HF ϕ decay angle

Figure 7.11: Two-dimensional plots of the invariant mass of $K^-\pi^+$ vs the four decay angles of $X \to Y + K^+$, $Y \to K^- + \pi^+$ - after the application of missing mass sWeights.

K^* weights applied are show in Figure 7.14.

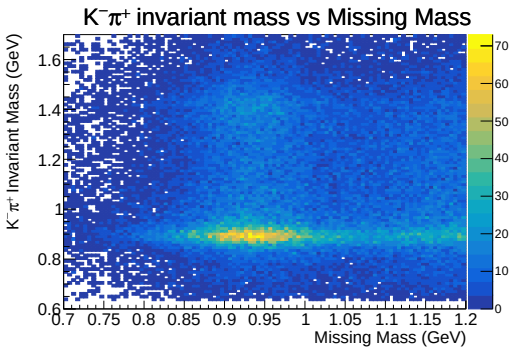

(a) The $K^-\pi^+$ invariant mass vs the missing mass before an sWeights have been applied.

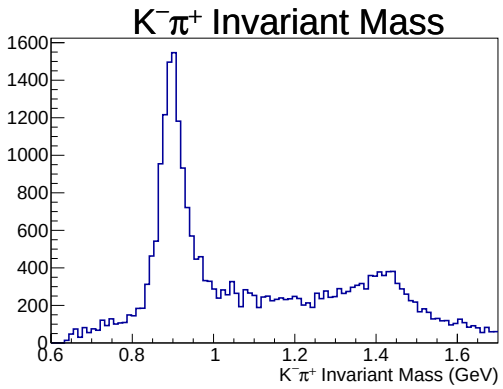

(b) The signal-weighted invariant mass of $K^-\pi^+$.

Figure 7.12: The $K^-\pi^+$ invariant mass vs the missing mass before the application of missing mass sWeights and the $K^-\pi^+$ invariant mass after the application of the sWeights.

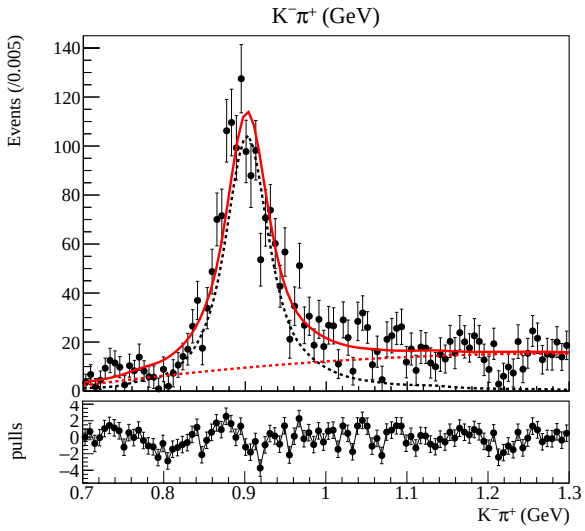

Figure 7.13: Illustration of the fit of a Breit-Wigner signal fit with Chebyshev background to the $K^-\pi^+$ invariant mass in the 1.9 - 2.0 GeV invariant mass bin. The signal is shown as the black curve, the background is the dashed red line with the full fit shown in the solid red line.

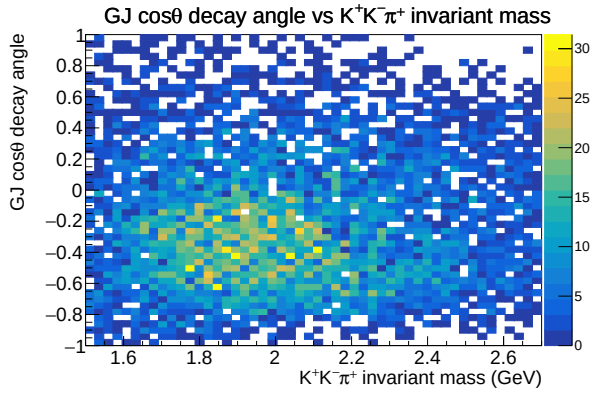

(a) GJ $\cos\theta$ decay angle

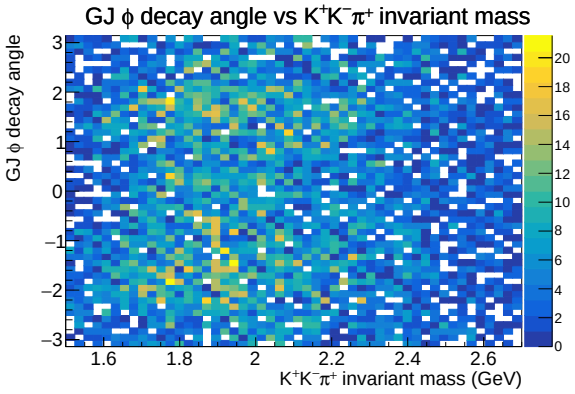

(b) GJ ϕ decay angle

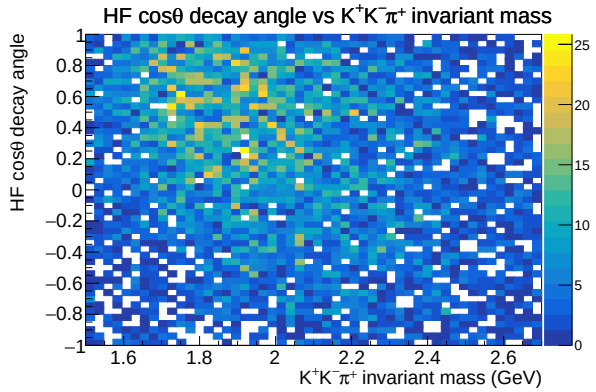

(c) HF $\cos\theta$ decay angle

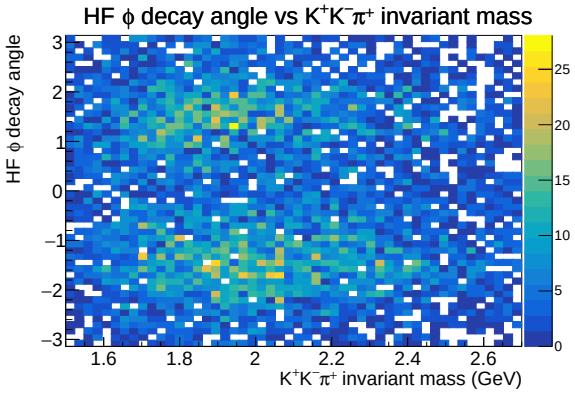

(d) HF ϕ decay angle

Figure 7.14: Two-dimensional plots of the invariant mass of $K^+K^-\pi^+$ vs the four decay angles of $X \to K^* + K^+$, $K^* \to \pi^+ + K^-$ - after the application of K^* sWeights.

7.4.3 Other Decay Processes to K^*K^+

There are processes that can also decay to the $K^+K^-\pi^+$ final state through an intermediate K^* that are considered background in this reaction. These processes involve excited baryon states, with the reaction diagrams shown in Figure 7.15. Evidence of a significant hyperon background would be apparent in the relevant invariant mass plots. For example, peaks in the invariant mass distribution of the $(n+K^+)$ would have suggested an enhancement in the process shown in Figure 7.15a. Likewise for the hyperon decays to $(n+K^-+\pi^+)$, there would have been evidence for the process shown in Figure 7.15b. Invariant mass plots are shown in Figures 7.16 with potential hyperon invariant mass on a plot with the $K^-\pi^+$ invariant mass. The event sample used for these plots was taken after the missing mass sWeights were applied. Strong contamination from hyperon production would show as horizontal bands in these plots. No strong hyperon signal is seen in these plots. Possible effects of any residual hyperon contamination on the angular distributions is discussed in the Sections on the simulation 7.5.4 and systematics 10.2.

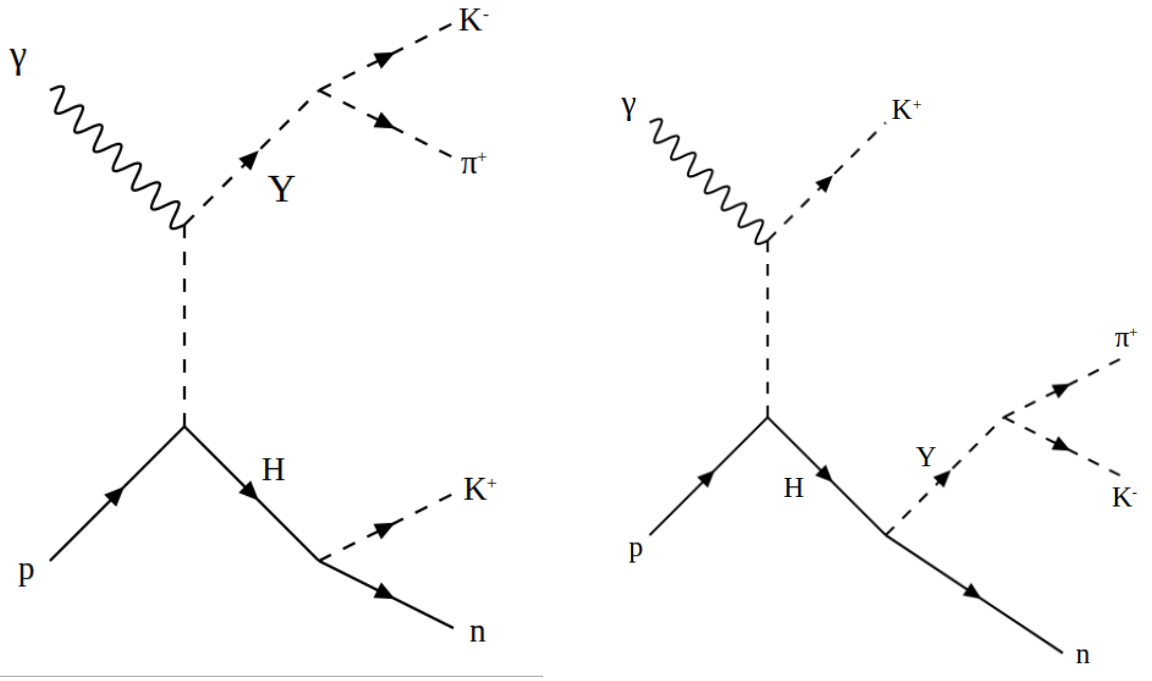

(a) Isobar produced at the upper vertex.

(b) Isobar produced at lower vertex.

Figure 7.15: Two background processes decaying to the $K^+K^-\pi^+$ final state. H is an unknown excited hyperon.

7.4.4 t distribution

As discussed previously, in the reaction mechanism in which the three final state mesons are produced at the top vertex the reaction is characterised by very low momentum transfer to the $K^+K^-\pi^+$ system. The final state diagram in which one or more of the hadrons is produced from

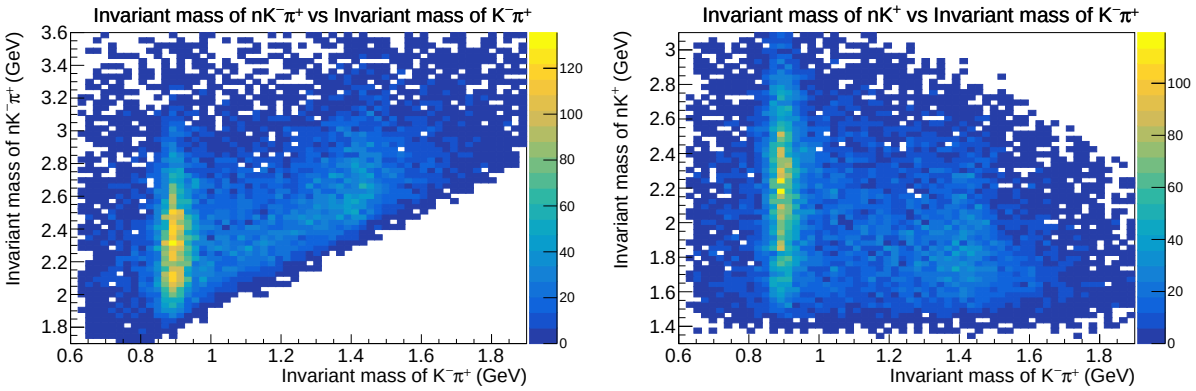

(a) Invariant mass of $nK^-\pi^+$ vs the invariant mass of $K^-\pi^+$.

(b) Invariant mass of nK^+ vs the invariant mass of $K^-\pi^+$.

Figure 7.16: Invariant mass plots of the two background processes that could have contributed to the final K^*K^+ event sample. No clear structure was observed in the invariant mass of either process.

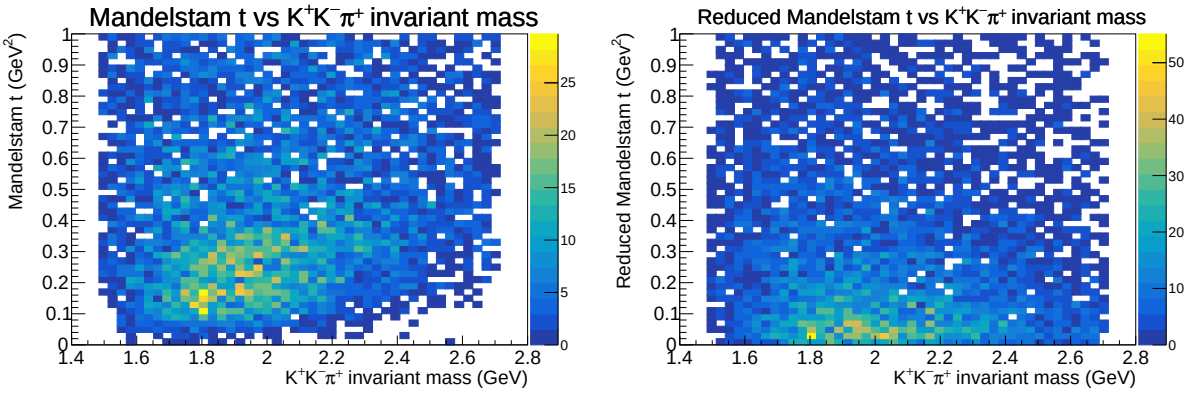

(a) Standard Mandelstam t.

(b) Reduced Mandelstam t.

Figure 7.17: Plots of the standard Mandelstam t and the reduced Mandelstam t vs the invariant mass of $K^+K^-\pi^+$. Correlations are observed between the standard definition of Mandelstam t and the invariant mass of X, however no such effect is seen in the reduced Mandelstam t variable.

the bottom vertex would result in an increase in the value of the Mandelstam variable t, defined as

$$t = (p_\gamma - p_X)^2, \tag{7.11}$$

where p_γ, p_X are the 4-momenta of the photon and $K^+K^-\pi^+$ system respectively. Since the primary reaction takes place at low t, contributions from other processes in the final event sample are reduced by restricting events to a low t region. Another often used term is the 'reduced t', defined by:

$$t' = (p_\gamma - p_X)^2 + 2E_\gamma(E_X - |\underline{p}_X|) - 2M_X^2, \tag{7.12}$$

with E_γ the photon energy, E_X the energy of the resonance, $|\underline{p}_X|$ the magnitude of the momentum of the resonance and M_X the mass of the produced $K^+K^-\pi^+$ system. The principle of the reduced t variable is that the momentum transfer becomes mass-independent as shown in Figure 7.17. Notably, correlations are visible between the invariant mass of $K^+K^-\pi^+$ and the standard definition of Mandelstam t that are not present in the plot of reduced Mandelstam t, as expected. Events involving the production of hyperon resonances would have been characterised with increased values of t. Plots of the decay angles against the momentum transfer t are shown in Figure 7.18. In this analysis, a cut was place on t' such that $0 \leq t' \leq 1$.

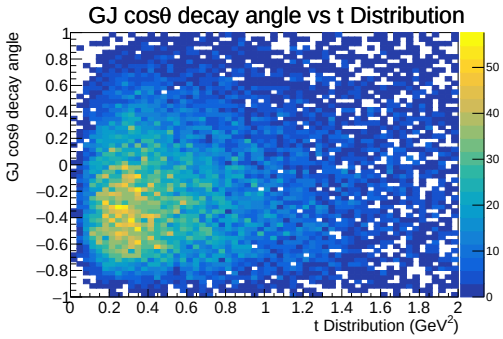

(a) GJ $\cos\theta$ decay angle

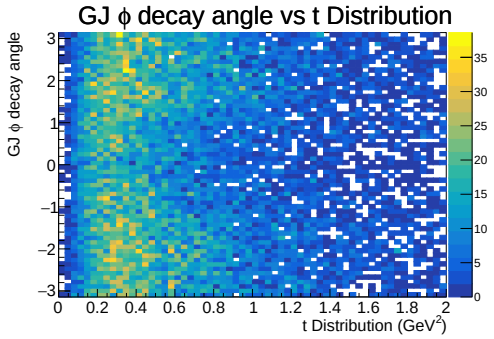

(b) GJ ϕ decay angle

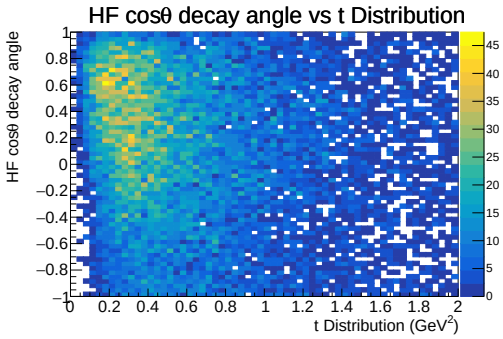

(c) HF $\cos\theta$ decay angle

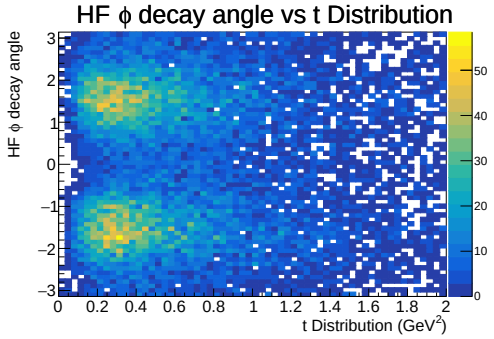

(d) HF ϕ decay angle

Figure 7.18: Two-dimensional plots of the four decay angles of $X \to Y + K^+$, $Y \to K^- + \pi^+$ vs the t distribution with missing mass weights applied.

7.5 Reaction Simulation

Generation of simulated events was important in order to study effects such as detector resolution and acceptance, as well as other factors such as to construct a model for the shape of the missing mass as discussed in Section 7.4.

Simulated events were generated using the *elSpectro* software package [103]. This package was designed specifically to generate events in electron scattering reactions such as this one. Reaction parameters such as the electron scattering angle, scattered electron momentum and the momentum transfer can be adjusted by the user. Generated events from *elSpectro* are output as text files. The full CLAS12 *gemc* simulation was used in order to simulate the effect the detector had on reconstruction of measured events. The *gemc* package stands for GEant4 Monte-Carlo and simulates the passage of particles produced in the reaction through the materials of the detector [104]. Generated event files were simulated by being passed through the Open Science Grid (OSG) portal. The DST files that were output from the reconstruction were written to the JLab server where they were transferred to Glasgow to be analysed.

7.5.1 Simulation Tuning

The events that were used in this analysis were tuned so that the t and the mass of the X meson distributions of the real data were reproduced in the simulation. This was necessary to provide correct integrated acceptances when fitting. The scattered electron range was set to be representative of an electron detected in the Forward Tagger and the MesonEx trigger. Events for this analysis were generated with the electron in the polar angle range 2.5° - 4.5° and with momentum between 1 and 5.5 GeV. These ranges for the electron were fixed by the specifications of the Forward Tagger. For the decay $X \rightarrow K^* + K^+$, the mass distribution comparison between simulation and data can be seen in Figure 7.19a. The mass distributions that were output from the simulation were tuned by inputting mass distributions for the $K^+K^-\pi^+$ and $K^-\pi^+$ in the generated data. The $K^-\pi^+$ mass distribution was set as a Breit-Wigner distribution with position and width given by the PDG values for the $K^*(892)$ and the $K^+K^-\pi^+$ was generated to reproduce the mass distribution given by the data. The configuration given for the generated data in *elSpectro* in given in Table 7.1

Secondly, in *elSpectro* the production mechanism was specified as a given mixture of t-channel and s-channel (flat) reaction mechanisms. In this analysis, events were generated as 95% t-channel and 5% s-channel. Further, the slope of the generated the t-distribution was specified as 2.8 GeV^2 with the intention of getting a fair match between t-distributions for accepted simulated events and data. The comparison between the reduced-t distribution (as defined in Section 7.4.4) for data and accepted simulated events is shown in Figure 7.19b.

In terms of attaining a final event sample, the simulation was used to construct a template signal shape for the sPlot fits. The missing mass distribution from the simulation is shown in

Parameter in *elSpectro*	Relevant Notes
K^* mass distribution	Breit-Wigner of mass = 0.892 GeV and width = 0.047 GeV
$K^+K^-\pi^+$ mass distribution	Series of Breit-Wigner distributions with relative intensity, position and widths given in Table 7.2
t slope	Generated with $t = 2.8$ GeV^2
Relative s-channel and t-channel production	0.05 s-channel and 0.95 t-channel
Electron θ range	$(2.5, 4.5)^\circ$
Electron Momentum range	$(1.0, 5.5)$ GeV

Table 7.1: Configuration for the generated data in *elSpectro*.

Intensity	Mass (GeV)	Width (GeV)
0.245	1.55	0.15
0.185	1.65	0.15
0.175	1.77	0.15
0.175	1.82	0.15
0.2	1.9	0.15
0.11	2.0	0.15
0.075	2.1	0.15
0.075	2.2	0.15
0.08	2.35	0.15
0.08	2.6	0.15

Table 7.2: Configuration used in *elSpectro* to create the $K^+K^-\pi^+$ mass distribution.

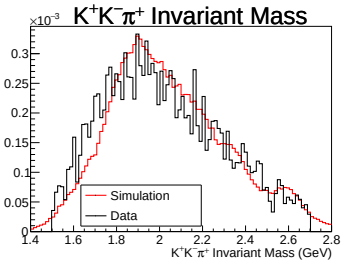

(a) The normalised invariant mass distributions for $K^+K^-\pi^+$ for data and simulation.

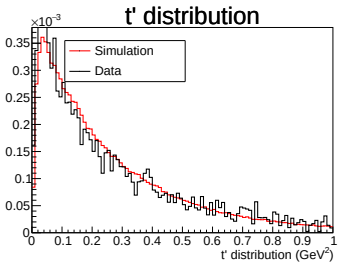

(b) Comparison between t distribution for data and simulation.

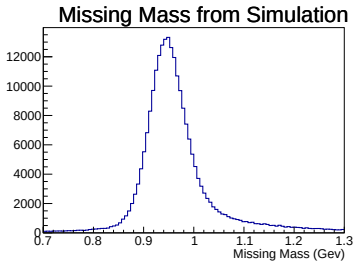

(c) Missing Mass from simulation.

Figure 7.19: Data distributions from simulation.

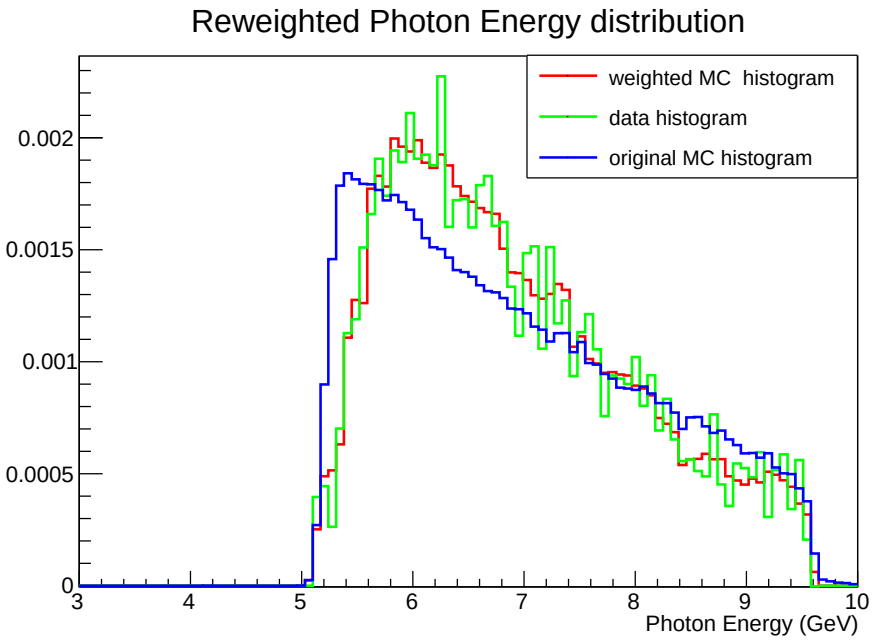

Figure 7.20: Effect of histogram reweighting the simulation to match the data with respect to the photon energy.

Figure 7.19c. Using *brufit*, it was possible to load this missing mass template as a histogram PDF on which the signal PDF was modelled.

7.5.2 Variable Reweighting

In some variables it was more straightforward to reweight the variable rather than tune it at the generation stage. The photon energy is defined by:

$$E_\gamma = E_{beam} - E_e, \tag{7.13}$$

where E_{beam} is the beam energy, given from the run database and E_e is the energy of the scattered electron as measured in the Forward Tagger. This distribution was required to be matched between the reconstructed simulation and data. To do this the simulated data was reweighted based on the ratio of experiment and simulation in a 1D histogram. The effect of reweighting the scattered electron energy is shown in Figure 7.20. Weights were stored and using *brufit* were applied to the simulated data when performing the Monte Carlo integration of the PDF.

7.5.3 Truth Matching

One important feature of the simulation analysis was truth-matching. As noted in Section 7.3.1, there was often more than one physics event created from each possible combinatorial. If truth-matching was used, the correct combinatorial event was selected from all those that were gen-

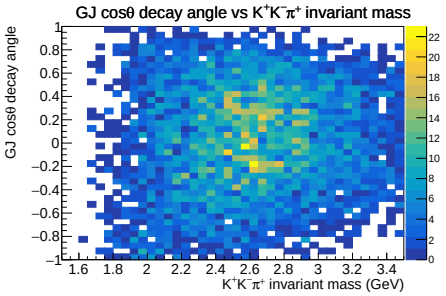

(a) GJ $\cos\theta$ decay angle

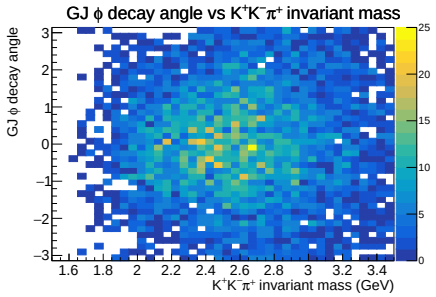

(b) GJ ϕ decay angle

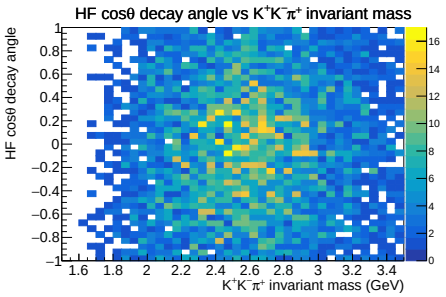

(c) HF $\cos\theta$ decay angle

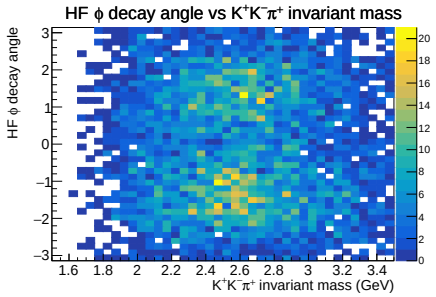

(d) HF ϕ decay angle

Figure 7.21: Two-dimensional plots of the four decay angles of $X \to K^* + K^+$, $K^* \to K^- + \pi^+$ vs the invariant mass of $K^+K^-\pi^+$ for the phase space Monte Carlo data for the reaction $X \to K^* + K^+$, $K^* \to K^- + \pi^+$.

erated. Using truth-matched simulated data therefore removed effects arising from misreconstructed events that in the real data were removed by the sPlot subtractions.

7.5.4 Background Investigation using Monte Carlo Data

Further study of background production in this reaction was done using simulated data. In addition to simulating the production of the meson X that was described as a bound state of $K^+K^-\pi^+$, simulations were also performed for events that followed the decay channel shown in Figure 7.15. Plots of the decay angles for each set of simulated data are shown in Figures 7.21, 7.22, 7.23. Figure 7.21 shows the decay angles for the process $X \to K^* + K^+$, $K^* \to K^- + \pi^+$ as generated by the simulation. These plots show the phase space for each of the decay angles in this reaction.

Figures 7.22 and 7.23 show the decay angle distributions for the background processes shown in Figures 7.15a and 7.15b respectively. Significant differences were observed in these distributions, in particular the background process shown in Figure 7.15a was shown at large *GJ* ϕ and that shown in Figure 7.15b at *GJ* ϕ around 0. These are both in contrast to the signal distribution in which the *GJ* ϕ distribution is more evenly spread. In order to investigate the levels of background in the data a series of toy studies were performed as described in Section 10.2 which mixed these distributions with $X \to K^+K^-\pi^+$ events to see the effect on the extracted

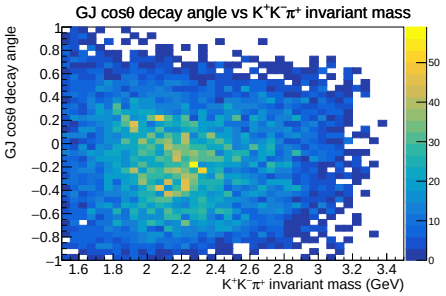

(a) GJ $\cos\theta$ decay angle

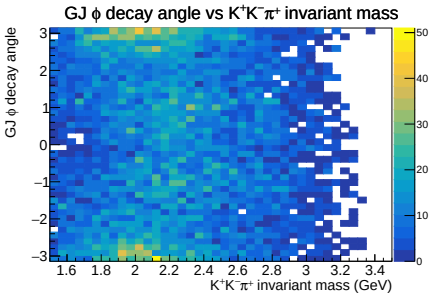

(b) GJ ϕ decay angle

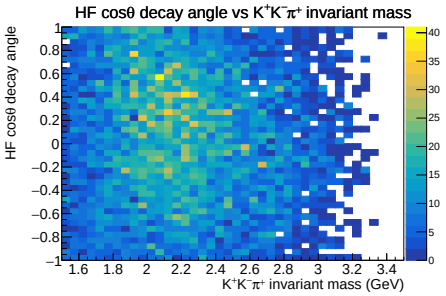

(c) HF $\cos\theta$ decay angle

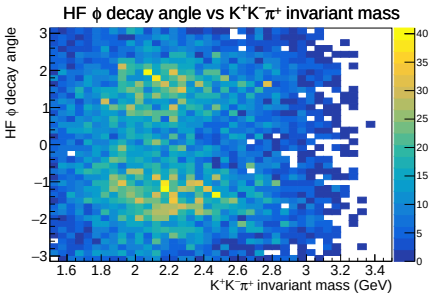

(d) HF ϕ decay angle

Figure 7.22: Two-dimensional plots of the four decay angles of $X \to K^* + K^+$, $K^* \to K^- + \pi^+$ vs the invariant mass of $K^+K^-\pi^+$ for the phase space Monte Carlo data for the reaction shown in Figure 7.15a.

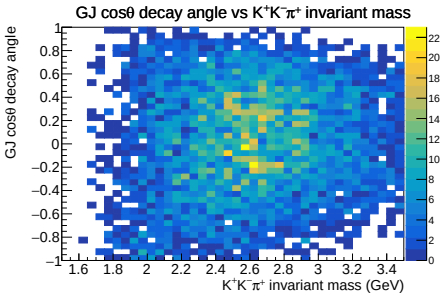

(a) GJ $\cos\theta$ decay angle

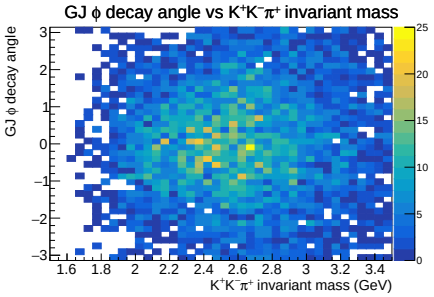

(b) GJ ϕ decay angle

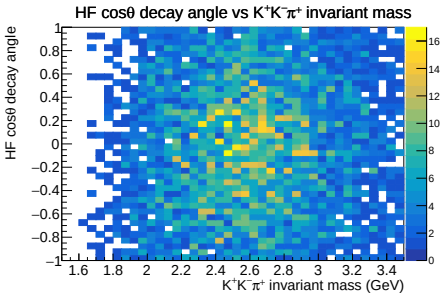

(c) HF $\cos\theta$ decay angle

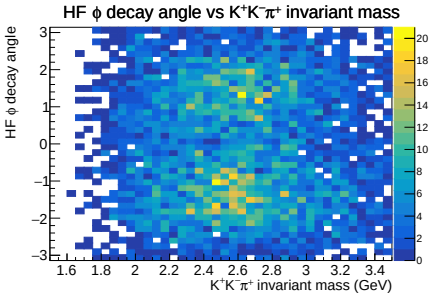

(d) HF ϕ decay angle

Figure 7.23: Two-dimensional plots of the four decay angles of $X \to K^* + K^+$, $K^* \to K^- + \pi^+$ vs the invariant mass of $K^+K^-\pi^+$ for the phase space Monte Carlo data for the reaction shown in Figure 7.15b.

moments.

7.6 Chapter Conclusion

In summary, this chapter has detailed the process of taking calibrated and reconstructed track data to a dataset from which higher level analysis was performed. The cuts that were applied served the purpose of reducing the background in the sample as much as possible and corrections that were applied accounted for inconsistencies in detection and reconstruction. The sPlot technique was employed as a means of isolating signal events and to select events that decay uniquely through the K^* isobar. Simulated events were used to model the detector based effect on the reaction as well as to provide a model signal for the data. The tools provided in *elSpectro* and *brufit* were used to create a simulation that was as representative of the data as possible. Further details on the extraction of results using the final event sample and the simulation are given in the following section.

Chapter 8

Moments of Decay Angle Distributions: Fit Setup

This section will describe the process by which the moments of the meson decay angle distributions were extracted from the final event sample that was achieved in Chapter 7. Extraction of parameters was performed in *brufit*, the same framework that was used to perform sPlot analyses as described in Section 7.4 To obtain reliable results the MCMC algorithms described in Chapter 6 were used.

8.1 Fit Variables and Parameters

As noted previously, a two body decay in the centre of mass frame can be modelled using two angular decay variables - (θ, ϕ). This reaction was composed of two such decays so there were four angular decay variables in this fit. These were denoted (θ_{GJ}, ϕ_{GJ}) for the decay of the resonance in the Gottfried-Jackson system and (θ_{HF}, ϕ_{HF}) for the decay of the isobar in the Helicity system. Collectively, the set of the four decay angles $(\theta_{GJ}, \phi_{GJ}, \theta_{HF}, \phi_{HF})$ are denoted as Ω. Additionally, there are two variables that arise as the photon is linearly polarised. These are the degree of linear polarisation, denoted $\mathscr{P}$, and the angle of the photon polarisation relative to the production plane, denoted Φ.

As shown in Appendix B, it is only the real part of the product of 2 D-Wigner functions which contributes to the intensity:

$$\Re\{D^{J*}_{M,\Lambda}(\phi_{GJ}, \theta_{GJ}, 0) D^{S*}_{\Lambda,0}(\phi_{HF}, \theta_{HF}, 0)\} = d^{J*}_{M,\Lambda}(\theta_{GJ}) d^{S*}_{\Lambda,0}(\theta_{HF}) \cos(M\phi_{GJ} + \Lambda\phi_{HF}). \quad (8.1)$$

From Chapter 5, eqn 5.59 gave the intensity as:

$$\mathscr{I}^{\alpha}(\Omega,\Phi) = \sum_{S\Lambda JM}\left(\frac{2J+1}{4\pi}\right)\left(\frac{2S+1}{4\pi}\right)H^{\alpha}(S,\Lambda,J,M) \times D^{J*}_{M,\Lambda}(\phi_{GJ},\theta_{GJ},0)D^{S*}_{\Lambda,0}(\phi_{HF},\theta_{HF},0), \quad (8.2)$$

and therefore the explicit form of the intensity is

$$\mathscr{I}^{\alpha}(\Omega,\Phi) = \sum_{S\Lambda JM}\left(\frac{2J+1}{4\pi}\right)\left(\frac{2S+1}{4\pi}\right)H^{\alpha}(S,\Lambda,J,M) \times d^{J*}_{M,\Lambda}(\theta_{GJ})d^{S*}_{\Lambda,0}(\theta_{HF})\cos(M\phi_{GJ}+\Lambda\phi_{HF}). \quad (8.3)$$

The small Wigner d-functions were dependent on parameters (S,Λ,J,M) that defined the order of the d-functions of the sum. Together, the set of (S,Λ,J,M) defined the parameters of interest, the moments $H(S,\Lambda,J,M)$.

8.2 Moment Selection

The choice of the set of moments used in the fit was taken from the expected partial waves. It was assumed to have contributions from resonances of total spin j such that $0 \leq j, j' \leq 3$. From Section 5.9, in the Kronecker product of Wigner D-functions the value of J can take all values such that $J = 0,1,...,j+j'$, with further restrictions placed on the allowed values of J dictated by the Clebsch-Gordan coefficients. Since $0 \leq j, j' \leq 3$, this gives $J = 0,1,...,6$. In other words, $J_{max} = 6$. Since $m \leq j$, the moment parameter M was restricted by $M \leq J$. The parameter S of the moment referenced the total spin of the isobar in the same way that the quantum number J referred to the total spin of the resonance. Since in this decay model the isobar was fixed as the $K^*(892)$ state, the total spin of the decay products was fixed as 1. Subsequently, this fixed $s = s' = 1$. The parameter S was determined as $S = 0,1,...,s+s'$ for the same reason as described for J above. However, the intensity included the Clebsch-Gordan coefficient $(s,0;S,0|s',0)$ - when $S = 1$ this gives $(1,0;1,0|1,0) = 0$ and consequently no moments are allowed with $S = 1$. Allowed values of S were therefore fixed to $(0,2)$. Finally, the Helicity parameter Λ was restricted by $\Lambda \leq \min\{S,J\}$ since $\lambda \leq s, j$ and $\lambda' \leq s', j'$. In summary, the values of (S,Λ,J,M): $S = 0,2; J = 0,1,2,...,6; \Lambda \leq \min\{S,J\}$ and $M \leq J$.

8.3 Binning

The data was split into eleven bins of $K^+K^-\pi^+$ invariant mass, 0.1 GeV in width, from 1.6 - 2.7 GeV. This binning scheme was chosen to cover the acceptance range of the data. Bins were chosen to be wide enough that the statistics per bin were sufficient such that reliable fits could

be performed on the data, but narrow enough relative to the width of expected resonant states such that any enhancement across the mass range could be detected. Fits on the eleven invariant mass bins were done independently.

8.4 MCMC parameter space

For normalisation purposes, the $H^0(0,0,0,0)$ moment was set as a constant value of 2 as a consequence of summing two reflectivities. In the moments expansion in terms of partial waves given in eqn 5.60, $H^0(0,0,0,0)$ is the sum of the squares of all the wave amplitudes. To be physical (i.e. to have a positive intensity), the allowed values of each moment must be inside the range $[-H^0(0,0,0,0), H^0(0,0,0,0)]$. To evaluate the range of values each moment can take, a Monte Carlo method was used in which a random value for each wave amplitude was generated, normalised and then used to calculate the value for each moment as given by eqn 5.60. Repeating this process 100,000 times produced a range of results for each moment such as that shown for the $H^0(2,0,0,0)$ moment in Figure 8.1 for different wave content. For each moment, the resulting range of values is shown in Figure 8.2. For each moment, it can be seen that the range of values is dependent on the wave content - in other words, it was not possible to fix an allowed range for each parameter since the wave content of the decay was not explicitly known.

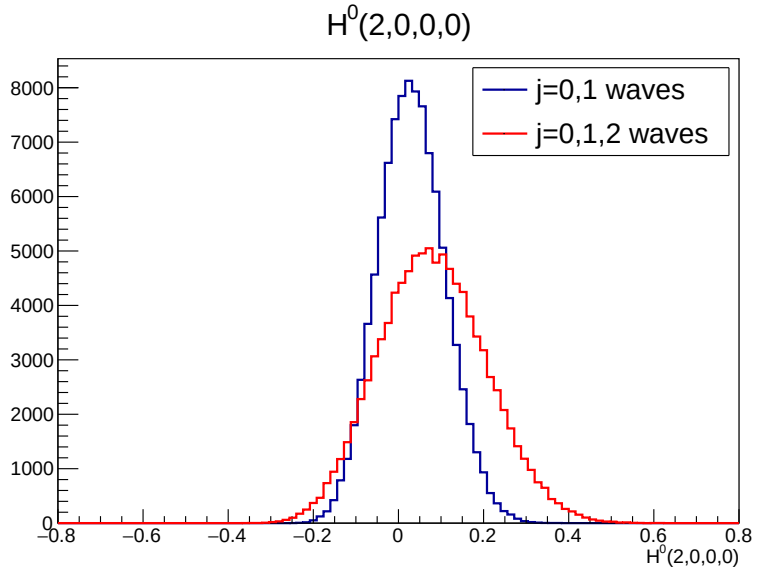

Figure 8.1: The value of the $H^0(2,0,0,0)$ moment from 100,000 randomly generated wavesets.

In the fitting process, it was also possible to fit the moments excluding the $\left(\frac{2J+1}{4\pi}\right)\left(\frac{2S+1}{4\pi}\right)$ factors from eqn 8.3. By removing these factors, moments can be visualised on a scale comparable to each other (as the values of higher order moments are not suppressed by their prefactors). The validation of this method is shown in Section 10.1.3. During the fitting process, the $\left(\frac{2J+1}{4\pi}\right)\left(\frac{2S+1}{4\pi}\right)$ terms were removed and the range of each moment was set to $[-5,5]$ as the

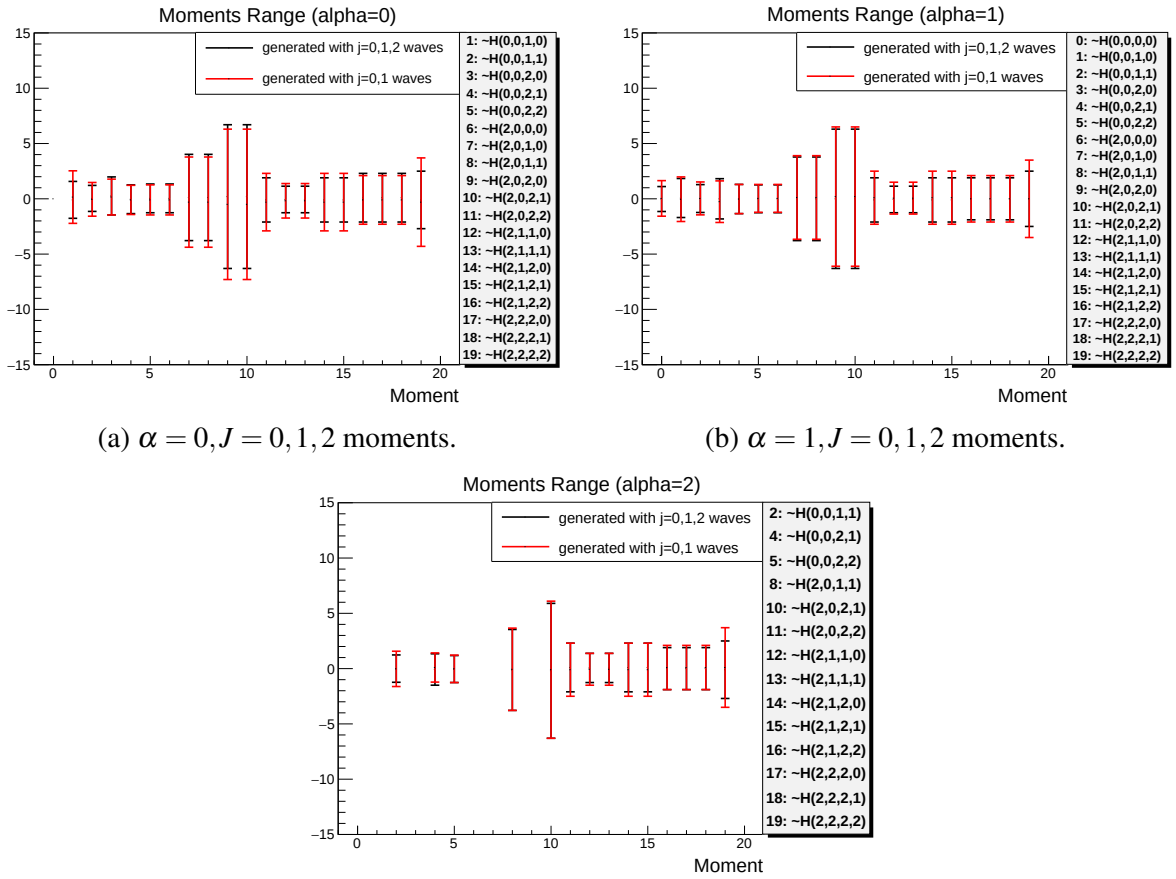

(a) $\alpha = 0, J = 0, 1, 2$ moments.

(b) $\alpha = 1, J = 0, 1, 2$ moments.

(c) $\alpha = 2, J = 0, 1, 2$ moments.

Figure 8.2: Range of possible values for each moment.

physical limit of each moment was within this range after their removal from the fit function. This was checked using the criteria detailed in Chapter 6. Correct values for the moments could be found by including the $\left(\frac{2J+1}{4\pi}\right)\left(\frac{2S+1}{4\pi}\right)$ terms in the model after the fit.

8.5 Visualising the results

The extraction of the moments required the data, the weights from the sPlot used to subtract background events and simulated events. The optimisation was done using the RMS MCMC algorithm described in Section 6.7. The visualisation of the fit on the data points was saved for each bin and each of the six variables, shown as an example in Figure 8.3. For each variable, the plot showed the fit on the data as well as the pulls. The pulls were the difference between the fit model and the data, normalised by the standard deviation of the fit. A one-dimensional projection of the pulls from Figure 8.3 is shown in Figure 8.4. A fit that was well-posed would have had the the pulls normally distributed around zero with a standard deviation of one. A shift of the mean of the residuals from zero would indicate a systematic uncertainty in the fit, whereas if the standard deviation was significantly greater or less than one then there would have been

a degree of underfitting or overfitting respectively. The projection of the PDF integrated over the other variables was shown as the red line in Figure 8.3. These fits were done via simulated Monte-Carlo data, and so acceptance effects and statistical fluctuations are visible.

8.6 The Fitting Process

One optimisation of a MCMC procedure is the length of the burn-in, as discussed in Section 6.5.1. In this analysis, two chains needed to be considered - the sequential proposal chain that was used to create the RMS matrix and the chain that was based on the RMS matrix step proposal from which the results were taken. Each chain had specific requirements. The first chain only needed to be long enough such that a reliable RMS matrix could be found. The second chain needed to be of a satisfactory length such that reliable results were obtained consistent with the statistical information in the data.

8.6.1 MCMC Chain Length

In calculating the posterior distribution for the moments, the role of the sequential proposal chain was to create a RMS matrix that could be used as a proposal function for the following chain. It was found a sequential proposal chain of 20,000 steps with 5000 steps as burn-in was sufficient to produce a reliable RMS matrix.

The second part of the analysis was to use the RMS matrix created by the first chain to obtain posterior distributions for each of the parameters. In this case, 40,000 steps were used in the chain with 100 burn-in steps. The final point of the sequential proposal chain was used as the initial point for the RMS chain so the length of the burn-in period could be reduced. An evaluation of the chain could be done using the criteria detailed in Section 6 and is shown in detail in Appendix E.

8.6.2 Minuit Fit

Parameter estimation based solely on a minuit fit was robust, as discussed in Chapter 6. However, it was possible to use a combination of MCMC methods and minuit to evaluate the moments. The values and error for the values of the moments from the RMS matrix MCMC were given as the mean and standard deviation of the moments in the chain respectively. It was the mode of the final distribution that is ideally given as the quoted value for the moment. This was found by running a minuit fit at the completion of the MCMC chain using the mean values in the chain as initial values for the minuit fitter, in other words, very close in parameter space to the likelihood maximum. The standard deviation of each moment could not be reliably evaluated using minuit so the uncertainty on the moment was taken as the standard deviation of the moment in the MCMC chain.

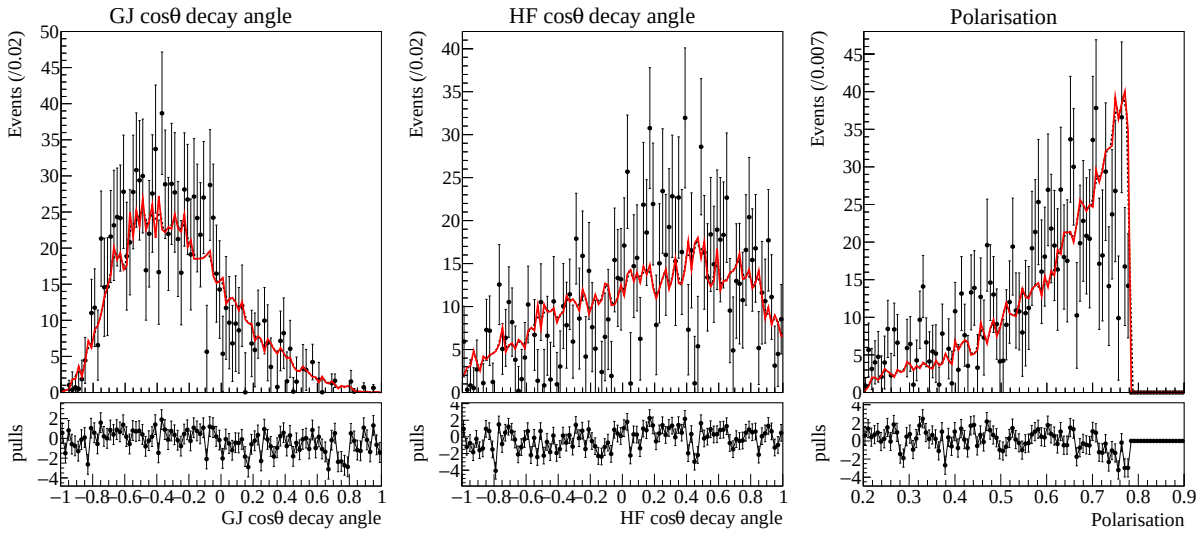

(a) $\cos\theta_{GJ}$ decay angle (b) $\cos\theta_{HF}$ decay angle (c) Polarisation

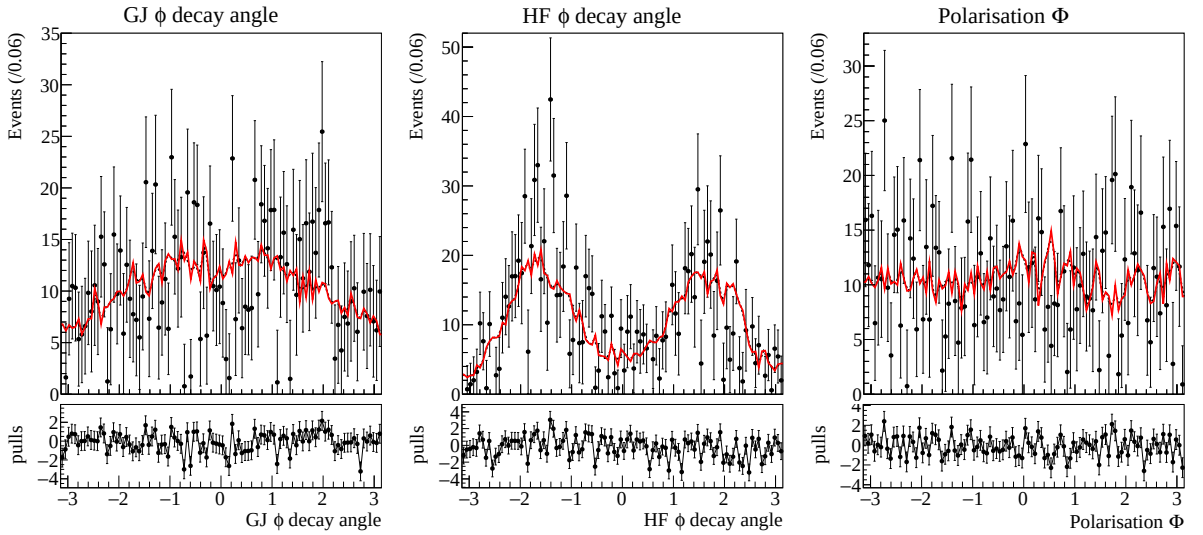

(d) ϕ_{GJ} decay angle (e) ϕ_{HF} decay angle (f) Polarisation Φ

Figure 8.3: Example plots showing the model fit function on the signal weighted data. Negative histogram values are possible as the sPlot method uses both positive and negative weights. In each example, the fit is plotted on the upper canvas with the pulls below.

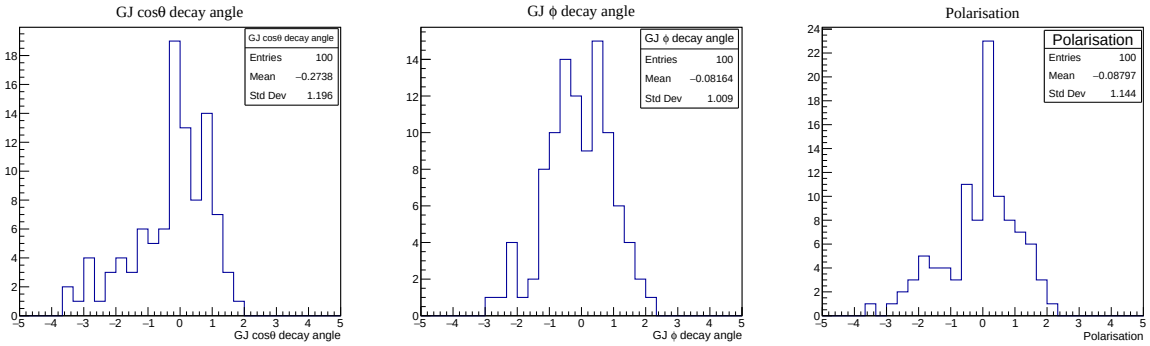

(a) $\cos\theta_{GJ}$ decay angle (b) $\cos\theta_{HF}$ decay angle (c) Polarisation

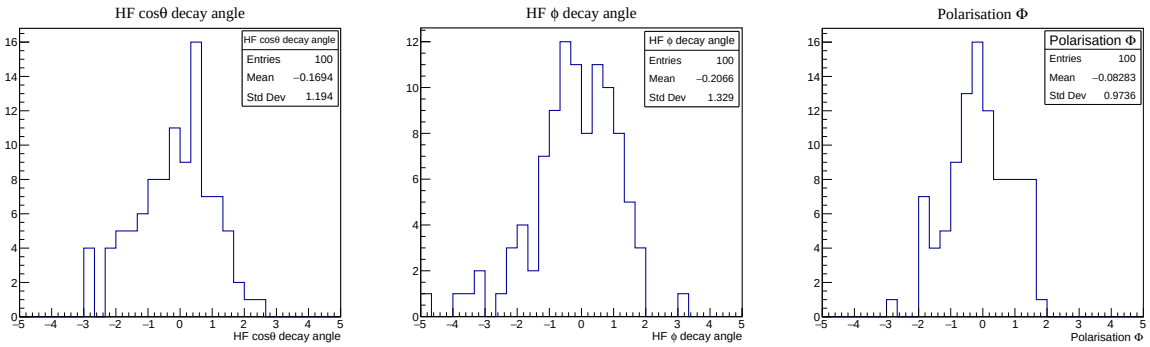

(d) ϕ_{GJ} decay angle (e) ϕ_{HF} decay angle (f) Polarisation Φ

Figure 8.4: Plots of the pulls from each of the fit variables from Figure 8.3 projected onto a single axis.

Chapter 9

Systematic Uncertainties: Part 1 - Background Subtraction

It was important in this analysis to reduce the uncertainties resulting from systematic effects as far as possible. To this end, each part of the analysis chain was checked in a systematic way in order to reduce uncertainties arising in this way. The most significant systematic uncertainties were the backgrounds. This section will focus on the sPlot procedure. Effects of varying the PID cuts given in Chapter 7 were tested and found to be negligible compared to the effects seen in the sPlot subtraction. Any effects that were induced in the PID cuts were corrected for by the sPlot subtraction.

9.1 Missing Mass sPlot

It was expected that the dominating systematic uncertainty in this analysis relating to background subtraction would arise from the sPlot. The shape of the signal was taken from the simulation (with the position and width able to be adjusted during the fit), however other factors such as the background shape and fit range will be discussed in this section.

The set of fit ranges and background orders used for these studies are detailed in Table 9.1. For these fits, the covariance matrix MCMC was used to do the sPlot. Each of these fits used a binning scheme that mirrored that used when analysing the data, that is, using eleven bins of $K^+K^-\pi^+$ invariant mass. For each sPlot fit, the 1.9 - 2.0 GeV mass bin is shown in Figure 9.1.

In some cases, it was clear that the model was not appropriate for the data. For example, fit A cannot model the background shape. For these reasons, this configuration was discarded. In other cases, the higher order terms in the background polynomial were consistent with zero, which was evidence for the fact that these higher order terms were not required in the fit function. This was the case in fit C, H and I. For this reason, these fit configurations were not used further. For some of the remaining fits, B, D, E and G, a subsequent fit of the $J = 2, \alpha = 0$ moments is shown in Figure 9.2. Results for the moments are self-consistent for fit configuration B, D and E.

	Order of polynomial background		
Fit range	First	Second	Third
0.6 - 1.3 GeV	A	B	C
0.7 - 1.2 GeV	D	E	F
0.75 - 1.1 GeV	G	H	I

Table 9.1: Table showing the fit label for each sPlot variation.

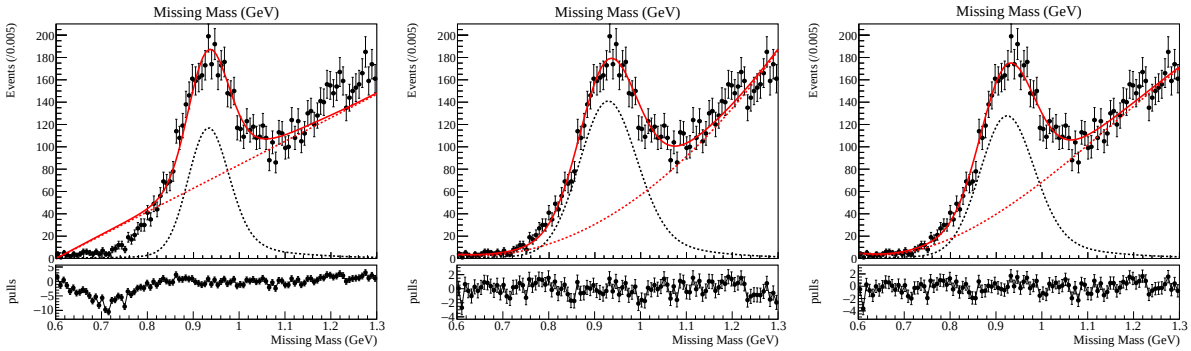

(a) fit A (b) fit B (c) fit C

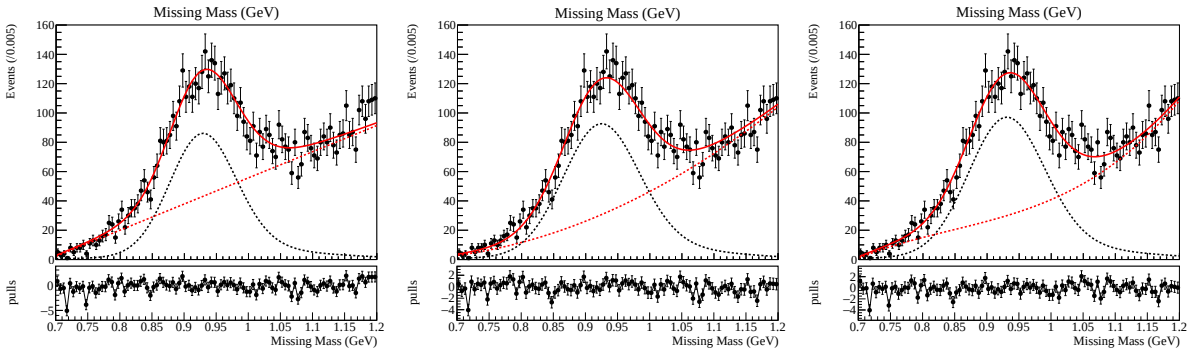

(d) fit D (e) fit E (f) fit F

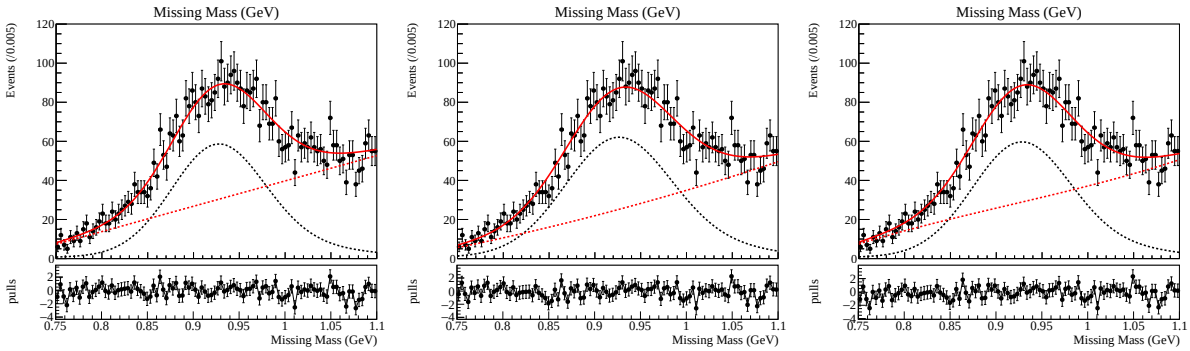

(g) fit G (h) fit H (i) fit I

Figure 9.1: Illustration of missing mass fit A - I for the 1.9 - 2.0 $K^+K^-\pi^+$ invariant mass bin.

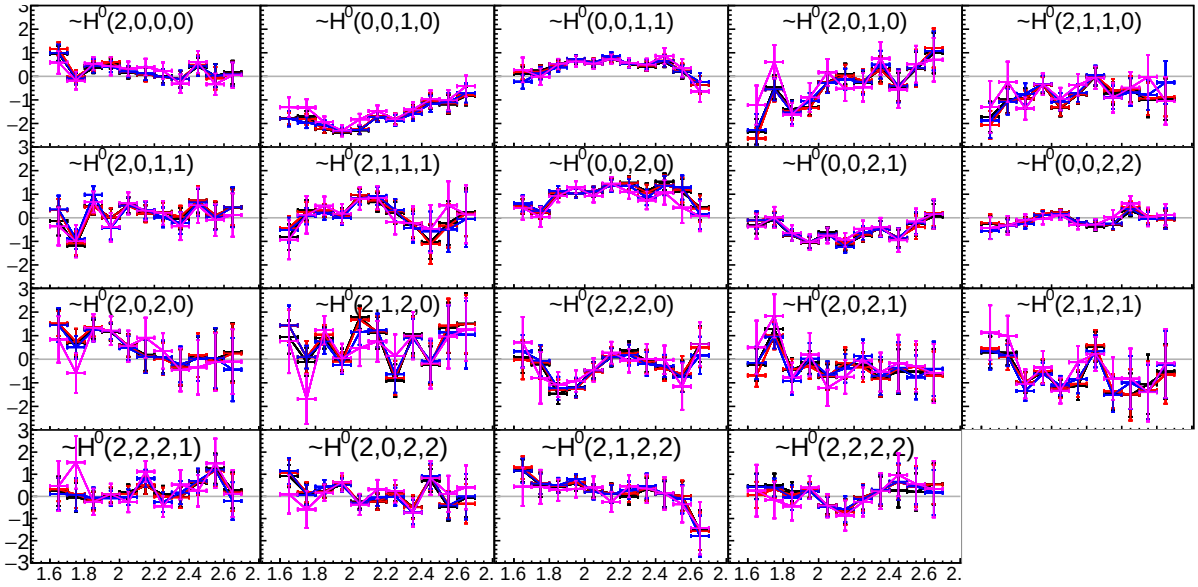

Figure 9.2: The moments results extracted for each of the missing mass sPlot configurations. fit B - black. fit D - red. fit E - blue. fit G - magenta.

Deviations from these other values are shown for fit G, the fit that was done on a narrower range. Increasing the sPlot range worked to reduce the statistical effects of the background subtraction as a greater number of events were included in the sPlot, however a narrower range would reduce the systematic effects that derive from modelling the background shape. Each of the fits B, D and E are consistent with each other and confirm that statistical uncertainties associated with these fits dominated any systematic effects arising from the missing mass sPlot.

For each of the fits that were done, the RMS uncertainty was calculated relative to fit E, the fit configuration that was used to extract the results shown in Chapter 11. A histogram showing the RMS uncertainty relative to fits B, C and G is shown in Figure 9.3. It was seen that fit G, that narrowed the width of the sPlot range, produced results that varied more significantly than fits B or C. The RMS values for each fit that differentiate between fits B/C and G are shown in Figure 9.4. There was an increase in the RMS uncertainty from fit G and this confirmed that the narrower fit range was the dominating systematic uncertainty involved from the missing mass sPlot. Further work in this area would look to model the sPlot background to mitigate its systematic effect on the moments results.

9.2 The K^* sPlot

The same study was done on the K^* sPlot by altering the background shape and width of the sPlot and investigating the results on the moments results. The K^* sPlot followed from the missing mass sPlot from fit E from Section 9.1. Four configurations of K^* sPlot were used as detailed in Table 9.2. Plots of the K^* sPlot for each configuration are shown in Figure 9.5.

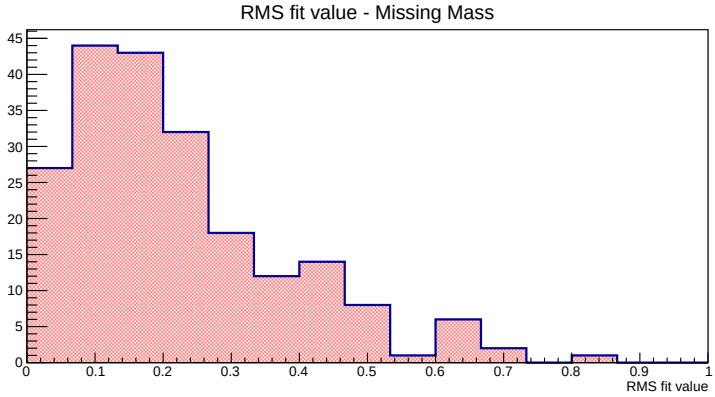

Figure 9.3: The RMS uncertainty from the Missing Mass sPlot.

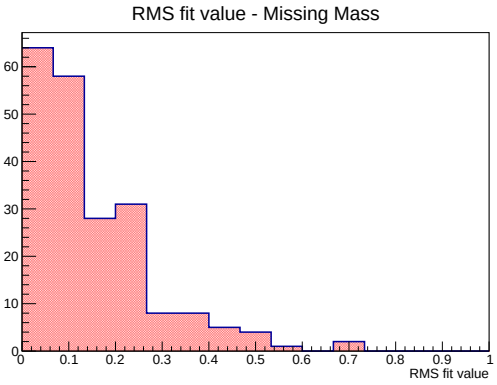

(a) The RMS uncertainty from fits B/C.

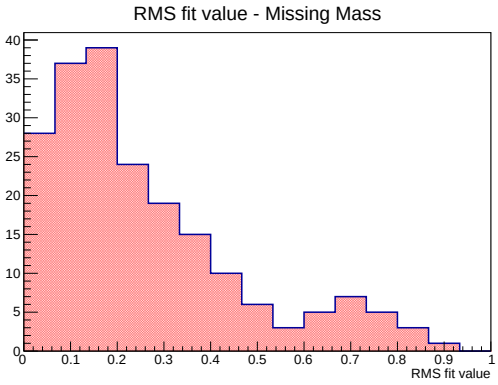

(b) The RMS uncertainty from fit G.

Figure 9.4: The RMS uncertainty differentiating between fits B/C and G.

	Order of polynomial background	
Fit range	First	Second
0.7 - 1.3 GeV	K	L
0.75 - 1.15 GeV	M	N

Table 9.2: Table showing the fit label for each K^* sPlot variation.

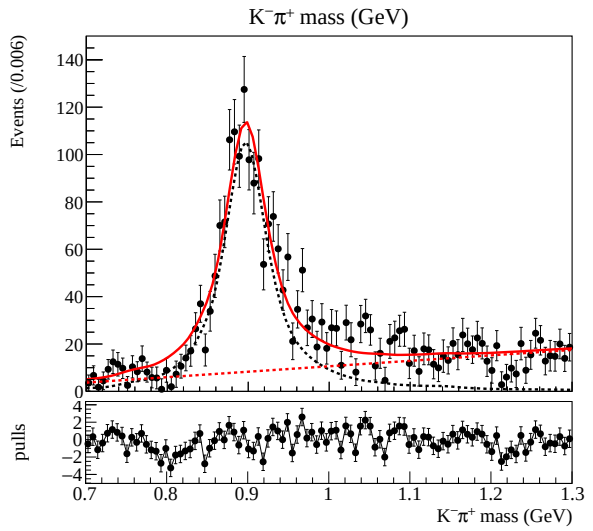

(a) fit K

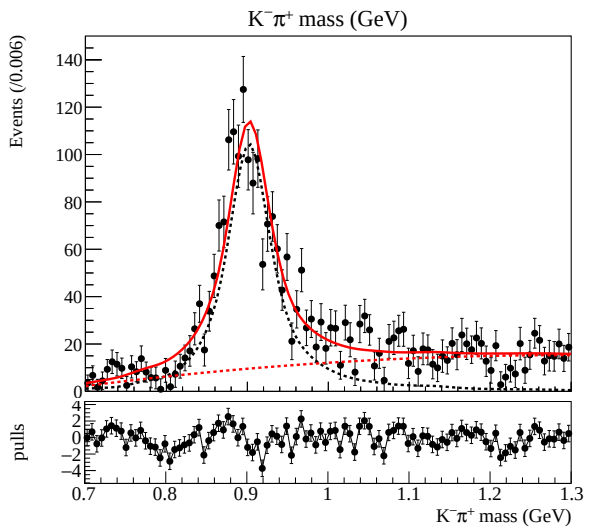

(b) fit L

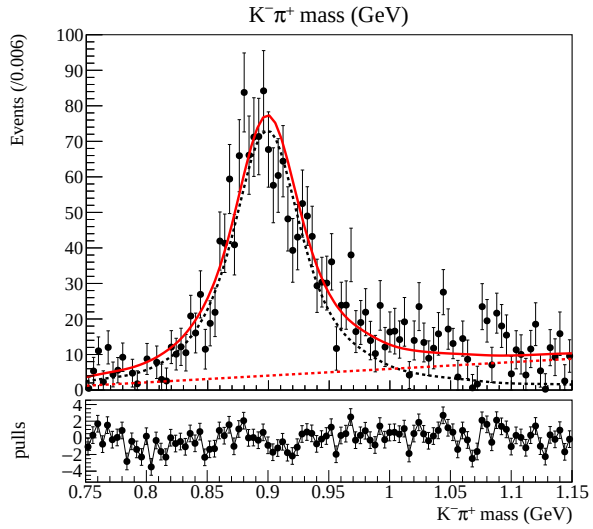

(c) fit M

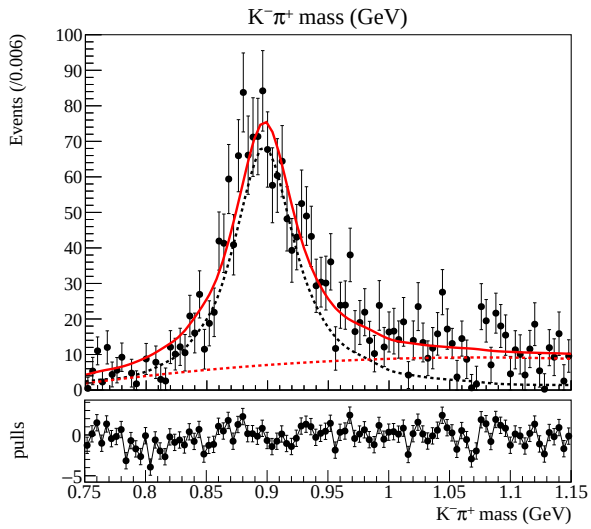

(d) fit N

Figure 9.5: Illustration for the K^* fit K - N for the 1.9 - 2.0 GeV $K^+K^-\pi^+$ invariant mass bin.

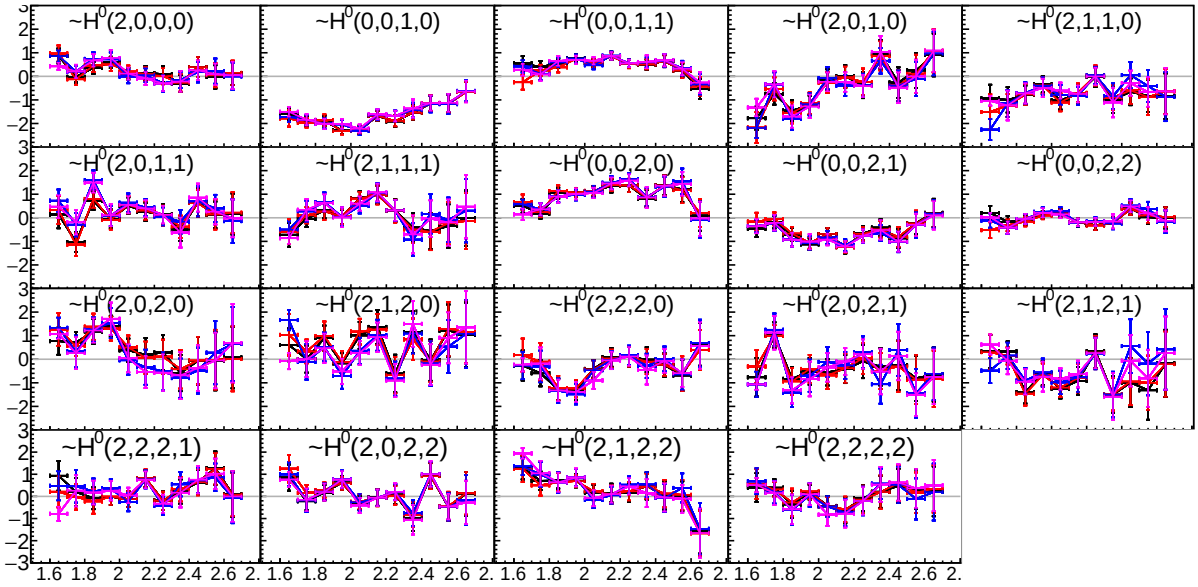

Figure 9.6: The moments results extracted for each of the K^* sPlot configurations. fit K - black. fit L - red. fit M - blue. fit N - magenta.

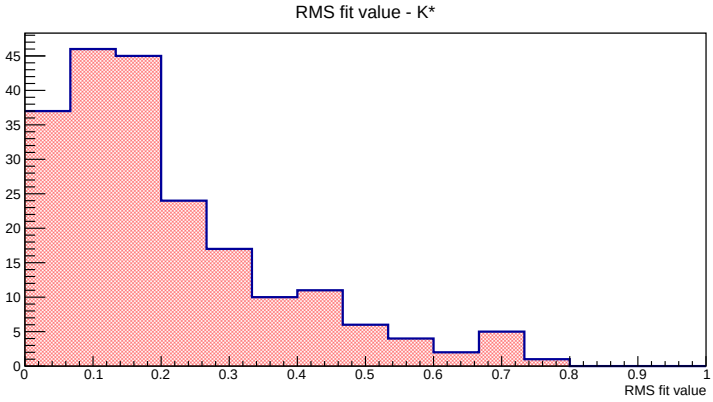

Figure 9.7: The RMS uncertainty from the K^* sPlot.

For each K^* sPlot configuration, the moments results are shown in Figure 9.6. In each of these cases, results for the moments are consistent with each other given the associated statistical error. The conclusion from this section follows that of Section 9.1, any systematic effects arising from the K^* sPlot are negligible relative to the statistical effects arising from the data used in this analysis.

In a similar manner to the missing mass sPlot, the RMS uncertainty was calculated for each of the K^* sPlot fits relative to fit L that was used in Chapter 11 to derive final results. The histogram of RMS uncertainty values is shown in Figure 9.7. In the case of the K^* sPlot there was no dominating systematic uncertainty observed. Further systematic studies should follow when there is increased data availability and smaller statistical effects.

Chapter 10

Systematic Uncertainties: Part 2 - Reconstruction, Acceptance and Resolution Effects

This section documents a series of studies where data was generated with known moment values and fitted to see how close the results were to the true values, or 'toy studies'. These were used to validate the method of moments fitting and to investigate the effect of other background processes in the data, as well as the effect of detector acceptance and resolutions.

10.1 The Decay Distribution Moments Extraction

In principle, the moments of angular distribution were orthogonal to each other and therefore could be extracted independently of each other, either by fitting all moments at once or by extracting moments one at a time. In reality, detector acceptance means that this is not true in practice and so fitting procedures were first investigated using toy data.

The premise of fitting toy data was as follows. Using a dataset of 10,000 simulated events, sets of toy data were generated with known partial wave content. This was done via an accept/reject algorithm based on the intensity function in eqn 5.59 i.e. the same function used to fit the data. Detector acceptance was built into the model using simulated events for the $K^+K^-\pi^+$ system. The truth variables were used for this procedure rather than the reconstructed versions. Subsequent fitting of this data would be expected to return results that were consistent with the true values. Deviation from the true values would indicate a systematic bias in the fitting procedure. On the other hand, if the results were consistent with the generated values this would be a validation for the fit method that was used. The following sections detail the sets of studies that were performed.

10.1.1 Fitting Moments in Batches vs Fitting all moments together

It was observed during preliminary fitting that an instability was prominent when fitting waves differing only in their modelling of the $\cos\theta_{GJ}$ decay angle (for example, the $H^0(0,0,1,0)$ and $H^0(0,0,2,0)$ moments). Therefore in this study, the comparison was made between fitting moments in batches of distinct J against fitting all moments together. In this case, data was generated using $j = 0,1,2$ waves and therefore fitted using moments with $J \leq 4$. The strategy for fitting moments in batches was as follows:

1. Fit all moments with $J = 0,1,2$.
2. Fix the values of the moments extracted in step 1 and fit all moments with $J = 3$.
3. Fix the values of the moments extracted in steps 1 and 2 and fit all moments with $J = 4$.

This process could be extended further to include higher order moments in the fit if required. As shown in Appendix D, the data could not be suitably modelled using only $J = 1$ moments so for this reason the primary fit was done with all moments with $J = 0,1,2$. For $J_{max} = 2$ there are 53 moments, additionally there are 46 moments with $J = 3$ and 58 with $J = 4$. The results of this study are shown in Figures 10.1 and 10.2. Compared to fitting the moments in batches, there was increased instability in the results when all moments were fitted together. This is particularly evident in the $\alpha = 1$ polarised moments when comparing Figures 10.1b and 10.2b. The other noticeable effect was the bias associated with the $H^0(0,0,1,0)$ and $H^0(0,0,2,0)$ moments when fitting all moments in the same fit. This is observed as in Figure 10.2a as the fitted values are skewed to values less than the generated value. The same effect is not observed when the moments are fitted in batches of J. One explanation for this is the correlation in these moments that is induced by the acceptances.

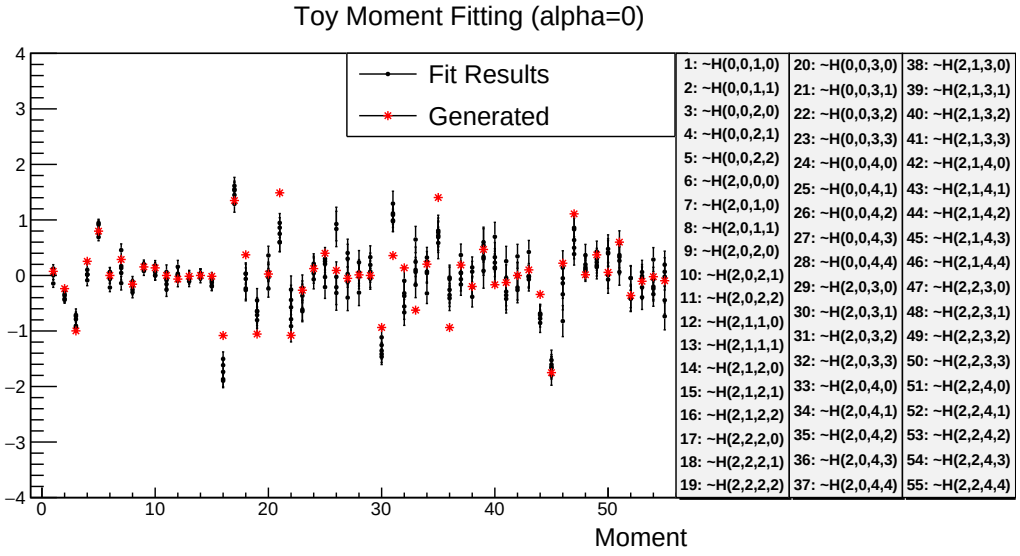

(a) $\alpha = 0$ moments

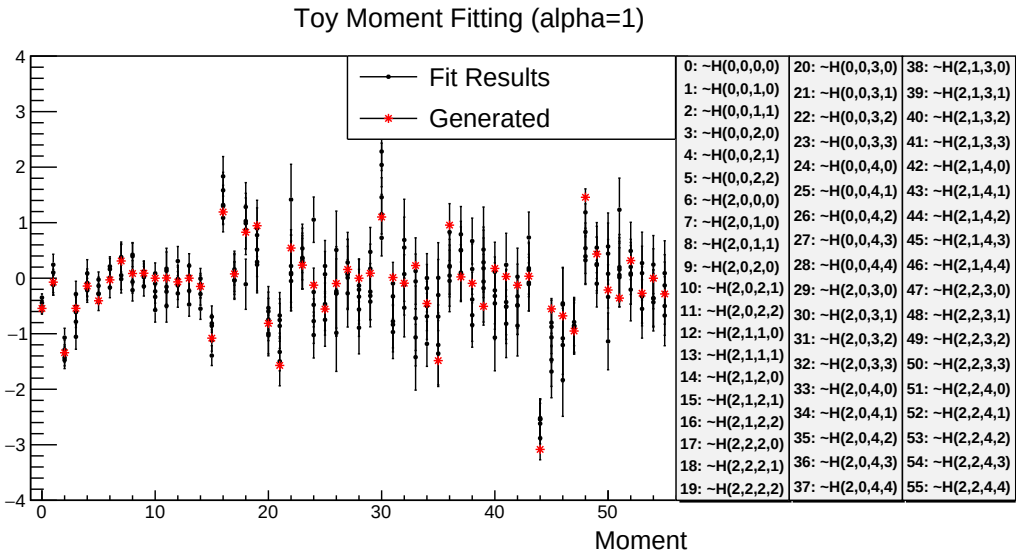

(b) $\alpha = 1$ moments

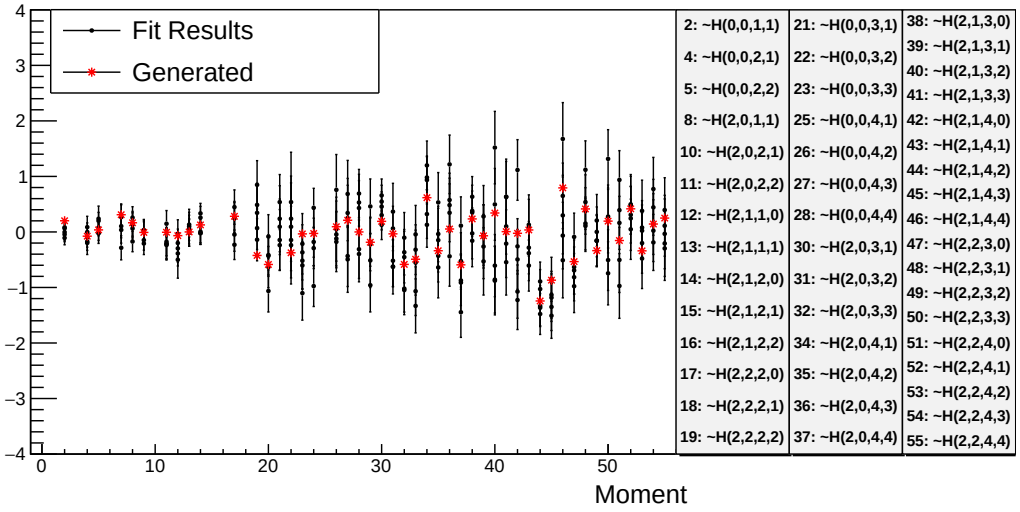

(c) $\alpha = 2$ moments

Figure 10.1: Moments extracted in batches compared to generated values.

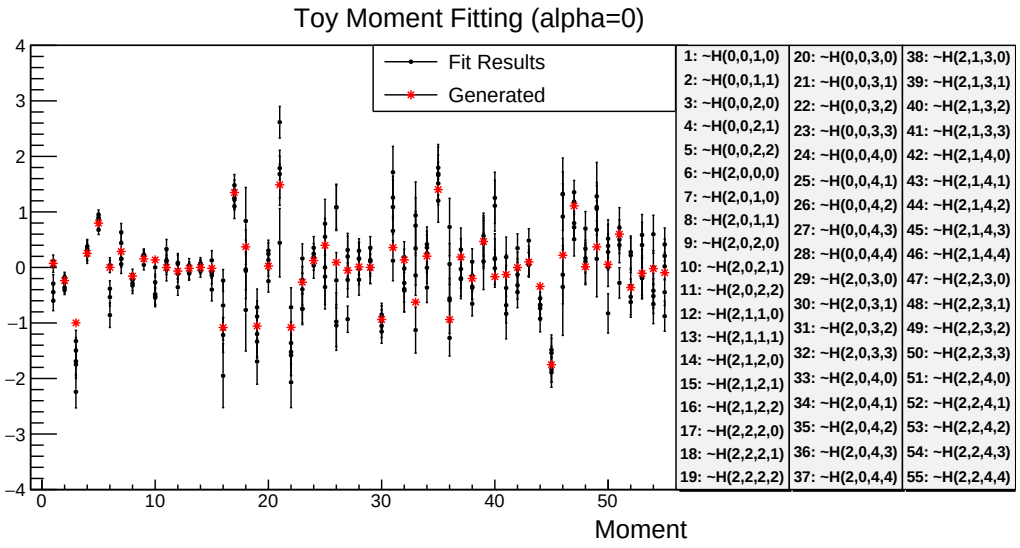

(a) $\alpha = 0$ moments

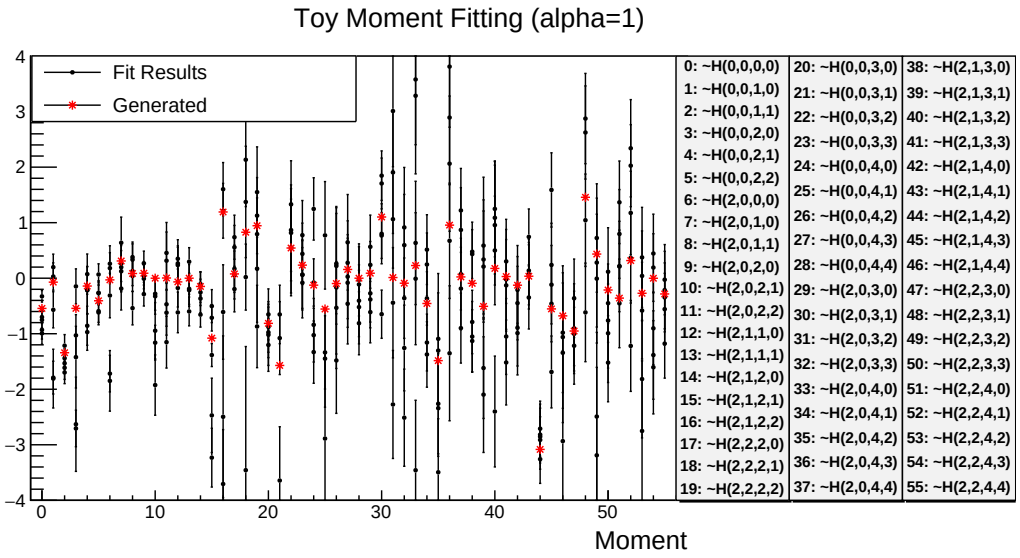

(b) $\alpha = 1$ moments

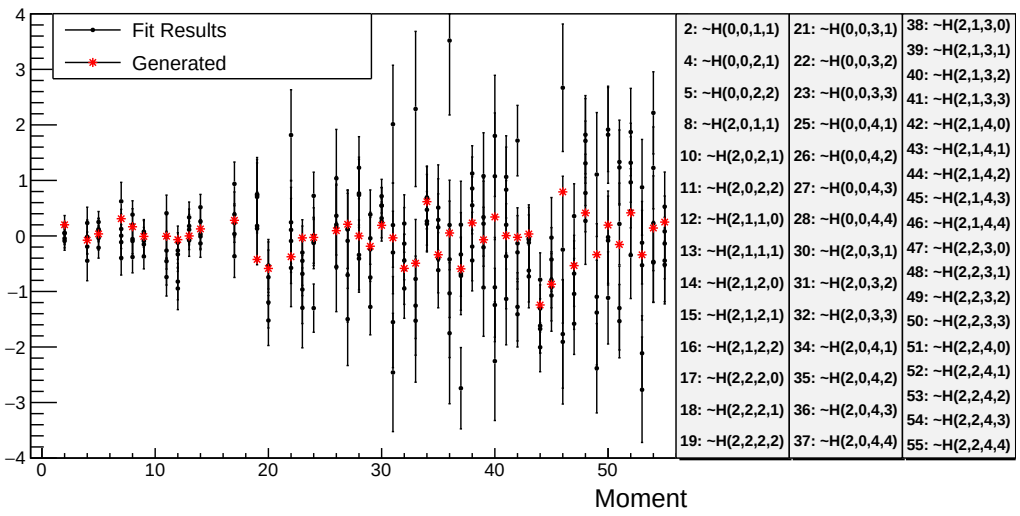

(c) $\alpha = 2$ moments

Figure 10.2: Moments extracted in a single fit compared to generated values.

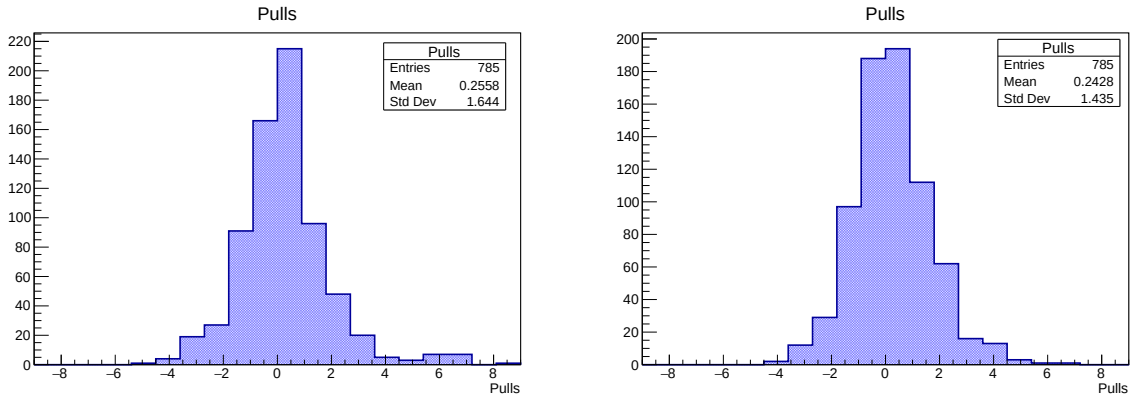

(a) Pulls from a fit done in batches of J.

(b) Pulls from a single fit.

Figure 10.3: Comparison of the pulls from the two different fit methods.

The comparison between the two methods can also be made when comparing the pull distributions of the two fits. These are shown in Figure 10.3. The pulls are defined as

$$P = \frac{H_{Tru} - H_{Fit}}{\sigma_{Fit}}, \tag{10.1}$$

where P is the pull value, H_{Tru} is the true value, H_{Fit} is the value from the fit and σ_{Fit} is the standard deviation from the fit result. In an optimised example, the pulls distribution would have mean, $\mu = 0$ and standard deviation, $\sigma = 0$. Both methods have a mean of ~ 0.25 and a standard deviation greater than 1, indicating that the errors associated with the fit are being underestimated in both cases. The higher value of the standard deviation when fitting moments in batches can be attributed to the fact that fitting with fewer parameters will lead to less of an uncertainty in the fitted values. It may also be the case that an iterative fitting process would be more appropriate when fitting these moments. For example, once the highest order moments in the fit have been calculated, begin the process again with the fixed moments taking the values from the previous fit. Work on this area of the fitting process is ongoing. It was seen that there were unphysical values found for moments when fitting all moments in a single fit with real data. This was attributed to acceptance effects in the final fit. For this reason, final results were extracted using moments fit in batches of J as the same unphysical effects were not observed using this method.

10.1.2 Fitting Polarised Moments

In addition to fitting moments in sets of J, it was also possible to fit unpolarised and polarised moments with the same strategy. In other words, fitting only the unpolarised $J = 0, 1, 2$ moments, then followed by fixing these values and fitting the polarised components of these moments. Plots showing the results of fitting via this strategy compared to fitting all polarisation components together are shown in Figure 10.4. There was no significant improvement in the

fits by fitting the unpolarised and polarised moments independently. It was concluded that the unpolarised and polarised moments could be evaluated in the same fit without introducing any additional systematic bias to the results.

10.1.3 Fitting Moments with Prefactors

The toy data in all of these studies was generated as described by eqn (5.59). In the fitting process this same fit function could be used to fit the data, however it was also possible to fit the moments excluding the $\left(\frac{2J+1}{4\pi}\right)\left(\frac{2S+1}{4\pi}\right)$ factors. By removing these factors, moments can be visualised on a scale comparable to each other (as the values of higher order moments are not suppressed by their prefactors). One study that was done was to check that fitting with or without the $\left(\frac{2J+1}{4\pi}\right)\left(\frac{2S+1}{4\pi}\right)$ factors did not introduce any bias into the final results once the scale factors had been reapplied. The results of fitting with the prefactors included vs fitting with the prefactors omitted and scaling the fit result by $\left(\frac{2J+1}{4\pi}\right)\left(\frac{2S+1}{4\pi}\right)$ is shown in Figure 10.5. As shown, there is no effect on the final results from using either method.

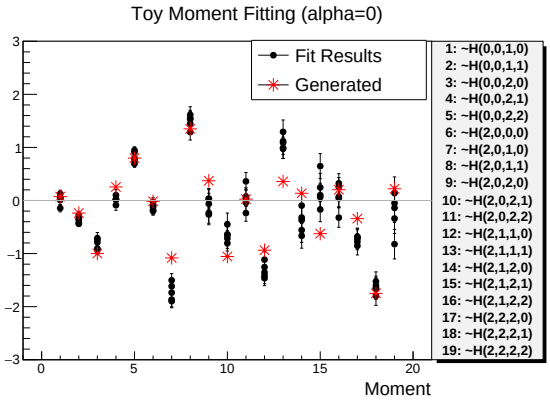

(a) Fitting polarised components together.

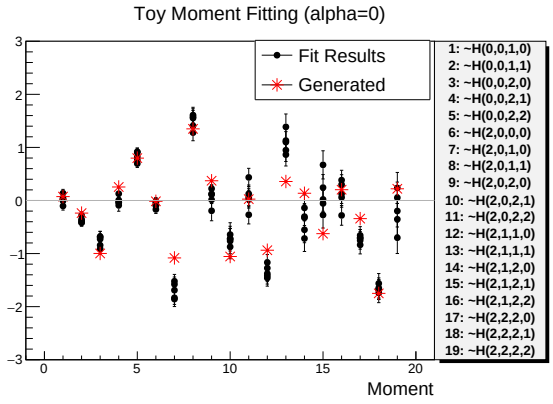

(b) Fitting polarised components separately.

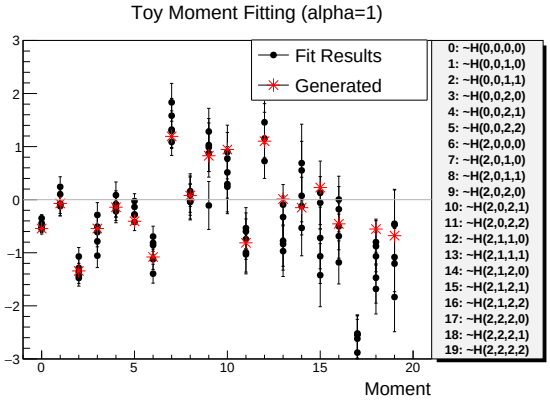

(c) Fitting polarised components together.

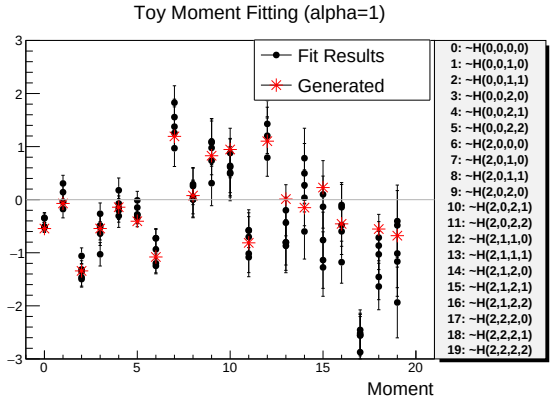

(d) Fitting polarised components separately.

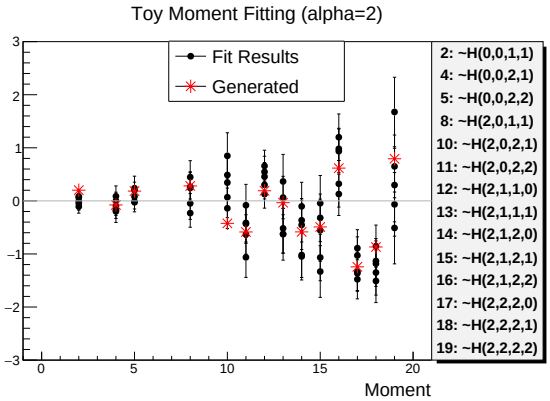

(e) Fitting polarised components together.

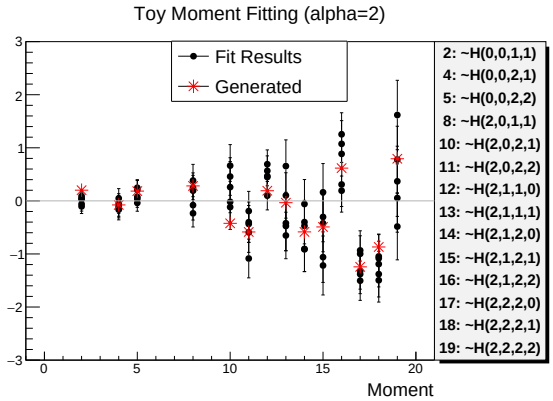

(f) Fitting polarised components separately.

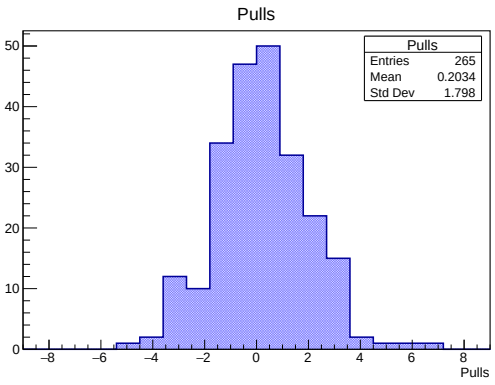

(g) Fitting polarised components together.

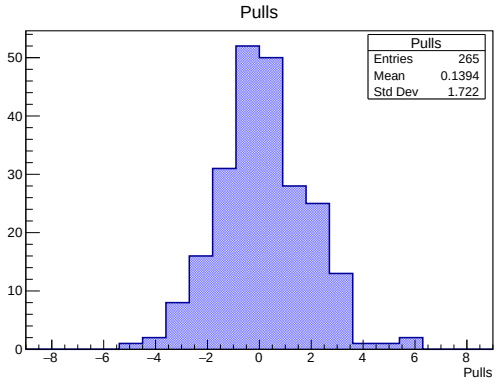

(h) Fitting polarised components separately.

Figure 10.4: Results from fitting unpolarised and polarised moments together in a single fit (left) vs fitting the polarised components separately (right).

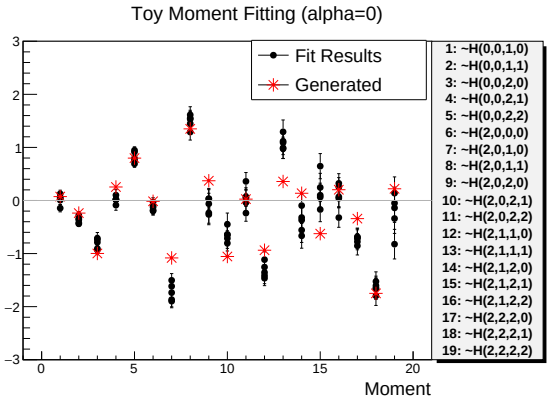

(a) Fitting moments with prefactors.

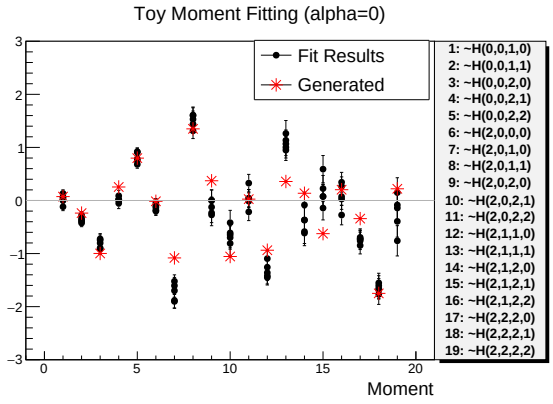

(b) Fitting moments without prefactors.

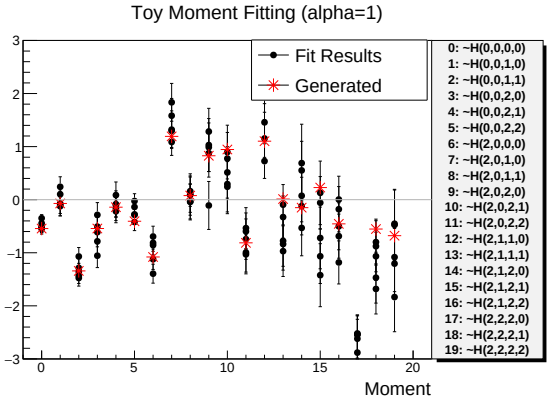

(c) Fitting moments with prefactors.

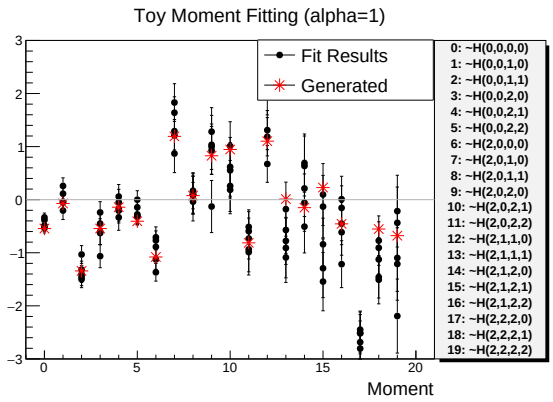

(d) Fitting moments without prefactors.

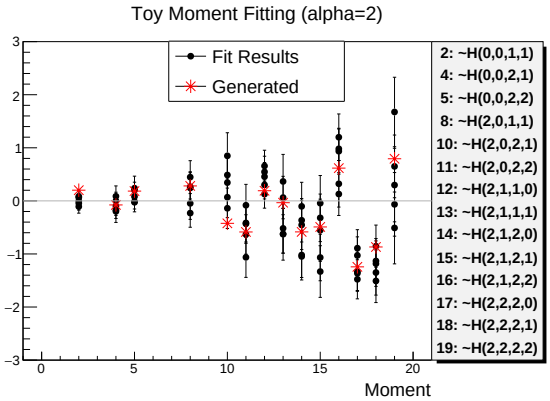

(e) Fitting moments with prefactors.

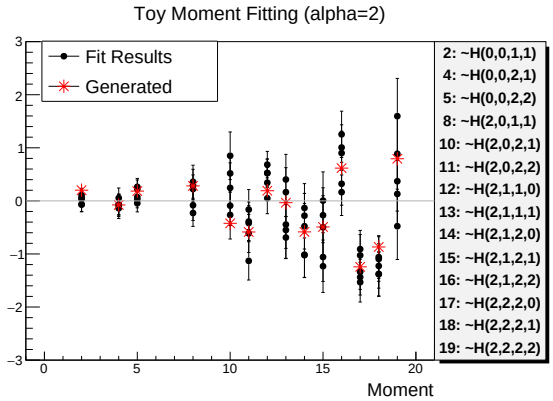

(f) Fitting moments without prefactors.

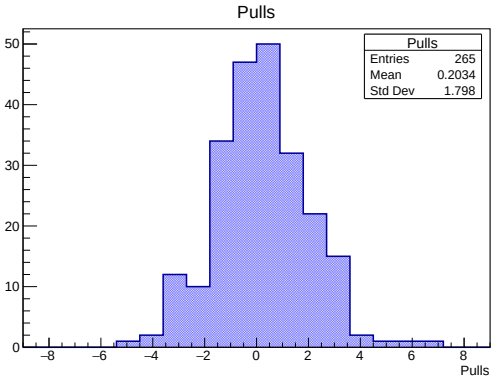

(g) Fitting moments with prefactors.

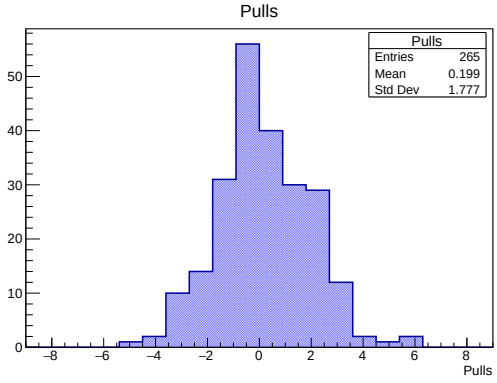

(h) Fitting moments without prefactors.

Figure 10.5: A comparison of fitting moments with the $\left(\frac{2J+1}{4\pi}\right)\left(\frac{2S+1}{4\pi}\right)$ factors included (left) vs omitting the factors during the fit and scaling the results by $\left(\frac{2J+1}{4\pi}\right)\left(\frac{2S+1}{4\pi}\right)$ (right).

10.2 Background studies

The practice of generating and fitting toy data was also used here to estimate the contribution from background processes in real data. Toy data for both the K^* and hyperon production processes ($H \to K^+ + n$ and $H \to K^* + n$) was simulated, see Section 7.4.3. This was fit in two cases as described below:

- Using only generated background events as the data sample.
- Using a fraction of background events included with toy data events.

Only background studies using $H \to K^+ + n$ events were used as it was assumed that events producing $H \to K^* + n$ were negligible when analysing the data.

10.2.1 Fitting only background events

As noted above, background events were generated using gemc. This event sample was split into three sets, each containing around 3000 events. The results of fitting each of these three sets of background toy data is shown in Figure 10.6. As the generator for the background effects was unpolarised only the $\alpha = 0$ moments are shown. Fitting on data from hyperon production caused a number of moments to have non-zero values - but no 'unphysical' behaviour of any moments was observed in any of the moments.

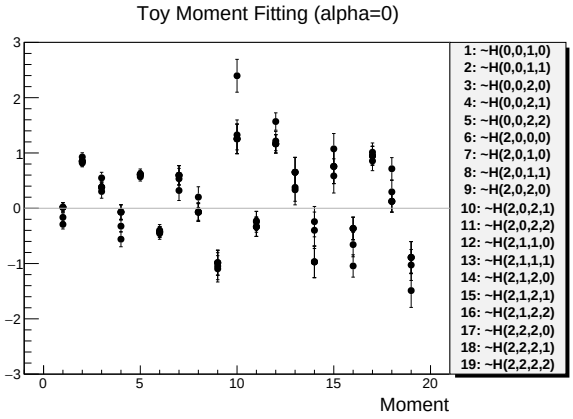

Figure 10.6: Fitting simulated background events ($\alpha = 0$ moments).

10.2.2 Including background events in the toy data sample

In addition to fitting only background events, there was a study done in which samples of background data were added to toy meson production data. This was carried out such that the final result sample was 70% meson production data (with known wave content) and 30% background data. The results of these fits are shown in Figure 10.7a. Fit results would be expected to tend

to the generated values as the background data percentage tended to zero. Including the background data in the event sample had the effect of biasing the values of the moments towards the values shown in Figure 10.6 by some degree. The degree to which results were biased was consistent with the percentage of background data that was added, for example, the absolute value of the moment was reduced by a factor of 30% when 30% of the event sample was background data in this case. To demonstrate this effect, the ratio:

$$R = \frac{(val_{toy+BG} - val_{toy})}{(val_{BG} - val_{toy})} \tag{10.2}$$

was calculated for each moment, where val_{toy+BG} is the value of each moment for the 30% background toy fit, val_{BG} is that of fitting the background only and val_{toy} that of fitting only the toy data. These results are shown as a histogram in Figure 10.7b. If the background events had no effect on the results then it would be expected that $val_{toy+BG} = val_{toy}$ and the histogram would have been centred on 0. A greater deviation from 0 for the histogram mean indicates a greater effect from the presence of the background in the combined fit. In reality, this histogram is has a mean close to 0.3 and this is consistent with the hypothesis that a data sample that includes 30% background events will result in a 30% systematic shift from the true value resulting from the background events. From Section 7.5.4, there was no significant contribution from background processes observed in the data, therefore from this study it can be assumed the results of the moments were not strongly affected by contributions from background processes. Further study is possible into the presence of background in the data. This involves incorporating a model for other background processes in the intensity function and work is ongoing in this regard.

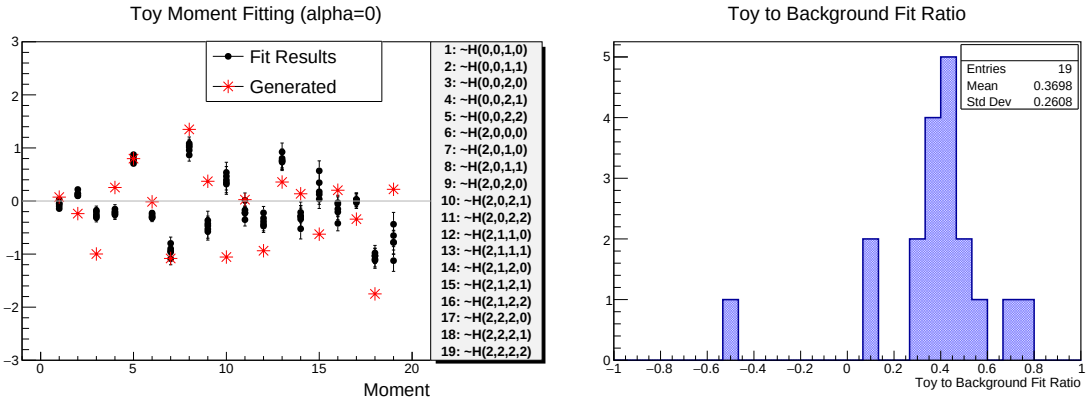

(a) Fitting toy data with 30% background events.

(b) The relative shift of the fit results.

Figure 10.7: Introducing background events to the toy fit.

10.3 Systematics Summary

It was noted from Chapter 7 that the main source of systematic error arose from the modelling of the sPlot. Figures 9.2 and 9.6 showed the effect of a systematic change to the sPlot model shape on the $J = 2, \alpha = 0$ moments for four different sPlot configurations for the missing mass and K^* sPlot respectively. In each of the moments shown, the statistical error (shown from the error bars) dominates any systematic effect (shown from the different colour moments). Using this dataset it can be concluded that any systematic error is completely dominated by the statistical errors. Further analysis of systematic effects could be performed using the pass-2 data that is to come.

Increased statistics should provide further ground on which to study the fitting procedure in more detail. It was suspected that acceptance effects were still present in the fitting method to some degree, with these effects mitigated as far as possible as shown in this Chapter. Improvements in the data would reduce statistical effects and allow fitting procedure systematics to be better understood, as well as possible improvements to the fitting algorithm.

Chapter 11

Moments of Decay Angle Distributions: Results

This Chapter presents results for the moments of decay angle distributions that were discussed in Chapter 8

11.1 Final Results

Presented are results for each measured moment of angular distribution using the fitting procedure described above, shown in Figure 11.1. The moments denoted $\sim H$ have the $\left(\frac{2J+1}{4\pi}\right)\left(\frac{2S+1}{4\pi}\right)$ terms removed and therefore allow moments to be visualised on the same relative scale. In Appendix F there are further visualisations of the results including the normalised moments H and moments from the MCMC chain mean values.

11.2 Results Discussion

Some of the phenomena that would be expected in these moments can be seen from the plots. For example, the $H(0,0,6,5)$ moments are exclusively determined by the interference terms of waves with spin projection $m = \pm 2$ and $m = \pm 3$, while the $H(0,0,6,6)$ moment is determined only by waves with $m = \pm 3$. It would be expected that contributions from waves with higher order spin projections would be suppressed relative to those with lower order spin projections. The results from the data are consistent with this hypothesis as the $H(0,0,6,5)$ and $H(0,0,6,6)$ moments are largely consistent with zero across the invariant mass range.

Moments that allow contributions from waves with lower order spin do show some behaviour that would be consistent with that produced from resonance decays. Values of the moments changing sign, such as in $H(0,0,4,0)$, and of peak-like structures in the moments, such as in $H(0,0,6,0)$, are both indicative of resonance behaviour. In the case of the $H(0,0,6,0)$ moment, contributions will come only from resonant states with $j = 3$. The PDG gives a number of states

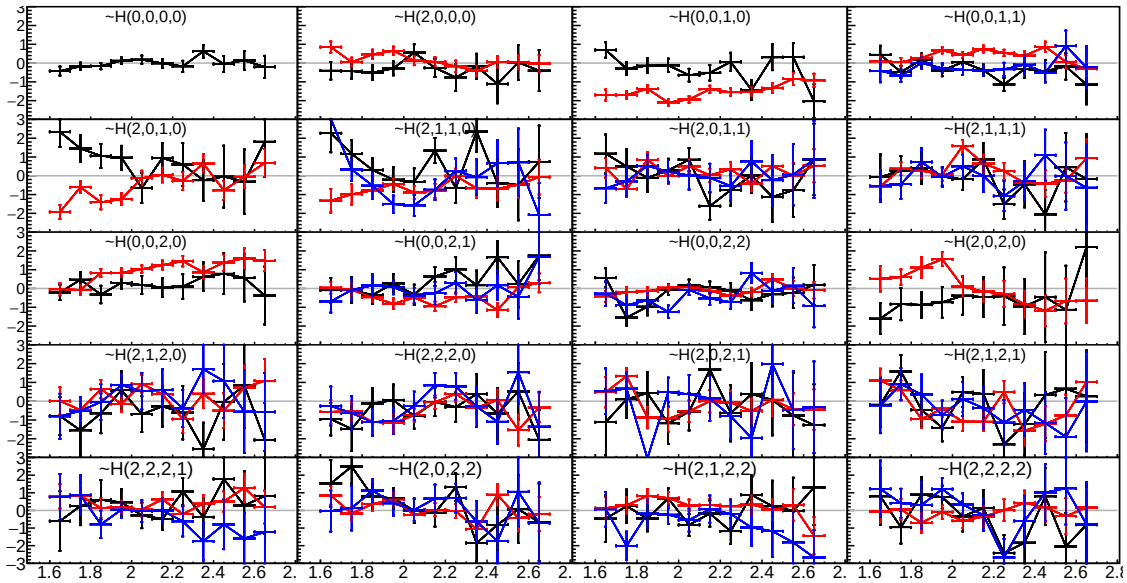

(a) $J = 2$ moments with $\alpha = 0$ - red, $\alpha = 1$ - black and $\alpha = 2$ - blue.

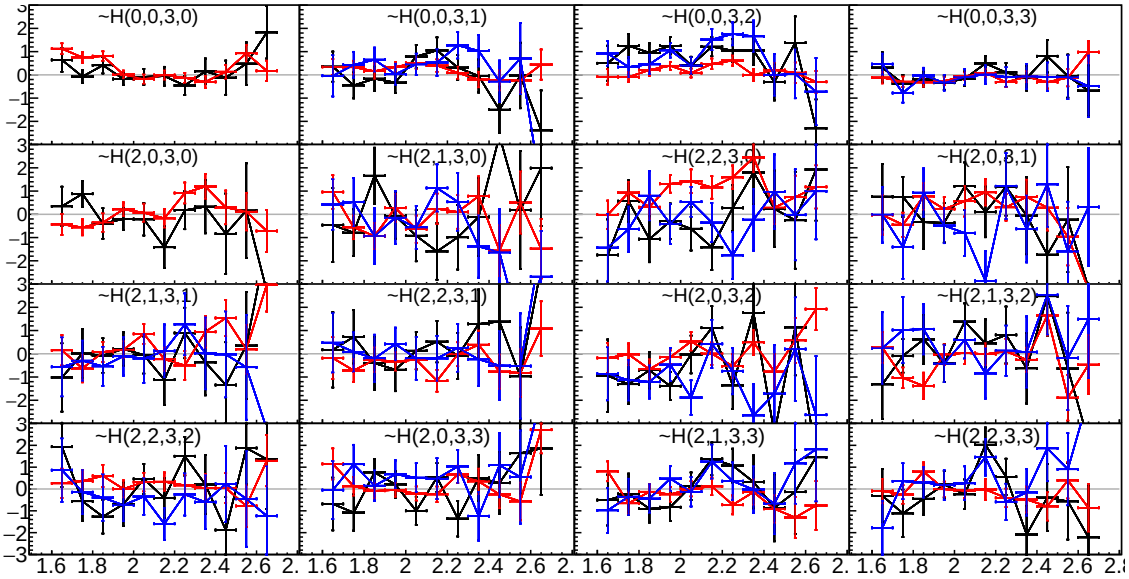

(b) $J = 3$ moments with $\alpha = 0$ - red, $\alpha = 1$ - black and $\alpha = 2$ - blue.

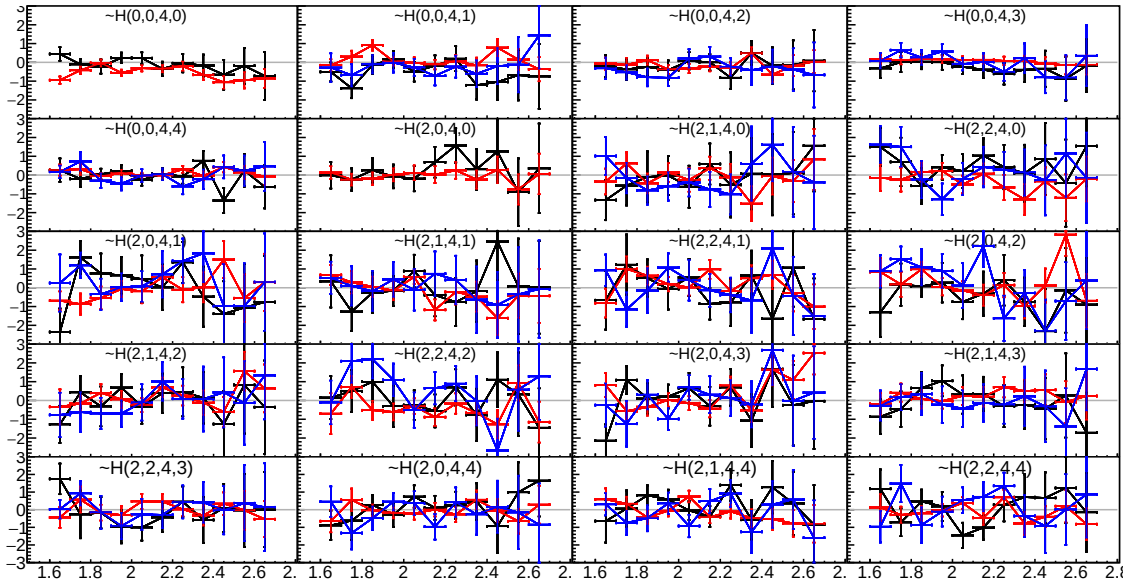

(c) $J = 4$ moments with $\alpha = 0$ - red, $\alpha = 1$ - black and $\alpha = 2$ - blue.

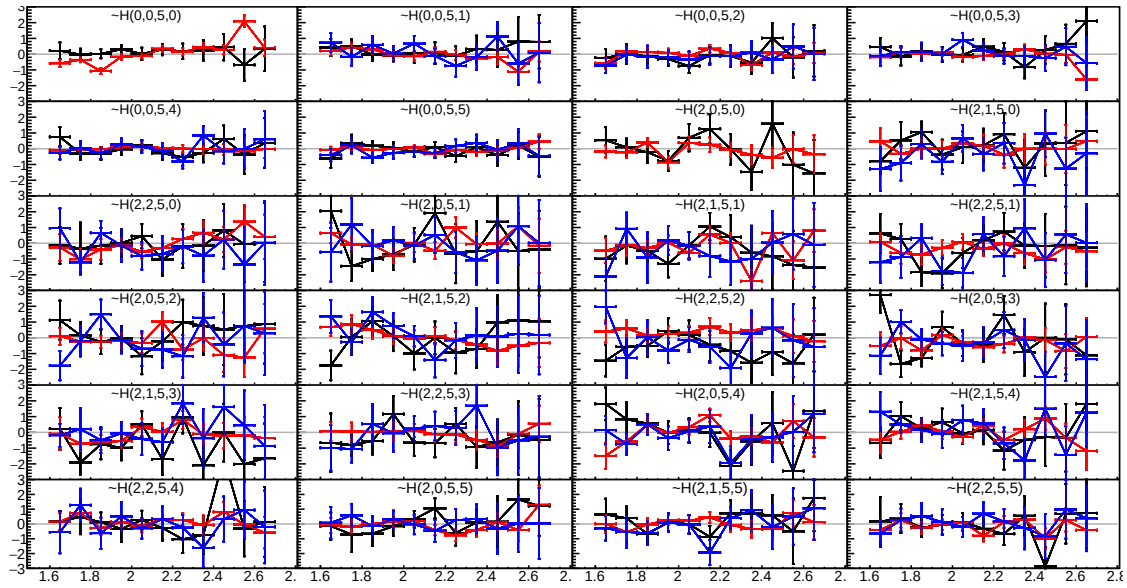

(d) $J = 5$ moments with $\alpha = 0$ - red, $\alpha = 1$ - black and $\alpha = 2$ - blue.

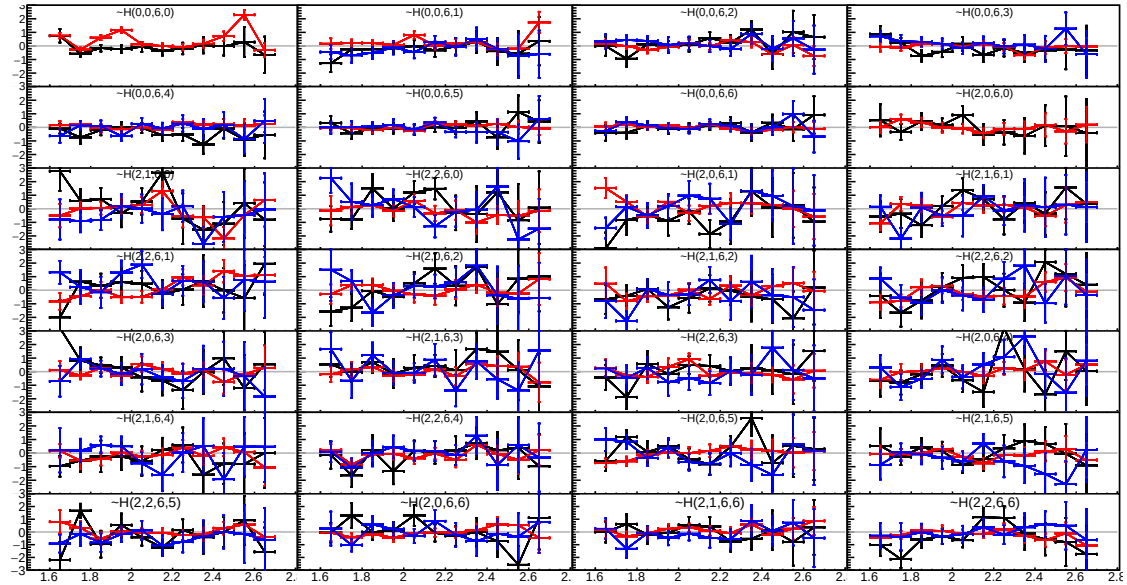

(e) $J = 6$ moments with $\alpha = 0$ - red, $\alpha = 1$ - black and $\alpha = 2$ - blue.

Figure 11.1: Results from fitting the moments of angular distribution. Polarisation components are shown with $\alpha = 0$ - red, $\alpha = 1$ - black and $\alpha = 2$ - blue.

with $j = 3$ in the $1.6 - 2.0$ GeV mass range that decay to K^*K^+: $\omega_3(1670), \rho_3(1690), \phi_3(1850)$ and $\rho_3(1990)$ [81]. The results shown in Figure 11.1e could be used to show the presence of these resonance decays in the data.

These moments results could be used in further analyses to establish evidence for mesonic states. From Section 5.14 it was shown that results for waves could, in theory, be unambiguously extracted from the moments results. This would require a matrix-like inversion of the set of variables (wave parameters) and constraints (moments results). Work to this effect is ongoing in this and in other analyses. However, it would not be explicitly necessary to extract wave amplitudes

from the moments before resonant behaviour in the data could be determined. In collaboration with our theory colleagues, mass-dependent fits could be done directly to the moments. The details of this are however beyond the scope of this analysis.

The primary aim of this experiment was to probe the existence of the 1^{-+} hybrid state. In regards to the results presented here, no conclusive evidence can as yet be put forward. However, it is known what moments can take contributions from the exotic state. Magnitude terms for the 1^{-+} can appear only in moments with $J = 0,1,2$ and $M = 0,2$. Interference terms including exotic waves can appear in many moments, up to and including $J = 4$. For the reason that there are so many SDMEs contained in each moment it is not possible to conclusively claim the existence of any states (particularly exotics) simply by inspecting moments values. Stronger evidence for the appearance of particular resonance states will be gained from mass-dependent fits to the moments. The results shown here however show promise that interesting results will be found in such analyses and provide motivation for the continuation of this work. With the full RG-A dataset and upgraded CLAS12 reconstruction at least an order of magnitude more events are expected.

Chapter 12

Conclusion

This thesis presented a model for the production of a vector-pseudoscalar final state from a linearly polarised photon, developed the tools to extract the moments of angular distribution from data and put forward preliminary results for these moments.

This analysis would greatly benefit from the soon to be released pass-2 data from the CLAS Collaboration. The preliminary results presented in this document are based on a dataset that is expected to increase by an order of magnitude when the full dataset is available. Results shown in this thesis included a significant statistical uncertainty that would be expected to be reduced with the pass-2 cooking. This will also be improved with the inclusion of the Spring 2019 data in addition to the Fall 2018 that was used here. An increased dataset will also allow a deeper understanding to be gained into the systematic effects of the analysis procedure.

The overarching aim of this experiment was to probe the existence of exotic mesons at CLAS12. With this in mind, work remains in this analysis in collaboration with theory colleagues to perform mass dependent fits to examine the possibility of exotic behaviour in the data. In terms of fitting the moments, the strategy that was described in this analysis could be expanded in a number of ways. For example, it might be possible to begin by fitting moments in batches and once the highest order fits have been done, iteratively re-fit lower order moments with higher order values fixed. This is a direct extension of the method that was used and could result in more reliable values for the moments being found. Another fitting strategy that has been considered would be to perform an initial fit, to then remove moments from the set that are consistent with zero and then re-fit the moments that are expected to be non-zero. This may also improve the reliability of the results. Going forward, toy studies using each of the methods described above would be needed to assess the effectiveness of each. If found to be successful they could be implemented in the analysis framework. In addition to the moments, work has also begun on assessing the possibility of fitting waves directly to the data. In conjunction with the considerations that come with fitting the moments, fitting directly with waves comes with it's own unique set of concerns to keep in mind. The partial waves differ from the moments in that partial waves are not mutually orthogonal, and therefore cannot be fit individually in the way

that is possible with moments. The partial wave amplitudes are also limited in their parameter space to $[0,1]$. This can cause particular issues relating to waves that should be consistent with zero and their interference with non-zero terms. Sophisticated fitting techniques will be required in order to adequately deal with these problems. If it was possible to fit using both moments and partial waves this would make the identification of resonances in the data more powerful given the two self-independent methods of parameter extraction.

The application of the vector-pseudoscalar model that was developed here is not limited to the K^*K^+ final state. There were other final states produced in this data sample, such as the $\rho\pi$ and $\phi\pi$ final state, that are as yet unexplored. The motivation for the exploration of these data sets comes from the need for evidence from more than one decay channel to fully understand the production mechanism of possible exotic states.

Appendix A

Frames of Reference

The frames of reference that are described in the main body of the text are defined here. For the purpose of this definition, write $p_a^\mu, p_b^\mu, p_c^\mu, p_X^\mu, p_Y^\mu$ as the 4-momentum of the photon beam, proton target, recoil neutron, resonance X and isobar Y respectively. Any transformation between frames could be achieved using the Poincaré group, that is, using a combination of Lorentz boosts and translations in space.

A.1 The Lab Frame

The lab frame was defined by the relation

$$p_b^\mu = (m_b, 0, 0, 0). \tag{A.1}$$

In other words the target was at rest with $\underline{p}_b = 0$. The target was defined to be at the origin of the Cartesian system with the y-axis vertically upwards, the z-axis given by the beamline (pointing downstream) such that

$$p_a^\mu = (E_a, 0, 0, p_a^z) \tag{A.2}$$

and the x-axis making up the right-handed system.

A.2 The Gottfried-Jackson (GJ) frame

The Gottfried-Jackson frame could be described as being the frame in which the resonance X was at rest. The z-axis was once again defined by the downstream direction of the beam, the y-axis by the normal to the production plane and the x-axis completed the right-handed system. A normal to the production plane was given by, for example, $\hat{\underline{p}}_a \times \hat{\underline{p}}_X$.

Since in the GJ frame, the decay of the resonance was back-to-back so by construction, only one pair of (θ_{GJ}, ϕ_{GJ})-decay angles with respect to one of the decay particles were necessary to fully describe the reaction - the other pair of angles was simply an addition of π which illustrates

clearly the dependence that exists. It was not important what decay particle was used to calculate the angles used in the analysis, but it was critical to be consistent within the reaction framework.

A.3 The Helicity frame (HF)

Just as the GJ frame was described as being the frame in which the resonance was at rest, the helicity frame was said to be the frame in which the isobar was at rest. In this frame, the z- axis was defined to be in the direction of one of the decay products of the resonance decay (chosen consistently in this analysis to be the direction of the momentum of the isobar). The y-axis was defined by $\hat{y} = \hat{p}_Y^{GJ} \times \hat{p}_a$ and the x-axis produces a right-handed system. As with the GJ frame, the isobar decay could be fully characterised by two decay angles (θ_{HF}, ϕ_{HF}).

Appendix B

Proof of Realness of Intensity

To show that the intensity of eqn (5.59) is always real, consider a general term in the sum,

$$H(S,\Lambda,J,M)\,D^{J*}_{M,\Lambda}(\phi_{GJ},\theta_{GJ},0)D^{S*}_{\Lambda,0}(\phi_{HF},\theta_{HF},0), \tag{B.1}$$

where the $\left(\frac{2J+1}{4\pi}\right)\left(\frac{2S+1}{4\pi}\right)$ terms have been factored out as they are constant for given J,S. In the case where $M=0$ or $\Lambda=0$ the imaginary part of the Wigner D-function vanished as it contains the factor $\sin(M\phi)$ and the intensity term was purely real. Consider the instance where $M,\Lambda\neq 0$. Expanding the sum over $\pm M$ and $\pm\Lambda$ gives the following:

$$\begin{aligned}\mathscr{I}(S,\Lambda,J,M) = {} & H(JMS\Lambda)\,D^{J*}_{M,\Lambda}(\phi_{GJ},\theta_{GJ},0)D^{S*}_{\Lambda,0}(\phi_{HF},\theta_{HF},0)\\ & + H(S,-\Lambda,J,M)\,D^{J*}_{M,-\Lambda}(\phi_{GJ},\theta_{GJ},0)D^{S*}_{-\Lambda,0}(\phi_{HF},\theta_{HF},0)\\ & + H(S.-\Lambda,J,-M)\,D^{J*}_{-M,-\Lambda}(\phi_{GJ},\theta_{GJ},0)D^{S*}_{-\Lambda,0}(\phi_{HF},\theta_{HF},0)\\ & + H(S,\Lambda,J,-M)\,D^{J*}_{-M,\Lambda}(\phi_{GJ},\theta_{GJ},0)D^{S*}_{\Lambda,0}(\phi_{HF},\theta_{HF},0).\end{aligned} \tag{B.2}$$

Rewriting the Wigner D-functions in terms of complex exponentials and small d-functions and using the symmetry relations defined by [80]

$$d^{J}_{-M-\Lambda} = d^{J}_{M\Lambda}(-1)^{M-\Lambda} \tag{B.3}$$

and

$$H(S,-\Lambda,J,-M) = (-1)^{M}H(S,\Lambda,J,M) \tag{B.4}$$

gives

$$\begin{aligned}\mathscr{I}(S,\Lambda,J,M) = {} & H(S,\Lambda,J,M)\, e^{iM\phi_{GJ}} d^{J*}_{M,\Lambda}(\theta_{GJ}) e^{i\Lambda\phi_{HF}} d^{S*}_{\Lambda,0}(\theta_{HF}) \\ & + H(S,-\Lambda,J,M)\, e^{iM\phi_{GJ}} d^{J*}_{M,-\Lambda}(\theta_{GJ}) e^{-i\Lambda\phi_{HF}} d^{S*}_{-\Lambda,0}(\theta_{HF}) \\ & + H(S,\Lambda,J,M)\, e^{-iM\phi_{GJ}} d^{J*}_{M,\Lambda}(\theta_{GJ}) e^{-i\Lambda\phi_{HF}} d^{S*}_{\Lambda,0}(\theta_{HF}) \\ & + H(S,-\Lambda,J,M)\, e^{-iM\phi_{GJ}} d^{J*}_{M,-\Lambda}(\theta_{GJ}) e^{i\Lambda\phi_{HF}} d^{S*}_{-\Lambda,0}(\theta_{HF}). \quad \text{(B.5)}\end{aligned}$$

$$\begin{aligned}\implies \mathscr{I}(S,\Lambda,J,M) = {} & H(S,\Lambda,J,M)\, d^{J*}_{M,\Lambda}(\theta_{GJ}) d^{S*}_{\Lambda,0}(\theta_{HF}) [e^{iM\phi_{GJ}} e^{i\Lambda\phi_{HF}} + e^{-iM\phi_{GJ}} e^{-i\Lambda\phi_{HF}}] \\ & + H(S,-\Lambda,J,M)\, d^{J*}_{M,-\Lambda}(\theta_{GJ}) d^{S*}_{-\Lambda,0}(\theta_{HF}) [e^{iM\phi_{GJ}} e^{-i\Lambda\phi_{HF}} + e^{-iM\phi_{GJ}} e^{i\Lambda\phi_{HF}}] \quad \text{(B.6)}\end{aligned}$$

$$\begin{aligned}\implies \mathscr{I}(S,\Lambda,J,M) = {} & H(S,\Lambda,J,M)\, d^{J*}_{M,\Lambda}(\theta_{GJ}) d^{S*}_{\Lambda,0}(\theta_{HF}) [2\cos(M\phi_{GJ} + \Lambda\phi_{HF})] \\ & + H(S,-\Lambda,J,M)\, d^{J*}_{M,-\Lambda}(\theta_{GJ}) d^{S*}_{-\Lambda,0}(\theta_{HF}) [2\cos(M\phi_{GJ} - \Lambda\phi_{HF})]. \quad \text{(B.7)}\end{aligned}$$

Eqn (B.7) is now purely real. Expanding the square brackets and using the symmetry relations to write it in the original form gives:

$$\begin{aligned}\mathscr{I}(S,\Lambda,J,M) = {} & H(S,\Lambda,J,M)\, d^{J*}_{M,\Lambda}(\theta_{GJ}) d^{S*}_{\Lambda,0}(\theta_{HF}) \cos(M\phi_{GJ} + \Lambda\phi_{HF}) \\ & + H(S,-\Lambda,J,M)\, d^{J*}_{M,-\Lambda}(\theta_{GJ}) d^{S*}_{-\Lambda,0}(\theta_{HF}) \cos(M\phi_{GJ} - \Lambda\phi_{HF}) \\ & + H(S,-\Lambda,J,-M)\, d^{J*}_{-M,-\Lambda}(\theta_{GJ}) d^{S*}_{-\Lambda,0}(\theta_{HF}) \cos(M\phi_{GJ} + \Lambda\phi_{HF}) \\ & + H(S,\Lambda,J,-M)\, d^{J*}_{-M,\Lambda}(\theta_{GJ}) d^{S*}_{\Lambda,0}(\theta_{HF}) \cos(M\phi_{GJ} - \Lambda\phi_{HF}). \quad \text{(B.8)}\end{aligned}$$

From eqn (B.8), it was clear to see that the imaginary part of the terms in the intensity cancelled to zero when the sum is considered. It also showed that the correct intensity expansion was found simply by taking the $\cos(M\phi_{GJ} + \Lambda\phi_{HF})$ part of the exponential with the small d-function. This was for some given M, Λ but from induction arguments holds for all M, Λ.

Appendix C

The $\phi\pi$ decay channel

Since there was two decay channels in this dataset there will be a further two sets of decay angles. One in which the isobar is defined as a $Y = K^-\pi^+$ bound state and the X decay as $X \to Y + K^+$ and the other in which $Y = K^+ + K^-$ with $X \to Y + \pi^+$. The $Y = K^*$ decay channel was analysed in the main body of this thesis. The $Y = K^+ + K^-$ channel was not analysed in full, however plots of the relevant decay angles are shown in Figures C.1, C.2.

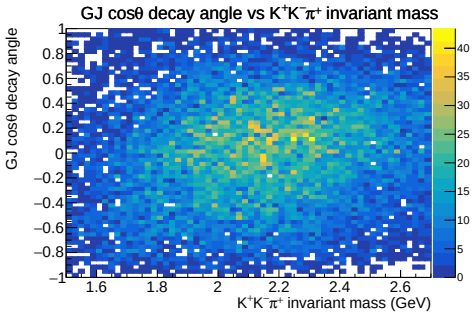

(a) GJ $\cos\theta$ decay angle

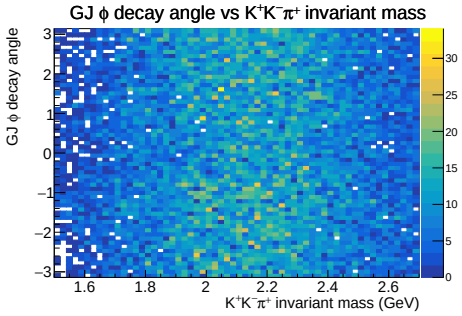

(b) GJ ϕ decay angle

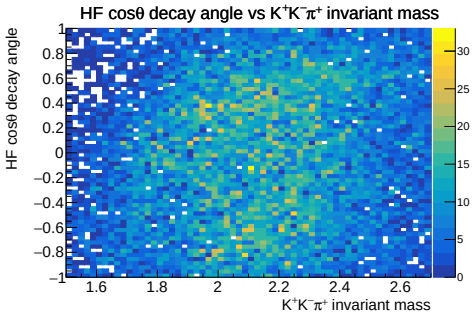

(c) HF $\cos\theta$ decay angle

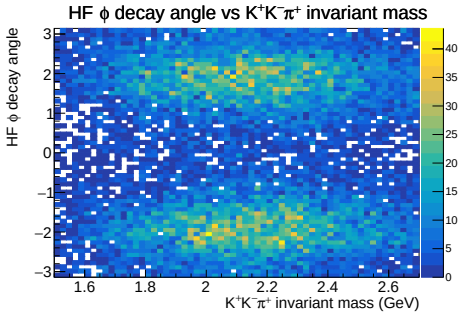

(d) HF ϕ decay angle

Figure C.1: Two-dimensional plots of the invariant mass of $K^+K^-\pi^+$ vs the four decay angles of $X \to Y + \pi^+, Y \to K^+ + K^-$.

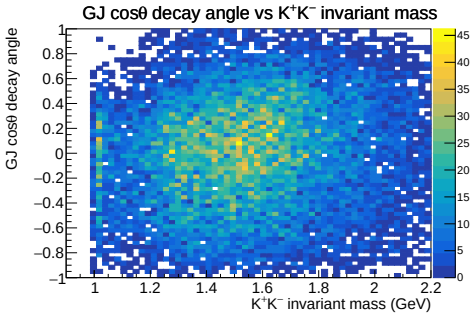

(a) GJ $\cos\theta$ decay angle

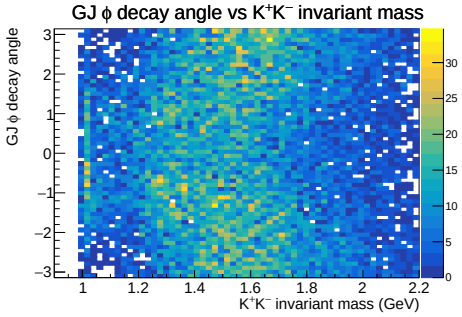

(b) GJ ϕ decay angle

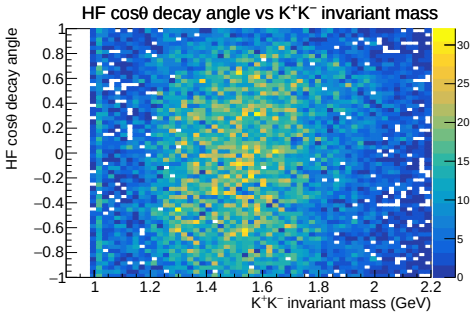

(c) HF $\cos\theta$ decay angle

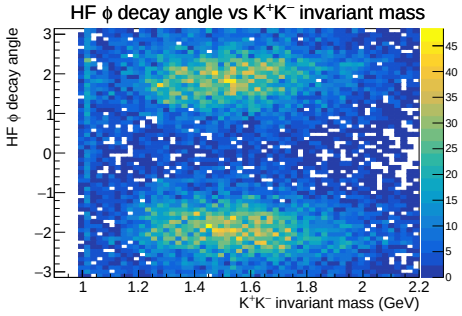

(d) HF ϕ decay angle

Figure C.2: Two-dimensional plots of the invariant mass of K^+K^- vs the four decay angles of $X \to Y + \pi^+, Y \to K^+ + K^-$.

Appendix D

Fitting $J = 1$ moments

The moments fits that were done in batches as described in Section 10.1.1 were done using subsequent fits of increasing J, with the first fit composing of all $J = 0, 1, 2$ moments. A parameter set consisting of only $J = 0, 1$ moments was not able to model adequately the data, as shown in Figure D.1. As expected, it is the fit parameters denoted GJ - relating to the decay of the resonance and dependent on J - that are not sufficiently modelled using only the $J = 0, 1$ moments. The solution to this was to use all $J = 0, 1, 2$ moments in the first batch fitting as this set of moments was able to model the data sufficiently well.

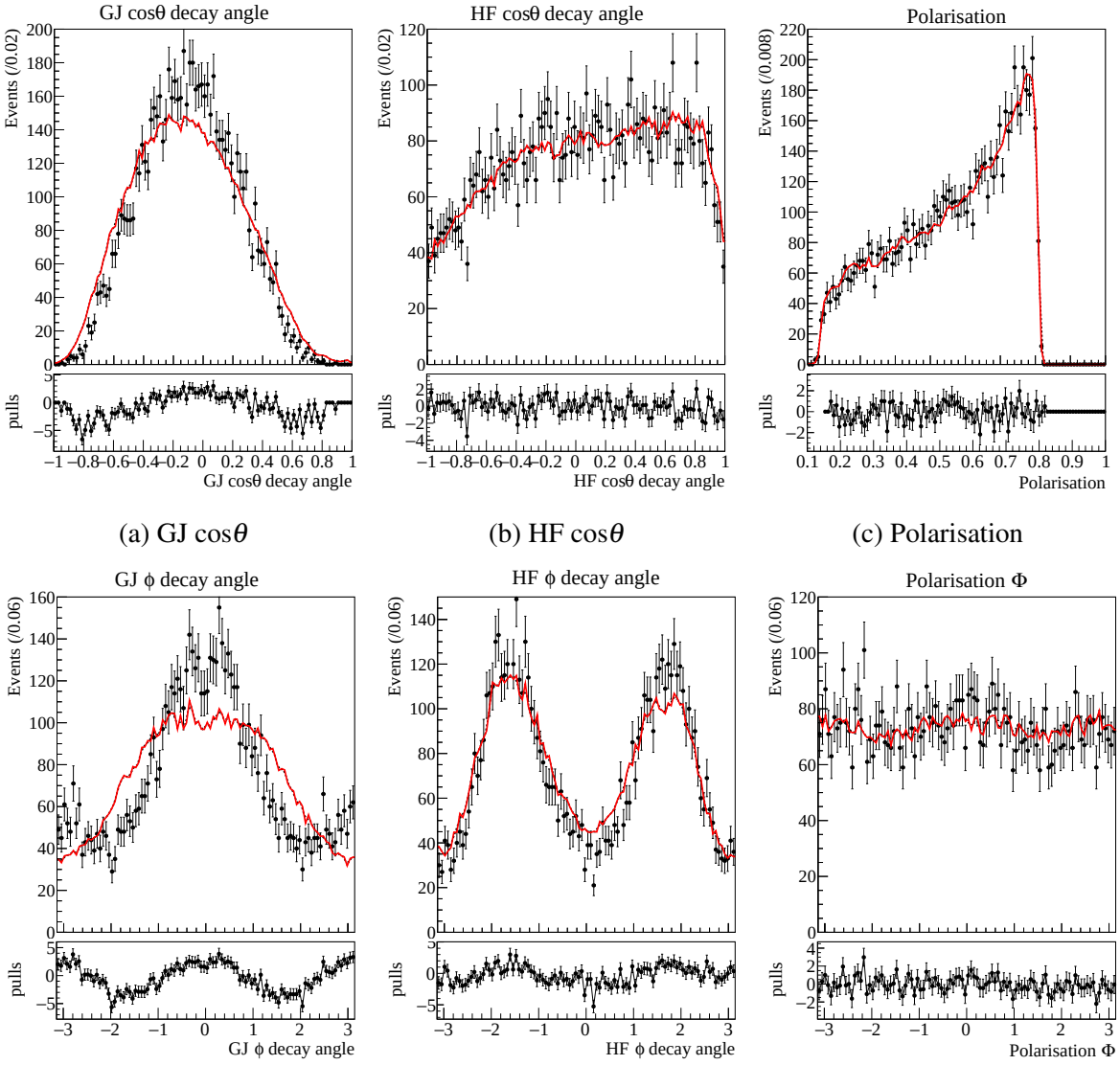

(a) GJ cosθ (b) HF cosθ (c) Polarisation

(d) GJ ϕ (e) HF ϕ (f) Polarisation Φ

Figure D.1: Visualisation of the fit parameters of a fit to toy data with only $J = 0, 1$ moments.

Appendix E

Validation of the MCMC Moments Fit

This Appendix contains a validation of the MCMC procedure that was used in Chapter 8 in terms of the criteria that were given in Chapter 6. To sample from the moments parameter space the RMS MCMC algorithm was used in five batches of moments of different J. Plots of the log likelihood vs chain entry are shown in Figure E.1. A short burn-in period could be used in the RMS matrix chain as the initial value of this chain was taken to be the end value from the sequential proposal chain. This is shown in Figure E.1 as the chain immediately begins fluctuating around a minimum in the log likelihood.

Although the RMS matrix approach reduced the chain autocorrelation, some autocorrelation still appears in these chains due to the large number of parameters that are being estimated in each MCMC. For this reason, 40,000 MCMC entries were specified so that the small autocorrelation in the chain did not bias the sampled distributions. For each of the moments fit, posterior distributions for a small number of the moments are shown in Figure E.2. These final distributions are indicative of convergent MCMC chains. This is reinforced by the subsequent Minuit fit that is shown in red in Figure E.2, the relative proximity of the Minuit minimiser to the mean of the MCMC samples is expected of chains that have suitably converged.

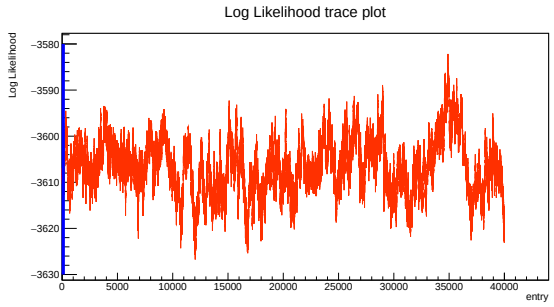

(a) $J = 2$ moments

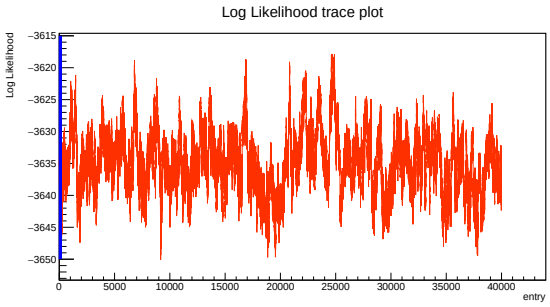

(b) $J = 3$ moments

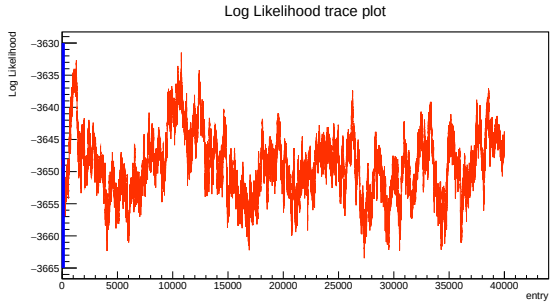

(c) $J = 4$ moments

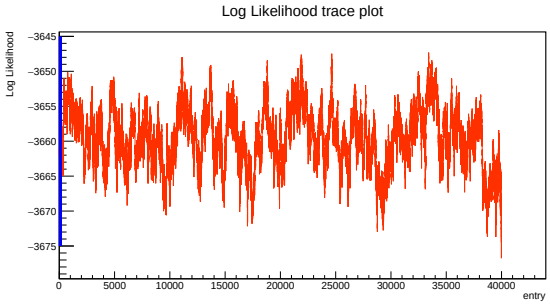

(d) $J = 5$ moments

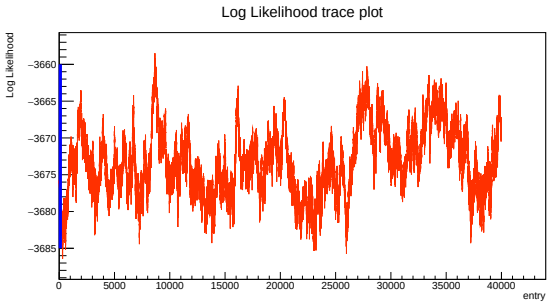

(e) $J = 6$ moments

Figure E.1: For each of the moments fits, the log likelihood is plotted vs chain entry. The burn in period is shown by the blue line at entry = 100.

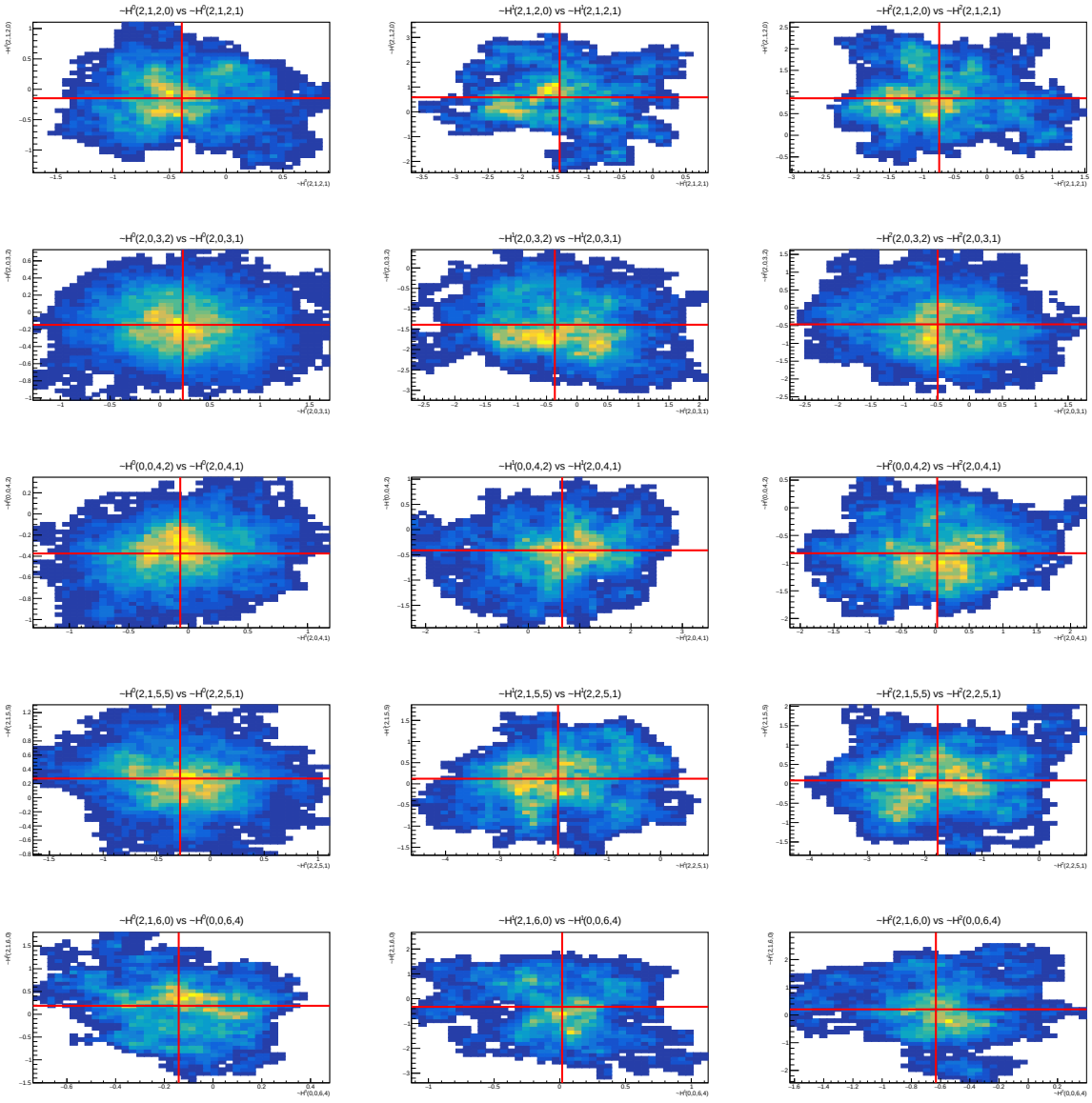

Figure E.2: The samples from the posterior distribution for a subset of the moments. Results from the subsequent Minuit fit are shown as the red lines.

Appendix F

Further Moments Results

As noted in Section 10.1.3, results could be extracted from data with the $\left(\frac{2J+1}{4\pi}\right)\left(\frac{2S+1}{4\pi}\right)$ terms removed, these were shown in Figure 11.1. Results for the moments with the $\left(\frac{2J+1}{4\pi}\right)\left(\frac{2S+1}{4\pi}\right)$ terms included are shown in Figure F.1.

It was also noted that the results shown in Figure 11.1 were found using the final value of the MCMC as the starting values for a minuit fit. Final values were quoted with the value of the moment taken from the minuit result and the error from the MCMC. It was not expected that the values from the minuit fit would vary in a large relative way compared to the result from the MCMC. Figure F.2 shows the results when the value of the moments were taken from the MCMC rather than a subsequent minuit fit. Some small variations in the values for the moments were seen compared to the minuit values with no significant change, as expected.

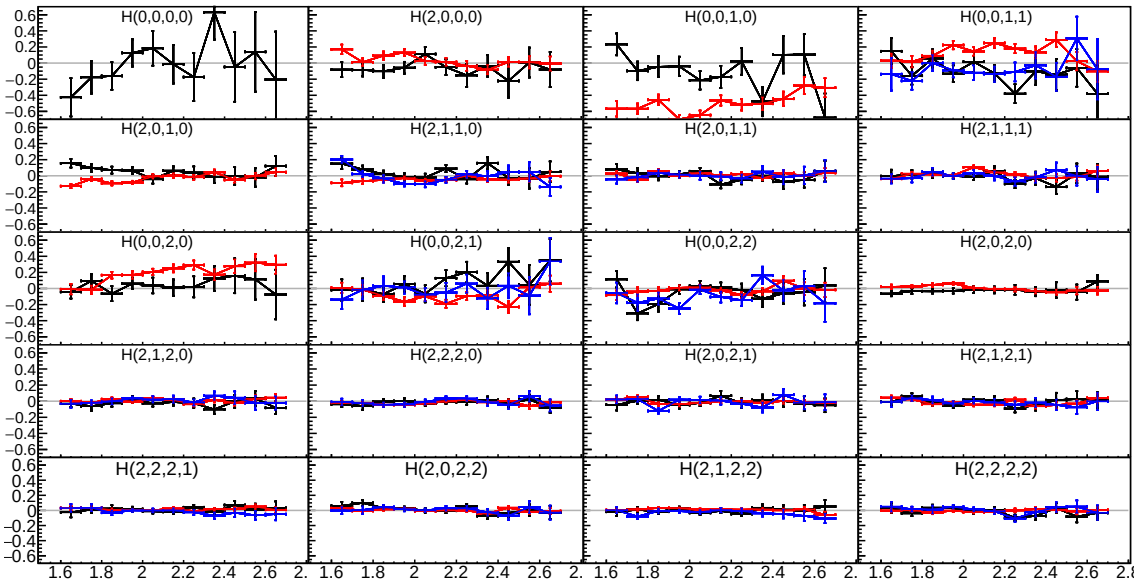

(a) $J = 2$ moments with $\alpha = 0$ - red, $\alpha = 1$ - black and $\alpha = 2$ - blue.

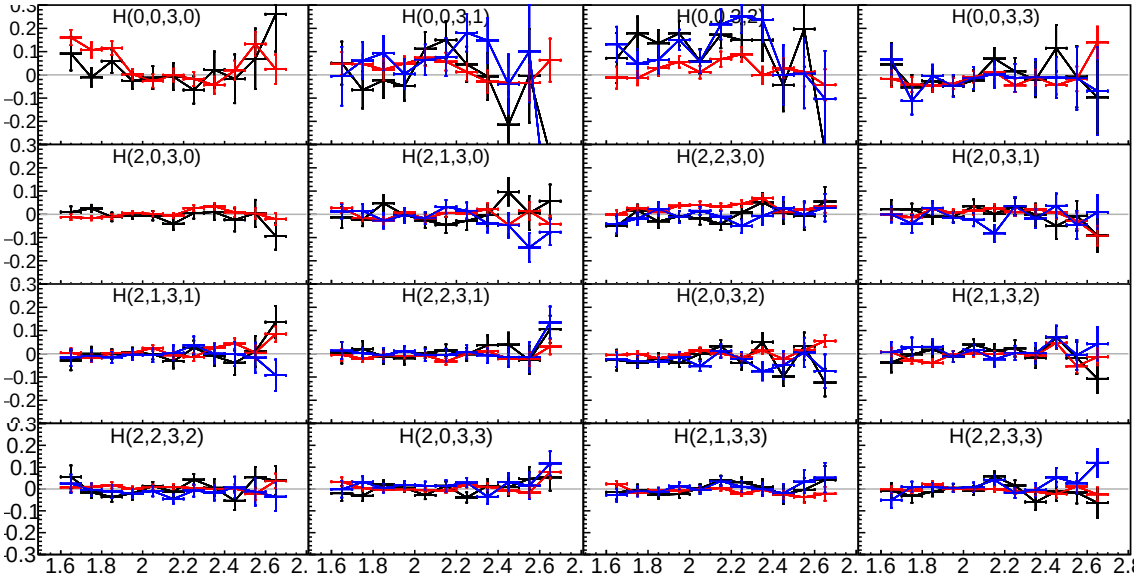

(b) $J = 3$ moments with $\alpha = 0$ - red, $\alpha = 1$ - black and $\alpha = 2$ - blue.

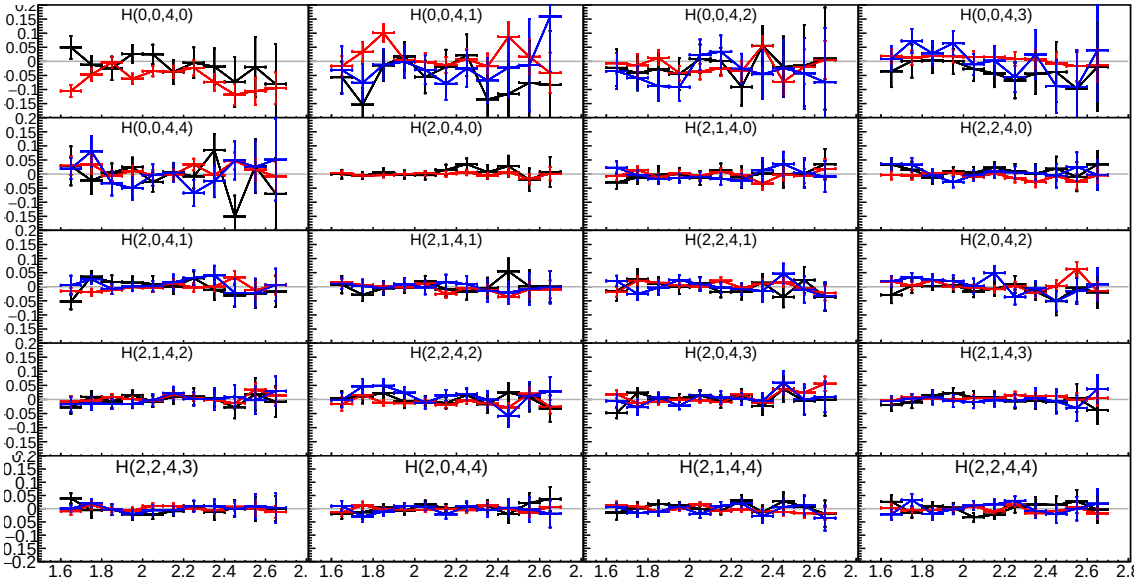

(c) $J = 4$ moments with $\alpha = 0$ - red, $\alpha = 1$ - black and $\alpha = 2$ - blue.

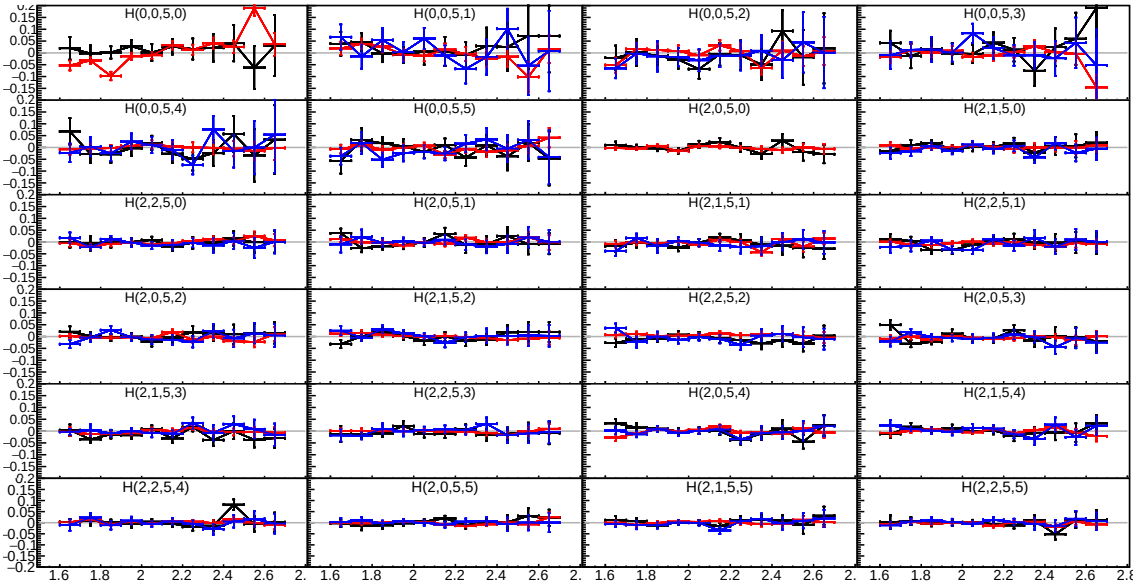

(d) $J = 5$ moments with $\alpha = 0$ - red, $\alpha = 1$ - black and $\alpha = 2$ - blue.

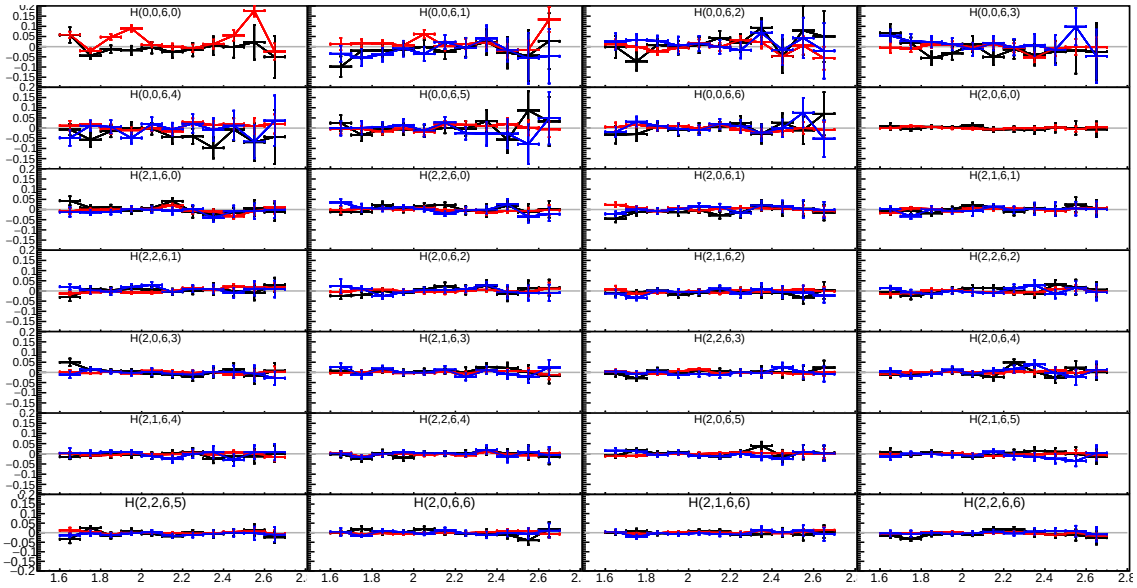

(e) $J = 6$ moments with $\alpha = 0$ - red, $\alpha = 1$ - black and $\alpha = 2$ - blue.

Figure F.1: Results from fitting the moments of angular distribution with $\left(\frac{2J+1}{4\pi}\right)\left(\frac{2S+1}{4\pi}\right)$ terms removed from the fit function. Polarisation components are shown with $\alpha = 0$ - red, $\alpha = 1$ - black and $\alpha = 2$ - blue.

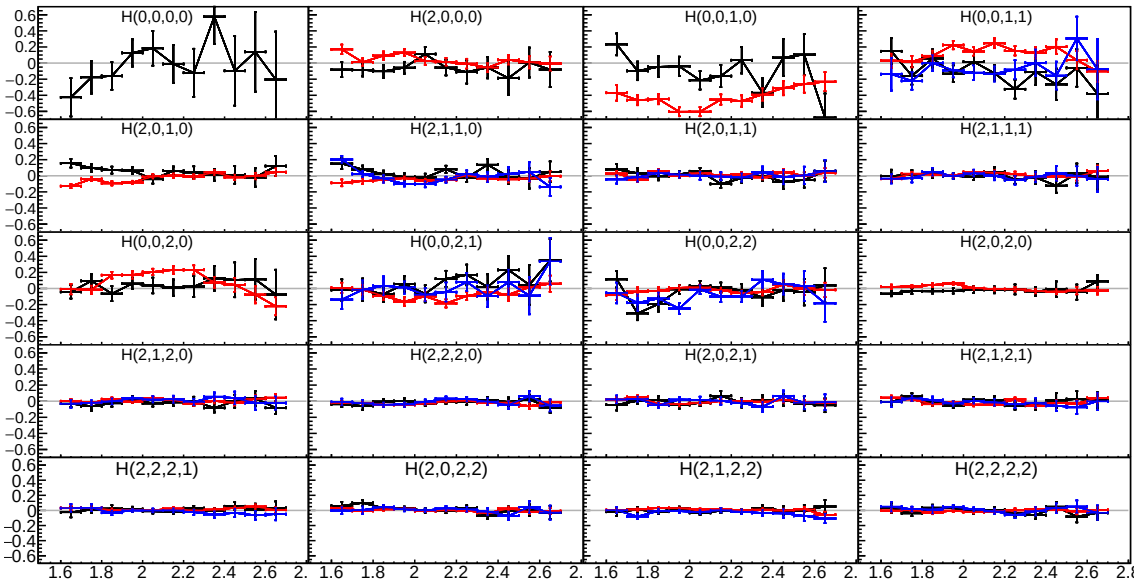

(a) $J = 2$ moments with $\alpha = 0$ - red, $\alpha = 1$ - black and $\alpha = 2$ - blue.

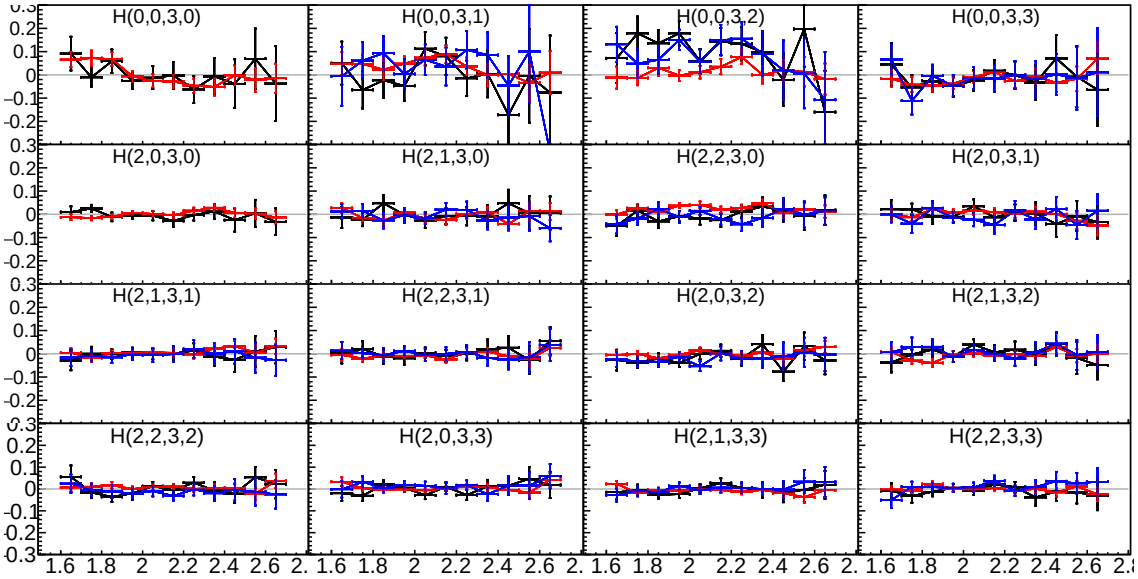

(b) $J = 3$ moments with $\alpha = 0$ - red, $\alpha = 1$ - black and $\alpha = 2$ - blue.

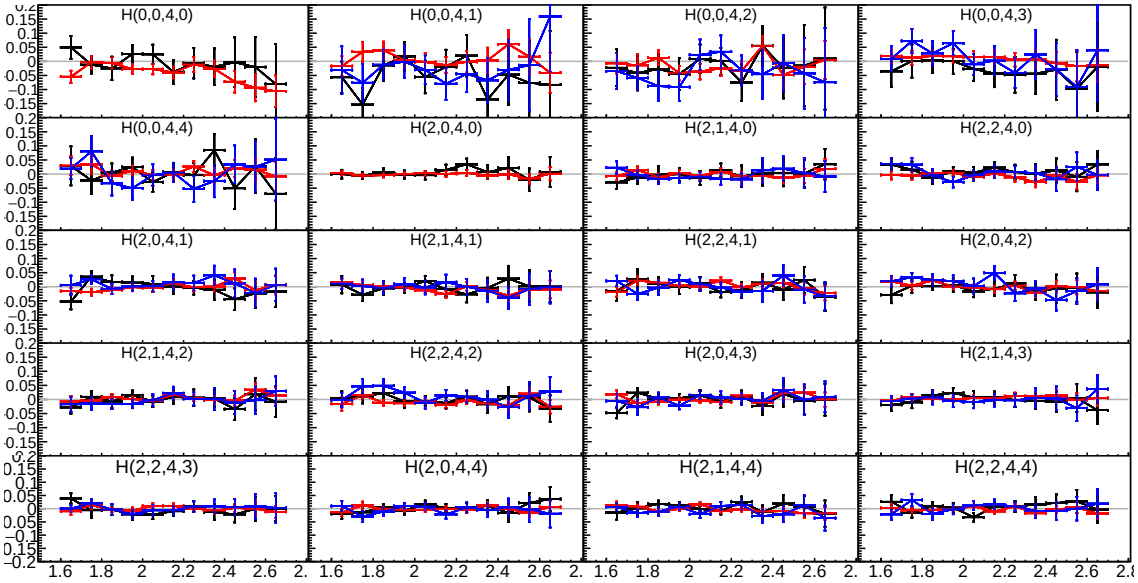

(c) $J = 4$ moments with $\alpha = 0$ - red, $\alpha = 1$ - black and $\alpha = 2$ - blue.

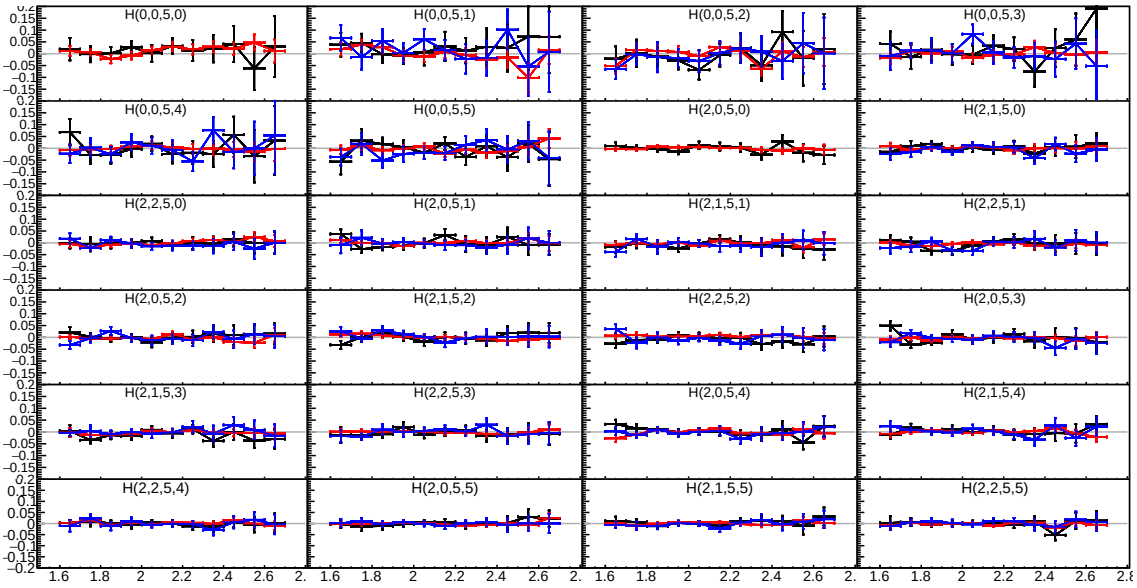

(d) $J = 5$ moments with $\alpha = 0$ - red, $\alpha = 1$ - black and $\alpha = 2$ - blue.

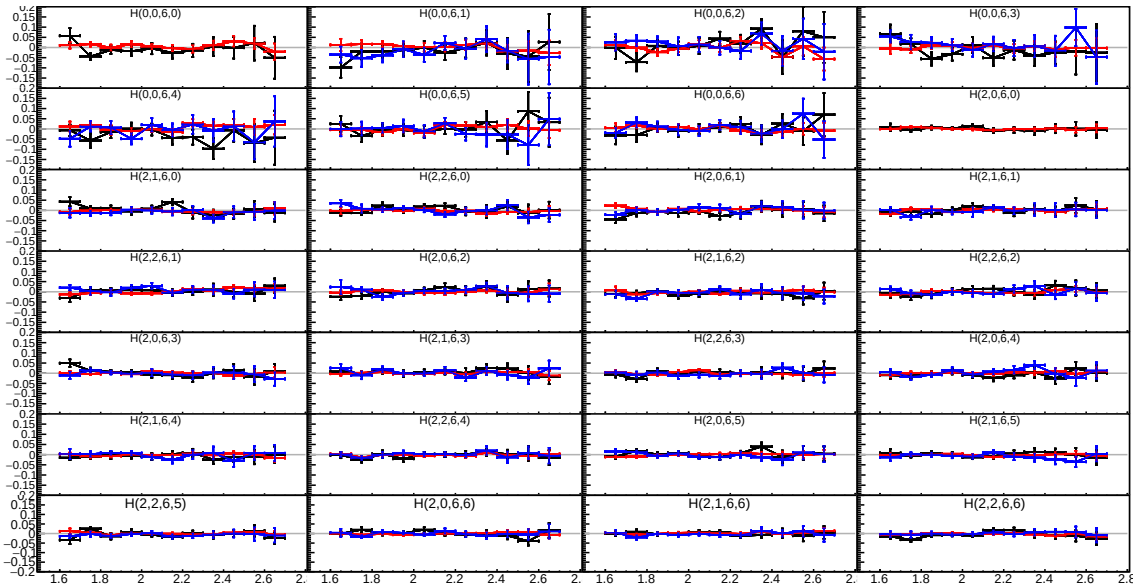

(e) $J = 6$ moments with $\alpha = 0$ - red, $\alpha = 1$ - black and $\alpha = 2$ - blue.

Figure F.2: Results from fitting the moments of angular distribution with results from the moments quoted from the MCMC rather than the minuit fit. Polarisation components are shown with $\alpha = 0$ - red, $\alpha = 1$ - black and $\alpha = 2$ - blue.

Bibliography

[1] S. Bethke. *The 2009 world average of α_S.* European Physics Journal C, 2009.

[2] Taken from Wikipedia. `https://en.wikipedia.org/wiki/Meson`. - Accessed on 28/06/23.

[3] J.J. Dudek et al. *Toward the excited isoscalar meson spectrum from lattice QCD.* arXiv:1309.2608 [hep-lat], 2013.

[4] A.J. Woss et al (Hadron Spectrum Collaboration). *Decays of an exotic 1^{-+} hybrid meson resonance in QCD.* Physical Review D **103**, 2021.

[5] D.R. Thompson et al. (The E852 Collaboration). *Evidence for Exotic Meson Production in the Reaction $\pi^- p \to \eta\pi^- p$ at 18 GeV/c.* Physical Review Letters **79**, 1997.

[6] G.M. Beladidze et al. (VES Collaboration). *Study of $\pi^- N \to \eta\pi^- N$ and $\pi^- N \to \eta'\pi^- N$ reactions at 37-GeV/c.* Phys. Lett B **313**, 1993.

[7] V. Dorofeev (VES Collaboration). *New Results from VES.* arXiv:hep-ex/9905002, 1999.

[8] G.S. Adams et al. (E852 Collaboration). *Observation of a New $J^{PC} = 1^{-+}$ Exotic State in the Reaction $\pi^- p \to \pi^+\pi^-\pi^- p$ at 18 GeV/c.* Physics Review Letters **81**, 1998.

[9] M. Aghasyan et al. (The COMPASS Collaboration). *Light isovector resonances in $\pi^- p \to \pi^-\pi^-\pi^+ p$ at 190 GeV/c.* Phys. Rev D **98**, 2018.

[10] A. Rodas et al. (Joint Physics Analysis Center). *Determination of the pole position of the lightest hybrid meson candidate.* arXiv:1810.04171v2 [hep-ph], 2019.

[11] M. Nozar et al. (CLAS Collaboration). *Search for the Photoexcitation of Exotic Mesons in the $\pi^+\pi^+\pi^-$ System.* Physical Review Letters **102**, 2009.

[12] M. Atkinson et al. (The Omega Photon Collaboration). *A SPIN-PARITY ANALYSIS OF THE $\omega\pi^0$ ENHANCEMENT PHOTOPRODUCED IN THE ENERGY RANGE 20 TO 70 GeV.* Nuclear Physics B243, 1984.

[13] G.D. Alexeev et al. *Triangle Singularity as the Origin of the $a_1(1420)$*. Physical Review Letters **127**, 2021.

[14] A. Celentano. *The BDX Experiment at Jefferson Laboratory*. EPJ Web of Conferences, 2015.

[15] Taken from Wikipedia. `https://en.wikipedia.org/wiki/Thomas_Jefferson_National_Accelerator_Facility`. - Accessed on 28/06/23.

[16] S. Stepanyan et al. *The CLAS12 beamline and its performance*. Nuclear Inst. and Methods in Physics Research A, 2020.

[17] R. Fair et al. *The CLAS12 superconducting magnets*. Nuclear Inst. and Methods in Physics Research A, 2020.

[18] V. Burkert et al. *The CLAS12 Spectrometer at Jefferson Laboratory*. Nuclear Inst. and Methods in Physics Research A, 2020.

[19] D.S. Carman et al. *The CLAS12 Central Time-of-Flight System*. Nuclear Inst. and Methods in Physics Research, A, 2020.

[20] P. Chatagnon et al. *The CLAS12 Central Neutron Detector*. Nuclear Inst. and Methods in Physics Research, A, 2020.

[21] M. Mestayer et al. *The CLAS12 drift chamber system*. Nuclear Inst. and Methods in Physics Research, A, 2020.

[22] C. Smith et al. *The CLAS12 forward electromagnetic calorimeter*. Nuclear Inst. and Methods in Physics Research, A, 2020.

[23] M. Battaglieri et al. *The CLAS12 Forward Tagger*. Nuclear Inst. and Methods in Physics Research, A, 2020.

[24] Simon Funke. `https://fenicsproject.org/pub/course/lectures/2017-nordic-phdcourse/lecture_14_from_sensitivities_to_optimisation.pdf`. - accessed 29/06/23.

[25] `https://www.turing.ac.uk/research/research-projects/adaptive-multilevel-mcmc-sampling`. - last accessed: 18/04/2023.

[26] `https://bookdown.org/marklhc/notesbookdown/markov-chain-monte-carlo.html`. - last accessed: 18/04/2023.

[27] J. Greensite. *An introduction to the confinement problem. Lecture Notes in Physics. Vol. 821*. Springer, 2011.

[28] D. Griffiths. *Introduction to Elementary Particles*. John Wiley and Sons, 1987.

[29] C. Patrignani et al (Particle Data Group). *Chin. Phys. C, 40.* 100001, 2016.

[30] D. Gross and F. Wilczek. *Asymptotically Free Gauge Theories I.* Physical Review D., 1973.

[31] D. Gross and F. Wilczek. *Ultraviolet Behaviour of Non-Abelian Gauge Theories.* Physical Review Letters, 1973.

[32] D. Politzer. *Asymptotic freedom: An approach to Strong Interactions*. Physical Review Letters, 1973.

[33] Nobel Web. *The Nobel Prize in Physics 2004*. - last accessed: 18/04/2023.

[34] W. Fulton. *Young Tableaux: with Applications to Representation Theory and Geometry*. Cambridge University Press, 1997.

[35] A. Chodos et al. *New extended model of hadrons*. Physical Review D **9**, 1974.

[36] T. Barnes. *Exotic Mesons, Theory and Experiment*. arXiv:hep-ph/0007296v1, 2000.

[37] N. Isgur and J. Paton. *Flux-tube model for hadrons in QCD*. Physical Review D **31**, 1985.

[38] K.G. Wilson. *Confinement of quarks*. Phys. Rev. D **10**, 1974.

[39] A. Bazavov et al. *Nonperturbative QCD simulations with 2+1 flavors of improved staggered quarks*. Reviews of Modern Physics **82**, 2010.

[40] H. Wittig. *QCD on the Lattice. In: Schopper H. (eds) Particle Physics Reference Library.* Springer, Cham, 2020.

[41] S. Dürr; Z. Fodor and J. Frison. *Ab Initio Determination of Light Hadron Masses*. Science **322**, 2008.

[42] J.J. Dudek et al. (Hadron Spectrum Collaboration). *Toward the excited meson spectrum of dynamical QCD*. Phys. Rev. D **82**, 2010.

[43] C.A. Meyer and Y. Van Haarlem. *The Status of Exotic-quantum-number Mesons*. arXiv:1004.5516v2 [nucl-ex], 2010.

[44] J.J. Dudek et al. (Hadron Spectrum Collaboration). *Toward the excited isoscalar meson spectrum from lattice QCD*. Phys. Rev. D **88**, 2013.

[45] A.P. Szczepaniak and M. Swat. *ROLE OF PHOTOPRODUCTION IN EXOTIC MESON SEARCHES*. Phys. Lett. B **516**, 2001.

[46] D. Alde et al. *EVIDENCE FOR A* 1^{-+} *EXOTIC MESON*. Physics Letters B, **205**, 1988.

[47] H. Aoyagi et al. *Study of the* $\eta\pi^-$ *system in the* $n-p$ *reaction at 6.3 GeV/c*. Physics Letter B **314**, 1993.

[48] D.V. Amelin et al. (VES Collaboration). *STUDY OF RESONANCE PRODUCTION IN DIFFRACTIVE REACTION* $\pi^- A \to \pi^+\pi^-\pi^- A$. Phys. Lett., 1995.

[49] C. Amsler. *Proton-antiproton annihilation and meson spectroscopy with the Crystal Barrel*. Rev. Mod. Phys. **70**, 1998.

[50] A.R. Dzierba et al. *A partial wave analysis of the* $\pi^-\pi^-\pi^+$ *and* $\pi^-\pi^0\pi^0$ *systems and the search for a* $J^{PC} = 1^{-+}$ *meson*. Phys. Rev. D **73**, 2006.

[51] C.A. Meyer and E.S. Swanson. *Hybrid Mesons*. arXiv:1502.07276v2 [hep-ph], 2015.

[52] C.Adolph et al. (The COMPASS Collaboration). *Odd and Even partial waves of* $\eta\pi^-$ *and* η' *in* $\pi^- p \to \eta^{(\prime)}\pi^- p$. Physics Letters B. **740**, 2015.

[53] A. Afanasev and P.R. Page. *Photo– and Electroproduction of* $J^{PC} = 1^{-+}$ *exotics*. Phys. Rev. D **57**, 1998.

[54] P. Eugenio et al. (CLAS Collaboration). *Search for Exotic Mesons in Photoproduction at JLAB CLAS*. AIP Conf. Proc. **1560**, 2013.

[55] A. Foda. *Photoproduction of the* $b1(1235)$ *Meson off the proton at Egamma = 6-12 GeV*. Thesis: PhD Univ. of Regina, SK (Canada), Regina U., 2021.

[56] S.K. Choi et al. (Belle Collaboration). *Observation of a Narrow Charmoniumlike State in Exclusive* $B\pm \to K\pm\pi+-J/\psi$ *Decays*. Physical Review Letters. **91**, 2003.

[57] *Oddball Particle Surprises Physicists at Fermilab*. redOrbit, 2009.

[58] S.K. Choi et al. (Belle Collaboration). *Observation of a resonance-like structure in the* $\pi^\pm\Psi'$ *mass distribution in exclusive* $B \to K\pi^\pm\Psi'$ *decays*. Physical Review Letters **100**, 2008.

[59] R. Aaij et al. (LHCb Collaboration). *Observation of New Resonances Decaying to* $J/\psi K+$ *and* $J/\psi\phi$. Physical Review Letters **127**, 2021.

[60] *Observation of a strange pentaquark, a doubly charged tetraquark and its neutral partner*. CERN, 2022.

[61] C. Hovater et al. *OPERATION OF THE C100 MV CRYOMODULES*. Proceedings of the LINAC2016, East Lansing, MI, USA, 2017.

[62] A. Freyberger. *Commission and Operation of 12 GeV CEBAF*. 6th International Particle Accelerator Conference (IPAC 2015), 2015.

[63] T. Allison et al. *CEBAF SRF Performance During Initial 12 GeV Commisioning*. 6th International Particle Accelerator Conference (IPAC 2015), 2015.

[64] B.A. Mecking et al. *The CEBAF Large Acceptance Spectrometer (CLAS)*. Nuclear Instruments and Methods in Physics Research A, 2003.

[65] M. Mestayer et al. *The CLAS12 drift chamber system*. Nucl. Instrum. Methods A, 2020.

[66] S. Stepanyan. *Radiological Safety Analysis Document for the Hall B CLAS12 Run Group A And K Run*. Radiation Control Department, JLab, 2018.

[67] Y. Gotra et al. *The CLAS12 Silicon Vertex Tracker*. Nuclear Inst. and Methods in Physics Research, A, 2020.

[68] Y.G. Sharabian et al. *The CLAS12 high threshold Cherenkov counter*. Nuclear Inst. and Methods in Physics Research, A, 2020.

[69] D.S. Carman et al. *The CLAS12 Forward Time-of-Flight system*. Nuclear Inst. and Methods in Physics Research, A, 2020.

[70] M. Amarian et al. *The CLAS forward electromagnetic calorimeter*. Nuclear Instruments and Methods in Physics Research Section A: Accelerators, Spectrometers, Detectors and Associated Equipment, 2001.

[71] A. Acker et al. *The CLAS12 Micromegas vertex tracker*. Nuclear Inst. and Methods in Physics Research, A, 2020.

[72] S. Boyarinov et al. *The CLAS12 Data Acquisition System*. Nuclear Inst. and Methods in Physics Research, A, 2020.

[73] B. Ketzer et al. *Light-Meson Spectroscopy with COMPASS*. arXiv:1909.06366 [hep-ex], 2019.

[74] C. W. Salgado and D.P. Weygand. *On the Partial-Wave Analysis of Mesonic Resonances Decaying to Multiparticle Final States Produced by Polarized Photons*. arXiv:1310.7498 [nucl-ex], 2018.

[75] F.Halzen and A.Martin. *Quarks & Leptons: An Introductory Course in Modern Particle Physics*. J.Wiley and Sons, 1984.

[76] N. Dombey. *Scattering of Polarised Leptons at High Energy*. Rev. Mod. Phys. **41**, 1969.

[77] K. Schilling and G. Wolf. *How to analyse vector-meson production in inelastic lepton scattering*. Nuclear Physics B, Vol 61, 1973.

[78] V. Mathieu et al. *Moments of angular distribution and beam asymmetries in $\eta\pi_0$ photoproduction at GlueX*. arXiv:1906.04841v2 [hep-ph], 2019.

[79] C.W. Salgado and V. Mathieu. *Comparing Formalisms for the Analysis of Two-pseudoscalar Mesons Produced by Linearly Polarized Photons*. 2020.

[80] S.U. Chung. *Spin Formalisms (Updated Version)*. Brookhaven National Laboratory, 2014.

[81] P.A. Zyla et al. (Particle Data Group). *The Review of Particle Physics*. Prog. Theor. Exp. Phys. (2020 and 2021 update), 2021.

[82] C. Bookwalter. *Ph.D. thesis - The Search for Exotic Mesons in $\gamma p \to \pi^+\pi^+\pi^- n$ with CLAS at Jefferson Lab*. 2012.

[83] R. Escribano et al. *On the mass, width and coupling constants of the $f_0(980)$*. arXiv:hep-ph/0204338, 2003.

[84] F. James. *Minuit - Function Minimization and Error Analysis*. CERN Reference Manual, 1994.

[85] J. Backus. *The History of FORTRAN I, II and III*. Academic Press Inc., 1981.

[86] R. Bruns and F. Rademakers. *ROOT - Data Analysis Framework*. A CERN maintained program library, 1994.

[87] K.P. Murphy. *Machine Learning: A Probabilistic Perspective*. 2012.

[88] G.A Barnard. *Thomas Bayes - a biographical note*. Biometrika **45**, 1958.

[89] P. Frame. *Liberty's Apostle - Richard Price, His Life and Times*. University of Wales Press, 2015.

[90] W. R. Gilks A. Gelman and G. O. Roberts. *Weak convergence and optimal scaling of random walk Metropolis algorithms*. Ann. Appl. Prob., 1997.

[91] A. Sokal. *Monte Carlo Methods in Statistical Mechanics: Foundations and New Algorithms*. Lectures at the Cargèse Summer School on 'Functional Integration: Basics and Applications', 1996.

[92] P.J. Rousseeuw and K. Van Dreissen. *A Fast Algorithm for the Minimum covariance Determinant Estimator*. Technometrics, August 1999, Vol 41., 1999.

[93] G. Gavalian. https://github.com/gavalian/hipo. - last accessed: 18/04/2023.

[94] D. Glazier. https://github.com/dglazier/chanser. - last accessed: 18/04/2023.

[95] Jefferson Lab software. https://github.com/JeffersonLab/clas12root. - last accessed: 18/04/2023.

[96] L. Elouadrhiri et al. CLAS12 RG-A - Analysis Note Overview and Procedures. https://clas12-docdb.jlab.org/DocDB/0007/000732/001/RGA_Analysis_Overview_and_Procedures-14.pdf, 2020.

[97] A. Rogozhnikov. http://arogozhnikov.github.io/2015/10/07/splot.html, 2015. - last accessed: 18/04/2023.

[98] M. Pivk and F.R. LeDiberder. *sPlot: A statistical tool to unfold data distributions"*. Nuclear Instruments and Methods in Physics Research Section A: Accelerators, Spectrometers, Detectors and Associated Equipment, 2005.

[99] RooStats. https://root.cern/doc/master/groupRoostats.html. - last accessed: 18/04/2023.

[100] D. Glazier. https://github.com/dglazier/brufit. - last accessed: 18/04/2023.

[101] R. Aaij et al. *Observation of $J/\psi p$ Resonances Consistent With Pentaquark States in $\Lambda_b^0 \to J/\psi K^- p$ Decays*. Physical Review Letters, 115(7), 2015.

[102] S. Gardner et al. *Photon asymmetry measurements of $\gamma p \to \pi^0 p$ for $E_\gamma = 320 - 650$ MeV*. The European Physical Journal A, 52(11), 2016.

[103] D. Glazier. https://github.com/dglazier/elSpectro. - last accessed: 18/04/2023.

[104] gemc. https://gemc.jlab.org/gemc/html/index.html. - last accessed: 18/04/2023.